UNIVERSITAT POLITÈCNICA DE VALÈNCIA

DEPARTAMENT DE COMUNICACIONS

Distributed Radiofrequency Signal Processing based on Space-Division Multiplexing Fibers

PhD THESIS

Sergi García Cortijo

Supervisors:

Ivana Gasulla Mestre

José Capmany Francoy

València, June 11th 2020

A ma mare.

A les meues àvies.

Agradecimientos

En primer lugar, me gustaría agradecer a mis directores de Tesis, Ivana y José, por darme la oportunidad de realizar esta Tesis doctoral. Han pasado ya 6 años desde aquel 2014 en que empezamos esta nueva etapa con la realización de mi proyecto fin de carrera, que siguió en 2015 con el trabajo fin de máster, y que finaliza ahora con esta Tesis doctoral. Han sido unos años en los que he aprendido mucho y ha sido un placer formar parte de este grupo de investigación. En particular, quisiera agradecer a Ivana la dedicación y la ayuda que me ha proporcionado durante todos estos años.

Me gustaría agradecer también a todos/as mis compañeros/as del PRL por estos años, donde el buen ambiente y el compañerismo ha destacado por encima de todo. En especial, al "equipo de básquet", Mario y Rubén, y a Javi, por todos esos buenos coloquios, cafés, almuerzos y momentos en el laboratorio.

Agradezco al Ministerio de Economía y Competitividad del Gobierno de España por la financiación recibida mediante la ayuda FPI.

También quisiera dar las gracias a todos mis compañeros durante mi estancia en CREOL, Rodrigo, Enrique, Juan Carlos, Daniel, Selim, … Pero en especial a Stefan y Steffen, que desde el primer día me hicisteis sentir uno más. Y a mi compañero de estancia, Andrés, por toda la ayuda y buenos consejos.

Por supuesto, a Natalia. Gracias por estar siempre ahí (y sí, también por aguantarme todos estos años). Al "Peña team", Marcos, Alex y mi hermano, Álvaro, que, aunque estemos dispersos, siempre nos quedará la volta a peu. A mi padre, y a mi familia. Gracias a todas y todos, porque siempre me habéis apoyado y confiado en mí.

Y, por último, a mi madre. Porque sin ti nunca hubiese llegado hasta aquí. Porque siempre te has sacrificado por nosotros; no importa que fuese Paterna, Barcelona o Girona, que tú siempre nos has acompañado. Y porque eres (y serás) la mejor profesora que he tenido.

Abstract

Space-division multiplexing fibers emerged as a promising solution to overcome the imminent capacity crunch of conventional singlemode fiber networks. Despite these fibers were initially conceived as distribution media for long-haul high-capacity digital communications, they can be applied to a wide variety of scenarios including centralized radio access networks for wireless communications, data-center interconnects, Microwave Photonics signal processing and fiber sensing. Particular interest is raised by emerging communications paradigms, such as 5G and The Internet of Things, which require a full integration between the optical fiber and the wireless networks segments. Microwave Photonics, discipline that focuses on the generation, processing, control and distribution of radiofrequency signals by photonics means, is called to play a decisive role. One of the major challenges that Microwave Photonics has to overcome to satisfy next-generation communication demands relates to the reduction of size, weight and power consumption while assuring broadband seamless reconfigurability and stability. There is one revolutionary approach that has however been left untapped in finding innovative ways to address that challenge: exploiting space, the last available degree of freedom for optical multiplexing.

In this Thesis, we propose to exploit the inherent parallelism of multicore and few-mode fibers to implement sampled discrete true time delay lines, providing, in a single optical fiber, a compact and efficient approach for both Microwave Photonics signal distribution and processing. For the multicore fiber approach, we study the influence of the refractive index profile of each heterogeneous core on the propagation characteristics as to feature specific group delay and chromatic dispersion values. We designed and fabricated two different heterogeneous trench-assisted 7-core fibers that behave as sampled true time delay lines. While one of them was fabricated by using 7 different preforms to feature a plenary performance, the other one employed a single preform with the aim of minimizing fabrication costs. In the case of few-mode fibers, we propose the implementation of a tunable true time delay line by means of a custom-designed fiber with a set of inscribed long period gratings that act as mode converters to properly tailor the sample group delays. We designed and fabricated a true time delay line on a 4-mode fiber by inscribing 3 long period gratings at specific positions along the fiber link. As a proof-of-concept validation, we experimentally demonstrated different Microwave Photonics signal processing functionalities implemented over both multicore and few-mode fiber

approaches. This work opens the way towards the development of distributed signal processing for microwave and millimeter wave signals in a single optical fiber. These true time delay lines can be applied to a wide range of Information and Communication Technology paradigms besides fiber-wireless communications such as broadband satellite communications, distributed sensing, medical imaging, optical coherence tomography and quantum communications.

Resumen

La multiplexación por división espacial en fibras ópticas surgió como una solución prometedora al inminente colapso en la capacidad de las redes de fibra monomodo convencionales. Aunque estas fibras fueron concebidas inicialmente como medio de distribución en comunicaciones digitales de larga distancia y alta capacidad, pueden emplearse en una amplia variedad de escenarios, incluyendo redes de acceso radio centralizadas para comunicaciones inalámbricas, interconexiones en centros de datos, así como procesado de señal en Fotónica de Microondas y sensado en fibra. Los paradigmas de comunicaciones emergentes despiertan un interés particular, como 5G y el Internet de las Cosas, que requieren una integración total entre el segmento de red de fibra óptica y el inalámbrico. La Fotónica de Microondas, disciplina que se focaliza en la generación, procesado, control y distribución de señales de radiofrecuencia por medio de la fotónica, está destinada a jugar un papel decisivo. Uno de los mayores desafíos que la Fotónica de Microondas debe superar para satisfacer los requisitos de las nuevas generaciones de comunicaciones se basa en la reducción de tamaño, peso y consumo de potencia, mientras se garantiza reconfiguración y estabilidad de banda ancha. Encontramos aquí un enfoque revolucionario capaz de abordar este desafío de una manera innovadora que, sin embargo, no ha sido aprovechado en este contexto: la explotación del espacio, el último grado de libertad para multiplexación óptica.

En esta Tesis, proponemos explotar el paralelismo inherente de las fibras ópticas multinúcleo y de pocos modos para implementar líneas de retardo en tiempo real muestreadas que proporcionan, en una sola fibra óptica, una solución compacta y eficiente tanto para distribución como para procesado de señales de Fotónica de Microondas. En el caso de fibras multinúcleo, estudiamos la influencia del perfil de índice de refracción de cada núcleo heterogéneo en las características de propagación para que exhiba unos valores concretos de retardo de grupo y dispersión cromática. Diseñamos y fabricamos dos fibras distintas de 7 núcleos con zanjas que se comportan como líneas de retardo en tiempo real muestreadas. Mientras que una de ellas se fabricó utilizando 7 preformas diferentes para garantizar un funcionamiento completo, la segunda se fabricó utilizando una única preforma con el objetivo de minimizar costes de fabricación. En el caso de fibras de pocos modos, proponemos la implementación de líneas de retardo en tiempo real sintonizables mediante el uso de una fibra específicamente diseñada y la inscripción de un conjunto de redes de difracción de periodo largo que actúan como conversores de modos para ajustar

adecuadamente el retardo de grupo de las muestras. Diseñamos y fabricamos una línea de retardo en tiempo real en una fibra de 4 modos mediante la inscripción de 3 redes de difracción de periodo largo en posiciones concretas a lo largo de enlace de fibra. Como validación de prueba de concepto, demostramos experimentalmente diferentes funcionalidades de procesado de señal de Fotónica de Microondas implementadas en fibras multinúcleo y de pocos modos. Este trabajo abre el camino hacia el desarrollo del procesado de señal distribuido para señales de microondas y ondas milimétricas en una única fibra óptica. Además, las líneas de retardo en tiempo real desarrolladas pueden aplicarse a una amplia variedad de paradigmas de Tecnologías de la Información y Comunicaciones más allá de las comunicaciones radio sobre fibra, como es el caso de las comunicaciones de banda ancha por satélite, el sensado distribuido, la imagen médica, la tomografía óptica coherente y las comunicaciones cuánticas.

Resum

La multiplexació per divisió espacial en fibres òptiques va sorgir com una solució prometedora a l'imminent col·lapse en la capacitat de les xarxes de fibra monomode convencionals. Encara que estes fibres foren concebudes inicialment com a mitjà de distribució en comunicacions digitals de llarga distància i alta capacitat, poden emprar-se en una àmplia varietat d'escenaris, incloent xarxes d'accés radio centralitzades per a comunicacions sense fils, interconnexions en centres de dades, així com processat de senyal en Fotònica de Microones i sensat en fibra. Els paradigmes de comunicacions emergents desperten un interès particular, com el 5G i la Internet de les Coses, que requereixen una integració total entre els segments de xarxa de fibra òptica i el de sense fils. La Fotònica de Microones, disciplina que es focalitza en la generació, processat, control i distribució de senyals de radiofreqüència per mitjà de la fotònica, està destinada a jugar un paper decisiu. Un dels majors desafiaments que la Fotònica de Microones ha de superar per satisfer els requisits de les noves generacions de comunicacions es basa en la reducció de grandària, pes i consum de potència, mentre es garanteix reconfiguració i estabilitat de banda ampla Trobem ací un enfocament revolucionari capaç d'abordar aquest desafiament d'una manera innovadora que, no obstant això, no ha sigut aprofitat encara en este context: la explotació de l'espai, l'últim grau de llibertat per a multiplexat òptic.

En aquesta Tesi, proposem explotar el paral·lelisme inherent de les fibres òptiques multinucli i de pocs modes per a implementar línies de retard en temps real de mostres discretes que proporcionen, en una sola fibra òptica, una solució compacta i eficient tant per a distribució com per a processat de senyals de Fotònica de Microones. En el cas de fibres multinucli, estudiem la influència del perfil d'índex de refracció de cada nucli heterogeni en les característiques de propagació perquè exhibisca uns valors concrets de retard de grup i dispersió cromàtica. Dissenyem i fabriquem dues fibres distintes de 7 nuclis amb rases que es comporten com a línies de retard en temps real mostrejades. Mentre que una d'elles es va fabricar utilitzant 7 preformes diferents per a garantir un funcionament complet, la segona va fabricar-se utilitzant una única preforma amb l'objectiu de minimitzar costos de fabricació. En el cas de fibres de pocs modes, proposem la implementació de línies de retard en temps real sintonitzables mitjançant l'ús d'una fibra específicament dissenyada i la inscripció d'un conjunt de xarxes de difracció de període llarg que actuen com a convertidors de modes per tal d'ajustar adequadament el retard de grup de les mostres. Dissenyem

i fabriquem una línia de retard en temps real en una fibra de 4 modes mitjançant la inscripció de 3 xarxes de difracció de període llarg en posicions concretes al llarg de l'enllaç de fibra. Com a validació de proba de concepte, demostrem experimentalment diferents funcionalitats de processat de senyal de Fotònica de Microones implementades en fibres multinucli i de pocs modes. Aquest treball obri el camí cap al desenvolupament del processat de senyal distribuït per a senyals de microones i ones mil·limètriques en una única fibra òptica. A més, aquestes línies de retard en temps real poden aplicar-se a una àmplia varietat de paradigmes de Tecnologies de la Informació i Comunicacions més enllà de les comunicacions radio sobre fibra, com es el cas de les comunicacions de banda ampla per satèl·lit, el sensat distribuït, la imatge mèdica, la tomografia òptica coherent i les comunicacions quàntiques.

Contents

List of Figures

List of Tables

List of Acronyms

AF: Array Factor

ASE: Amplified Spontaneous Emission

BS: Broadband Source

CME: Coupled Mode Equation

CMT: Coupled Mode Theory

CPE: Coupled Power Equation

CPT: Coupled Power Theory

C-RAN: Centralized (or Cloud) Radio Access Network

CSE: Carrier Suppression Effect

DGD: Differential Group Delay

DMGD: Differential Mode Group Delay

DPO: Digital Phosphor Oscilloscope

DSP: Digital Signal Processing

EDFA: Erbium Doped Fiber Amplifier

EOM: Electro-Optic Modulator

FBG: Fiber Bragg Grating

FIR: Finite Impulse Response

FMF: Few-Mode Fiber

FM-MCF: Few-Mode Multicore Fiber

FSR: Free Spectral Range

FUT: Fiber Under Test

GI: Graded-Index

IIR: Infinite Impulse Response

IoT: Internet of Things

LP: Linearly Polarized

LPG: Long Period Grating

MCC: Mode Coupling Coefficient

MCF: Multicore Fiber

MIMO: Multiple-Input Multiple-Output

mm-Wave: Millimeter-Wave

MWP: Microwave Photonics

OSA: Optical Signal Analyzer

PCC: Power Coupling Coefficient

PD: Photodetector

PDM: Polarization-Division Multiplexing

PON: Passive Optical Network

RAN: Radio Access Network

RCF: Ring-Core Fiber

RF: Radiofrequency

RIN: Relative Intensity Noise

RoF: Radio-over-Fiber

SDM: Space-Division Multiplexing

SEM: Scanning Electron Microscope

SI: Step-Index

SMF: Singlemode Fiber

SWaP: Size, Weight and Power consumption

TA: Trench-Assisted

TDM: Time-Division Multiplexing

TE: Transverse Electric

TM: Transverse Magnetic

TTDL: True Time Delay Line

UV: Ultra-Violet

VDL: Variable Delay Line

VNA: Vector Network Analyzer

VOA: Variable Optical Attenuator

VSG: Vector Signal Generator

WDM: Wavelength-Division Multiplexing

WLS: White-Light Source

5G: 5^{th} Generation

Chapter 1
Introduction and Thesis objectives

1.1. Introduction

Next-generation Information Technology paradigms, such as 5G & Beyond wireless communications and the Internet of Things (IoT) have originated new challenges to existing communication networks, [1, 2, 3, 4, 5, 6, 7]. Exigent demand requirements are envisaged in terms of cell coverage (from a few meters up to several kilometers), number of connected devices (over 5 billion connected IoT devices in 2025 predicted by Ericsson, [8]), transmission formats diversity (from single-input single-output to multiple-input multiple-output), multiple spectral regions (from a few hundreds of MHz up to 100 GHz), supported applications, increased bandwidth per end used (up to 10 GHz), smooth and adaptive integration of the fiber and wireless segments, and efficient energy management, [1, 2]. It will begin the era of the hyperconnectivity. Everything will be connected with everything. Person-person, person-machine and machine-machine communications will exponentially grow, [9].

The traditional radio access network (RAN) will not be able to deal with such demands and, thus, new infrastructures and technologies will be required to address these limitations. The solution will be the migration to centralized (or cloud) radio access network (C-RAN) architectures, [5, 6]. The C-RAN aims to move most of the RAN control and signal processing functionalities from the cell site to centralized locations within the network, enabling as a consequence a dynamic assignment of resources, [2]. In addition, next-generation communication scenarios will require C-RAN architectures to support high-performance reconfigurable radiofrequency (RF) signal processing systems operating at high-radiofrequencies (up to the millimeter band).

Neither photonic or RF technologies can address this challenge on their own. The key here will lie in a full synergy between the optical fiber network segment and the wireless network segment. The C-RAN optical fiber fronthaul must not only act as a signal distribution and control architecture interconnecting the RF infrastructure (at the wireless base stations) with the centralized baseband unit pool (at the central office). But also, it must provide multiple-input multiple-output (MIMO) antenna connectivity and broadband signal processing systems that enable key tasks such as antenna beamforming for phased array antennas, RF signal filtering and arbitrary waveform generation. Fiber-wireless communications, supported by Microwave Photonics (MWP), is the natural option to cope with such network demands, [10, 11, 12, 13, 14, 15, 16, 17].

MWP is an interdisciplinary field that merges the worlds of RF and photonics. It pursues the generation, processing, and distribution of microwave and millimeter wave signals by photonics means, benefiting from the unique advantages inherent to photonics, such as low loss and high bandwidth. It also provides key features such as fast tunability and reconfigurability that are not possible using classic electronic approaches. At the heart of a MWP system is the true time delay line (TTDL), an optical subsystem that provides a frequency-independent and tunable group delay within a given frequency range enabling, as a consequence, important functionalities such as controlled signal distribution, signal filtering, antenna beam-steering, arbitrary waveform generation and multi-gigabit-per-second analogue-to-digital conversion, [18, 19, 20, 21, 22]. These functionalities, in turn, are required in a variety of Information Technology scenarios, not only in broadband wireless and satellite communications (as the above-mentioned 5G & Beyond and the Internet of Things), but also in distributed antenna systems, signal processing, sensing, medical imaging and optical coherence tomography.

Despite the aforementioned potential applications, the widespread adoption of MWP is still limited by the non-compact, heavy and power-consuming nature of its up-to-date systems, in both signal processing and radio-over-fiber distribution scenarios. The challenge is to develop innovative technologies that must go beyond mere distribution and connectivity functionalities and embrace, at the same time, high-performance microwave and millimeter-wave signal processing functionalities that will be critical in 5G smart radiating systems. In particular, Integrated MWP, which aims to integrate the highest number of photonic components either in a monolithic or hybrid platform, has been proposed to address signal processing functionalities in isolation, [23]. Nevertheless, there is still a paramount need for a compact and efficient fiber-based technology able to address both processing and distribution functionalities as a whole, supporting the required parallelization in distribution networks. This second scenario, which includes applications such as wireless access networks and fiber-to-the-home, usually resorts to the brute-force replication of a basic subsystem where the TTDL is built from discrete and bulky components.

The C-RAN fronthaul infrastructure will potentially use space-division multiplexing (SDM) techniques to support the massive capacity requirements of next-generation communications systems, [24]. By exploiting the space dimension –the last available degree of freedom for optical multiplexing–, SDM has become the solution for the

capacity bottleneck in digital communications by establishing independent transmission channels in a single fiber via SDM fibers, using either the different cores of a multicore fiber (MCF) or the different spatial modes in a few-mode fiber (FMF). In this Thesis, we propose to address the challenges brought by next-generation fiber-wireless communications by extending the concept of SDM to the area of fiber-wireless communications. More specifically, by exploiting the inherent parallelism of SDM fibers, we envision the implementation of sampled discrete TTDLs using a single optical fiber, without the need to resort to bulky, heavy, power-consuming and expensive fiber replication architectures. This approach will not only go beyond the state-of-the-art properties of TTDLs, but it will also lead to the novel concept of *fiber-distributed signal processing* that can be implemented, for instance, in the link connecting a central office and different remote base stations. Figure 1.1 depicts a generic example of a next-generation fiber-wireless communications scenario. Here, SDM fibers are placed not only in the C-RAN fronthaul segments, but also for instance, in aircraft, satellites or in-building networks. With our proposal, each SDM fiber offers multiple parallel channels to provide MWP signal processing functionalities simultaneously to signal distribution and delivery. Optical beamforming networks that enable beam-steering in phased array antennas, RF signal filtering or generation are some examples of functionalities that can be performed over the proposed SDM-based TTDLs.

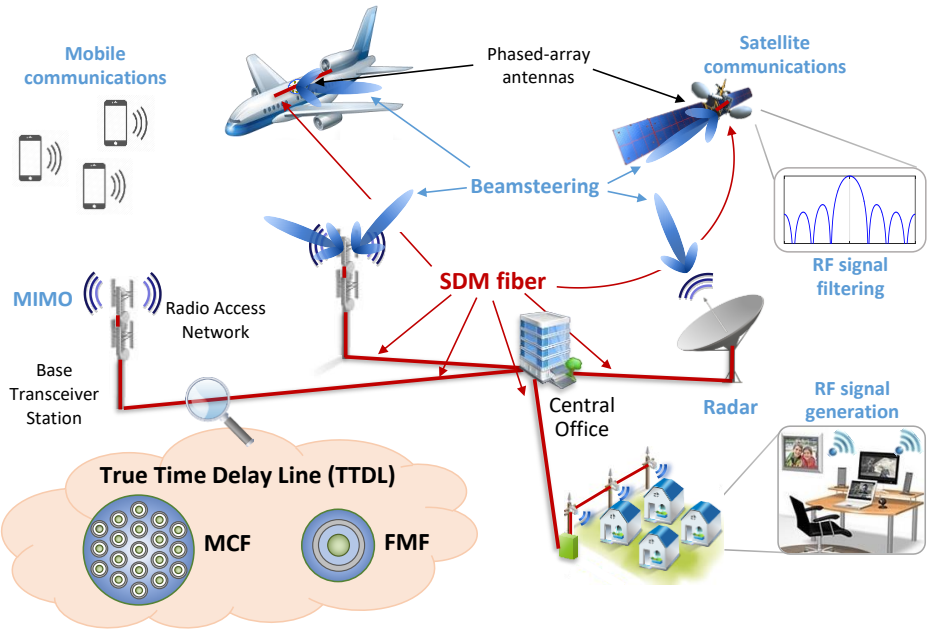

Fig. 1.1. Example of a typical Microwave photonics fiber-wireless communications scenario.

In summary, our key challenge lies in the development of innovative technologies that must go beyond mere distribution and connectivity functionalities and embrace –at the same time– high-performance microwave and millimeter-wave signal processing functionalities that will be critical in 5G & Beyond radiating systems. We

propose to use SDM fibers to implement compact broadband tunable TTDLs that can provide both functionalities simultaneously by using either FMFs for short-reach (up to a few km) scenarios or MCFs for short- and medium-reach scenarios (up to tens of km). This approach features unique properties beyond the current state-of-the-art in terms of compactness and weight, but also in terms of flexibility and versatility, as we will see in this PhD Thesis.

1.2. Thesis objectives

This PhD Thesis has been carried out in the Photonics Research Labs (www.prl.upv.es), group within the iTEAM Research Institute (www.iteam.upv.es), at the Universitat Politècnica de València, Valencia, Spain. The financial support has been provided by the *Ministerio de Economía y Competitividad* of the Spanish government by means of the doctoral fellowship *beca de Formación del Personal Investigador* (FPI), inside the Spanish project *Fotónica de Microondas para Aplicaciones Emergentes*. The work performed in this Thesis has contributed to the Spanish project *Multicore fibers for next-generation fiber-wireless applications* and the European project *Revolutionizing fibre-wireless communications through space-division multiplexed photonics* from the European Research Council (ERC).

The general objective of the Thesis is the design, implementation and experimental demonstration of distributed signal processing for microwave signals built upon multicore and few-mode fibers. The achievement of the general Thesis objective entails a series of specific research objectives that follow a logical sequence order that goes from the study of wave propagation in SDM fibers in chapter 3, up to the final experimental validation of MWP signal processing functionalities built upon the proposed optical TTDLs in chapter 6. The Thesis is structured in a series of 7 chapters, including a first introductory chapter and a last one that encompasses the summary, conclusions and future work that result from this Thesis.

In chapter 2, we review the current state-of-the-art of MWP signal processing and SDM fibers, focusing on both multicore and few-mode fibers. We describe the basis of the optical TTDL, a key element that takes place in the majority of MWP signal processing system. This chapter is essential to understand the basic advantages entailed by the solutions developed in the Thesis.

The design of the tunable optical TTDLs built upon SDM fibers requires a precise knowledge about the propagation characteristics of the different spatial modes that propagate along the fiber, such as the group delay and chromatic dispersion, as well as the interaction between them. In this regard, we develop in chapter 3 a theoretical model to obtain the universal characteristic equation for optical fibers whose refractive index profile comprises an arbitrary number of concentric circular layers. This model allows us to calculate basic fiber propagation parameters required for TTDL design. We also review the fundamentals of mode coupling between the different spatial paths that propagate in both multicore and few-mode fibers.

Chapter 4 presents, for the first time, the proposed optical TTDLs. There, we describe the concept, design process and performance of both MCF- and FMF-based

approaches. We show that a heterogeneous MCF can behave as a sampled tunable TTDL by properly designing the refractive index profile of each single core, while a FMF requires the inscription of long period gratings (LPGs) at specific locations along the fiber that act as selective mode converters to properly adjust the differential delay between samples. As we deal with time-delay sensitive applications, we also study the main sources of degradation that can affect the time-delay behavior of the spatial paths and different possibilities to reduce their impact.

In chapter 5, we design, fabricate and characterize 3 different TTDLs based on SDM fibers. In the case of the MCF approach, we fabricated two different heterogeneous 7-core MCFs. The first one was fabricated by the Chinese company YOFC from 7 different fiber preforms, while the second one was fabricated from only 1 fiber preform in the research group CREOL, the College of Optics and Photonics, in the University of Central Florida (USA), during my 3-month stay. For the FMF approach, we implemented a TTDL in a commercial 4-mode FMF by inscribing three LPG-based mode converters.

In chapter 6, we experimentally demonstrate the implementation of different MWP signal processing functionalities over the developed SDM-based solutions. For the MCF approach, we validate the performance of the TTDL built upon the YOFC fiber when it is applied to both RF signal filtering and optical beamforming for phased array antennas. We also propose and experimentally demonstrate the implementation of multi-cavity optoelectronic oscillators (OEOs) built upon MCFs. Finally, we validate the FMF-based TTDL device when it is applied to RF signal filtering functionalities.

Finally, chapter 7 contains the summary and conclusions of this Thesis and provides the main future work to be developed in a near future to consolidate the concept of distributed radiofrequency signal processing over SDM fibers in fiber-wireless communications scenarios.

1.3. Original contributions of the Thesis

We would like to highlight several original research contributions presented in this Thesis:

- The development of a universal model to obtain the characteristic equation of generic single-core optical fibers with a refractive index profile comprising an arbitrary number of concentric circular layers. (Chapter 3)

- The proposal of dispersion-engineered heterogeneous MCFs as tunable sampled TTDLs. (Chapter 4)

- The proposal of custom FMF together with the inscription of selective mode converters based on LPGs for tunable sampled TTDL operation. (Chapter 4)

- The theoretical modelling and experimental evaluation of the influence of bends and twists on the core differential group delays of a MCF-based TTDL. (Chapter 4)

- The design and fabrication of two different heterogeneous 7-core MCFs where each core features the required group delay and chromatic behavior for sampled TTDL operation. (Chapter 5)

- The design and fabrication of a 4-sample TTDL built upon a commercial 4-LP-mode FMF with inscribed LPGs that act as selective mode converters. (Chapter 5)

- The experimental demonstration of reconfigurable RF signal filtering and optical beamforming networking for phased array antennas over a 7-core heterogeneous MCF-based TTDL link. (Chapter 6)

- The proposal of different architectures for multi-cavity OEOs implemented on both homogeneous and heterogeneous MCFs. (Chapter 6)

- The experimental validation of multi-cavity OEOs built on a commercial homogeneous 7-core MCF. (Chapter 6)

- The experimental demonstration of RF signal filtering implemented over a 4-sample FMF-based TTDL. (Chapter 6)

Chapter 2
State of the art

2.1. Challenges of Microwave Photonics

Microwave Photonics is an interdisciplinary area that brings together the worlds of RF and optoelectronics. It pursues the generation, processing, transport and measurement of high-speed radiofrequency signals by photonic means, [10, 11, 12, 13, 14, 15, 16, 17]. The key advantages of MWP links over conventional electrical transmission systems, such as coaxial cables or waveguides, include reduced size, weight and power consumption, low and constant attenuation over the entire microwave and millimeter-wave (mm-wave) modulation frequency ranges, immunity to electromagnetic interferences, low dispersion and high data transfer capacity, [11, 12, 13, 14, 15, 17]. But MWP brings also considerable added value to traditional microwave and RF systems as photonics allows the realization of key functionalities which are either very complex or even impossible to achieve in the RF domain, such as fast tunability and reconfigurability, [12, 15, 16, 17].

A typical MWP system consists of a combination of microwave and photonic components configured such that microwave signals are transported (and usually processed) in the optical domain. Figure 2.1 shows the basic concept of a simple analog MWP system. There, the RF signal is up-converted to the optical domain (optical source and electro-optical modulator (EOM)), transmitted and/or processed in the optical system (optical fibers, optical delay lines, optical amplifiers and filters, etc.) and then recovered at the receiver in the electrical domain (photodetector).

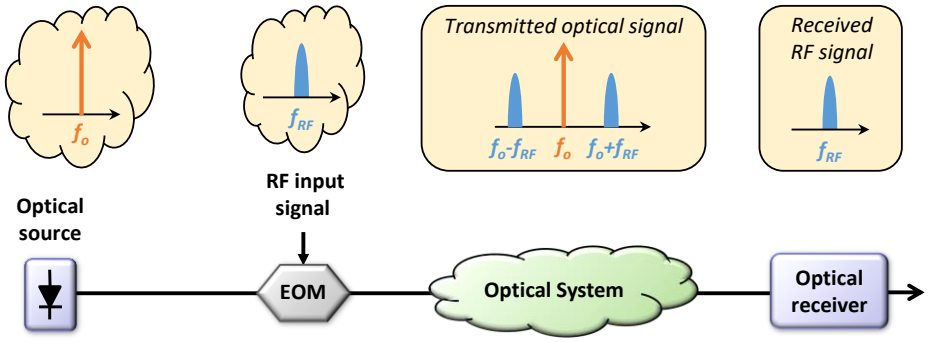

Fig. 2.1. Illustrative example showing the basic idea of a simple analog microwave photonics system.

Since the early experiments during the late 1970s, the field of MWP has expanded to address a considerable number of applications including high-performance analog microwave photonic fiber links for antenna remoting in radar systems, microwave photonic links for cellular, wireless, satellite and radio-astronomy applications, cable television systems and optical signal processing. This includes as well emerging fields such as converged fiber-wireless and in-home networks, medical imaging systems, wireless body and personal area networks, advanced instrumentation and the internet of things, [11, 15, 16].

Up to date, the predominant commercial application of microwave photonic technology is the transport and distribution of radio signals over optical fibers. Fiber optic remoting of radio signals is used in a wide number of wireless networks, including indoor distributed antenna systems and outdoor cellular networks. Nowadays, the proliferation of connected high-capacity smart devices as well as the increase in the number of broadband multimedia services has led to an unprecedented demand for wireless access to high-speed data communications. The full integration between the optical fiber and the wireless networks that can successfully and cost-effectively support current and future capacity demands, traffic growth rates, new services, as well as multiple wireless standards, is presenting new challenges and opportunities for emerging advanced radio-over-fiber (RoF) technologies, [25]. The principal attraction of RoF systems is that they allow a flexible approach for multiple antenna remote connectivity with reduced system complexity. This results from centralizing most of the transceiver functionality in the central office, transmitting the wireless signals in their modulated format over the fiber and, thus, incorporating a simplified antenna module closer to the customer, [11, 26].

Another striking application field of MWP relates to signal processing approaches. The processing of RF signals in the optical domain provides unprecedented advantages as compared to traditional electronic technologies; not only those inherent to photonics, but it can also: (1) overcome the sample speed limitation of electronic signal processors -enabling to handle high-speed RF signals-; (2) provide adaptive and reconfigurable operation; and (3) enable integration into existing fiber-optic systems (since the signals to be processed are already transported in the optical domain), [10, 11, 12, 26, 27, 28]. A considerable amount of work has been carried

out within the field of microwave and millimeter-wave signal processing as it is the basis for the implementation of many functionalities, including signal filtering [18], frequency up/down conversion [19], arbitrary waveform generation or shaping [20], beamforming networks for phased array antennas [21] or multigigabit-per-second analog-to-digital conversion [22]. These approaches are fundamental in a wide variety of Information Technology scenarios, such as 5G and beyond and the Internet of Things, [4, 29, 30].

Despite the aforementioned potential application, the widespread adoption of MWP is still limited by the non-compact, heavy, and power-consuming nature of its up-to-date systems, in both signal processing and radio-over-fiber scenarios. Thus, one of the major challenges that MWP has to overcome nowadays is related to the reduction of size, weight and power consumption (SWaP) while assuring broadband seamless reconfigurability and stability. In particular, many of the above mentioned novel application areas will demand ever-increasing values for speed, bandwidth, processing capability and dynamic range while, at the same time, will require devices that are small, lightweight and with low power consumption, exhibiting large tunability and strong immunity to electromagnetic interference, [11, 16]. The ever-increasing capacity demand requires strategies to augment the wireless transmission data rate, such as increasing the wireless spectral efficiency and moving to higher frequency wireless windows; and, in addition, it requires MWP signal processing approaches that implement versatile, tunable and reconfigurable multiband structures featuring small size and low power consumption, [16]. This challenge implies the development of new technologies that must go beyond mere distribution and connectivity functionalities and deal, at the same time, with high-performance microwave and millimeter-wave signal processing functionalities that will be critical in future 5G systems and beyond, [4, 29].

2.2. Microwave Photonics signal processing

A MWP signal processor is a photonic subsystem designed with the aim of modifying the spectral characteristics of the RF signal directly in the optical domain. It consists of a combination of photonic devices that act over the optical RF-modulated signal, processing it to fulfill a specific requirement, [12, 31]. The concept of signal processing is present in any MWP system. It appears in any functionality in which an optical RF-modulated signal passes throw a dispersive medium that, at the end, alter its spectral characteristics, such as in RoF multipoint wavelength division multiplexing networks, optoelectronic oscillators, analog-to-digital converters, frequency measurements subsystems, optical beamforming networks and microwave signal filters, [12]. In general, most of MWP signal processing approaches rely on a key optical component: the true time delay line (TTDL). A TTDL is a device that yields the possibility of controlling the propagation delay of an incoming signal, ensuring true time delay operation (i.e., independent of the RF frequency) on a large operative bandwidth, [32, 33]. Its basic working principle consists of providing, at its output, a set of different time-delayed and weighted replicas of the input signal. Different technologies have been proposed for the implementation of optical TTDLs, which are either based on optical fiber or photonic integrated approaches. Solutions

based on fiber optics include the use of parallel fibers with different length [34], dispersive fibers [35] or fiber Bragg gratings (FBGs) [21, 36, 37], as well as stimulated Brillouin scattering [38]. On the other hand, photonic integration approaches include those based on ring cavities in Silicon on Insulator and racetrack resonators in Si_3N_4 [14], as well photonic crystal structures [39] and semiconductor optical amplifiers [40] based on InP.

Here, we review the principle of operation of the three MWP signal processing applications that will be addressed in this PhD Thesis: signal filtering, radio beam-steering in phased array antennas and optoelectronic oscillation. All of them are built upon sampled true time delay lines.

A microwave photonic filter is a photonic architecture designed with the aim of replacing a standard microwave filter, bringing the aforementioned supplementary advantages of MWP, [18]. The most versatile approach towards the implementation of MWP filters is based on discrete-time signal processing, where a number of weighted and time-delayed samples of the RF signal to be processed are produced in the optical domain and combined upon detection. MWP filters can operate under incoherent regime (i.e., the samples differential delay $\Delta\tau >> \tau_c$, being τ_c the coherence time of the optical source) or under coherent regime (i.e., $\Delta\tau << \tau_c$). In practice, the majority of the proposed schemes work under incoherent regime as this allows the implementation of structures that are immune to environmental changes, [12, 18, 31]. There are two main approaches to implement MWP filters. First, finite impulse response (FIR) filters, which combine at their output a finite set of time-delayed and weighted replicas or taps of the input optical signal; and, second, infinite impulse response (IIR) filters that are based on recirculating cavities to provide an infinite number of samples, [12, 18]. Taking into account, for instance, the FIR configuration, the filter electrical transfer function is given by, [12],

$$H(f_{RF}) = \sum_{k=0}^{N-1} a_k e^{-i2\pi k f_{RF} \Delta\tau}, \tag{2.1}$$

where a_k represents the weight of the k-th sample, N is the number of samples, $\Delta\tau$ is the time delay between adjacent samples and f_{RF} is the RF frequency. From Eq. (2.1), we see that the filter is periodic in the frequency domain, where the period, known as free spectral range (FSR), is given by FSR = $1/\Delta\tau$. To generate the signal samples, the use of a TTDL brings time delay tunability, and thus allows filter reconfigurability. Figure 2.2 shows the basic idea beyond the implementation of an N-tap MWP filter using a time-discrete FIR structure, where an optical source is modulated by the RF signal, split and injected into a TTDL. At the TTDL output, the signals are optically combined prior photodetection to create the frequency filtering response.

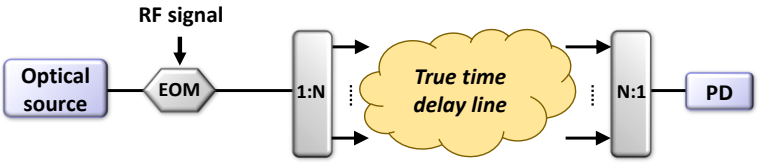

Fig. 2.2. Principle of operation of a *N*-tap microwave photonic filter using a FIR architecture implemented with an *N*-sample optical true time delay line. EOM: electro-optic modulator; PD: photodetector.

Optical beamforming networks for phased array antennas have received increasing attention in recent years for applications in modern radar and wireless communications systems, [3, 41, 42, 43, 44]. Phased array antennas consist of multiple radiating elements that collectively operate as a single antenna, in which its elements are fed coherently and the relative phase of each of them is controlled independently with the aim of steering the radiated electric field's beam to scan a given spatial angular direction, [45]. True time delay beamforming is required to achieve wide instantaneous bandwidth and squint-free operation on the antenna array. In this regard, beamforming networks based on optical TTDLs can further benefit from MWP while providing true time delay line operability, [10, 11, 17, 26, 44]. The basic architecture of an optical beamforming network is similar to that of a MWP filter, with the unique difference that each TTDL sample feeds a different antenna element instead of optically combining all the samples. As shown in Fig. 2.3, each signal sample is photodetected independently at the TTDL output and radiated by a different antenna element. The normalized angular far-field pattern of the radiated electric field, or antenna array factor $AF(\theta)$, of the phased array antenna results from the combination of the overall spatial electric field distribution at the output of the radiating elements as, [45],

$$AF(\theta)=\sum_{k=0}^{N-1} a_k e^{-i2\pi k f_{RF}\left(\Delta\tau - d\sin(\theta)/c\right)}, \tag{2.2}$$

where θ is the far field angular coordinate, N is the number of antennas, d is the separation between radiating elements and c is the light speed in vacuum.

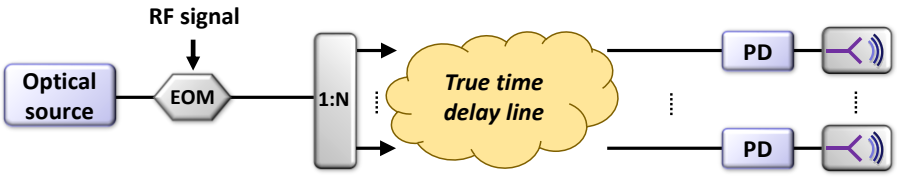

Fig. 2.3. Schematic of an optical true time delay beamforming network for phased array antenna systems. EOM: electro-optic modulator; PD: photodetector.

A particularly interesting MWP application is the OEO. Optoelectronic oscillators are devices that convert energy from a continuous light source into stable and spectrally pure microwave and RF signals, [46, 47, 48]. They are key elements in any system that receives or transmits an RF signal, such as communications systems, radar or signal processing. As opposed to electronic microwave oscillators, that are

relatively noisy and do not have very high stability, OEOs are characterized by high spectral purity, high frequency generation capability (up to tens or hundreds of GHz) and high frequency stability performance, [46, 47, 48, 49, 50, 51, 52]. Generally speaking, an OEO consists of a pump laser and a feedback loop that is formed by a combination of optical and electrical components, including an intensity modulator, an optical fiber, a photodetector and RF amplification, as shown in Fig. 2.4. The inclusion of an RF filter in the feedback loop allows the selection of a certain oscillation frequency and suppress the harmonics generated by the nonlinear response of the EOM, leading to a stable and low-phase-noise RF signal. The conditions for self-sustained oscillations are the coherent addition between the signals after each loop and a loop gain proportional to the overall loop losses, [46, 47, 48].

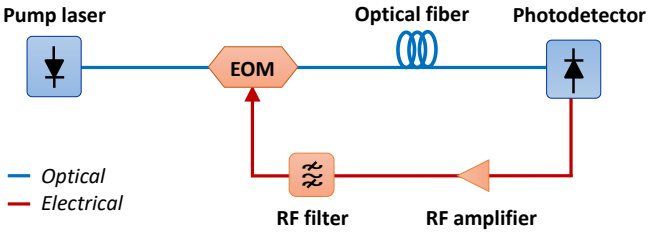

Fig. 2.4. Basic concept of an optoelectronic oscillator. EOM: electro-optic modulator.

In an OEO, in general, since high spectral purity signals require large time delay in the feedback loop, typical implementations are based on optical fiber approaches. However, a long fiber loop translates into a large number of oscillation modes that are separated by a small frequency period, and thus a high-selectivity RF filter is necessary in the electronic part of the loop. To overcome this limitation, dual-loop [49] and multiloop [50] OEO configurations were proposed, where a long cavity provides the required spectral purity and a short fiber cavity provides the required spectral separation between adjacent oscillating modes, what considerably alleviates the narrowband requirement for the internal RF filter. Other solutions have also been proposed, including the incorporation of a highly selective whispering gallery optical filter in the optical segment of the oscillator [53] that can lead to extremely compact [54], broadly tunable [55] and low phase noise [56] devices with the possibility of exploiting as well optomechanical effects [57]. Coupled optoelectronic oscillators, which simultaneously produce spectrally pure microwave signals as in an OEO and short optical pulses as in a mode locked laser [58, 59], and, more recently, photonic integrated OEO approaches [60] have also been considered.

2.3. Space-Division Multiplexing fiber technologies

2.3.1. Increasing the fiber capacity: exploiting the space dimension

The demand for data transmission has grown exponentially during the past three decades, and it is still increasing around 40% per year. As a result, the capacity of singlemode fiber (SMF) is reaching its fundamental limit (i.e., the Shannon limit) mainly due to the Kerr fiber nonlinearity, leading to an imminent capacity crunch,

[61]. Furthermore, this capacity limit applies to all segments of the network, ranging from mobile wireless and fixed access to supercomputer systems, data-centers interconnects and long-haul transport. Of course, this includes MWP signal processing systems as well as RoF distribution networks. Under this adverse situation, it has come up the urgency of finding new cost-efficient solutions to increase the fiber capacity, [62, 63, 64, 65, 66].

Figure 2.5 shows the evolution of core and metro optical transport networks in NTT Group companies, extracted from [67]. Up to now, the fiber capacity has been improved by using time-division multiplexing (TDM), wavelength-division multiplexing (WDM) and polarization-division multiplexing (PDM); space is the last degree of freedom that is being considered for optical fiber communications, [61, 62, 63, 67, 68]. The development of systems using space-division multiplexing in optical fibers appears as a promising solution to increase the capacity of optical networks by increasing the capacity per fiber, including either few-mode fibers [69], multicore fibers [70], or few-mode multicore fibers (FM-MCFs) [71]. The availability of compact, low-loss spatial channel multiplexers and demultiplexers is particularly critic for any SDM system to inject/extract the light to/from the spatial modes. There have been proposed different solutions for SDM mode multiplexing, including free-space optics approaches such as multi-plane light converters [72], fiber-based solutions such as photonic lanterns [73, 74], and integrated waveguide-based devices [75].

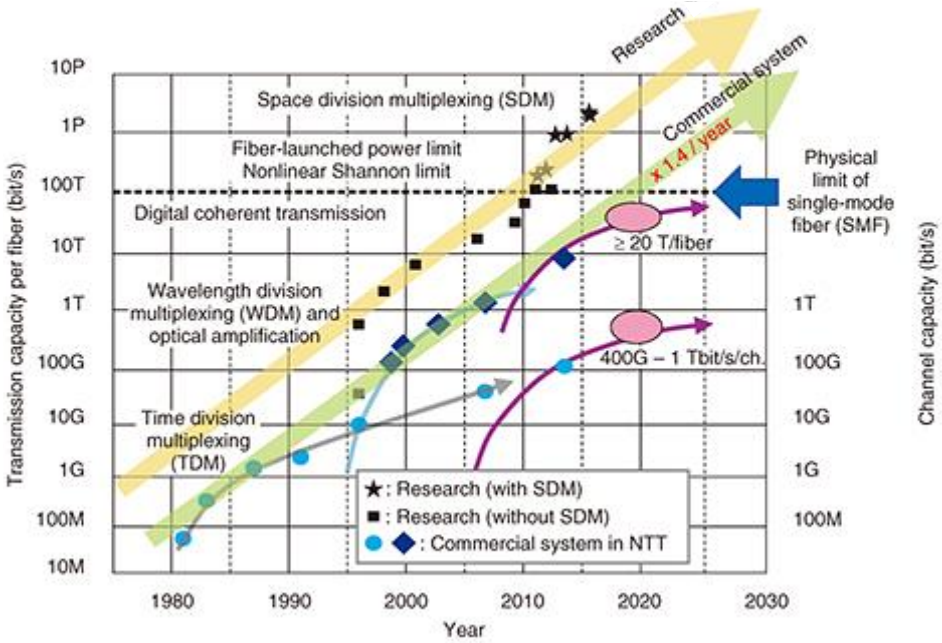

Fig. 2.5. Evolution of high-capacity optical transport network, extracted from [67].

The total transmission capacity C of an optical fiber link can be expressed as, [64],

$$C = B \times SE \times N_{ch} \ , \tag{2.3}$$

where B is the fiber effective transmission bandwidth (limited to the gain bandwidth of the erbium-doped fiber amplifier (EDFA)), SE is the spectral efficiency and N_{ch} is the number of independent spatial channels. For typical SMFs, B is around 10 THz, SE is limited to the fiber optical nonlinearity to approximately 5^{-10} bit/s/Hz per polarization and $N_{ch} = 2$ (the two orthogonal polarizations), resulting in a maximum capacity per fiber of around 100 Tbit/s. In order to enhance the capacity per fiber, from Eq. (2.3) we see that, while B and SE are subjected to the current state-of-the-art photonic components (amplifiers, lasers, etc.), N_{ch} can be substantially increased by exploiting the last degree of freedom of the physical dimensions: the spatial domain, [64, 65].

2.3.2. Multicore fibers

Multicore fibers comprise various cores inside the fiber cross section. The spatial capacity of a MCF increases with the core density (i.e., the core count per cross-sectional area) and it can be further improved by reducing the core-to-core distance. MCFs can be classified in two types according to the coupling between cores. Weakly-coupled MCFs are those in which each core acts as an individual transmission channel and thus require low inter-core crosstalk levels. In this case, each core has to be properly arranged as to keep the intercore crosstalk small enough for long-haul transmissions. The second approach is called strongly-coupled MCF, in which the core-to-core distance is further reduce to intentionally induce high crosstalk between the cores, resulting in the core density improvement. They support several super-modes strongly mixed and thus require MIMO digital signal processing (DSP) at the receiver to undo the signals. Comparing both approaches, SDM based on weakly coupled MCFs is a simple and promising approach for increasing the spatial capacity of the fiber, [70].

One of the major concerns in weakly-coupled MCFs is the intercore crosstalk management. The number of cores that can be arranged in the fiber is limited by the core-to-core distance that guarantees a certain intercore crosstalk level along a given propagation length for a fixed outer cladding diameter, [70, 76]. In the last 10 years, there has been a lot of effort to find methods for intercore crosstalk suppression to increase the core density (i.e., the fiber capacity) and enable larger transmission lengths.

Initially, the so-called homogeneous MCFs were employed, where all the cores are identical. Signal transmission over homogeneous MCFs can be significantly affected by intercore crosstalk unless the core-to-core distance remain sufficiently large (typically above 30 or 40 μm), limiting the number of cores that can be arranged inside the fiber cross-section. Early experiments were based on hexagonal 7-core MCF configurations, where a central core is surrounded by 6 outer cores placed in hexagonal disposition. In 2011, B. Zhu *et al.*, [77], achieved a 112-Tb/s transmission along 76.8 km on a hexagonal 7-core homogeneous MCF. By increasing the core pitch up to 46.8 μm and setting the cladding diameter to 186.5 μm, they reach a maximum intercore crosstalk below -30 dB. With the aim of further reducing the intercore crosstalk, MCF with trench-assisted (TA) (where a depressed-layer or trench surrounds each core) or hole-/wall-assisted (where air-holes are placed

surrounding each core or separating adjacent cores) configurations were used to improve the mode confinement on the cores, [70, 76]. In 2012, J. Sakaguchi *et al.*, [78], arranged 19 homogeneous trench-assisted cores inside a 200-μm cladding diameter by reducing the core pitch down to 35 μm. There, they achieved a capacity transmission of 305 Tb/s along 10.1 km with an intercore crosstalk level below -30 dB. More recently, in 2015 B. Puttnam *et al.*, [79], achieved a record 2.15-Pb/s transmission along a 31.4-km length link by using a 22-core homogeneous MCF. They use trench-assisted cores and a 3-layer configuration with core pitches of 41 and 48 μm in a 260-μm cladding diameter, reaching a worst-case intercore crosstalk below -45 dB/km.

In 2009, Koshiba *et. al*. found that the insertion of different cores reduces the intercore crosstalk by avoiding phase matching conditions between cores. They were called as heterogeneous MCF, since dissimilar cores characterized by different propagation constants were arranged inside a single cladding, [80]. Heterogeneous MCFs appear as a solution to increase the core density by allowing shorter core-to-core distances. In order to minimize the number of distinct cores required, triangular-lattice (where only 3 types of different cores are needed) and square-lattice (with 4 types of different cores) are commonly used to ensure that each pair of neighboring cores are of a different type, [80, 81]. Core packaging up to 37 cores have been reported. In 2017, Mizuno *et. al*., [81], reported a 32-core heterogeneous MCF with an outer cladding diameter of 243 μm and a 29-μm core pitch. They employ a square-lattice arrangement to minimize the intercore crosstalk. A record transmission length of 1644.8 km was achieved by using a recirculating loop system, with an intercore crosstalk penalty below -34.5 dB/51.4 km. In the same year, Y. Sasaki *et al*., [82], reported a 37-core trench-assisted heterogeneous MCF based on a triangular-lattice configuration. The cladding diameter and core pitch were 248 μm and 29 μm, respectively. The intercore crosstalk was below -50 dB/km.

Finally, the inclusion of few-mode transmission in each core further improved the spatial channel density over 100. Few-mode multicore fibers are hybrid approaches that combine multiple few-mode cores inside a single fiber. Because of the outer cladding is limited to a certain value and the number of aggregated cores in a MCF is restricted, FM-MCFs appear as a solution to further increase the capacity per fiber by increasing spatial channel density. FM-MCFs are promising candidates for ultra-dense SDM systems, where higher and higher data capacity demand will be required, [71, 83, 84]. Recently, a record-breaking transmission capacity of 10.16 petabit/s was achieved by D. Soma *et. al*. using dense SDM/WDM transmission over a 6-mode 19-core fiber with a cladding diameter of 267 μm, where 114 SDM channels were transmitted along 11.3-km fiber length, [84].

Figure 2.6 shows some examples of different types of MCFs. From left to right, we have: (a) weakly-coupled homogeneous MCF; (b) strongly-coupled MCF; (c) weakly-coupled heterogeneous MCF; and (d) trench-assisted homogeneous MCF.

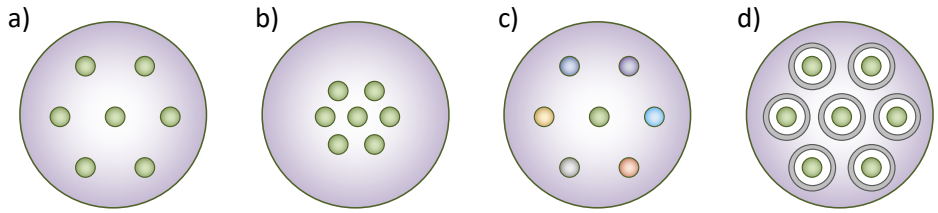

Fig. 2.6. Different types of MCFs: (a) weakly-coupled homogeneous MCF; (b) strongly-coupled MCF; (c) weakly-coupled heterogeneous MCF; and (d) trench-assisted homogeneous MCF.

2.3.3. Few-mode fibers

Another approach for increasing the spatial capacity of the fiber relies on the use of few-mode fibers. A FMF is a single-core multimode fiber that is designed to support a few number of modes -usually below 20 spatial modes- with the aim of reducing the inter-modal coupling and allowing higher mode selectivity, [61]. In FMFs, the distinct spatial paths can be formed either by the particular orthogonal modes supported by the fiber or by combinations of these modes (what is called mode groups). A mode group comprises a set of modes (including their distinct polarizations) that have similar effective indices and thus propagate as a unique entity due to the high intra-mode group coupling. Since the modes have significant spatial overlap, the data signals couple randomly between spatial channels during propagation. SDM over FMFs can be performed in two different regimes: (1) low coupling regime; and (2) low differential group delay regime. In the first regime, the low mode coupling between modes can be achieved by keeping higher effective index differences between the fiber modes, what can be addressed by using different types of step-index (SI) configurations. In the strong-coupling regime, coherent detection followed by MIMO DSP solutions is required at the receiver to mitigate the coupling effects between the spatial modes. This approach operates under the assumption of strong mode coupling, so that reducing the differential mode group delays (DMGDs) prevails over the mode coupling to reduce the associated complexity of the inevitable MIMO DSP. In this case, graded-index (GI) FMFs are commonly used to minimize the DMGDs, [64, 69]. Figure 2.7(a) illustrates a comparison between a single-core SMF and a single-core FMF, showing that FMFs used to have larger core radius than SMFs to support few-mode transmission. Figures 2.7 (b) and (c) represent the refractive index profiles of a SI and GI configurations, respectively.

For long-haul SDM systems, strong mode coupling is inevitable. Thus, if N is the number of spatial modes, a $2N$x$2N$ MIMO matrix is required to uncouple the signals after coherent detection (2 polarizations per spatial mode). Reducing the DMGDs is crucial in this case to minimize the MIMO DSP complexity. In this regard, J. van Weerdenburg *et al*., [85], reported a 138 Tbit/s transmission over 650 km by using the 12 SDM channels of a 6-mode GI-FMF. In this case, a 12x12 MIMO equalizer was needed to resolve the mode mixing after detection. More recently, in in 2019, G. Rademacher *et al*., [86], reached a 159 Tbit/s transmission over a 3-mode GI-FMF along 1045-km transmission length, where they achieved higher capacity

transmission for larger length and with lower MIMO complexity (only a 6x6 MIMO DSP matrix was required in this experiment).

In short-reach SDM scenarios (up to a few km), we can maintain weak mode coupling between mode groups with differential effective indices above 10^{-3} or 10^{-4}. This strategy potentially enables partial-MIMO or even MIMO-free schemes, reducing as a consequence the receiver complexity. In this weak-coupling regime, both SI- and GI-FMF configurations can perform MIMO-free transmission by using mode-group division multiplexing, where all the degenerate modes within each mode group act as a single data channel. This means that, if N is the number of spatial modes and $M < N$ the number of spatial modes that pertain at the biggest mode group, the maximum MIMO DSP complexity is based on a $2M$x$2M$ matrix instead of a $2N$x$2N$ matrix. For instance, in 2018, D. Soma *et. al*. reached a record data transmission of 257 Tbit/s over a weakly-coupled 10-mode fiber along a 48-km link featuring an average modal crosstalk below -17 dB, [87]. They used a weakly coupled SI-FMF, requiring only partial-MIMO matrices of 2x2 and 4x4 to undo the mode coupling between degenerated modes instead of a full 20x20 matrix. In addition to simple SI and GI profiles, ring-core fibers (RCFs) have attracted considerable interest recently since they feature large effective areas for reducing nonlinear effects and enable as well simple coupling between RCFs and SMFs, [88, 89, 90].

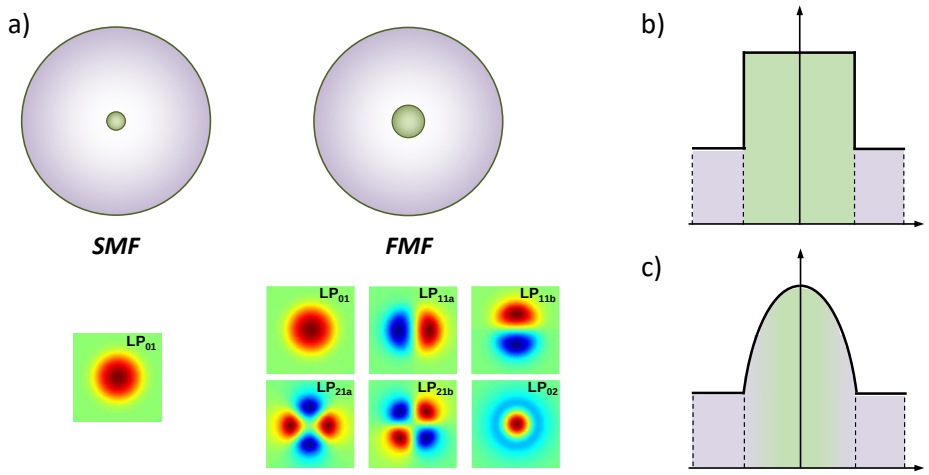

Fig. 2.7. (a) Comparison between a single-core singlemode fiber (SMF) and a single-core few-mode fiber (FMF) and propagated modes; (b) Step-index profile; (c) Graded-index profile.

Chapter 3
Propagation in space division multiplexing fibers

3.1. Introduction

In this chapter, we study the fundamentals of signal propagation in SDM fibers and the basic concepts that will be essential for the implementation of TTDLs based on SDM fibers in the next chapter. These elements will require a proper fiber design as to provide specific propagation characteristics, such as the group delay and the chromatic dispersion, while assuring low crosstalk between their spatial modes. Here, we will analyze how the spatial modes propagate and interact in a SDM fiber.

Electromagnetic wave propagation in optical fibers is governed by the well-known Maxwell equations, [91]. The modes that propagate along the fiber are solutions of the wave equation in the form of Bessel functions. They are referred as TE, TM or hybrid modes (HE or EH), [92, 93]. For weakly guiding fibers, these modes can be approximated as linearly polarized modes (LP), [91, 92]. The characteristic equation determines the modal solutions of the wave equation subject to boundary conditions. However, for optical fibers in which the refractive index profile is composed of several layers, finding an expression for the characteristic equation implies solving a high-order and complex determinant whose numerical solution becomes unfeasible. In section 3.2, we propose a simple universalization of the characteristic equation for arbitrary refractive index profiles that avoids solving any determinant.

In the particular case of SDM fibers, where multiple spatial paths propagate along the fiber, one of the main sources of degradation relates to coupling between these paths, either between the cores in a MCF or orthogonal modes in a FMF. In general, crosstalk limits the maximum transmission length without degradation as well as the maximum transmission capacity, so that there has been significant research interest in finding methods for crosstalk suppression in the different types of SDM fibers. In

section 3.3, we review the basic concepts behind intercore crosstalk in MCFs and mode coupling in FMFs.

3.2. Universal characteristic equation for arbitrary optical fibers

3.2.1. Introduction

In its simplest form, an optical fiber comprises a single cylindrical core of doped silica glass surrounded by a pure-silica cladding whose refractive index is lower than that of the core, [94]. In the past 50 years, more complex index profiles have been developed beyond the simple step-index profile by incorporating different layers that act either as rings (higher refractive index than silica, up-doped with GeO_2 or P_2O_5 among others) or trenches (lower refractive index than silica, down-doped with fluorine or B_2O_3 among others) for different purposes, [91]. Representative examples of multilayer refractive index profiles are gathered in Fig. 3.1. For instance, the introduction of a down-doped intermediate layer between core and cladding gives rise to depressed-cladding fibers [95] (also named as W-type fibers [96, 97, 98]) and trench-assisted fibers, (see Fig. 3.1(a) and (b)), allowing a stronger confinement of the mode than a usual single cladding fiber and thus reducing losses and intercore crosstalk in the case of multicore fibers. On the other hand, double-cladding fibers where the intermediate layer has a refractive index higher than the external cladding, have been developed mainly for high-power amplifiers and lasers [95, 96, 97, 98, 99], (see Fig. 3.1(c)). Ring-core fibers find application in mode-division multiplexing system since they are able to minimize distributed intermodal coupling and thus reduce MIMO DSP complexity at reception [89, 100, 101, 102], (see Fig. 3.1(d)). In addition to step-index profiles, the core of the fiber can present a non-constant refractive index value, as the case of graded-index or triangular-index profiles. Fig. 3.1(e) shows a graded-index trench-assisted fiber commonly used to decrease intermodal dispersion in mode-division multiplexing systems [103], while Fig. 3.1(f) depicts a dispersion-shifted fiber with a triangular index profile incorporating a raised intermediate cladding or ring, [104]. More complex structures with a higher number of layers, such as four-cladding (or quadruple-cladding) fibers, can be found in different dispersion-flattened fibers, [105, 106].

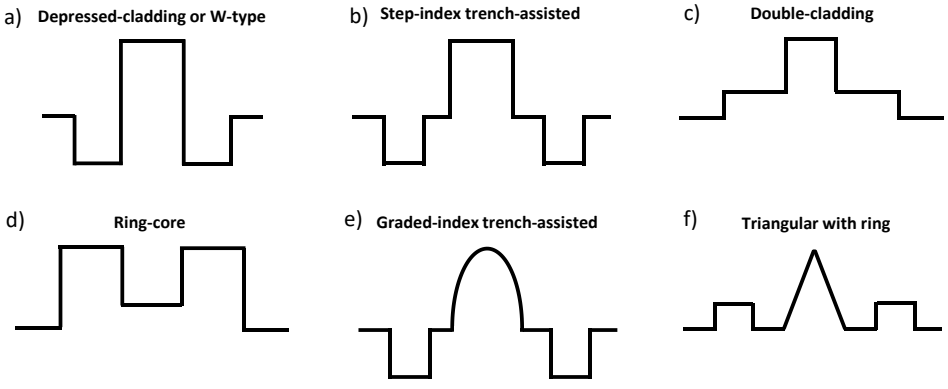

Fig. 3.1. Refractive index profiles of different optical fibers beyond step-index.

Fiber propagation of the electric and magnetic fields of optical waves is governed by the Maxwell equations and must satisfy the boundary conditions imposed at every interface between two refractive index layers. In the case of two-layer fibers (as single step-index or graded-index), the application of boundary conditions over weakly guided modes at the core-cladding interface $r = a$, (where a is the core radius), leads to the well-known compact form of the characteristic or eigenvalue equation, [92]. The solution of the characteristic equation requires graphical or numerical methods and provides the propagation constants of the different modes that propagate though the fiber. Beyond two layers, the characteristic equations of only a few three-layer refractive index profiles have been developed up to date: ring-core profile, [100]; step-index trench-assisted profile [107] where the characteristic equation is expressed in the form of a determinant; as well as double-cladding profile where the intermediate cladding has either a refractive index either lower (see Fig. 3.1 (a)) or higher (see Fig. 3.1(c)) than that of the external cladding, [95].

If the refractive index profile comprises a higher number of different radial layers, the derivation of the characteristic equation for the whole structure becomes a complex mathematical procedure that is usually not overtaken. Instead, one has to resort to numerical software tools to solve the modes that propagate through the fiber without having any valuable insight about the fiber propagation characteristics before running the software tool. We present here the development of a general closed expression for the characteristic equation of multi-layer optical fibers with any number of layers, where each concentric layer has arbitrary radial dimensions and refractive index. This formula will play an important role in the design process of multi-layer optical fibers, providing a useful tool to obtain the phase propagation constant for all the propagated modes and also to derive other propagation parameters such as the group delay or the chromatic dispersion.

Figure 3.2 shows the refractive index profile as a function of the radial coordinate r and the cross-section area of a general optical fiber with p+1 concentric layers, where the layer p+1 behaves as the external cladding. Each layer k (k = 1, 2, …, p+1,) is characterized by a radius a_k, ($a_k > a_{k-1}$ for $k > 2$) and a refractive index value n_k that remains constant among each layer, that is, $n_k(r) = n_k$ for $a_k > r > a_{k-1}$. Refractive index profiles that do not follow this flat-step structure, for instance those comprising graded or triangular shape sections, will be approximated by a multi-step structure where we discretize that continuous section into the required number of flat layers where $n_k(r) = n_k$. We will refer those cases as “continuous” refractive index profiles.

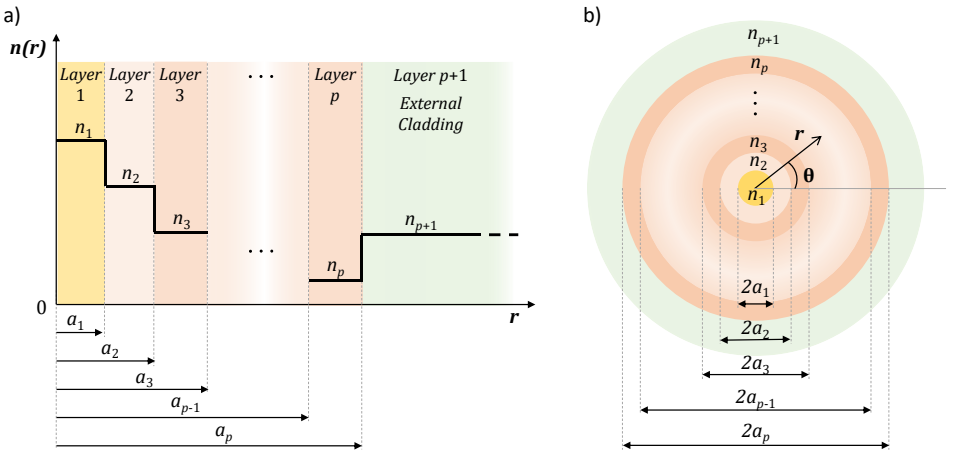

Fig. 3.2. a) Refractive index profile and b) cross-section area of a general multi-layer optical fiber with p+1 refractive index layers.

Section 3.2.2 provides the model that derives the general expression for the characteristic equation of the described multi-layer optical fibers. In section 3.2.3, we determine the general expressions for the main propagation parameters that describe the modes propagating through multi-layer fibers. The validation of the model and its applicability are addressed in section 3.2.4 by particularizing the generic expressions to specific refractive index profiles, considering both discrete and continuous refractive index profiles. Finally, section 3.2.5 gathers further discussion about the application domain of the developed model.

3.2.2. Characteristic equation for multi-layer index profile

The general geometry and refractive index distribution of the multi-layer optical fiber we consider here are depicted in Fig. 3.2. We must take into account that the highest refractive index layer does not necessarily correspond to the first layer; it could be actually located in any layer between the 1st and the p^{th}. The outer cladding is assumed to extend to infinity in the radial dimension. Let n_{co} be the highest refractive index, $n_{co} = \max_{1\le i\le p}\{n_i\}$, and n_{clad} the refractive index of layer p+1, $n_{clad} = n_{p+1}$. In the following, we will consider weakly guiding fibers, assuming $n_{co} - n_{clad} << n_{co}$, [92]. Guided modes must then satisfy:

$$k_0 n_{clad} < \beta < k_0 n_{co}\,, \tag{3.1}$$

where k_0 is the vacuum wavenumber and β is the mode propagation constant. We must take into account that we assume dielectric optical fibers where the propagation constant β gets real values.

We use a cylindrical coordinate system (r,θ,z) and assume time- and z-dependent fields of the form $\exp(i(\omega t - \beta z))$. The axial field components are then expressed as [93]:

$$\begin{cases} E_z = f(r)\cos\left[(l+1)\theta\right], \\ H_z = n_1\sqrt{\dfrac{\varepsilon_0}{\mu_0}}\, f(r)\sin\left[(l+1)\theta\right], \end{cases} \tag{3.2}$$

being n_1 the refractive index in the central layer, and ε_0 and μ_0 the dielectric constant and the magnetic permeability in vacuum, respectively. In Eq. (3.2), the term $\exp(i(\omega t - \beta z))$ has been omitted for simplicity. Assuming weakly guidance approximation, guided modes can be approximated as linearly polarized modes, LP_{lm}, where the integer l corresponds to the azimuthal mode number and the integer m is the radial mode number that labels the roots for a given value of l. It is well known that each LP mode is composed of a set of degenerated modes: hybrid (HE and EH), TE, and TM modes, [92, 93]. Furthermore, each LP mode always degenerates at least into an HE mode, [92, 93]. Due to this mode degeneracy, we particularized Eq. (3.2) for HE modes without loss of generality. The following analysis will then be focused on $HE_{l+1,m}$ modes, which after all define the $LP_{l,m}$ modes we are interested on, $l \geq 0$. The other degenerate modes can be trivially determined in a similar way.

Considering a refractive index profile structured around p dielectric discontinuities or layer interfaces, as shown in Fig. 3.2, for each refractive index layer k, $k = 1, 2, \ldots, p+1$, the radial function $f(r)$ for a particular azimuthal mode number l is given by:

$$f(r) = \begin{cases} A_1 B_{l+1}\left(\dfrac{x_1 r}{a_1}\right), & r < a_1, \quad k = 1 \\ A_{2(k-1)} B_{l+1}\left(\dfrac{x_k r}{a_1}\right) + A_{2(k-1)+1} V_{l+1}\left(\dfrac{x_k r}{a_1}\right), & a_{k-1} < r < a_k, \quad 1 < k \leq p, \\ A_{2p} V_{l+1}\left(\dfrac{x_{p+1} r}{a_1}\right), & r > a_p \quad k = p+1 \end{cases} \tag{3.3}$$

where A_i, $i = 1, 2, \ldots, 2p$, are arbitrary constants, the functions B_{l+1} represent the Bessel functions (or modified Bessel functions) of the first kind, $B_{l+1} = J_{l+1}$ (or $B_{l+1} = I_{l+1}$), the functions V_{l+1} represent the Bessel functions (or modified Bessel functions) of the second kind, $V_{l+1} = Y_{l+1}$ (or $V_{l+1} = K_{l+1}$), and the variables x_k are the normalized transverse propagation constants, $x_k = u_k$ (or $x_k = w_k$), of layer k. In the previous definitions, terms inside the parentheses are used when the corresponding layer acts as cladding, while terms without parentheses lead for core layers. That means that if the refractive index of layer k, n_k, is higher than the effective index of a given mode, n_{eff}, then this layer will act as core for that mode, while in the other case it will act as cladding. In other words, the core layers satisfy $\beta < k_0 n_k$, while the cladding layers satisfy $k_0 n_k < \beta$ (note the analogy to Eq. (3.1)). Table 3.1 summarizes, for each layer k and a given azimuthal mode number l, the corresponding variables: normalized transverse propagation constants x_k, auxiliary Bessel functions B_{l+1} and V_{l+1} that appear in the axial field components (see previous Eq. (3.3)), and auxiliary Bessel functions B_l and V_l that appear in the tangential field components (as we indicate later in Eq. (3.7)). For a better understanding, the identification of the Bessel functions (or modified Bessel functions) is shown in Fig. 3.3(a), where, as an

example, we show the particularization for layers 1 and 3 following Table 3.1 when considering two arbitrary propagating modes, named as modes a and b. The normalized transverse propagation constants for each layer k are expressed as

$$\begin{cases} u_k = k_0 a_1 \sqrt{n_k^2 - n_{eff}^2}, & n_{eff} < n_k, \\ w_k = k_0 a_1 \sqrt{n_{eff}^2 - n_k^2}, & n_{eff} > n_k. \end{cases} \tag{3.4}$$

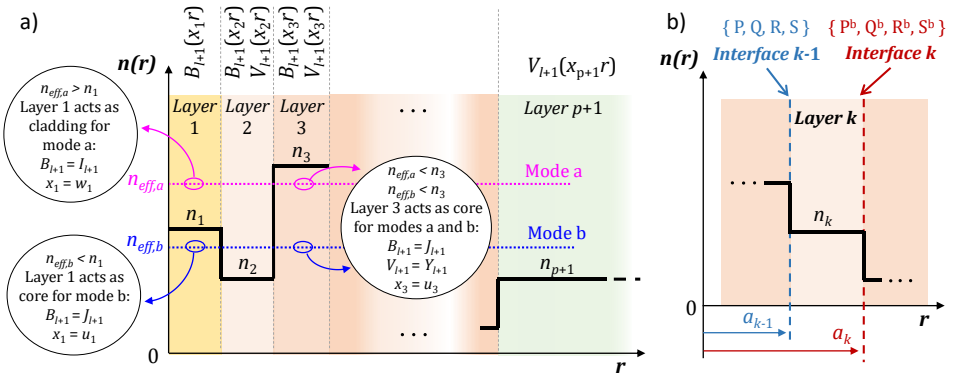

Fig. 3.3. a) Identification of Bessel functions in each refractive index layer and particularization for two modes (mode a and mode b) in layers 1 and 3; b) Identification of the minor determinants around the k^{th} refractive index layer.

Table 3.1. Bessel functions and normalized transverse propagation constants of layer *k* for a given azimuthal mode number *l*

	$B_{l+1}(x_k)$	$V_{l+1}(x_k)$	$B_l(x_k)$	$V_l(x_k)$	x_k
$n_k > n_{eff}$	$J_{l+1}(x_k)$	$Y_{l+1}(x_k)$	$J_l(x_k)$	$Y_l(x_k)$	u_k
$n_k < n_{eff}$	$I_{l+1}(x_k)$	$K_{l+1}(x_k)$	$-I_l(x_k)$	$K_l(x_k)$	w_k

Once any of the transverse propagation constants in Eq. (3.4) is determined, the longitudinal mode phase propagation constant β is given by

$$\begin{cases} \beta^2 = (k_0 n_{eff})^2 = (k_0 n_k)^2 - (u_k / a_1)^2, & n_{eff} < n_k, \\ \beta^2 = (k_0 n_{eff})^2 = (w_k / a_1)^2 + (k_0 n_k)^2, & n_{eff} > n_k. \end{cases} \tag{3.5}$$

Using Maxwell equations, we can derive the other field components from E_z and H_z as, [93],

$$\begin{pmatrix} E_\theta \\ -E_r \end{pmatrix} = \frac{1}{n_1}\sqrt{\frac{\mu_0}{\varepsilon_0}} \begin{pmatrix} -H_r \\ -H_\theta \end{pmatrix} = \frac{i n_1 k_0}{\omega^2 \varepsilon \mu - \beta^2} \left[f'(r) + (l+1)\frac{f(r)}{r} \right] \begin{Bmatrix} \sin[(l+1)\theta] \\ \cos[(l+1)\theta] \end{Bmatrix}. \tag{3.6}$$

where ω is the angular optical frequency and $f'(r)$ is the derivative of $f(r)$ with respect to r. In order to maintain the generality of the expressions, we remain treating the radial function $f(r)$ on the general form introduced in Eq. (3.3) for the tangential field components. For simplicity, the derivatives of the generic Bessel functions B and V are treated as if they are Bessel functions of the first and second kinds, respectively,

so a sign correction is applied later in the cladding regions due to Bessel functions derivative properties (see Table 3.1). The tangential field components result:

$$\begin{pmatrix} E_\theta \\ -E_r \end{pmatrix} = in_1 k_0 a_1 \begin{pmatrix} \sin(l+1)\theta \\ \cos(l+1)\theta \end{pmatrix} \begin{cases} A_1 \dfrac{B_l\left(\dfrac{x_1 r}{a_1}\right)}{x_1}, & r < a_1, \quad k = 1, \\ A_{2(k-1)} \dfrac{B_l\left(\dfrac{x_k r}{a_1}\right)}{x_k} + A_{2(k-1)+1} \dfrac{V_l\left(\dfrac{x_k r}{a_1}\right)}{x_k}, & a_{k-1} < r < a_k, \quad 1 < k \le p, \\ A_{2p} \dfrac{V_l\left(\dfrac{x_{p+1} r}{a_1}\right)}{x_{p+1}}, & r > a_p \quad k = p+1. \end{cases} \tag{3.7}$$

The characteristic equation is derived by matching both the axial and the tangential field components at the dielectric discontinuities $r = a_j$, $j = 1, 2, \ldots, p$. From Eqs. (3.2), (3.3) and (3.7), the continuity conditions of E_z, H_z, E_θ and H_θ, lead to:

$$\mathrm{M} \begin{pmatrix} A_1 \\ A_2 \\ \vdots \\ A_{2p} \end{pmatrix} = 0, \tag{3.8}$$

where M is a $2p$ x $2p$ matrix in which odd rows come from the axial fields continuity and even rows come from the tangential fields continuity. Existence of nontrivial solution to Eq. (3.8) leads to equate the determinant of the matrix M to zero, $|\mathrm{M}| = 0$:

$$\begin{vmatrix}
B_{l+1}(x_1) & B_{l+1}(x_2) & V_{l+1}(x_2) & 0 & 0 & \cdots & 0 & 0 & 0 \\
\dfrac{B_l(x_1)}{x_1} & \dfrac{B_l(x_2)}{x_2} & \dfrac{V_l(x_2)}{x_2} & 0 & 0 & \cdots & 0 & 0 & 0 \\
0 & B_{l+1}(\eta_2 x_2) & V_{l+1}(\eta_2 x_2) & B_{l+1}(\eta_2 x_3) & V_{l+1}(\eta_2 x_3) & \cdots & 0 & 0 & 0 \\
0 & \dfrac{B_l(\eta_2 x_2)}{x_2} & \dfrac{V_l(\eta_2 x_2)}{x_2} & \dfrac{B_l(\eta_2 x_3)}{x_3} & \dfrac{V_l(\eta_2 x_3)}{x_3} & \cdots & 0 & 0 & 0 \\
0 & 0 & 0 & B_{l+1}(\eta_3 x_3) & V_{l+1}(\eta_3 x_3) & \cdots & 0 & 0 & 0 \\
0 & 0 & 0 & \dfrac{B_l(\eta_3 x_3)}{x_3} & \dfrac{V_l(\eta_3 x_3)}{x_3} & \cdots & 0 & 0 & 0 \\
\vdots & \vdots & \vdots & \vdots & \vdots & \ddots & \vdots & \vdots & \vdots \\
0 & 0 & 0 & 0 & 0 & \cdots & B_{l+1}(\eta_{p-1} x_p) & V_{l+1}(\eta_{p-1} x_p) & 0 \\
0 & 0 & 0 & 0 & 0 & \cdots & \dfrac{B_l(\eta_{p-1} x_p)}{x_p} & \dfrac{V_l(\eta_{p-1} x_p)}{x_p} & 0 \\
0 & 0 & 0 & 0 & 0 & \cdots & B_{l+1}(\eta_p x_p) & V_{l+1}(\eta_p x_p) & V_{l+1}(\eta_p x_{p+1}) \\
0 & 0 & 0 & 0 & 0 & \cdots & \dfrac{B_l(\eta_p x_p)}{x_p} & \dfrac{V_l(\eta_p x_p)}{x_p} & \dfrac{V_l(\eta_p x_{p+1})}{x_{p+1}}
\end{vmatrix} = 0, \tag{3.9}$$

being $\eta_j = a_j/a_1$. After suppressing denominators in Eq. (3.9), the resulting determinant |M'| can be easily solved by cofactors. We start by solving the determinant |M'| by the cofactors of the last column (2p-th column), obtaining the corresponding two minor determinants as

$$|\mathrm{M}| = x_p V_l(\eta_p x_{p+1}) \begin{vmatrix} B_{l+1}(x_1) & B_{l+1}(x_2)\cdots & 0 \\ x_2 B_l(x_1) & x_1 B_l(x_2)\cdots & 0 \\ \vdots & \vdots & \vdots \\ 0 & 0 & \cdots V_{l+1}(\eta_p x_p) \end{vmatrix} - x_{p+1} V_{l+1}(\eta_p x_{p+1}) \begin{vmatrix} B_{l+1}(x_1) & B_{l+1}(x_2)\cdots & 0 \\ x_2 B_l(x_1) & x_1 B_l(x_2)\cdots & 0 \\ \vdots & \vdots & \vdots \\ 0 & 0 & \cdots V_l(\eta_p x_p) \end{vmatrix}, \tag{3.10}$$

We now continue by solving the two determinants of Eq. (3.10) by cofactors of the first column, obtaining again two new minor determinants per each of the previous ones,

$$\begin{aligned} |\mathrm{M}| = {} & x_p V_l(\eta_p x_{p+1}) \left(x_1 B_{l+1}(x_1) \begin{vmatrix} B_l(x_2)\cdots & 0 \\ \vdots & \vdots \\ 0 & \cdots V_{l+1}(\eta_p x_p) \end{vmatrix} - x_2 B_l(x_1) \begin{vmatrix} B_n(x_2)\cdots & 0 \\ \vdots & \vdots \\ 0 & \cdots V_n(\eta_p x_p) \end{vmatrix} \right) - \\ & x_{p+1} V_{l+1}(\eta_p x_{p+1}) \left(x_1 B_{l+1}(x_1) \begin{vmatrix} B_l(x_2)\cdots & 0 \\ \vdots & \vdots \\ 0 & \cdots V_l(\eta_p x_p) \end{vmatrix} - x_2 B_l(x_1) \begin{vmatrix} B_{l+1}(x_2)\cdots & 0 \\ \vdots & \vdots \\ 0 & \cdots V_l(\eta_p x_p) \end{vmatrix} \right), \\ = {} & x_p V_l(\eta_p x_{p+1}) \left[x_1 B_{l+1}(x_1)\mathbf{P}_2 - x_2 B_l(x_1)\mathbf{Q}_2 \right] \\ & - x_{p+1} V_{l+1}(\eta_p x_{p+1}) \left[x_1 B_{l+1}(x_1)\mathbf{R}_2 - x_2 B_l(x_1)\mathbf{S}_2 \right] \end{aligned} \tag{3.11}$$

where the variables $\mathbf{P}_2$, $\mathbf{Q}_2$, $\mathbf{R}_2$ and $\mathbf{S}_2$ refer to the resulting four minor determinants. While the range of the resulting determinants is higher than 2, the same procedure should be applied to expand again the preceding minor determinants by cofactors, starting again from the upper left corner but alternating row and column cofactors at each step. The recursive form of Eq. (3.11) satisfies then the following expressions for the minor determinants associated to the k^{th} layer, where $k = 2, 3, \ldots, p\text{-}1$,

$$\begin{cases} \mathbf{P}_k = B_l(\eta_{k-1} x_k)\mathbf{P}_k^b - V_l(\eta_{k-1} x_k)\mathbf{Q}_k^b \\ \mathbf{Q}_k = B_{l+1}(\eta_{k-1} x_k)\mathbf{P}_k^b - V_{l+1}(\eta_{k-1} x_k)\mathbf{Q}_k^b \\ \mathbf{R}_k = B_l(\eta_{k-1} x_k)\mathbf{R}_k^b - V_l(\eta_{k-1} x_k)\mathbf{S}_k^b \\ \mathbf{S}_k = B_{l+1}(\eta_{k-1} x_k)\mathbf{R}_k^b - V_{l+1}(\eta_{k-1} x_k)\mathbf{S}_k^b \end{cases} \text{, layer } k\text{, interface } k\text{-}1,$$

$$\begin{cases} \mathbf{P}_k^b = x_k V_{l+1}(\eta_k x_k)\mathbf{P}_{k+1} - x_{k+1} V_l(\eta_k x_k)\mathbf{Q}_{k+1} \\ \mathbf{Q}_k^b = x_k B_{l+1}(\eta_k x_k)\mathbf{P}_{k+1} - x_{k+1} B_l(\eta_k x_k)\mathbf{Q}_{k+1} \\ \mathbf{R}_k^b = x_k V_{l+1}(\eta_k x_k)\mathbf{R}_{k+1} - x_{k+1} V_l(\eta_k x_k)\mathbf{S}_{k+1} \\ \mathbf{S}_k^b = x_k B_{l+1}(\eta_k x_k)\mathbf{R}_{k+1} - x_{k+1} B_l(\eta_k x_k)\mathbf{S}_{k+1} \end{cases} \text{, layer } k\text{, interface } k. \tag{3.12}$$

The identification of these minor determinants around the k^{th} refractive index layer is shown in Fig. 3.3(b). Finally, in the last iteration (i.e., for layer p), the last minor determinants $\mathbf{P}_p$, $\mathbf{Q}_p$, $\mathbf{R}_p$ and $\mathbf{S}_p$ are

$$\begin{cases} \mathbf{P}_p = \begin{vmatrix} B_l(\eta_{p-1}x_p) & V_l(\eta_{p-1}x_p) \\ B_{l+1}(\eta_p x_p) & V_{l+1}(\eta_p x_p) \end{vmatrix} = B_l(\eta_{p-1}x_p)V_{l+1}(\eta_p x_p) - V_l(\eta_{p-1}x_p)B_{l+1}(\eta_p x_p) \\ \mathbf{Q}_p = \begin{vmatrix} B_{l+1}(\eta_{p-1}x_p) & V_{l+1}(\eta_{p-1}x_p) \\ B_{l+1}(\eta_p x_p) & V_{l+1}(\eta_p x_p) \end{vmatrix} = B_{l+1}(\eta_{p-1}x_p)V_{l+1}(\eta_p x_p) - V_{l+1}(\eta_{p-1}x_p)B_{l+1}(\eta_p x_p) \\ \mathbf{R}_p = \begin{vmatrix} B_l(\eta_{p-1}x_p) & V_l(\eta_{p-1}x_p) \\ B_l(\eta_p x_p) & V_l(\eta_p x_p) \end{vmatrix} = B_l(\eta_{p-1}x_p)V_l(\eta_p x_p) - V_l(\eta_{p-1}x_p)B_l(\eta_p x_p) \\ \mathbf{S}_p = \begin{vmatrix} B_{l+1}(\eta_{p-1}x_p) & V_{l+1}(\eta_{p-1}x_p) \\ B_l(\eta_p x_p) & V_l(\eta_p x_p) \end{vmatrix} = B_{l+1}(\eta_{p-1}x_p)V_l(\eta_p x_p) - V_{l+1}(\eta_{p-1}x_p)B_l(\eta_p x_p) \end{cases}, \quad (3.13)$$

The general expression for the characteristic equation of Eq. (3.8) can then be expressed in a compact form as

$$x_{p+1}\frac{V_{l+1}(\eta_p x_{p+1})}{V_l(\eta_p x_{p+1})} = x_p \frac{x_1 B_{l+1}(x_1)\mathbf{R}_2 - x_2 B_l(x_1)\mathbf{S}_2}{x_1 B_{l+1}(x_1)\mathbf{P}_2 - x_2 B_l(x_1)\mathbf{Q}_2}, \quad (3.14)$$

where the variables $\mathbf{P}_2$, $\mathbf{Q}_2$, $\mathbf{R}_2$ and $\mathbf{S}_2$ satisfy the recursive relations of Eqs. (3.12) and (3.13). If the number of interfaces is 2, $p = 2$, then Eq. (3.12) is omitted and the characteristic equation is simply given by Eqs. (3.13) and (3.14). If $p = 1$, then a classic step-index fiber is obtained and the characteristic equation is directly derived from Eq. (3.10) as

$$x_2\frac{V_{l+1}(x_2)}{V_l(x_2)} = x_1\frac{B_{l+1}(x_1)}{B_l(x_1)}, \quad (3.15)$$

and, in particular, $n_1 > n_2$ and thus $V = K$, $B = J$, $x_1 = u_1$ and $x_2 = w_2$, leading to the classical step index characteristic equation, [92].

The strategy beyond regrouping terms as in Eq. (3.14) is to intuitively build the characteristic equation of any refractive index profile without the actual need of solving it. Figure 3.4 shows a block diagram that summarizes the process to follow in order to reconstruct the characteristic equation of an arbitrary refractive index profile. Starting from the identification of the cladding layer ($k = p+1$), (green box in the upper left corner of Fig. 3.4), the process proceeds with the analysis of layer 1 (dark yellow elements) and continues with the recursive scheme to analyze each intermediate layer (orange elements) from $k = 2$ up to p. Following the characteristic equation in Eq. (14), this translates into the following process. First, we obtain the left-hand-side of Eq. (14) for every mode by determining the Bessel function V, the transverse propagation constant x_{p+1} and the parameter η_p that define the cladding layer ($p+1$), (green box). Then, we build the right-hand side of Eq. (14) recursively, starting from the first layer ($k = 1$, dark yellow elements). If the refractive index profile is composed of only 2 layers (i.e., if $p = 1$), then the characteristic equation is that of the classic step-index profile given by Eq. (15). If $p > 1$, then we have a multi-layer structure and we have to determine, for each intermediate layer k, $2 \le k \le p$ (orange elements), the Bessel functions V and B, the transverse propagation constant

x_k and the parameter η_k that define that layer, together with the minor determinants $\boldsymbol{P}_k$, $\boldsymbol{Q}_k$, $\boldsymbol{R}_k$, $\boldsymbol{S}_k$, $\boldsymbol{P}_k^b$, $\boldsymbol{Q}_k^b$, $\boldsymbol{R}_k^b$, $\boldsymbol{S}_k^b$. Once the recursive process is finished, i.e., $k = p$, the final characteristic equation is built by combining all these terms as in Eq. (14).

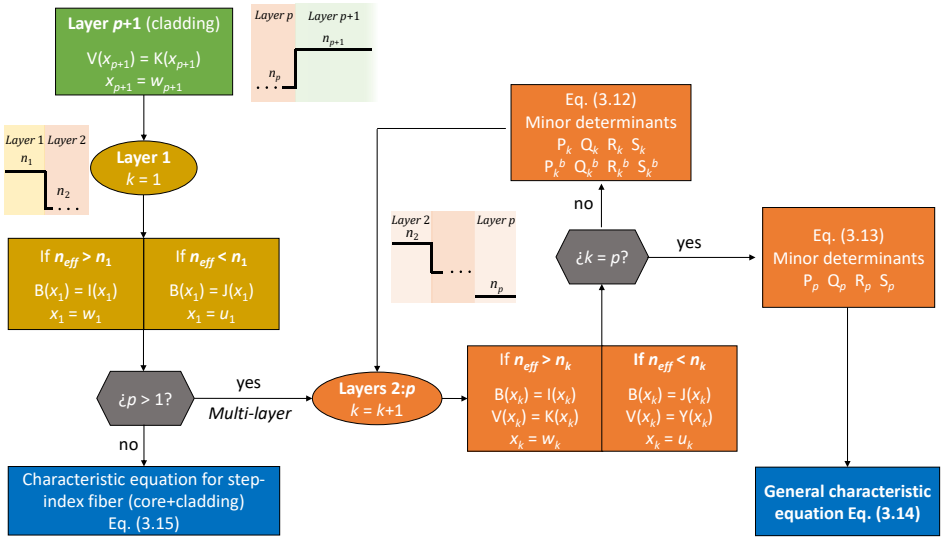

Fig. 3.4. Block diagram describing the process that reconstructs the characteristic equation of an arbitrary refractive index profile with p+1 concentric layers.

3.2.3. Derivation of the main propagation characteristics

The phase propagation constant of a propagating mode for an arbitrary refractive index profile is obtained by Eq. (3.5) given any of the p+1 eigenvalues u_k/w_k, k = 1, 2, …, p+1, of the p+1 layers. In case that Eq. (3.5) is particularized for the highest refractive index layer, $n_{co} = \max_{1\le i\le p}\{n_i\}$, then $n_{eff} < n_{co}$ for every fiber mode (i.e., this layer will always act as core). Let u_{co} be the normalized transverse propagation constant of the highest refractive index profile layer given by Eq. (3.4). Then, the propagation constant is given, for each guided mode, by

$$\beta = k_0 n_{eff} = \sqrt{\left(k_0 n_{co}\right)^2 - \left(u_{co}/a_1\right)^2}. \tag{3.16}$$

The mode group delay per unit length, τ_g/L, can be derived from Eq. (3.16) as

$$\frac{\tau_g}{L} = \frac{d\beta}{d\omega} = \frac{1}{c}\frac{d}{dk_0}\left(\sqrt{k_0^2 n_{co}^2 - \frac{u_{co}^2}{a_1^2}}\right) = \frac{1}{c\beta}\left[k_0 n_{co}^2 - 2\pi n_{co}\frac{dn_{co}}{d\lambda} + \frac{2\pi}{a_1^2 k_0^2} u_{co}\frac{du_{co}}{d\lambda}\right]. \tag{3.17}$$

Here, the refractive index n_{co} can be approximated by Sellmeier's equation and, thus, it can be analytically differentiated with respect to the optical wavelength. We see in Eq. (3.17) that the first two terms inside the square brackets do not depend on u_{co}, so they are the same for all modes. The last term depends on both u_{co} and its derivative with respect to the optical wavelength. Since u_{co} must be numerically determined, its derivative must be approximated.

The chromatic dispersion D results from the derivative of the group delay per unit length with respect to the optical wavelength. From Eq. (3.17), we get

$$D=\frac{d\left(\tau_g/L\right)}{d\lambda}=\frac{1}{c\beta}\left[\begin{array}{l} c\frac{\tau_g}{L}\frac{k_0}{\beta}\left(\frac{k}{\lambda}n_{co}^2-k_0 n_{co}\frac{dn_{co}}{d\lambda}+\frac{1}{a_1^2 k_0}u_{co}\frac{du_{co}}{d\lambda}\right)+ \\ \frac{d\left(k_0 n_{co}^2\right)}{d\lambda}-2\pi\frac{d}{d\lambda}\left(n_{co}\frac{dn_{co}}{d\lambda}\right)+\frac{2\pi}{a_1^2}\frac{d}{d\lambda}\left(\frac{u_{co}}{k_0^2}\frac{du_{co}}{d\lambda}\right) \end{array}\right], \tag{3.18}$$

being

$$\frac{d\left(k_0 n_{co}^2\right)}{d\lambda}=-\frac{k_0 n_{co}^2}{\lambda}+2k_0 n_{co}\frac{dn_{co}}{d\lambda}, \tag{3.19}$$

$$\frac{d}{d\lambda}\left(n_{co}\frac{dn_{co}}{d\lambda}\right)=\left(\frac{dn_{co}}{d\lambda}\right)^2+n_{co}\frac{d^2 n_{co}}{d\lambda^2}, \tag{3.20}$$

$$\frac{d}{d\lambda}\left(\frac{u_{co}}{k_0^2}\frac{du_{co}}{d\lambda}\right)=\frac{\left(\frac{du_{co}}{d\lambda}\right)^2+u_{co}\left[\frac{d^2 u_{co}}{d\lambda^2}+\frac{2}{\lambda}\frac{du_{co}}{d\lambda}\right]}{k_0^2}. \tag{3.21}$$

We see again in Eqs. (3.18)-(3.21) that the chromatic dispersion depends on differentiations with respect to the optical wavelength of: (1) n_{co}, which can be solved analytically and is common to all guided modes; and (2) u_{co}, which has to be numerically approximated and is different for each LP fiber mode.

Equations (3.16)-(3.21) are applicable for any multi-layer concentric refractive index profile and, once u_{co} is determined, they are transparent to any profile being evaluated.

3.2.4. Validation of the model

Aiming to confirm the validity of the proposed model, we particularize here the general model to five different refractive index profiles and evaluate their propagation characteristics by comparing the results brought by our model with those provided by the commercial numerical solver *Fimmwave* (from the company *Photon Design*). Figure 3.5 depicts the five optical fiber structures under evaluation. From left to right: (a) trench-assisted step-index profile, (b) ring-core index profile, (c) four-cladding profile and (d) triangular (black) and graded index (red) profiles. Green and blue zones delimit, respectively, the areas in which the mode effective index can be lower than the refractive index of a given layer (candidates for core layers), and the area in which the mode effective index is always higher than the refractive index of a given layer (cladding layers).

For each profile, we evaluate the normalized propagation constant b, the group index n_g ($n_g = c\cdot(\tau_g/L)$) and the chromatic dispersion D of the non-cutoff modes as a function of the scale factor, which is defined as the parameter that compacts/expands all the refractive index profile radii by the same value given by the scale factor parameter;

(a scale factor of 1 leaves invariant the refractive index profile). The normalized propagation constant is defined from Eq. (3.16) as:

$$b=\frac{(\beta/k_0)^2-n_{cl}^2}{n_{co}^2-n_{cl}^2}, \tag{3.22}$$

where n_{co} is the fiber highest refractive index and n_{cl} is the outer cladding refractive index.

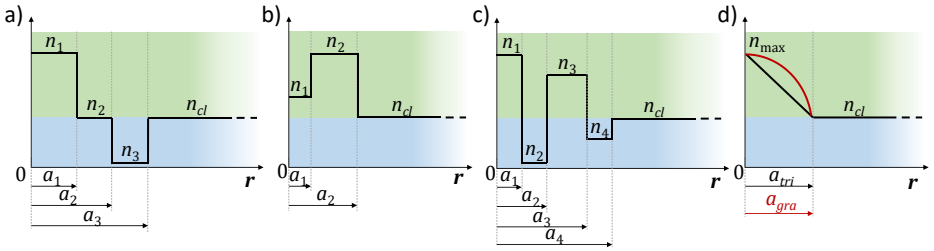

Fig. 3.5. Particular refractive index profiles evaluated: (a) trench-assisted step-index, (b) ring-core index, (c) four-cladding and (d) triangular and graded index profiles.

3.2.4.1. Trench-assisted step-index profile

Trench-assisted step-index optical fibers consist of a central core surrounded by an inner cladding region, a trench (or depressed layer) and the outer cladding [95]. We consider the trench-assisted profile of Fig. 3.5(a), where the material composition of both the inner (n_2) and the outer claddings (n_{cl}) are chosen to be pure silica, the core layer (n_1) is SiO_2 doped with a 5-mol. % of GeO_2 and the lower refractive index of the trench layer (n_3) is achieved by doping the SiO_2 with a 2 mol. % of fluorine (F). The layer radii are a_1 = 7.5, a_2 = 12.5 and a_3 = 17.5 μm. The mode effective indices can vary from n_{cl} up to n_1, and the only layer that can satisfy the condition $n_k > n_{eff}$, (k = 1, 2, 3), to act as the fiber core is the first layer, $n_1 = n_{co}$. The normalized transverse propagation constants for each layer are then

$$u_1=k_0a_1\sqrt{n_1^2-n_{eff}^2}, \tag{3.23}$$

$$w_2=k_0a_1\sqrt{n_{eff}^2-n_2^2}, \tag{3.24}$$

$$w_3=k_0a_1\sqrt{n_{eff}^2-n_3^2}, \tag{3.25}$$

$$w_4=k_0a_1\sqrt{n_{eff}^2-n_{cl}^2}. \tag{3.26}$$

The characteristic equation is obtained from the general formula in Eq. (3.14) as:

$$w_4\frac{K_{l+1}(\eta_3w_4)}{K_l(\eta_3w_4)}=w_3\frac{u_1J_{l+1}(u_1)\mathbf{R}_2+w_2J_l(u_1)\mathbf{S}_2}{u_1J_{l+1}(u_1)\mathbf{P}_2+w_2J_l(u_1)\mathbf{Q}_2}, \tag{3.27}$$

where the variables $\mathbf{P}_k$, $\mathbf{Q}_k$, $\mathbf{R}_k$ and $\mathbf{S}_k$, k = 2, 3, and $\mathbf{P}_2{}^b$, $\mathbf{Q}_2{}^b$, $\mathbf{R}_2{}^b$ and $\mathbf{S}_2{}^b$ are given by

$$\begin{cases} \mathbf{P}_2 = I_l(w_2)\mathbf{P}_2^b + K_l(w_2)\mathbf{Q}_2^b \\ \mathbf{Q}_2 = I_{l+1}(w_2)\mathbf{P}_2^b - K_{l+1}(w_2)\mathbf{Q}_2^b \\ \mathbf{R}_2 = I_l(w_2)\mathbf{R}_2^b + K_l(w_2)\mathbf{S}_2^b \\ \mathbf{S}_2 = I_{l+1}(w_2)\mathbf{R}_2^b - K_{l+1}(w_2)\mathbf{S}_2^b \end{cases} \quad \begin{cases} \mathbf{P}_2^b = w_2 K_{l+1}(\eta_2 w_2)\mathbf{P}_3 + w_3 K_l(\eta_2 x_2)\mathbf{Q}_3 \\ \mathbf{Q}_2^b = w_2 I_{l+1}(\eta_2 w_2)\mathbf{P}_3 - w_3 I_l(\eta_2 x_2)\mathbf{Q}_3 \\ \mathbf{R}_2^b = w_2 K_{l+1}(\eta_2 w_2)\mathbf{R}_3 + w_3 K_l(\eta_2 x_2)\mathbf{S}_3 \\ \mathbf{S}_2^b = w_2 I_{l+1}(\eta_2 w_2)\mathbf{R}_3 - w_3 I_l(\eta_2 x_2)\mathbf{S}_3 \end{cases} \tag{3.28}$$

$$\begin{cases} \mathbf{P}_3 = I_l(\eta_2 w_3)K_{l+1}(\eta_3 w_3) + K_l(\eta_2 w_3)I_{l+1}(\eta_3 w_3) \\ \mathbf{Q}_3 = I_{l+1}(\eta_2 w_3)K_{l+1}(\eta_3 w_3) - K_{l+1}(\eta_2 w_3)I_{l+1}(\eta_3 w_3) \\ \mathbf{R}_3 = I_l(\eta_2 w_3)K_l(\eta_3 w_3) - K_l(\eta_2 w_3)I_l(\eta_3 w_3) \\ \mathbf{S}_3 = I_{l+1}(\eta_2 w_3)K_l(\eta_3 w_3) + K_{l+1}(\eta_2 w_3)I_l(\eta_3 w_3) \end{cases}.$$

By using Eqs. (3.23)-(3.28), we compute the u_{co} variable and insert it in Eqs. (3.16)-(3.22) to calculate the normalized propagation constant, the group index and the chromatic dispersion of each fiber mode as a function of the scale factor. Figure 3.6 compares the results obtained by the present model (solid lines) and those from the commercial solver (dashed lines) for an operation wavelength of λ = 1.55 μm. The different colors correspond to different LP, whose mode profile can be observed in the legend. We see an excellent agreement between both solvers in all cases.

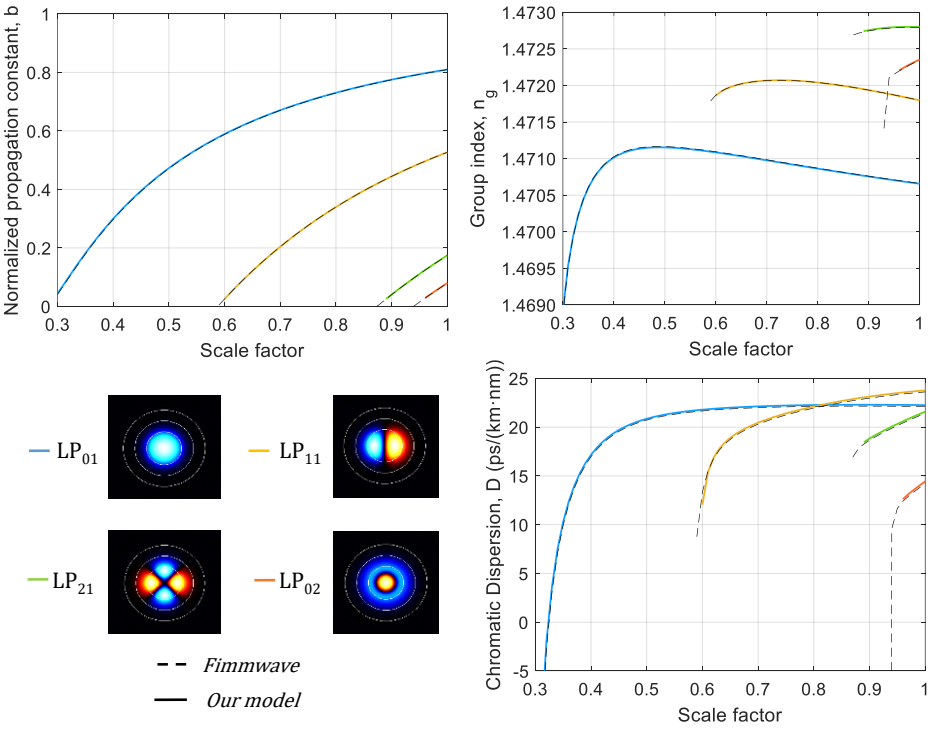

Fig. 3.6. Normalized propagation constant, group index and chromatic dispersion of each mode as a function of the fiber scale factor for a trench-assisted step-index profile and an operation wavelength of λ = 1.55 μm. Solid lines correspond to our model and dashed lines to the commercial solver. Bottom-left images: Mode profiles of the propagating modes.

3.2.4.2. Ring-core refractive index profile

Another interesting fiber structure is the ring-core refractive index profile. As opposed to the classic optical fiber structures, here the core (i.e., the layer with the highest refractive index) is not located in the center of the cross-sectional area, [89, 100, 101, 102]. We consider the ring-core optical fiber of Fig. 3.5(b), with radii a_1 = 2 and a_2 = 9.5 μm, where the inner hole (n_1) is based on SiO_2 doped with a 2-mol.% of GeO_2 and the core layer (n_2) is doped with a 5-mol.% of GeO_2. The mode effective indices can vary from n_{cl} up to n_2, being $n_{cl} < n_1 < n_2$, and therefore the second layer acts as the fiber core ($n_2 = n_{co}$), while the first layer can act either as core or as cladding. Thus, the normalized transverse propagation constants for each layer are, in this case,

$$\begin{cases} u_1 = k_0 a_1 \sqrt{n_1^2 - n_{eff}^2}, & n_{eff} < n_1 \\ w_1 = k_0 a_1 \sqrt{n_{eff}^2 - n_1^2}, & n_{eff} > n_1 \end{cases} \tag{3.29}$$

$$u_2 = k_0 a_1 \sqrt{n_2^2 - n_{eff}^2}, \tag{3.30}$$

$$w_3 = k_0 a_1 \sqrt{n_{eff}^2 - n_{cl}^2}. \tag{3.31}$$

The characteristic equation is then expressed as:

$$\begin{cases} w_3 \dfrac{K_{l+1}(\eta_2 w_3)}{K_l(\eta_2 w_3)} = u_2 \dfrac{u_1 J_{l+1}(u_1)\mathbf{R}_2 - u_2 J_l(u_1)\mathbf{S}_2}{u_1 J_{l+1}(u_1)\mathbf{P}_2 - u_2 J_l(u_1)\mathbf{Q}_2}, & n_{eff} < n_1 \\ w_3 \dfrac{K_{l+1}(\eta_2 w_3)}{K_l(\eta_2 w_3)} = u_2 \dfrac{w_1 I_{l+1}(w_1)\mathbf{R}_2 + u_2 I_l(u_1)\mathbf{S}_2}{w_1 I_{l+1}(w_1)\mathbf{P}_2 + u_2 I_l(u_1)\mathbf{Q}_2}, & n_{eff} > n_1 \end{cases} \tag{3.32}$$

where the variables $\mathbf{P}_2$, $\mathbf{Q}_2$, $\mathbf{R}_2$ and $\mathbf{S}_2$ are given by

$$\begin{cases} \mathbf{P}_2 = J_l(u_2) Y_{l+1}(\eta_2 u_2) - Y_l(u_2) J_{l+1}(\eta_2 u_2) \\ \mathbf{Q}_2 = J_{l+1}(u_2) Y_{l+1}(\eta_2 u_2) - Y_{l+1}(u_2) J_{l+1}(\eta_2 u_2) \\ \mathbf{R}_2 = J_l(u_2) Y_l(\eta_2 u_2) - Y_l(u_2) J_l(\eta_2 u_2) \\ \mathbf{S}_2 = J_{l+1}(u_2) Y_l(\eta_2 u_2) - Y_{l+1}(u_2) J_l(\eta_2 u_2) \end{cases}. \tag{3.33}$$

For an operation wavelength of λ = 1.55 μm, we computed the normalized propagation constant, the group index and the chromatic dispersion of the fiber as a function of the scale factor. Fig. 3.7 shows the comparison between the results reached via the present model (solid lines) and the ones obtained with the commercial software (dashed lines). The different colors correspond to different LP modes, whose mode profiles are shown in the legend. We see again that both solvers provide mostly identical results for all the parameters evaluated.

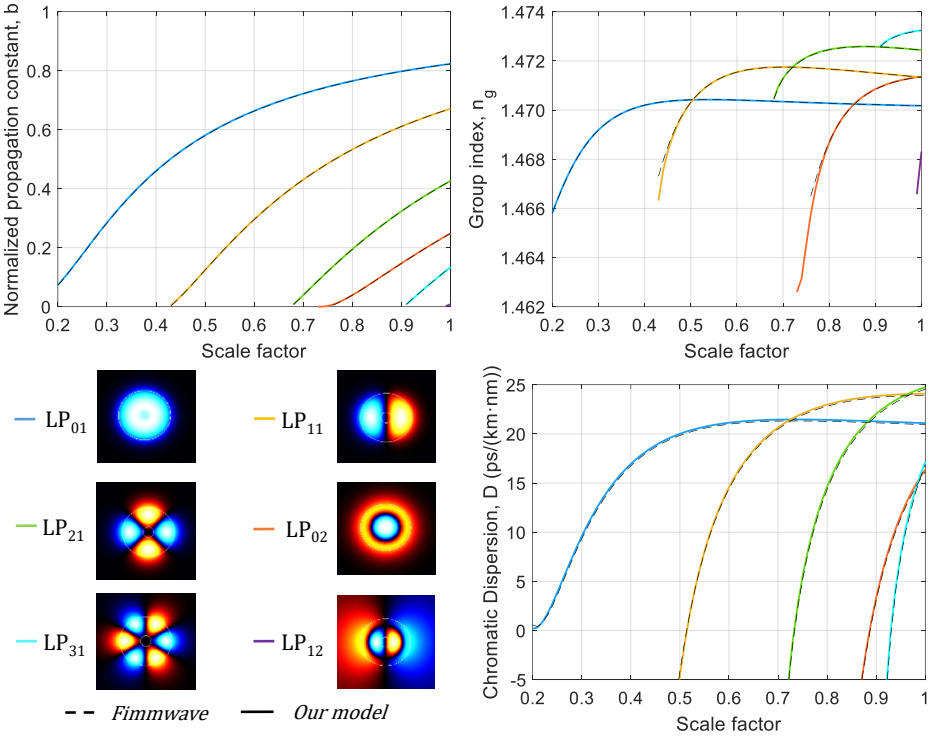

Fig. 3.7. Normalized propagation constant, group index and chromatic dispersion of each mode as a function of the fiber scale factor for a ring-core index profile and an operation wavelength of λ = 1.55 μm. Solid lines correspond to our model and dashed lines to the commercial solver. Bottom-left images: Mode profiles of the propagating modes.

3.2.4.3. Four-cladding refractive index profile

More complex refractive index profiles comprise a higher number of layers, as the four-cladding refractive index profile shown in Fig. 3.5(c). Here, the core layer is centered in the fiber cross-section, and it is surrounded by a combination of a depressed trench, an upper-index ring and a second trench layer, [105, 106]. We consider again pure silica for the infinite outer cladding region. Both the core layer (n_1) and the ring (n_3) are doped with GeO_2 (5 mol.% for the core and 3 mol.% for the ring), while the depressed index for the trenches are achieved by doping the SiO_2 with Fluorine (2-mol.% for the inner trench, n_2, and 1-mol.% for the outer trench, n_4). We set the radii to 4, 8, 16 and 20 μm, respectively for a_1, a_2, a_3 and a_4. The normalized transverse propagation constants are then

$$u_1 = k_0 a_1 \sqrt{n_1^2 - n_{eff}^2}, \tag{3.34}$$

$$w_2 = k_0 a_1 \sqrt{n_{eff}^2 - n_2^2}, \tag{3.35}$$

$$\begin{cases} u_3 = k_0 a_1 \sqrt{n_3^2 - n_{eff}^2}, & n_{eff} < n_3 \\ w_3 = k_0 a_1 \sqrt{n_{eff}^2 - n_3^2}, & n_{eff} > n_3 \end{cases} \tag{3.36}$$

$$w_4 = k_0 a_1 \sqrt{n_{eff}^2 - n_4^2}. \tag{3.37}$$

$$w_5 = k_0 a_1 \sqrt{n_{eff}^2 - n_{cl}^2}. \tag{3.38}$$

The characteristic equation is obtained from Eq. (3.14) as:

$$w_5 \frac{K_{l+1}(\eta_4 w_5)}{K_l(\eta_4 w_5)} = w_4 \frac{u_1 J_{l+1}(u_1)\mathbf{R}_2 - w_2 J_l(u_1)\mathbf{S}_2}{u_1 J_{l+1}(u_1)\mathbf{P}_2 - w_2 J_l(u_1)\mathbf{Q}_2}, \tag{3.39}$$

where the variables $\mathbf{P}_k$, $\mathbf{Q}_k$, $\mathbf{R}_k$ and $\mathbf{S}_k$, k = 2, 3, 4, and $\mathbf{P}_k{}^b$, $\mathbf{Q}_k{}^b$, $\mathbf{R}_k{}^b$ and $\mathbf{S}_k{}^b$, k = 2, 3, are given by

$$\begin{cases} \mathbf{P}_2 = -I_l(w_2)\mathbf{P}_2^b - K_l(w_2)\mathbf{Q}_2^b \\ \mathbf{Q}_2 = I_{l+1}(w_2)\mathbf{P}_2^b - K_{l+1}(w_2)\mathbf{Q}_2^b \\ \mathbf{R}_2 = -I_l(w_2)\mathbf{R}_2^b - K_l(w_2)\mathbf{S}_2^b \\ \mathbf{S}_2 = I_{l+1}(w_2)\mathbf{R}_2^b - K_{l+1}(w_2)\mathbf{S}_2^b \end{cases} \tag{3.40}$$

$n_{eff} > n_3$	$n_{eff} < n_3$
$\begin{cases} \mathbf{P}_2^b = w_2 K_{l+1}(\eta_2 w_2)\mathbf{P}_3 - w_3 K_l(\eta_2 w_2)\mathbf{Q}_3 \\ \mathbf{Q}_2^b = w_2 I_{l+1}(\eta_2 w_2)\mathbf{P}_3 + w_3 I_l(\eta_2 w_2)\mathbf{Q}_3 \\ \mathbf{R}_2^b = w_2 K_{l+1}(\eta_2 w_2)\mathbf{R}_3 - w_3 K_l(\eta_2 w_2)\mathbf{S}_3 \\ \mathbf{S}_2^b = w_2 I_{l+1}(\eta_2 w_2)\mathbf{R}_3 + w_3 I_l(\eta_2 w_2)\mathbf{S}_3 \end{cases}$	$\begin{cases} \mathbf{P}_2^b = w_2 K_{l+1}(\eta_2 w_2)\mathbf{P}_3 - u_3 K_l(\eta_2 w_2)\mathbf{Q}_3 \\ \mathbf{Q}_2^b = w_2 I_{l+1}(\eta_2 w_2)\mathbf{P}_3 + u_3 I_l(\eta_2 w_2)\mathbf{Q}_3 \\ \mathbf{R}_2^b = w_2 K_{l+1}(\eta_2 w_2)\mathbf{R}_3 - u_3 K_l(\eta_2 w_2)\mathbf{S}_3 \\ \mathbf{S}_2^b = w_2 I_{l+1}(\eta_2 w_2)\mathbf{R}_3 + u_3 I_l(\eta_2 w_2)\mathbf{S}_3 \end{cases}$
$\begin{cases} \mathbf{P}_3 = -I_l(\eta_2 w_3)\mathbf{P}_3^b - K_l(\eta_2 w_3)\mathbf{Q}_3^b \\ \mathbf{Q}_3 = I_{l+1}(\eta_2 w_3)\mathbf{P}_3^b - K_{l+1}(\eta_2 w_3)\mathbf{Q}_3^b \\ \mathbf{R}_3 = -I_l(\eta_2 w_3)\mathbf{R}_3^b - K_l(\eta_2 w_3)\mathbf{S}_3^b \\ \mathbf{S}_3 = I_{l+1}(\eta_2 w_3)\mathbf{R}_3^b - K_{l+1}(\eta_2 w_3)\mathbf{S}_3^b \end{cases}$	$\begin{cases} \mathbf{P}_3 = J_l(\eta_2 u_3)\mathbf{P}_3^b - Y_l(\eta_2 u_3)\mathbf{Q}_3^b \\ \mathbf{Q}_3 = J_{l+1}(\eta_2 u_3)\mathbf{P}_3^b - Y_{l+1}(\eta_2 u_3)\mathbf{Q}_3^b \\ \mathbf{R}_3 = J_l(\eta_2 u_3)\mathbf{R}_3^b - Y_l(\eta_2 u_3)\mathbf{S}_3^b \\ \mathbf{S}_3 = J_{l+1}(\eta_2 u_3)\mathbf{R}_3^b - Y_{l+1}(\eta_2 u_3)\mathbf{S}_3^b \end{cases}$
$\begin{cases} \mathbf{P}_3^b = w_3 K_{l+1}(\eta_3 w_3)\mathbf{P}_4 - w_4 K_l(\eta_3 w_3)\mathbf{Q}_4 \\ \mathbf{Q}_3^b = w_3 I_{l+1}(\eta_3 w_3)\mathbf{P}_4 + w_4 I_l(\eta_3 w_3)\mathbf{Q}_4 \\ \mathbf{R}_3^b = w_3 K_{l+1}(\eta_3 w_3)\mathbf{R}_3 - w_4 K_l(\eta_3 w_3)\mathbf{S}_3 \\ \mathbf{S}_3^b = w_3 I_{l+1}(\eta_3 w_3)\mathbf{R}_3 + w_4 I_l(\eta_3 w_3)\mathbf{S}_3 \end{cases}$	$\begin{cases} \mathbf{P}_3^b = u_3 Y_{l+1}(\eta_3 u_3)\mathbf{P}_4 - w_4 Y_l(\eta_3 u_3)\mathbf{Q}_4 \\ \mathbf{Q}_3^b = u_3 J_{l+1}(\eta_3 u_3)\mathbf{P}_4 - w_4 J_l(\eta_3 u_3)\mathbf{Q}_4 \\ \mathbf{R}_3^b = u_3 Y_{l+1}(\eta_3 u_3)\mathbf{R}_4 - w_4 Y_l(\eta_3 u_3)\mathbf{S}_4 \\ \mathbf{S}_3^b = u_3 J_{l+1}(\eta_3 u_3)\mathbf{R}_4 - w_4 J_l(\eta_3 u_3)\mathbf{S}_4 \end{cases}$

(3.41)

$$\begin{cases} \mathbf{P}_4 = -I_l(\eta_3 w_4)K_{l+1}(\eta_4 w_4) - K_l(\eta_3 w_4)I_{l+1}(\eta_4 w_4) \\ \mathbf{Q}_4 = I_{l+1}(\eta_3 w_4)K_{l+1}(\eta_4 w_4) - K_{l+1}(\eta_3 w_4)I_{l+1}(\eta_4 w_4) \\ \mathbf{R}_4 = -I_l(\eta_3 w_4)K_l(\eta_4 w_4) + K_l(\eta_3 w_4)I_l(\eta_4 w_4) \\ \mathbf{S}_4 = I_{l+1}(\eta_3 w_4)K_l(\eta_4 w_4) + K_{l+1}(\eta_3 w_4)I_l(\eta_4 w_4) \end{cases} \tag{3.42}$$

Figure 3.8 compares the normalized propagation constant, the group index and the chromatic dispersion computed from both the present solver (solid lines) and the commercial solver (dashed lines) for an operation wavelength of λ = 1.55 μm. The different colors correspond to different LP modes, whose mode profiles are shown in the legend. Once again, both solvers present almost identical results in all cases.

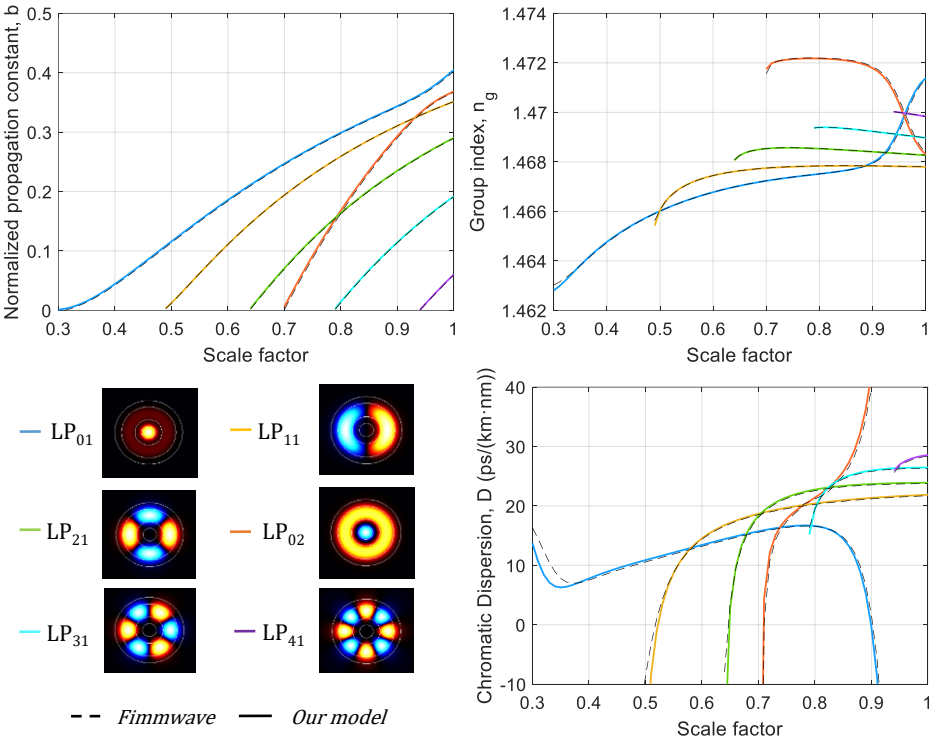

Fig. 3.8. Normalized propagation constant, group index and chromatic dispersion of each mode as a function of the fiber scale factor for a four-cladding refractive index profile and an operation wavelength of λ = 1.55 μm. Solid lines correspond to our model and dashed lines to the commercial solver. Bottom-left images: Mode profiles of the propagating modes.

3.2.4.4. Triangular refractive index profile

Finally, we study the viability of analyzing continuous (or non-stepped) refractive index profiles with the present model. First, we prove that a proper step-index discretization converges rapidly to the continuous profile. In particular, we consider the triangular refractive index profile, [104] depicted in of Fig. 3.5(d), where the refractive index at r = 0 has a material composition of SiO_2 doped with a 5-mol.% GeO_2 and decreases linearly with the radii until reaching the pure silica of the cladding region at the radius a_{tri} = 10 μm.

We study how to discretize the triangular profile by an n-step index profile with equal-width steps in which the material composition of each step decreases linearly with the step number. We can consider the superior discretization, in which each layer k, (k = 1, 2, …, n), is created by extending the corresponding value of the triangular function at $r = (k\text{-}1)\cdot 10/n$ up to the radius $r = k\cdot 10/n$. In a similar way, we can also consider the inferior discretization in which each layer k, (k = 1, 2, …, n), is created by extending the corresponding value of the triangular function at $r = k\cdot 10/n$ down to the radius $r = (k\text{-}1)\cdot 10/n$. It is clear that both the superior and the inferior discretization tend to the triangular profile when n tends to infinity, and they

correspond exactly to the superior and inferior limits of this linear step-index discretization, respectively. It is then reasonable to consider the half-point discretization, in which we extend the value of the index at $r = (k\text{-}1/2)\cdot 10/n$ from $r = (k\text{-}1)\cdot 10/n$ up to the radius $r = k\cdot 10/n$. Obviously, since this function is in-between the superior and inferior functions, it also converges to the triangular profile, and it is logical to think that it will converge faster than both the superior and the inferior discretization. Figure 3.9(a) depicts the comparison between all 3 functions for $n = 5$ steps. Red-dashed line corresponds to the superior (f_{sup}), blue-dashed to the inferior (f_{inf}), and green-solid to the medium function (f_{tri}). We can also observe that as long as n increases, the medium function converges rapidly to the triangular profile, as the purple dotted-line curve shows for $n = 10$ steps. Figure 3.9(b) shows the convergence on the propagation constant computed for the discretized profile (f_{tri}) as a function of the number of discretization steps n for the propagating modes. As we observe in the zoomed area in the inset of Fig. 3.9(b), the propagation constant mismatch for $n = 10$ steps is below 10^{-5} for both propagating modes, which is almost negligible, while the convergence for $n = 5$ is still acceptable, with a difference below $5\cdot 10^{-5}$. This shows that the discretized profile converges adequately to the ideal response even with a very low number of steps.

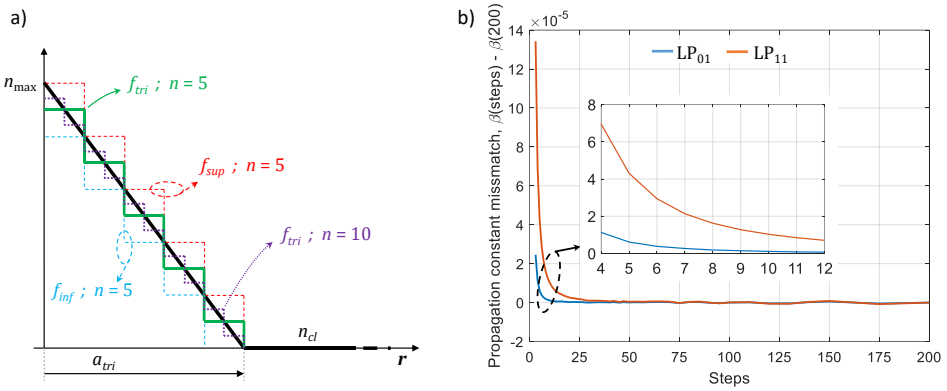

Fig. 3.9. (a) Discretization of the triangular refractive index profile; (b) Convergence of the propagation constant on the discretized triangular refractive index profile as a function of the discretization steps.

Once we prove the convergence of the discretized triangular profile, we evaluate the particular case in which the number of discretization steps is set to 5. In this case, for simplicity, we avoid the expression of the characteristic equation. However, the construction in this case is very simple: since the refractive index profile is a monotonically decreasing function with the radius, all layers with layer number below a given layer k, ($k = 1, 2, \ldots 5$), will satisfy the condition $n_k > n_{eff}$, and thus will act as core layers; layers numbered higher than k will then act as cladding layers. The characteristic equation is then formed in a similar way than the rest of the examples evaluated before. Figure 3.10 compares the computed normalized propagation constant, the group index and the chromatic dispersion as a function of the scale factor for both the proposed method and the commercial solver at $\lambda = 1.55$ μm. The mode profiles for both propagating modes are given in the legend. As in the previous

examples, we see again an excellent agreement between both solvers for all of the parameters.

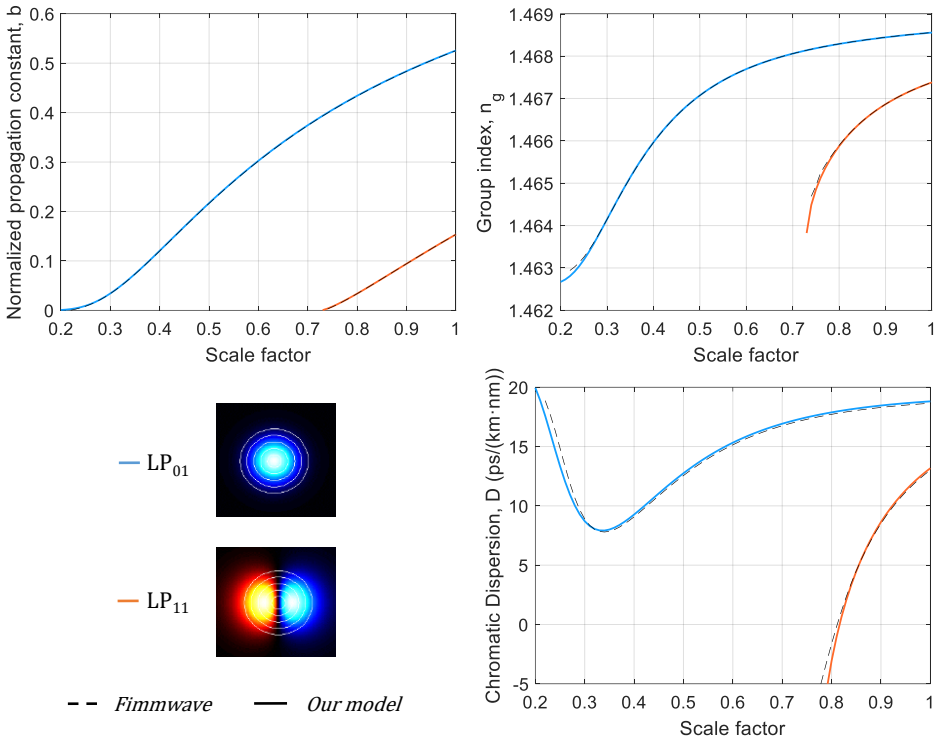

Fig. 3.10. Normalized propagation constant, group index and chromatic dispersion of each mode as a function of the fiber scale factor for a triangular index profile and an operation wavelength of λ = 1.55 μm. Solid lines correspond to our model and dashed lines to the commercial solver. Bottom-left images: Mode profiles of the propagating modes.

3.2.4.5. Graded index refractive index profile

As a second example of another discretized continuous profile, we analyze now a graded-index refractive index profile (see red curve in Fig. 3.5(d)). In this case, the refractive index profile distribution follows the well-known law of parameter α, [[91]], $n(r) = n_{max}[1 - \Delta(r/a)^{\alpha}]$ for $r < a_{gra}$, and $n(r) = n_{cla}$ for $r > a_{gra}$. We consider a graded-index fiber characterized by an α = 2.5, a core region of radius a_{gra} = 10 μm with a maximum refractive index at r = 0, n_{max}, with a material composition of SiO_2 doped with a 7-mol.% GeO_2, surrounded by a pure silica cladding region.

Analogously to the triangular profile, we start analyzing the convergence of the discretization. Again, we can, for instance, build 3 functions to discretize the profile: f_{sup}, f_{inf} and f_{gra}, as shown in Fig. 3.11(a). It is clear that as long as the number of steps increases, all 3 functions converge to the continuous profile, being f_{gra} the function with the fastest convergence. Figure 3.11(b) shows the convergence of the propagation constant computed for the discretized profile (f_{gra}) as a function of the

number of discretization steps n for the propagating modes. In the inset, we see that the absolute value of propagation constant mismatch for n = 10 decreases down to below $5 \cdot 10^{-5}$ for all the modes, while it remains below $10 \cdot 10^{-5}$ for n = 7 steps. Comparing with the triangular profile, we see that, in this case, the convergence is slower than before, requiring more steps to achieve an equivalent convergence. Nevertheless, we see again that the discretized profile converges adequately to the ideal response even with a very low number of steps.

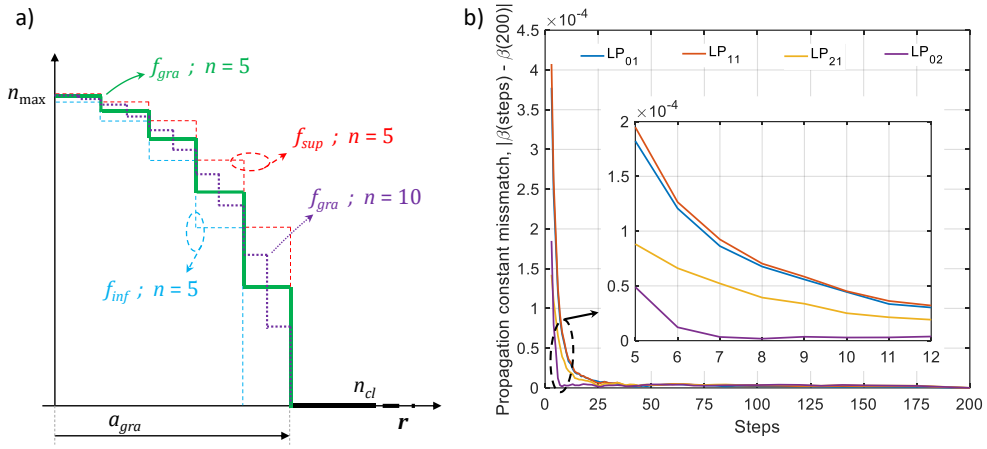

Fig. 3.11. (a) Discretization of the graded-index profile; (b) Convergence of the propagation constant on the discretized graded-index profile as a function of the discretization steps.

Once the convergence of the discretized profile is proved, we evaluate the particular case in which the number of discretization steps is set to 7. The expression of the characteristic equation is again very simple, following the same structure than that of the triangular profile, and it is omitted for simplicity. Figure 3.12 compares the computed normalized propagation constant, the group index and the chromatic dispersion as a function of the scale factor for both the proposed method and the commercial solver at λ = 1.55 μm. The mode profiles for the propagating modes can be observed in the legend. As in the previous examples, we see again an excellent agreement between both solvers for all the parameters.

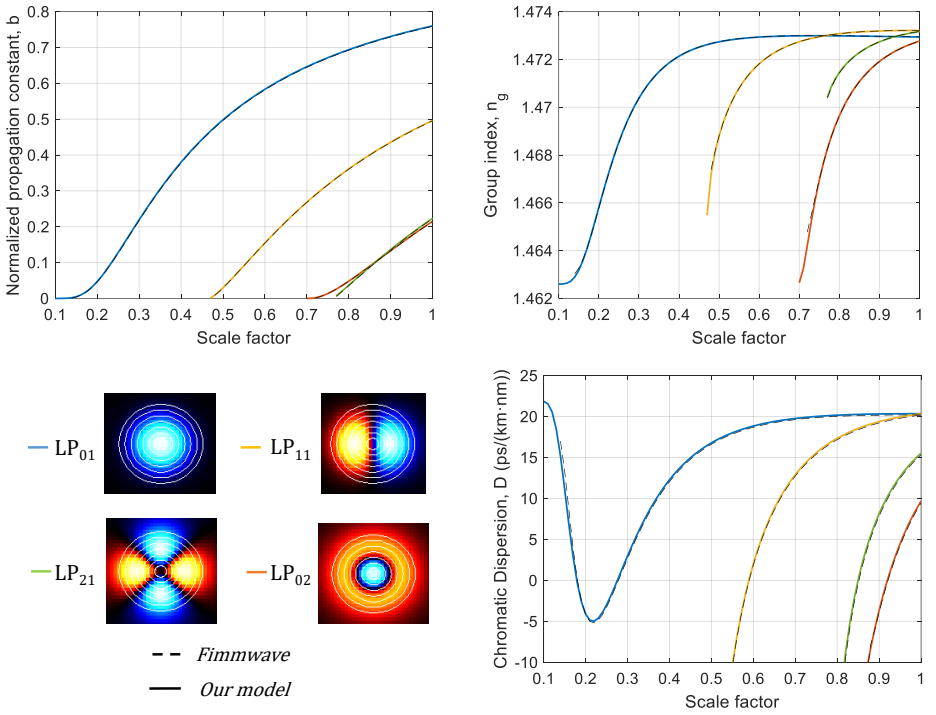

Fig. 3.12. Normalized propagation constant, group index and chromatic dispersion of each mode as a function of the fiber scale factor for a graded-index profile and an operation wavelength of λ = 1.55 μm. Solid lines correspond to our model and dashed lines to the commercial solver. Bottom-left images: Mode profiles of the propagating modes.

3.2.5. Discussion of the model applicability domain

The model we report in this work applies in general to multi-layer optical fibers comprising any number of concentric circular layers, where each layer has arbitrary radial dimensions as well as an arbitrary refractive index n_k with a constant value among that layer. This applies directly to discrete or stepped refractive index profiles, as step-index profiles comprising different trench and/or core structures. As we have seen in sections 3.2.4.4 and 3.2.4.5, continuous refractive index profiles can also be evaluated through this model if a discretization of the continuous segment of the profile is properly done. We demonstrated a fast convergence of the results for both a triangular and a graded index profiles, but this method can also be applied to any other continuous segmented profiles with similar convergence rates.

For any of the structures mentioned above, we can also use this model to calculate their cladding modes by simply adding an additional infinite external cladding and limiting the previous outer cladding to a finite value. The simplest example is the case of a classic step-index optical fiber with a single layer (p = 1) and the outer cladding region. We can compute the cladding modes if we restrict the outer cladding to a finite value (for example, a_2 = 62.5 μm) and include a new infinite external cladding (such as an air layer, for instance). Then, we can solve the characteristic

equation of this new 2-layer structure ($p = 2$) via Eq. (3.14) and obtain the propagating modes. The cladding modes of the initial monolayer structure correspond to the new modes that propagate in the bilayer structure that were in cutoff in the first layer.

We must take into account that this model applies to symmetrical optical fibers in the azimuthal direction (i.e., concentric layers), as the ones discussed in this work. In case, for instance, of core structures that are surrounded by air holes, (such as hole-assisted [108] or hole-walled [109] fibers), or elliptical fibers, one has to resort to numerical software tools.

Finally, although we have evaluated only single-core fibers, the propagation characteristics of multicore fibers can also be assessed if the refractive index profile of the different cores are treated as independent entities, [62]. This is the situation of weakly coupled multicore fibers where the level of intercore crosstalk is low enough as to model each core individually (under the assumption, as always, of infinite outer cladding region and the use of local coordinates for each core). In that regard, our model is effective for the design of each one of the cores (specially in heterogeneous multicore schemes), while the crosstalk performance can be computed from the coupled power theory [110], where in turn the average power coupling coefficient depends on the propagation parameters provided by our model.

3.3. Crosstalk

The solution of the characteristic equation defines the electromagnetic wave propagation in cylindrically-symmetric unperturbed single-core optical fibers in terms of the linearly polarized modes (the term unperturbed indicates here that the transmission medium is assumed to be invariant with the propagation length z). In a lossless system, under weakly guidance approximation and assuming that the unperturbed fiber has a refractive index profile $n(x,y)$, each mode n propagating along the z axis in the unperturbed medium satisfies the wave equation, [111, 112, 113],

$$\left[\nabla_t^2 + k^2 n^2(x,y) - \beta_n^2\right] E_n(x,y) = 0\,, \tag{3.43}$$

where the propagation constant β_n results from the characteristic equation (Eq. 3.16). Since all modes are orthogonal, the total electric field propagating along the fiber results from the linear combination of all the guided modes resulting from Eq. (3.43),

$$E(x,y,z) = \sum_n A_n E_n(x,y) e^{-i\beta_n z}\,, \tag{3.44}$$

where A_n is a constant coefficient that determines the amplitude of mode n at any position z.

However, the assumption that the fiber (or, more specifically, its refractive index profile) remains invariant with z is not actually reasonable; any irregularity that affects the refractive index profile distribution at any point of the fiber, such as temperature variations, vibrations, bends or fluctuations during the manufacture process, will break this fiber propagation homogeneity, [111, 114, 115, 116, 112]. An optical fiber with z-dependent non-uniformities is no longer cylindrically symmetric

and, thus, cannot support individual modes of the unperturbed fiber. In such a situation, the fields of the perturbed fiber at a given position z can then be described as a superposition of the fields of the complete set of modes of the unperturbed fiber. An individual mode of the set does not satisfy Maxwell's equations for the perturbed fiber, and hence, the perturbed fields must generally be distributed between all modes of the set, [112, 117, 118, 119, 120]. This effect is known as mode coupling.

Nevertheless, mode coupling can also occur between the different cores of a multicore fiber. In this case, mode coupling arises because the fields propagating along the cores extend indefinitely into the cladding and interact with any other nearby cores, [114, 116]. This interaction produces an exchange of power between the cores as the fields propagate.

In both the above situations, the electromagnetic wave propagation can be described by means of a set of coupled differential equations for the amplitudes of the modes supported by the waveguides involved. This method is known as coupled mode theory (CMT). The coupled mode equations (CMEs) result from the substitution of the modal expansion for the fields of the unperturbed waveguides into Maxwell's equations, leading to an infinite set of coupled, first-order differential equations for the z-dependent amplitude of each mode, [111, 114, 112, 121, 115, 122]. By adding z-dependence to the coefficients A_n in Eq. (3.44), the CMEs are written as follows, [112, 114],

$$\frac{dA_n(z)}{dz} = -i\sum_{m\neq n}\kappa_{nm}A_m(z)e^{-i(\beta_m-\beta_n)z}, \tag{3.45}$$

being κ_{nm} the mode coupling coefficients (MCCs) between modes n and m. For forward propagating modes, the MCCs are defined as, [123],

$$\kappa_{nm} = \frac{\omega\varepsilon_0\iint\left(n^2-n_m^2\right)e_n^*\cdot e_m\,dxdy}{\iint\hat{z}\cdot\left(e_n^*\times h_n + e_n\times h_n^*\right)dxdy}, \tag{3.46}$$

where ε_0 is the electric permeability in vacuum, n is the refractive index distribution of the perturbed waveguide, n_m is the refractive index distribution of the unperturbed waveguide, e_n (e_m), h_n (h_m) the normalized vector modes of the electric and magnetic fields of mode n (m), respectively, and * indicates the complex conjugate.

Although the CMT provides a rigorous solution to mode coupling in optical fibers, solutions of the coupled mode equations are difficult to obtain (and usually they cannot be solved) for a large number of modes since not only the mode amplitudes but also their relative phases are considered. In most cases, the coupling coefficient is a random function of distance and only the exchange of power between modes is of interest. A much simpler description than the CMT relies on limiting our interest to the average power carried by each mode, ignoring the extra information (phase) that is not required to solve this particular problem. This approach is known as coupled power theory (CPT). The coupled power equations (CPEs) in a lossless system are again first-order differential equations with z, [121, 115, 124],

$$\frac{dP_n(z)}{dz}=\sum_{m\neq n}h_{nm}(z)\left[P_m(z)-P_n(z)\right], \tag{3.47}$$

being $P_n(z)$ the average power carried by mode n and h_{nm} the power coupling coefficient (PCC) between modes n and m, [61],

$$h_{nm}=\left\langle\left|\int_0^L\kappa_{nm}e^{i(\beta_m-\beta_n)z}dz\right|^2\right\rangle, \tag{3.48}$$

where $\langle\cdot\rangle$ indicates the ensemble average.

The phenomenon of optical crosstalk is associated to the mode coupling between the different spatial channels involved. In multichannel communication systems, inter-channel crosstalk could become one of the principal sources of impairment. In general, inter-channel crosstalk levels above -20 dBs are desirable to avoid signal degradation and allow MIMO-free communication schemes, [125]. The management of the amount of crosstalk present in the system is essential to further exploit the maximum transmission capacity and enable long-haul transmission. This can be simply addressed in terms of the power coupling between the individual spatial channels by means of the PCCs. The average inter-channel crosstalk from spatial mode m to spatial mode n can be defined as, [61],

$$XT_{nm}\equiv P_{nm}/P_{mm}, \tag{3.49}$$

where P_{nm} is the output power of mode n when only mode m is excited. If XT is small enough, Eq. (3.49) can be approximated as, [61],

$$XT_{nm}\approx\int_0^L h_{nm}dz, \tag{3.50}$$

being L the fiber length. Different solutions have been found in the literature to estimate the PCCs for both multicore and few-mode fiber approaches.

3.3.1. Intermodal crosstalk in few-mode fibers

In a FMF, we can assume that the refractive index is modified by a small perturbation factorized in both transverse, δn, and longitudinal, $f(z)$, dependences, so that the total refractive index gets the form, [61],

$$n^2(x,y,z)=n_0^2(x,y)+\delta n^2(x,y)f(z), \tag{3.51}$$

being $n_0(x,y)$ the unperturbed refractive index. Equation (3.51) includes any perturbation source that can induce mode coupling, such as bends, twists or core non-uniformities caused by manufacturing tolerances, [120, 119, 126]. Substituting Eq. (3.51) into Eq. (3.46), the MCCs result in, [61],

$$\kappa_{nm}=\frac{\omega\varepsilon_0 f(z)\iint\delta n^2 e_n^*\cdot e_m dxdy}{\iint\hat{z}\cdot\left(e_n^*\times h_n+e_n\times h_n^*\right)dxdy}. \tag{3.52}$$

Splitting these MCCs as a product of a constant term (i.e., independent of z) times a random function of z, $f(z)$,

$$\kappa_{nm} = K_{nm} f(z), \tag{3.53}$$

where K_{nm} can be considered as redefined MCCs, the PCCs from Eq. (3.48) result in, [121, 115],

$$h_{nm} = |K_{nm}|^2 S(\beta_m - \beta_n), \tag{3.54}$$

being S the power spectral density or Fourier transform of the autocorrelation function $R(z)$ of $f(z)$. It can be assumed that R is a stationary process characterized by an exponential shape autocorrelation function, so that its Fourier transform S is a Lorentzian function and, therefore, Eq. (3.54) remains, [113],

$$h_{nm} = \frac{2\sigma^2 |K_{nm}|^2 d_c}{1 + \left[(\beta_m - \beta_n) d_c\right]^2}, \tag{3.55}$$

where σ is the standard deviation of the longitudinal perturbation and d_c is the correlation length. From Eq. (3.55), we observe that the strategy to reduce the PCCs (and thus the intermodal crosstalk) in a FMF relies on properly designing the fiber refractive index profile so as to maximize the difference between the effective indices (or propagation constants) of the modes.

3.3.2. Intercore crosstalk in multicore fibers

In the case of MCFs, the intercore crosstalk calculation requires, apart from the random structural fluctuations, the inclusion of the bend- and twist-induced perturbations. Bends play an important role in MCFs due to the fact that cores are not centered in the fiber cross-section and thus they are affected differently by fiber curvatures. They can be considered as a perturbation on the propagation constants of the cores. The bend-induced perturbation on the propagation constant of a given core n for a bending radius R_b can be expressed as, [61],

$$\beta_{b,n} \approx \beta_{c,n} \frac{r_n \cos\theta_n}{R_b}, \tag{3.56}$$

being $\beta_{c,n}$ the unperturbed propagation constant of core n in straight condition and (r_n,θ_n) the local polar coordinates of core n inside the cross-sectional area of the fiber. Twists produce a continuous-varying rotation of the fiber and can be understood as a random phase function that affects the core locations on the cross-sectional area of the fiber, [127]. With the inclusion of these perturbations, the CMEs for MCFs are written as, [127, 128],

$$\frac{d}{dz} A_n(z) = -i \sum_{m \neq n} K_{nm} A_m(z) e^{-i\Delta\beta_{eq,mn} z} f(z). \tag{3.57}$$

where

$$\Delta\beta_{eq,mn}=\Delta\beta_{c,mn}+\Delta\beta_{b,mn}=\left(\beta_{c,m}-\beta_{c,n}\right)+\left(\beta_{c,m}\frac{r_m\cos\theta_m}{R_b}-\beta_{c,n}\frac{r_n\cos\theta_n}{R_b}\right), \quad (3.58)$$

and $f(z)$ is a phase function that includes the random structural fluctuations perturbation and we have written the MCCs as K_{nm} to indicate the exclusion of the z-dependent perturbations. Thus, the PCCs for MCFs are expressed as in FMFs [Eq. (3.54)] but replacing the variable of the power spectral density S, β_m - β_n, by $\Delta\beta_{eq,mn}$, [127, 110, 70]. Again, the PCC depends on an unknown autocorrelation function $R(z)$ of $f(z)$, and it has been experimentally proved that crosstalk in MCFs follows a tendency that can be modelled by the use of an exponential autocorrelation function, [127, 110, 70]. Thus, the corresponding PCC at a certain z results in

$$h_{mn}(z)=\frac{2K_{mn}^2 d_c}{1+\left[\Delta\beta_{eq,mn}(z)d_c\right]^2}, \quad (3.59)$$

where d_c is the correlation length. Assuming that the MCF is bent at a constant radius R_b and is twisted at a constant twist rate, an analytical expression of the average PCC can be obtained by averaging the PCC of Eq. (3.59) over a turn, [110],

$$\bar{h}_{mn}=\sqrt{2}K_{mn}^2 d_c\left[\frac{1}{\sqrt{a\left(b+\sqrt{ac}\right)}}+\frac{1}{\sqrt{c\left(b+\sqrt{ac}\right)}}\right], \quad (3.60)$$

where

$$\begin{aligned} a&=1+\left(\Delta\beta_{c,mn}d_c-\Delta\beta_{b,mn}d_c\right)^2 \\ b&=1+\left(\Delta\beta_{c,mn}d_c\right)^2-\left(\Delta\beta_{b,mn}d_c\right)^2, \\ c&=1+\left(\Delta\beta_{c,mn}d_c+\Delta\beta_{b,mn}d_c\right)^2 \end{aligned} \quad (3.61)$$

and thus the crosstalk can be estimated as, [110],

$$XT_{nm}\approx\tanh\left(\bar{h}_{nm}L\right). \quad (3.62)$$

From Eqs. (3.59)-(3.62), we can distinguish two main contributions to the intercore crosstalk: the MCC K_{nm} and the difference between the core equivalent propagation constants $\Delta\beta_{eq,mn}$, including both the unperturbed propagation constants and the bend-induced perturbation. The crosstalk suppression techniques rely on minimizing these contributions. In order to suppress the mode coupling coefficient, there are several techniques to improve the mode confinement into the core region, such as using small-radius and high-index structures, and trench-/hole-assisted configurations, [61, 129, 70]. It is worth noting here that finding an analytical expression for the MCC requires to solve the characteristic equation of the individual refractive index profiles of the cores, so that our universal characteristic equation approach provides a very useful tool in this regard. For instance, under the assumption of low intercore crosstalk, the MCC between two adjacent homogeneous cores with step-index

refractive index profiles can be modeled as a directional fiber coupler and use the simplified MCC obtained in [123]:

$$K_{mn}=\frac{\sqrt{\Delta_1}}{a_1}\frac{u_1^2}{\left(u_1^2+w_1^2\right)^{3/2}K_1^2\left(w_1\right)}\sqrt{\frac{\pi a_1}{w_1\Lambda}}e^{-\frac{w_1}{a_1}\Lambda}, \tag{3.63}$$

being a_1 the core radius, Δ_1 the core-to-cladding relative index difference and Λ the separation between cores. In [130], with the help of the characteristic equation for trench-assisted refractive index profiles, they also found an expression for the MCC for trench-assisted step-index cores.

On the other hand, the phase matching suppression implies the maximization of the term $\Delta\beta_{eq,mn}$. From Eq. (3.58), we see clearly from the first term of the right-hand side that the one possible phase matching suppression technique relies on the use of trench assisted cores. However, there is a critical bending radius, the so-called threshold bending radius R_{pk}, in which the second term compensates the effect of the first one and thus the phase matching occurs even for heterogeneous configurations, [61],

$$R_{pk,mn}=\Lambda\frac{\left(\beta_{c,m}+\beta_{c,n}\right)/2}{\left|\beta_{c,m}-\beta_{c,n}\right|}=\Lambda\frac{\left(n_{eff,m}+n_{eff,n}\right)/2}{\left|n_{eff,m}-n_{eff,n}\right|}. \tag{3.64}$$

The threshold bending radius characterizes the intercore crosstalk robustness against fiber curvatures in heterogeneous MCFs. In chapter 4, keeping R_{pk} as low as possible will be one of the conditions imposed to the MCF design. In the case of homogeneous cores, $\beta_{c,m} = \beta_{c,n}$, and Eq. (3.58) results

$$\Delta\beta_{eq,mn}=\frac{\beta_{c,n}}{R_b}\left(r_m\cos\theta_m-r_n\cos\theta_n\right), \tag{3.65}$$

and we see that lower bending radii provide higher values of Eq. (3.65), so that bend-induced perturbations in homogeneous MCFs suppress the phase matching. Figure 3.13 illustrates an example of the intercore crosstalk behavior in both homogeneous and heterogeneous MCFs as a function of the bending radius.

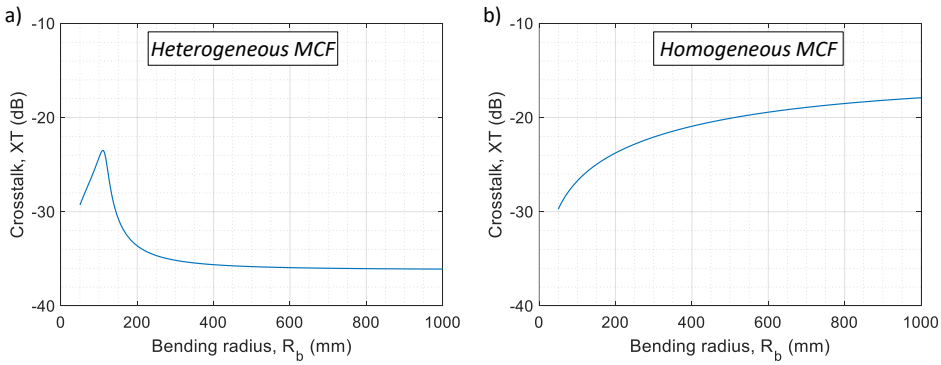

Fig. 3.13. Intercore crosstalk dependence on the bending radius R_b for (a) heterogeneous and (b) homogeneous 1-km MCFs.

Other effects, such as the inter-core crosstalk in nonlinear regimes, [131, 132], and intra-polarization dynamics, [133], which includes the effect of intra-core random polarization-mode coupling on the crosstalk of weakly-coupled MCFs, have also been reported and can be included in Eq. (3.57) by simply inserting the pertinent coupling coefficients.

3.4. Conclusions

In this chapter, we have studied the electromagnetic wave propagation in SDM fibers. First, we characterized the wave propagation as the modal solutions resulting from the wave equation assuming uniform ideal propagation; i.e., when coupling between the different spatial modes is neglected. Then, we introduce the mode coupling effect under the consideration of longitudinal perturbations during the fiber propagation. By using the coupled mode theory and the coupled power theory, we analyze the crosstalk between the spatial paths involved and the main parameters that contribute to enhance this effect.

In first place, we have presented, for the first time to our knowledge, a theoretical model deriving the universal characteristic equation for multi-layer optical fibers whose refractive index profile comprises any number of concentric circular layers with arbitrary radial dimensions and refractive index values. One of the main advantages of the model is that it evades the need of solving any determinant, substantially reducing the computational cost of the numerical solution of the problem even for a large number of layers. The closed-form expression we derived for the characteristic equation provides a useful tool to obtain relevant information about the propagation characteristics of all the propagated modes, such as the phase propagation constant, group delay and the chromatic dispersion. The model can be applied to both flat (or stepped) refractive index profiles (such as step-index, W-type or ring-core) and continuous profiles (such as graded-index or triangular) if a previous discretization process is applied properly. The validity of the proposed model has been accomplished by comparing the results offered by our theory with the ones provided by the numerical software *Fimmwave* form *Photon Design* for five different profiles: step-index trench-assisted, ring-core, triangular-index, graded-index and four-cladding. Excellent agreement is obtained in all the cases in terms of the normalized propagation constant, group index and chromatic dispersion for all the modes propagated.

The compact characteristic equation we present here will play an important role in optical fiber design processes, where the designer can actually get valuable physical insights without the need of resorting to numerical software tools. While other methods are based on the "brute force" resolution of Maxwell's equations without having any knowledge about the functions involved, our model enables to build the overall characteristic equation that defines wave propagation. More importantly, one can benefit from the possibility of evaluating the effect of the properties of a particular layer on the performance of the propagated modes without the need to evaluate the whole refractive index structure, since one has knowledge about the functions that are involved in that layer, as we can see in Eqs. (3.12)-(3.14). Another

remarkable usage relates to the management of crosstalk between spatial modes in few-mode or multimode fibers or between cores in MCFs. In this regard, finding an analytical expression for the MCC requires solving the characteristic equation of the individual refractive index profiles of the fibers or cores involved. Our universal characteristic equation approach provides a very useful tool when cores with any arbitrary refractive index profile are involved.

All in all, the advantages brought by this universal characteristic equation will benefit a variety of optical communications and signal processing scenarios where multi-layer fibers are particularly needed, such as space and mode-division multiplexing, fiber sensing, optical interconnects, loss and dispersion management, as well as high-power amplifiers and lasers.

Finally, we have reviewed the basic concepts behind crosstalk in both multicore and few-mode fibers. In the case of MCFs, we have seen that we can reduce the intercore crosstalk by decreasing the mode coupling coefficient and/or by avoiding the phase matching condition. For the first approach, we can resort to trench-assisted configurations or low-radius high-index cores. For the second one, we can avoid phase matching by inserting dissimilar cores in the cross-section (i.e., using heterogeneous configurations). However, bend-induced perturbations can also produce phase matching even in heterogeneous configurations. In that sense, the threshold bending radius is a critical parameter that must be evaluated conveniently. In contrast, in the case of homogeneous MCFs, bend-induced perturbations can suppress the original phase-matching condition between cores. Lastly, in the case of FMFs, we conclude that the only way to reduce the intermodal crosstalk to a certain extent relies on the design of the refractive index profile of the fiber as to provide larger effective index differences between the different guided modes.

Chapter 4
True time delay lines: Proposal

4.1. Introduction

A TTDL is a device that yields the possibility of controlling the propagation delay of an incoming signal in a continuous mode, ensuring a true-time-delay operation on large operative bandwidth, [32, 33]. It is the key element of many MWP signal processing applications built upon incoherent time-discrete approaches, such as microwave signal filtering, optical beamforming for phased array antennas and arbitrary waveform generation or shaping [12]. In general, it comprises a set of N parallel time delay units, each of them characterized by a particular time-delay parameter. A time delay unit i is a structure that brings a certain delay, τ_i, to an incoming signal. The TTDL splits the incoming signal into N time delay units, providing at its output N different time-delayed replicas of the input signal, as shown in Fig. 4.1. Each output signal i (or sample i) corresponds to an identical copy of the input signal delayed by τ_i temporal units; that is, if $s(t)$ is the input signal, $s(t - \tau_i)$ is the i-th output signal sample (ignoring, for simplicity, the amplitude scaling). In many cases, TTDLs with equally time-spaced samples are required; in those cases, the time delay units must provide incremental delays to the input signal, with a basic differential delay between adjacent samples of $\Delta\tau = \tau_{i+1} - \tau_i$, $i = 1, 2, \ldots, N\text{-}1$.

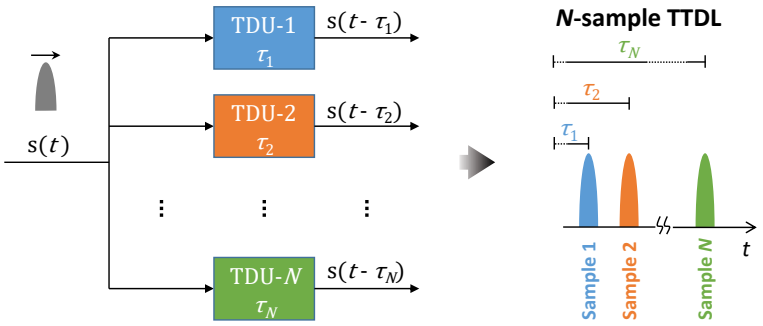

Fig. 4.1. Schematic representation of a *N*-sample true time delay line. TDU: Time delay unit; TTDL: True time delay line.

We propose the exploitation of the inherent parallelism of a single SDM fiber, either MCF or FMF, to behave as a tunable sampled TTDL. This implies the development of MCF and FMF solutions where the different spatial paths (core or modes) translate into different propagation characteristics (in terms of group delay and chromatic dispersion). Figure 4.2 depicts in general the principle of operation of this approach, where we see that when a modulated signal is injected into the SDM fiber, we obtain, at the fiber output, a set of time-delayed replicas of the modulated signal. Sampled TTDL operation requires, in first place, a constant group delay difference between adjacent signal samples. In addition, tunability of this delay difference with the optical wavelength requires incremental group delay slopes between adjacent samples, that is, incremental values of the chromatic dispersion. This way, we can change the differential group delay between adjacent samples by tuning the operation wavelength of the optical source. Since the sample diversity is provided by the different fiber spatial paths, we refer this mode of operation as spatial diversity.

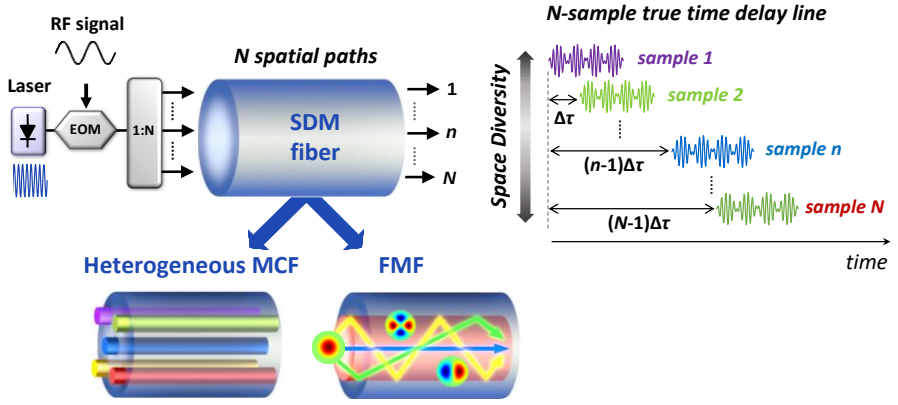

Fig. 4.2. Basic concept of a true time delay line built upon a single multicore or few-mode fiber by exploiting spatial diversity.

But this approach offers not only 1D (i.e., 1-dimensional) operation, but also unique 2D (i.e., 2-dimensional) operation by exploiting both wavelength- and spatial-diversity domains. If we replace the single optical source in Fig. 4.2 by an array of

lasers operating at different optical wavelengths, what we have at the SDM fiber output is different families of TTDLs, characterized by different basic differential delays, given by the combination of both optical wavelength and space (see Fig. 4.3).

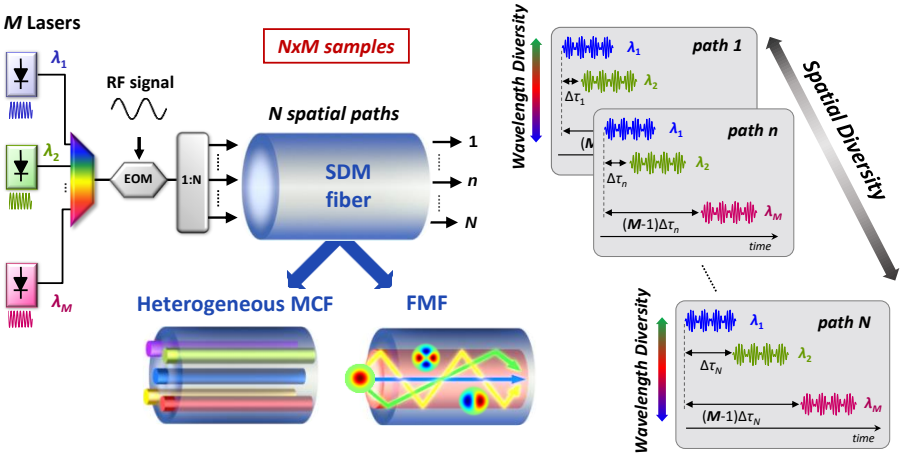

Fig. 4.3. Basic concept of a 2-dimensional true time delay line built upon a single multicore or few-mode fiber by exploiting both spatial and wavelength diversities.

In the case of MCFs, we can create a tunable sampled TTDL by designing a heterogeneous fiber structure with dispersion-engineered cores. For FMFs, we will see that external elements will be required to ensure a certain control over the group delay and chromatic dispersion of the signal samples. In particular, the use of broadband LPGs inscribed in the proper locations, together with the design of the fiber refractive index profile, allows TTDL operation over a certain optical wavelength range. While in the heterogeneous MCF-based approach, we can improve the wavelength operability range of the TTDL by properly tailoring the higher-order dispersion parameter, in the FMF solution this range will be limited by the spectral width of the inscribed broadband LPGs. Figure 4.4 illustrates the rationale of a fiber-wireless communications scenario where, once the SDM fiber is fabricated and deployed, we can use different optical wavelength bands, for instance, for passive optical network (PON) or Fiber-to-the-home distribution, MIMO antenna connectivity, squint-free radio beamsteering, arbitrary waveform generation, radar communications and microwave signal filtering.

In this chapter, we present the concept and design underlying sampled TTDL operation built upon MCFs and FMFs. By using the numerical software *Fimmwave*, from *Photon Design* company, together with the universal characteristic equation proposed in chapter 3, we design the physical parameters and the layer material compositions of the SDM fibers to obtain the desired group delay behaviors. Sections 4.2 and 4.3 describe the MCF- and FMF-based TTDL design techniques, respectively. In section 4.4, we will discuss the main detrimental effects that can degrade the performance of the proposed TTDLs and section 4.5 summarizes the main conclusions of the chapter.

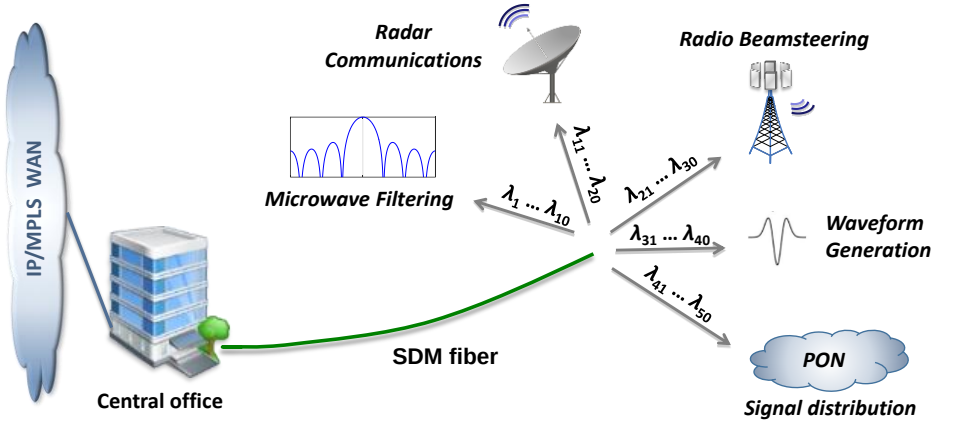

Fig. 4.4. Fiber-wireless communications scenario where a single SDM fiber exploits different optical bandwidths for a set of distribution and signal processing functionalities.

4.2. Implementation using heterogeneous multicore fibers

4.2.1. Concept

A group-index-variable delay line implies a variation in the propagation velocities of the optical spatial paths involved [134]. The design of a heterogeneous MCF to behave as a group-index-variable delay line requires that each core features an independent group delay with a linear dependence on the optical wavelength λ, as shown in Fig. 4.5. For each fiber core n, we can expand the group delay per unit length, $\tau_n(\lambda)$, in 2nd order Taylor series around an anchor wavelength λ_0 as:

$$\tau_n(\lambda) = \tau_n(\lambda_0) + D_n(\lambda - \lambda_0) + \frac{1}{2} S_n(\lambda - \lambda_0)^2, \tag{4.1}$$

where D_n is the chromatic dispersion parameter and S_n the dispersion slope of the core n, both at the anchor wavelength λ_0. For proper TTDL operation, we must design the refractive index profile of each core such that, first, all cores experience the same group delay at the anchor wavelength λ_0, $\tau_n(\lambda_0) = \tau_0$, and, secondly, D_n increases with the core number in an incremental fashion. In addition, we must ensure a linear behavior of the group delay within the desired wavelength range. As Eq. (4.1) shows, to reduce the quadratic wavelength-dependent term, we must address a rigorous higher-order dispersion analysis and management. This group-index-variable delay line can work on two different regimes whether we exploit the spatial or the optical wavelength diversities. The delay difference between adjacent samples, that is, the basic differential delay, follows a different law depending on the TTDL operation regime and, in consequence, we must address each regime individually for a proper dispersion optimization.

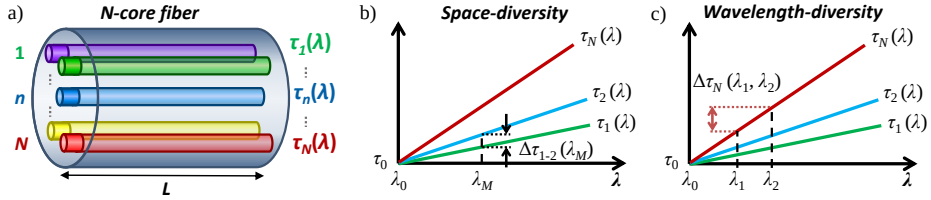

Fig. 4.5. (a) Heterogeneous *N*-core MCF. Group delay slopes for the *N* cores showing the (b) spatial-diversity and (c) the wavelength-diversity operation regimes.

In the case of spatial diversity (see Fig. 4.5(b)), the differential group delay $\Delta\tau_{n,n+1}$ is given by the propagation difference created between each pair of adjacent cores for a particular optical wavelength λ_m:

$$\Delta\tau_{n,n+1}(\lambda_m) = \Delta D(\lambda_m - \lambda_0) + \frac{S_{n+1} - S_n}{2}(\lambda_m - \lambda_0)^2, \tag{4.2}$$

where $\Delta D = D_{n+1} - D_n$ is the incremental dispersion parameter that have to be constant for every pair of adjacent cores. We see from Eq. (4.2), that the spatial-diversity differential group delay is affected by a quadratic term that depends on the difference between the dispersion slopes of the cores involved. We can define the differential group delay relative error induced by this nonlinear variation as the ratio between the second and the first terms of the right-hand side of Eq. (4.2), that is:

$$\Delta\tau_{n,n+1}(\lambda_m)\Big|_{rel\_err} = \frac{S_{n+1} - S_n}{2\Delta D}(\lambda_m - \lambda_0), \tag{4.3}$$

which shows that the detrimental nonlinear effect raised by the dispersion slope variability increases linearly with the optical wavelength of operation.

When the delay line operates in optical wavelength diversity (Fig. 4.5(c)), the differential group delay experienced between two contiguous wavelengths (λ_m, λ_{m+1}) in a particular core *n* is given by:

$$\Delta\tau_n(\lambda_m, \lambda_{m+1}) = D_n\delta\lambda + S_n(\lambda_1 - \lambda_0)\delta\lambda + \frac{1}{2}S_n(2m-1)\delta\lambda^2, \tag{4.4}$$

where $\delta\lambda = \lambda_{m+1} - \lambda_m$ is the separation between the two adjacent optical sources, λ_1 the wavelength of the first optical source and $1 \le m \le M-1$, being *M* the total number of optical sources. In this case, the undesired variation on $\Delta\tau_n$ is characterized by both the linear ($\delta\lambda$) and the quadratic ($\delta\lambda^2$) dependence on the dispersion slope in Eq. (4.4), leading to a differential group delay relative error defined as:

$$\Delta\tau_n(\lambda_m, \lambda_{m+1})\Big|_{rel\_err} = \frac{S_n\left[(\lambda_1 - \lambda_0) + \frac{1}{2}(2m-1)\delta\lambda\right]}{D_n}. \tag{4.5}$$

From Eq. (4.3) we see that, when we exploit the spatial-diversity domain, the nonlinear behavior of the differential group delay depends on the variabilities between cores $\Delta S_n = S_{n+1} - S_n$ and ΔD; more precisely, it depends on the quotient

$\Delta S_n/\Delta D$. In the case of the wavelength-diversity domain, Eq. (4.5) shows that the detrimental effect induced by the higher-order dispersion on the linear performance of the differential group delay depends on the quotient between the values S_n/D_n of the particular core used. Keeping in mind that the value of ΔD is fixed a priori (it determines, at the end, the tunability of the TTDL) and, in general, the value of the dispersion slope cannot be zero in common optical fibers (as we will see, for instance, later in Fig. 4.7(b)), we conclude that proper TTDL operability requires the use of cores that present high chromatic dispersion values with low dispersion slope variability between them.

4.2.2. Design

A MCF-based TTDL not only requires optimization in terms of nonlinear spectral group delay, but also in terms of intercore crosstalk. This implies that, first, we need dispersion-engineered cores in which both the chromatic dispersion and dispersion slope parameters fulfil a set of specific rules for TTDL operability; and, secondly, the fiber structure is designed as to reduce the intercore crosstalk. In this section, we present a new procedure for designing heterogeneous MCFs where one can tailor the propagation characteristics of each core independently. By suitable modifications of the material composition and radial dimensions of the refractive index profile of each fiber core, we can attain a particular set of cores that satisfies, at the same time, both TTDL operation and low intercore crosstalk requirements.

We consider a hexagonal 7-core fiber structure, where a central core is surrounded by 6 outer cores, with a core pitch Λ = 35 μm, as depicted in Fig. 4.6(a). We can assume, for simplicity, infinite external MCF cladding without loss of generality. The design of the MCF was carried out by means of the full-vector finite-element method implemented using the numerical software *Fimmwave*. Under the assumption of negligible intercore crosstalk level, the design of the refractive index profile of each core can be addressed individually.

First, we need to determine the refractive index profile of each fiber core. As we saw in chapter 3, the use of trench-assisted step-index cores reduces the intercore crosstalk as compared to the classic step-index profiles; but they also add more design versatility by increasing the number of design parameters, which is particularly important to properly manage, at the same time, the propagation characteristics of every core. As Fig. 4.6(b) shows, a trench-assisted step-index profile can be modified by a wide set of parameters, including the dimensions and material composition of each layer. In order to simplify the design (and further reduce the associated future fabrication costs), we restricted the number of design parameters to 4: the core radius (a_1), the core-to-trench distance (a_2), the trench width (w) and the core-to-cladding relative index difference (Δ_1) – or, more specifically, the dopant (GeO_2) concentration in the core layer. The cladding-to-trench relative index difference is fixed to Δ_2 = 1% in all cores.

Another important aspect to take into account on the fiber design is the distribution of the cores along the cross-section area of the MCF to reduce the intercore crosstalk. As we saw in chapter 3, one of the major challenges in the design of heterogeneous MCFs is the management of the crosstalk dependence on the phase-matching

condition between the cores when the fiber is bent. To prevent this phase matching, the curvature radius must be larger than the fiber threshold bending radius R_{pk} [Eq. (3.64)], which is inversely proportional to the difference between the effective refractive indices of two adjacent cores. Bend-insensitive MCFs require a minimum effective index difference between adjacent cores of 0.1% for a 35-μm core pitch, [135]. As shown in chapter 2, in the particular case of a 7-core fiber with hexagonal disposition, 3 types of different effective index cores are enough to ensure that any pair of neighboring cores can never be of the same type. And, even more, for a core pitch Λ = 35 μm, bend-insensitivity can be added if the effective index difference between different core types is above 0.1%, requiring at least a maximum effective index difference of 0.2% between any pair of cores. Keeping all this in mind, the MCF cross-sectional area must be composed of three core groups, where each group comprises cores that feature similar effective indices, ensuring that cores pertaining to the same group are not located in adjacent positions. The groups are formed as follows: (group 1) the central or inner core, identified with the lowest effective index; (group 2) three outer cores placed in non-adjacent positions, with intermediate effective index values; and (group 3) three outer cores placed in alternate positions featuring higher effective indices. The minimum effective index difference between cores of different group will determine the threshold bending radius R_{pk}. Figure 4.6(a) represents the core location along the MCF cross-sectional area, where each color represents the cores inside the same group.

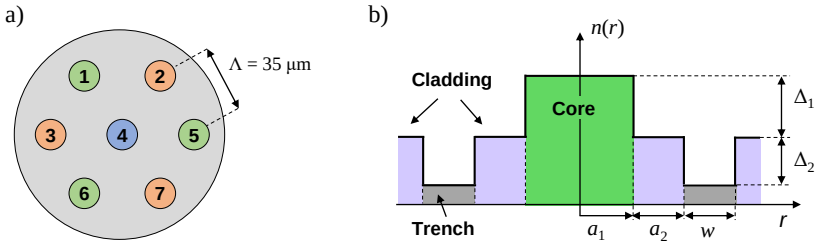

Fig. 4.6. (a) Cross-sectional area of a 7-core heterogeneous MCF with three types of similar effective index cores; cores of the same color comprise a group of cores with similar effective indices. (b) Refractive index profile of a trench-assisted core.

All in all, our design must satisfy: (1) all the cores must experience the same group delay at the anchor wavelength λ_0, which we fix to 1550 nm; (2) the chromatic dispersion values of each core must be as high as possible, increasing linearly with the core number; (3) the dispersion slope variability must be as low as possible between any pair of cores; and (4) three types of effective index cores are required, with a maximum effective index difference between the cores of at least 0.2%. In addition, we must establish the value of the incremental dispersion parameter ΔD, which determines the tunability of the TTDL; the higher ΔD, the larger differential group delay variability in a shorter wavelength range. As we will see later, the highest value of ΔD will be limited to the number of cores of the MCF, and it will be desirable to achieve the highest possible value to reduce the effect of possible fabrication errors that could modify the chromatic dispersion of the cores. Considering the limitations on the maximum range of chromatic dispersions available for a fixed value on the

group delay and, at the same time, maintain the single-mode condition with similar effective area (which is directly related with fiber nonlinearities, as we will discuss in section 4.4), we fixed ΔD = 1 ps/km/nm.

Figure 4.7 shows the computed dispersion parameter D, dispersion slope S and effective index n_{eff} as a function of the core radius a_1 for three representative groups of design parameters. Each colored zone corresponds to a particular range of values for the core-to-cladding relative index difference Δ_1, the core-to-trench separation a_2 and the trench width w. The yellow zone is characterized by having high core radii ($4.5 \leq a_1 \leq 6$ µm) and low core-to-cladding relative index differences ($0.25 \leq \Delta_1 \leq 0.31\%$), while the rest of the parameters are within the range $3 \leq a_2 \leq 7$ µm and $4 \leq w \leq 7$ µm. The orange areas have moderate core radii ($3.4 \leq a_1 \leq 5$ µm) and core-to-cladding relative index differences ($0.33 \leq \Delta_1 \leq 0.39\%$), for a combination of $2 \leq a_2 \leq 6$ µm and $3 \leq w \leq 6$ µm. Finally, the blue zones have low core radii ($2 \leq a_1 \leq 3.4$ µm), high core-to-cladding relative index differences ($0.72 \leq \Delta_1 \leq 0.8\%$), for $2 \leq a_2$ and $w \leq 5$ µm. In general, we have selected the upper and lower limits of each variable as to satisfy, respectively, the single-mode condition and low bend losses, [136, 137]. Furthermore, we observe that a value of a_2 above its upper limit decreases the value of D below the target range for delay line operability. This target range is chosen in a way that the values of D are high enough as to reduce the influence of the nonlinearities raised by S in the wavelength-diversity mode, as we conclude from Eq. (4.5).

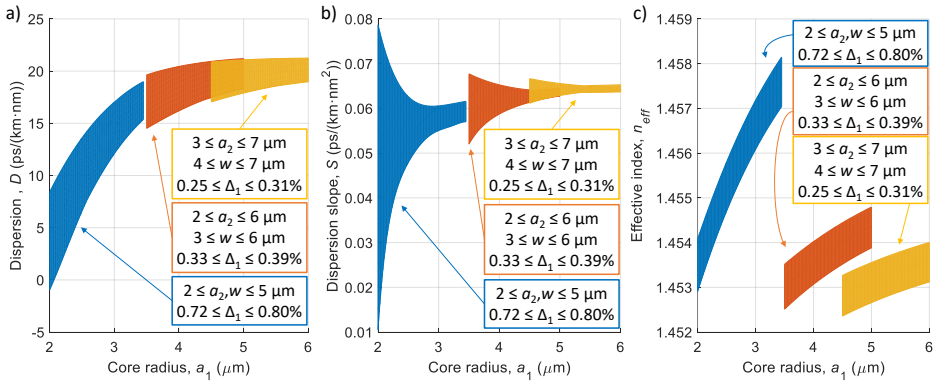

Fig. 4.7. Comparison between the possible (a) dispersion parameter D, (b) dispersion slope S and (c) effective index n_{eff} values versus the core radius (a_1) for three representative zones (different colors) that are characterized by a particular set of values of the core-to-cladding relative index difference (Δ_1), core-to-trench distance (a_2) and trench width (w).

Since we consider a 7-core MCF characterized by ΔD = 1 ps/(km·nm), we must assure first a range of dispersion parameters up to $D_7 - D_1$ = 6 ps/(km·nm) to implement a 7-sample delay line. From Fig. 4.7(a) we observe that, as long as the core radius increases, the range of dispersion values decreases, limiting the number of samples. In addition, we should choose a design zone that assures a range of effective index differences above 0.2% for bend insensitivity. Figure 4.7(c) shows that the areas with low core radii (blue zone) are the optimum ones in terms of

intercore crosstalk. We see also that this zone admits a large range of chromatic dispersion values, so it could be a good candidate for implementing TTDLs over MCFs. However, from the previous section, we learned that to reach broadband operability we must: (1) reduce the dispersion slope variability $S_{n+1} - S_n$ between cores as much as possible for spatial-diversity operation [Eq. (4.3)]; and (2) assure a dispersion parameter value D as high as possible for the wavelength-diversity regime [Eq. (4.5)]. From Figs. 4.7(a) and 4.7(b), we see that increasing the core radius leads to a lower dispersion slope variability and also to higher values of D. Thus, we conclude that the optimum zone for TTDL operation is the orange one, which allows the required 6 ps/(km·nm) dispersion range with the highest dispersion parameter values and the lowest dispersion slope variability possible. In addition, we can observe in Fig. 4.7(c) that this zone still provides the 0.2% effective index difference for crosstalk management. Therefore, we finally choose the orange design area as the candidate to build the proposed dispersion- and crosstalk-engineered MCFs.

We now proceed to finely evaluate how each of the design parameters affect individually the propagation characteristics of the trench-assisted cores while they vary within the chosen design area. In first place, we evaluate how the group index and the chromatic dispersion are affected. Figure 4.8(a) shows the computed group index when the core dimensions (both the refractive index value and the core radius) are varied while keeping the core-to-trench distance and the trench width at fixed values ($a_2 = w = 4$ μm). We see that the group index raises as a_1 and/or Δ_1 increase. In a similar way, Fig. 4.8(b) shows the dependence of the chromatic dispersion when the design parameters are modified within the same ranges. In this case, increasing a_1 leads to higher chromatic dispersions, but it slightly diminishes its value as Δ_1 increases. For the evaluation of the remaining design parameters (a_2 and w), we fixed the core radius and the core-to-cladding relative index difference to $a_1 = 4$ and $\Delta_1 = 0.36\%$, respectively. Figure 4.8(c-d) represent, respectively, the computed responses for the group index and the chromatic dispersion as a function of the core-to-trench distance for a particular set of trench widths. In both cases, we observe similar behaviors: both the group index and the chromatic dispersion decrease as a_2 increases, and they slightly grow as w increases.

We then analyze the behavior of the dispersion slope S. Figure 4.9(a) shows the dependence of the computed dispersion slope S on the core-to-trench distance a_2 for a 4-μm trench width w and three significant core radii a_1 (3.4, 4.3 and 5.0 μm plotted in different colors) and core-to-cladding relative index difference Δ_1 (0.33, 0.36 and 0.39% in different line styles). We observe that an increase in a_1 results in a shorter range of variability for S, as we have previously deduced from Fig. 4.7(b), while an increase in Δ_1 has a similar but less significant effect. We find as well that a_2 is the parameter that induces the highest variation on the dispersion slope, provided that a_1 is small enough. Figure 4.9(b) illustrates the computed dispersion slope behavior against a_2 for different values of w with fixed values of $a_1 = 4$ μm and $\Delta_1 = 0.36\%$. In this case, wider trenches result in a negligible increment on S for high values of a_2, which gradually gains relevance as a_2 decreases.

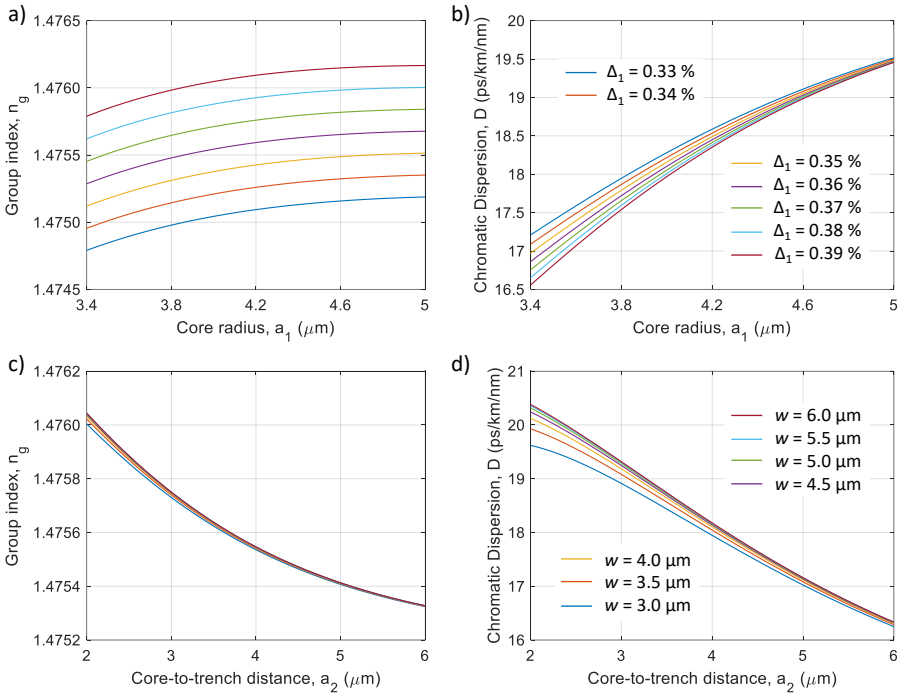

Fig. 4.8. Dependence on the core radius versus different core-to-cladding relative index differences for a fixed core-to-trench distance and trench width, $a_2 = w = 4$ µm of (a) the group index and (b) the chromatic dispersion. Dependence on the core-to-trench distance versus different trench widths for a fixed core radius and core-to-cladding relative index difference, $a_1 = 4$ µm and $\Delta_1 = 0.36\%$, of the (c) group index and (d) chromatic dispersion.

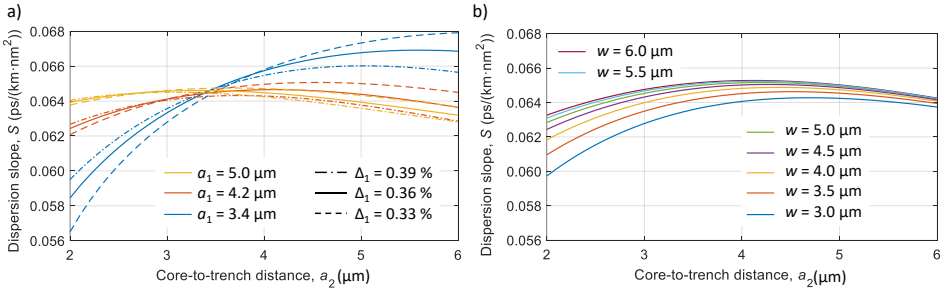

Fig. 4.9. Dispersion slope dependence on the core-to-trench distance a_2 versus (a) different core radii a_1 (color lines) and core-to-cladding relative index differences Δ_1 (line styles) for a fixed trench width $w = 4$ µm; and (b) different trench widths for $a_1 = 4$ µm and $\Delta_1 = 0.36\%$.

The last step in the optimization technique is the management of the crosstalk and its sensitivity against fiber curvatures. This requires a design of the refractive index profile that maximizes the effective index difference between adjacent cores. Figure 4.10(a) shows the dependence of the effective index n_{eff} with the core radius a_1 and the core-to-trench relative index difference Δ_1. We see that increasing a_1 and/or Δ_1 leads to higher effective indices. In this case, we can achieve a variation up to 0.15% by varying both a_1 and Δ_1 (for a fixed $a_2 = 4$ µm and $w = 4$ µm). Figure 4.10(b)

illustrates the effective index variation as a function of both a_2 and w for a_1 = 4 µm and Δ_1 = 0.36%. We see that the effective index is not affected by a variation in w at all, while it raises as a_2 increases. Actually, the separation between the core and the trench affects in a similar trend both the effective index and the dispersion slope in the sense that, as long as this distance is kept in a small range (up to 3 µm), a small change causes the higher variation on the effective index.

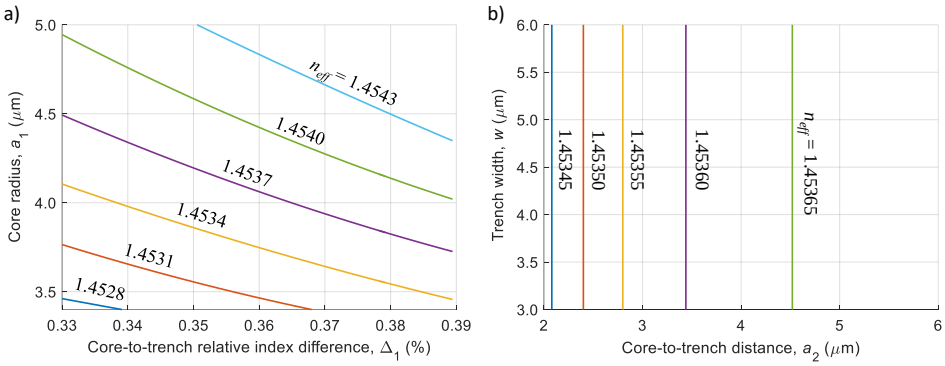

Fig. 4.10. Effective index dependence on (a) the core radius a_1 versus the core-to-cladding relative index difference Δ_1 for a core-to-trench distance a_2 = 4 µm and trench width w = 4 µm; and (b) the trench width w versus the core-to-trench distance a_2 for a_1 = 4 µm and Δ_1 = 0.36%.

Table 4.1 summarizes the general behavior of the main propagation characteristics when increasing the value of each one of the design parameters. Upward lines represent an increment on the value of the variable involved, while downward lines describe decreasing tendencies. Double arrows are used to specify that the effect on a certain parameter is much stronger than in the single arrow cases.

Table 4.1. Impact of the design parameters on the core propagation characteristics

	n_g	D	ΔS	n_{eff}
↑ a_1	↑↑	↑↑	↓↓	↑↑
↑Δ_1	↑↑	↓	↓↓	↑↑
↑ a_2	↓↓	↓↓	↓↓ / ↑↑	↑↑
↑ w	↑	↑	↓	-

4.2.2.1. Design optimization in terms of higher-order dispersion

Based on the previous analysis, we develop a particular higher-order-dispersion- and crosstalk-engineered 7-core MCF design that ensures a linear group delay in a broad input wavelength range. By using, again, the numerical software *Fimmwave*, we obtained, respectively for cores 1 up to 7, a set of D values ranging from 14.75 up to 20.75 ps/(km·nm) with an incremental dispersion ΔD = 1 ps/(km·nm). The fiber satisfies as well the common group index condition at λ_0 = 1550 nm. Table 4.2 gathers all the core design variables together with the computed dispersion slopes and effective indices. The table also includes the computed effective areas A_{eff} of the cores, parameter that will be used later on section 4.4 to discuss the possible degradation due to fiber nonlinearities.

Table 4.2. Core design parameters and properties for the dispersion-slope-optimized design

Core *n*	Core design parameters				Core Properties		
	a_1 (μm)	Δ_1 (%)	a_2 (μm)	w (μm)	S (ps/(km·nm^2))	n_{eff}	A_{eff} (μm^2)
1	3.42	0.3864	5.48	3.02	0.06527	1.453384	64
2	3.60	0.3762	5.03	2.61	0.06434	1.453465	66
3	3.62	0.3690	4.35	3.32	0.06496	1.453386	65
4	4.26	0.3588	4.92	4.67	0.06446	1.453881	75
5	3.49	0.3476	2.81	5.41	0.06431	1.452878	59
6	4.79	0.3435	3.35	3.32	0.06425	1.454041	81
7	4.98	0.3333	2.42	4.05	0.06422	1.453979	82

All the cores were designed as to perform almost identical dispersion slope parameters, with a maximum variability between them of around 0.001 ps/(km·nm^2), as shown in Table 4.2. We followed the design strategy of arranging three groups of similar effective index cores along the MCF cross-sectional area. The core labelled as 5 was chosen as the inner core and has the lowest effective index, $n_{eff} \approx 1.4529$. This low value must be achieved while preserving high chromatic dispersion (D_5 = 18.75 ps/km/nm), so, from Table 4.1, we see that the core radius and core-to-trench distance have to be small, while the trench width highly increases and the core-to-cladding relative index difference is set to an intermediate value. The group formed by cores 1, 2 and 3 has an effective index around 1.4534, and its cores feature the lowest chromatic dispersion values. They are characterized by having a low core radius, high core-to-cladding relative index difference and high core-to-trench distance. The remaining cores constitute the group with the highest refractive index, above 1.4539. They present a higher core radius, lower core-to-cladding relative index difference and lower core-to-trench distance. Figure 4.11 illustrates the computed group delay and chromatic dispersion parameter for each core as a function of the core radius, were the filled circles represent the selected core radius values and the corresponding group delays (Fig. 4.11(a)) and chromatic dispersions (Fig. 4.11(b)). We see there how all the cores satisfy the common group delay and the linearly incremental chromatic dispersion conditions.

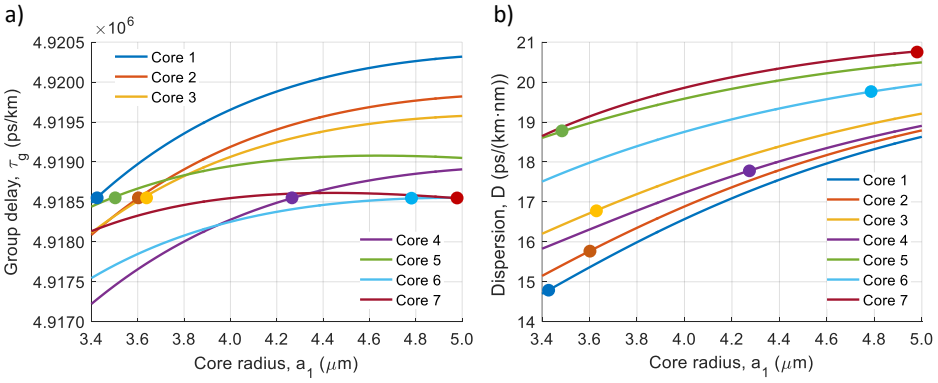

Fig. 4.11. (a) Group delay and (b) chromatic dispersion of each core as a function of the core radius. Filled circles represent the selected core radii for the 7 cores and their corresponding group delay and chromatic dispersions.

The design of the MCF reveals an important tradeoff between the dispersion slope and the effective index difference between adjacent cores in the sense that maximizing the effective index difference increases the range of variability of the dispersion slope. Figure 4.12 shows the computed dispersion slope versus the effective index for the set of design parameters that satisfy the target true time delay line requirements, i.e., common group index and dispersion requirements. Each small circle corresponds to the effective index and the dispersion slope obtained for particular values of the design variables. The seven colors are used to distinguish the values of the dispersion parameter *D* that are linked to specific core numbers. Filled squares represent each of the designed cores, named as C1-C7 respectively for cores 1 to 7. We see here how the magnitude of the dispersion slope is reduced as the effective index decreases, leading to an increment on the dispersion slope variability between the core featuring the lowest effective index (i.e., C5) and the rest. The reason of designing core 5 as the core that presents the lowest effective index can be now clearly understood from Fig. 4.12: it is the core than can have the lowest effective index possible without harming the target on the dispersion slope variability. As shown, all the core groups of the optimized MCF (i.e., filled squares) have the highest effective index difference possible with the most similar dispersion slope values. But we observe that the intercore crosstalk (i.e., the effective index difference between core groups) improves if the limitation on the maximum dispersion slope variability is less restrictive. Therefore, we propose to develop a second heterogeneous MCF in which we prioritize the effective index optimization over the dispersion slope optimization, so that we can compare both structures in terms of crosstalk and TTDL operation.

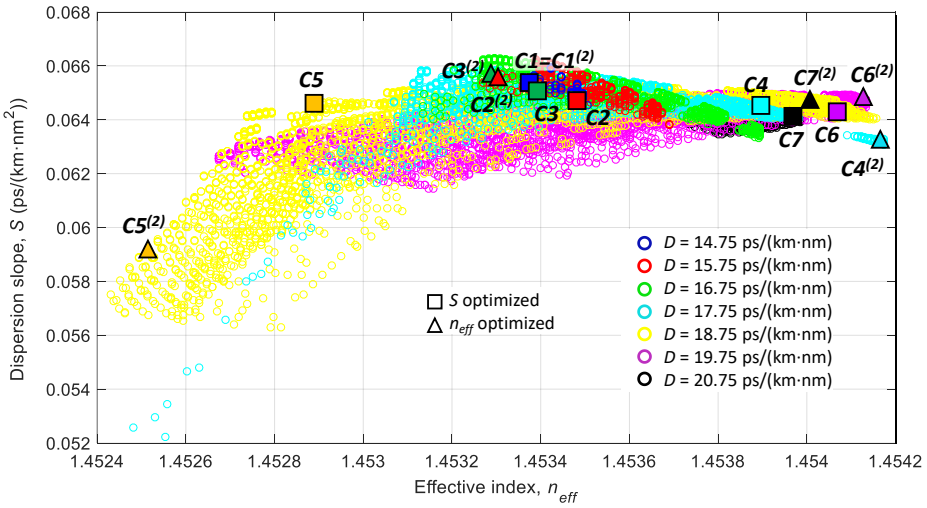

Fig. 4.12. Relationship between the computed dispersion slopes *S* and effective indices n_{eff} for a group index of 1.4755 and dispersion values *D* ranging from 14.75 up to 20.75 ps/(km·nm), plotted in different colored circles. Filled squares illustrate the *S* and n_{eff} of cores 1-7 for the dispersion-slope-optimized MCF, while filled triangles for the effective-index-optimized MCF.

4.2.2.2. Design optimization in terms of intercore crosstalk.

We present here a new design that prioritizes the optimization of the effective index over the optimization of the dispersion slope. This MCF shares the same TTDL requirements and characteristics, (such as the range of dispersion parameters *D* and the common group index) as the previous design reported in subsection 4.2.2.1. Table 4.3 gathers the core design parameters and propagation properties. The main difference between both fibers is that the core with the lowest effective index (core 5) is designed as to minimize the value of the effective index. This way, all the core radius, core-to-cladding relative index difference and core-to-trench distance have been reduced to achieve an effective index close to 1.4525, leading to a maximum dispersion slope variability between adjacent cores at least six times higher. Figure 4.12 shows the comparison between the effective indices and dispersion slopes, where we identify the cores of this new design with filled triangles and the superscript (2). This figure is actually very helpful to illustrate the tradeoff between S and n_{eff} that actually exists in heterogeneous MCFs. On one hand, this tradeoff limits the maximum effective index difference that we can reach if our goal is to reduce the variability in the higher-order dispersion and, on the other hand, it limits the minimum range of dispersion slope that we can obtain when our goal is to reduce the crosstalk.

Table 4.3. Core design parameters and properties for the effective-index-optimized design

Core	Core design parameters				Core Properties		
n	a_1 (μm)	Δ_1 (%)	a_2 (μm)	w (μm)	S (ps/(km·nm^2))	n_{eff}	A_{eff} (μm^2)
1	3.42	0.3864	5.48	3.02	0.06527	1.453384	64
2	3.40	0.3762	4.68	3.66	0.06591	1.453273	63
3	3.50	0.3690	4.22	4.45	0.06593	1.453270	63
4	4.59	0.3588	5.62	2.14	0.06293	1.454129	81
5	3.41	0.3476	2.20	4.09	0.05915	1.452534	56
6	4.89	0.3435	3.50	3.62	0.06451	1.454126	83
7	5.00	0.3333	2.51	5.12	0.06467	1.454012	83

4.2.3. Performance

Once we have designed both the higher-order-dispersion-optimized and the crosstalk-optimized fibers, we evaluate their performance in terms of true time delay line operation and intercore crosstalk robustness against curvatures. The developed delay lines serve as a compact and energy efficient solution to implement a variety of signal processing functionalities that will be especially demanded in fiber-wireless communications networks and subsystems. As a proof of concept, we evaluate their performance as distributed signal processing elements when they are applied to two typical functionalities in this type of scenarios: microwave signal filtering and optical beamforming for phased array antennas. This way, we can see the importance of properly engineering the higher-order dispersion of the heterogeneous MCF in terms of broadband TTDL operation in a more illustrative way.

4.2.3.1. True time delay operation

First, we must note that, since both fibers share the same chromatic dispersion values, they will feature very similar differential group delay relative error [as given by Eq. (4.5)] when the delay line operates in the wavelength-diversity regime. Furthermore, this error can be predicted and avoided, as we will see in section 4.2.3.3, when the fibers implement a microwave photonic filter operating in the wavelength-diversity domain. Thus, we restricted the evaluation of the delay lines performance to the spatial-diversity operation regime.

Figure 4.13(a) shows the computed group delay per unit length for each core as a function of the optical wavelength for both fibers. We can observe that, in both cases, all the cores share a common group delay at the anchor wavelength λ_0 = 1550 nm. As long as we move from the anchor wavelength, the basic differential delay increases; and, ideally, it should remain identical between any pair of adjacent samples. Here lies the difference between both designs: how long will take the higher-order-dispersion effect to break down this homogeneity. Figures 4.13(b) and 4.13(c) illustrate the differential group delay contribution due to the nonlinear terms of Eq. (4.2) as a function of the optical wavelength, respectively for the dispersion-slope-optimized and the effective-index-optimized fibers. As a reference, we also include in dashed lines the group delay relative error calculated from Eq. (4.3). We see how the maximum relative error due to the dispersion slope variability increases up to 15% within a 50-nm range for the effective-index-optimized design, while it is kept below 2.5% for the dispersion-slope-optimized fiber. In general, we can assume that a relative error around 5-10% could be considered as the lower limit from which the target response of a typical MWP application (such as signal filtering or radio beamsteering) is excessively damaged. This implies that the wavelength operation range is wider (larger than 100 nm) in the dispersion-optimized fiber than in effective-index-optimized one (25-35 nm range).

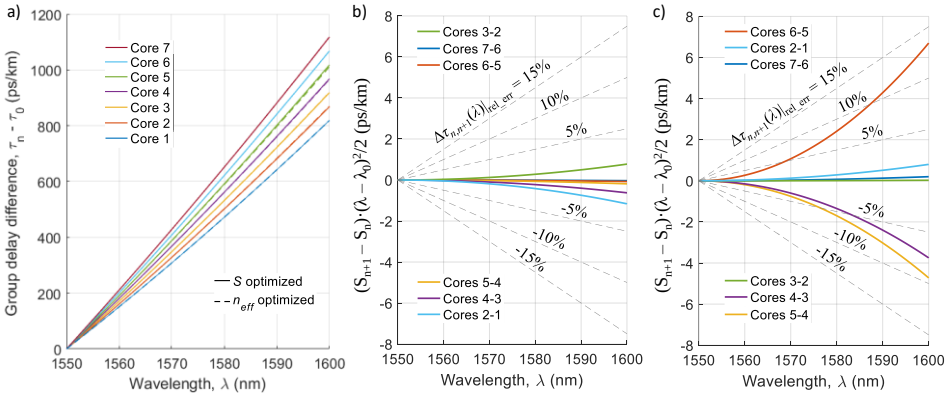

Fig. 4.13. (a) Computed core group delays versus wavelength for both MCFs (dashed lines); Computed differential group delay contribution due to the nonlinear dispersion effect (given by the nonlinear part of Eq. (4.2)) as a function of the wavelength for (b) the dispersion-slope-optimized fiber and (c) the effective-index-optimized fiber. Dashed lines represent the differential group delay relative error calculated from Eq. (4.3).

The simultaneous exploitation of the spatial- and wavelength-diversity domains in the implemented 2D sampled TTDLs add more versatility as compared to current approaches where only wavelength diversity is exploited, [38, 138]. For instance, if we consider a 10-km MCF, we can change the basic differential group delay in the spatial diversity domain, $\Delta\tau$, as 10 ps/nm by tuning the operation wavelength λ [Eq. (4.2)]. At $\lambda = \lambda_0$, we have 0-differential delay transmission between all the cores, which is ideal for avoiding DSP solutions in signal distribution scenarios. As long as the operation wavelength moves away from λ_0, the basic differential group delay increases from a few ps up to tens or hundreds of ps, which give rise to create MWP applications operating at μ-wave and mm-wave bands. And, if we feed the TTDLs by an array of lasers separated by $\delta\lambda$ wavelength units, we obtain a basic differential delay range spanning from $\Delta\tau_1 = 147.5 \cdot \delta\lambda$ ps up to $\Delta\tau_7 = 207.5 \cdot \delta\lambda$ ps when exploiting the wavelength diversity [Eq. (4.4)]. In section 4.2.3.3, we show an example of the tunability of these TTDLs when they operate as tunable MWP signal filters, where we can see easier the tuning effect when changing the optical wavelength of operation.

4.2.3.2. Crosstalk

One of the major detrimental effects that can degrade the performance of heterogeneous MCFs arises from the crosstalk dependence on the phase-matching condition between adjacent cores when the fiber is bent, [135, 76, 129]. To overcome this phenomenon, we have optimized our designs by maximizing, as much as possible, the effective index difference Δn_{eff} between adjacent cores as to improve the threshold bending radius R_{pk}, [136]. Figures 4.14(a) and 4.14(b) show the location of the cores on the cross-sectional area of the fiber for the effective-index-optimized and the dispersion-slope-optimized designs, respectively. As described in subsection 4.2.2, the selected spatial distribution ensures that each of the three groups of similar effective index cores are placed in nonadjacent positions. Figure 4.14(c) illustrates the numerical evaluation of the intercore crosstalk dependence on the fiber bending radius for the pair of cores bringing the worst-case scenario. These results have been computed with the numerical software *Fimmprop* by *Photon Design*. As shown, the fiber optimized in terms of effective index presents a threshold bending radius close to 69 mm that corresponds to $\Delta n_{eff} \approx 0.074\%$. On the other hand, the design optimized in terms of higher-order dispersion presents a threshold bending radius shifted to around 103 mm as the effective index difference is reduced down to 0.050%. In addition, we see that the worst-case crosstalk above the phase-matching region is kept below -80 dB in both designs, which stays in the order of the -70 dB reported for trench-assisted 7-core MCFs [76, 139].

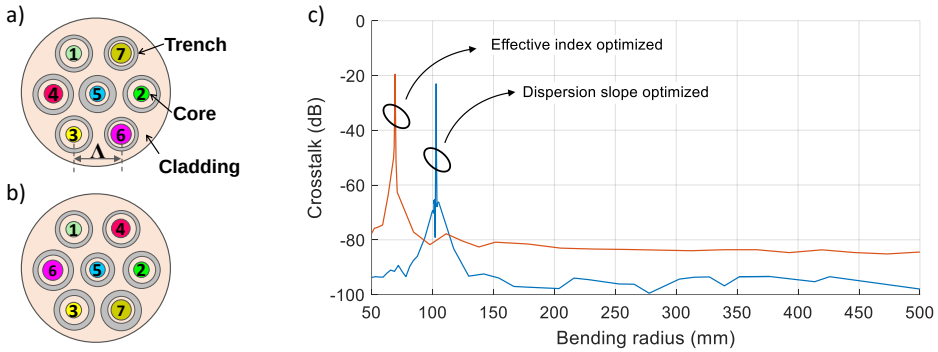

Fig. 4.14. Cross-sectional fiber view for (a) the effective-index-optimized and (b) the dispersion-slope-optimized designs; (c) Computed crosstalk as a function of the bending radius for the effective-index- (solid red) and dispersion-slope-optimized designs (solid blue).

4.2.3.3. Application to Microwave Photonics distributed signal processing

A frequency filtering effect over RF signals results from combining and collectively photodetecting (with a single receiver) the delayed signal samples coming from the TTDL output. This incoherent finite impulse response filter is characterized by a transfer function $H(f)$ that is given by Eq. (2.1). The frequency period or FSR of the filter is given by $FSR = 1/\Delta\tau$, where $\Delta\tau$ is the basic differential delay.

We evaluate the performance of the TTDLs implemented with a 10-km MCF comparing both spatial and wavelength modes of operation. Figures 4.15(a)-(d) illustrate the computed transfer function of the microwave filter as a function of the RF frequency when the TTDL operates in wavelength diversity. We compare the response of the filters implemented with the designed TTDLs (blue-solid line) to the ideal response (red-dashed line) obtained by setting S to zero in the basic differential delay given by Eq. (4.4). As commented before, we obtain the same performance in both dispersion- and crosstalk-optimized fibers when we exploit diversity in optical wavelength. Figure 4.15(a) corresponds to the case when we use an array of $M = 5$ lasers from $\lambda = 1550$ up to 1554 nm with a 1-nm separation. We see a perfect match between the responses from the ideal and the designed systems. If we increase the wavelength range up to 1590-1594 nm, we observe a considerable mismatch between both responses, as shown in Fig. 4.15(b). This is caused by the linear $\delta\lambda$-dependence of S in Eq. (4.4) (second term in right-hand side). However, this linear displacement does not distort the filter shape, so we can compensate a priori this effect by taking into account this displacement when designing the TTDL. Actually, we can re-tune the response by properly managing the operation wavelengths of the lasers, as shown in Fig. 4.15(c) where the separation between the input wavelengths is reduced down to 0.89 nm. We can as well compensate that effect by increasing the number of lasers, as shown Fig. 4.15(d) for $M = 10$. Note that the optical wavelength shift $\delta\lambda$' that compensates this displacement is obtained from Eq. (4.4) as:

$$\delta\lambda' = \frac{D_n}{D_n + S_n\left(\lambda_1 - \lambda_0\right)}\delta\lambda\,. \tag{4.6}$$

Figures 4.15(e)-(h) represent the computed transfer function of the microwave filter working in spatial diversity when we compare: (1) the MCF optimized in terms of higher-order dispersion (blue solid lines); (2) the MCF optimized in terms of effective index (green solid lines) and (3) the ideal response (red dashed lines). The 10-km MCF length results in a free spectral range of (e) 10 GHz for an operation wavelength of λ = 1560 nm, (f) 4 GHz for an operation wavelength of λ = 1575 nm, (g) 2 GHz for λ = 1600 nm and (h) 1 GHz for λ = 1650 nm. As shown, the dispersion-slope-optimized fiber overcomes the limitations induced by the nonlinear spectral group delay even for a wavelength range up to 100 nm, while the filter response for the-effective index-optimized fiber is highly degraded for wavelengths above 1575 nm.

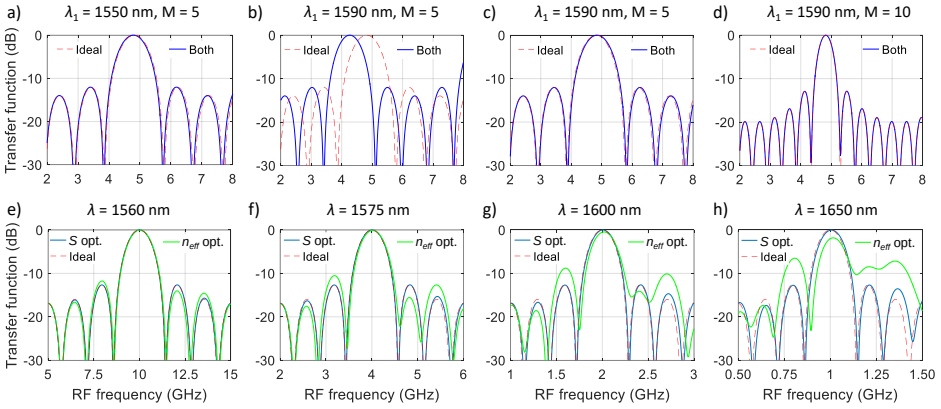

Fig. 4.15. Comparison of the computed wavelength-diversity transfer function H as a function of the RF frequency for both designs (blue solid line) and the ideal filter (red dashed line) for a 10-km fiber: (a)-(b) set of 5 lasers with a 1-nm separation at an initial wavelength λ_1 of (a) 1550 nm and (b) 1590 nm; (c)-(d) 0.89-nm wavelength separation and λ_1 = 1590 nm for (c) 5 lasers and (d) 10 lasers. Comparison of the computed spatial-diversity H between the dispersion-optimized (blue solid line), the effective-index-optimized (green solid line) and the ideal filters (red dashed line) for a 10-km fiber at an operation wavelength of (e) 1560 nm, (f) 1575 nm, (g) 1600 nm and (h) 1650 nm.

Optical beamforming networks are implemented using a similar configuration as in microwave signal filtering, with the particularity that each sample is individually photodetected and, then, feeds one of the radiating elements that conformed the phased array antenna, as we saw in chapter 2. In the case of 1D architectures, the normalized angular far-field pattern of the radiated electric field, or array factor $AF(\theta)$, is given by Eq. (2.2).

We evaluate now the influence of the nonlinear spectral group delay in both fibers in the case of a phased array antenna characterized by a separation between adjacent antennas of d_x = 3 cm, a 5-GHz RF signal and a link length of 10 km. As we have pointed out in the microwave filtering analysis, when we operate in wavelength diversity, the nonlinearities arisen in the basic differential delay [term proportional to $\delta\lambda$ in the second term of the right-hand side of Eq. (4.4)] can be further compensated. Then, for simplicity, our evaluation here focuses only on the use of the spatial diversity domain. We compare again the dispersion-optimized MCF (blue solid lines), the effective-index-optimized fiber (green solid lines) and the ideal response

(red dashed lines). Figure 4.16(a) shows the computed array factor as a function of the beam pointing angle (in degrees) in both polar coordinates (left) and decibels (right) at an operation wavelength of λ_m = 1570 nm. We see that, for a 20-nm wavelength range, the array factor offered by the effective-index-optimized MCF is slightly mismatched from the ideal one, while the one given by the dispersion-slope-optimized fiber matches it perfectly. If the operation wavelength increases up to 1600 nm, Fig. 4.16(b) shows that the array factor is highly degraded when we use the effective-index-optimized fiber, but stays practically unaltered when we resort to the dispersion-slope-optimized fiber instead.

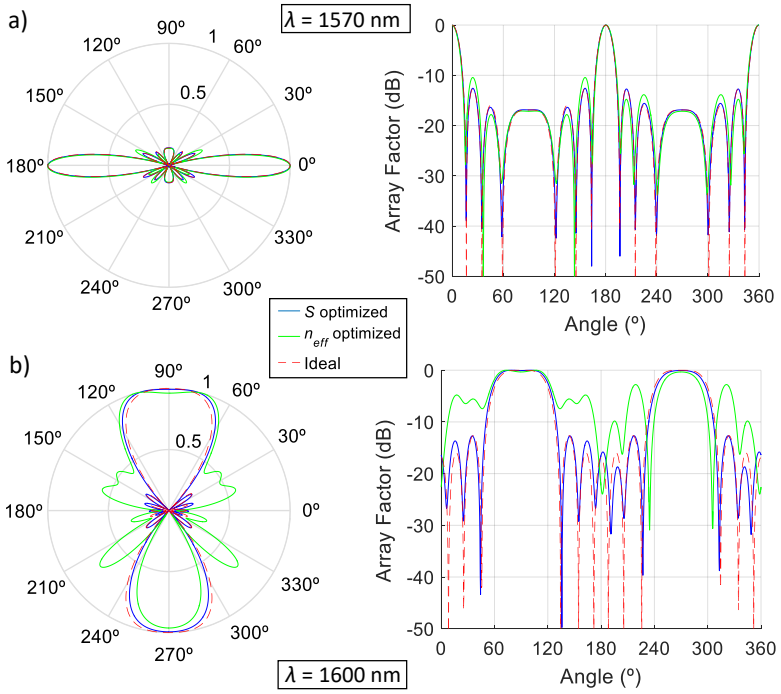

Fig. 4.16. Comparison between the computed array factor (AF) as a function of the beam pointing angle (in degrees) for the dispersion-slope-optimized MCF (blue solid line), the effective-index-optimized MCF (green solid line) and the ideal delay line for a 10-km fiber with a 3-cm separation between antennas for a RF frequency of 5 GHz at an operation wavelength of (a) 1570 nm and (b) 1600 nm. Left: in polar coordinates; Right: in decibels.

4.2.3.4. Discussion

In summary, we have seen the importance of properly optimizing the higher-order dispersion parameter in the proposed TTDLs in order to ensure proper tunability in a broad wavelength range. We saw that the dispersion-slope-optimized fiber can operate as a 2D distributed radiofrequency signal processing element in a wavelength range beyond 100 nm with almost negligible degradation caused by the higher-order dispersion, while the wavelength operability range of the effective-index-optimized fiber is restricted down to around 30 nm. In contrast, we found that the optimization

in terms of tunability range comes at the expense of intercore crosstalk and its sensitivity against fiber curvatures. In particular, the effective-index-optimized fiber presents a threshold bending radius around 69 mm (which is below the typical 75-mm-radius fiber spools), while that of the dispersion-slope-optimized fiber is around 103 mm. This second parameter gains more attention in those scenarios in which the fiber has to be coiled in a spool, since the dispersion-slope-optimized fiber would require a larger-radius spool to prevent possible degradations due to intercore crosstalk (with the associated increment on size, which could be a critical parameter). All in all, we must take into account that, in practice, the fiber link is not uniformly bent at the critical bending radius (which corresponds to the worst-case scenario). Instead, depending on the actual link deployment, the fiber will experience different curvatures and twists, being the total crosstalk an accumulation of the different crosstalk sources experienced along the link.

4.3. Implementation using few-mode fibers

In the case of sampled TTDL operation on FMFs, the multiple spatial paths are created by the different modes that propagate along the single core of the fiber. However, it is particularly complex to design a FMF to behave as a group-index-variable delay line in the sense that it is not possible to control each spatial path (mode) fully independently from the others. That is, all design parameters defining the refractive index profile of the FMF are shared between all the modes, so that varying any of them affects all the spatial paths. Thus, we will require a kind of external elements to ensure a certain control over the propagation characteristics of the signal samples. We propose here the inscription, in the proper positions, of broadband mode converters based on LPGs. These mode converters will also limit the wavelength operability range of the TTDL down to the spectral bandwidth of the LPGs, which rarely could be above 10 or 20 nanometers. Because of that, it is worth to note that it has no sense to analyze the higher-order-dispersion effects in these kind of TTDLs, since: (1) it will considerably increase the complexity of the design by adding one more variable (and thus the need of using a higher number of mode converters); and (2) the operation wavelength would never be far enough from the anchor wavelength as to consider using a higher-order Taylor series approximation.

4.3.1. Concept

In a similar way than in the heterogeneous MCF-based approach, we can expand the group delay per unit length of a given LP_{lm} mode, τ_{lm}, in Taylor series around a central or reference wavelength λ_0, but, in this case, we can make use of the simpler 1st-order approximation as

$$\tau_{lm}(\lambda)=\tau_{lm}(\lambda_0)+(\lambda-\lambda_0)D_{lm}\,, \tag{4.7}$$

where $\tau_{lm}(\lambda_0)$ is the group delay per unit length at λ_0 and D_{lm} is the chromatic dispersion at λ_0 for the LP_{lm} mode. We can proceed analogously than in Eqs. (4.2) and (4.4) and obtain the following expression for the differential group delay between adjacent samples (n+1) and n when operating in the spatial-diversity domain,

$$\Delta\tau_{n,n+1}(\lambda_m) = \Delta\tau(\lambda_0)+\Delta D(\lambda_m-\lambda_0), \tag{4.8}$$

and for the differential group delay between optical wavelengths λ_{m+1} and λ_m when operating in the wavelength-diversity domain

$$\Delta\tau_n(\lambda_m,\lambda_{m+1}) = D_n\delta\lambda, \tag{4.9}$$

being $\Delta\tau(\lambda_0) = \tau_{n+1}(\lambda_0) - \tau_n(\lambda_0)$ the incremental group delay at the anchor wavelength and $\Delta D = D_{n+1} - D_n$ the incremental dispersion. Note that, for simplicity, we have used the subindex n for designing the n^{th} sample instead of preserving the *lm*-mode nomenclature that could lead to confusion. From Eq. (4.8), we see that proper TTDL operation and tunability require: (1) constant basic differential group delay at the anchor wavelength; and (2) constant basic differential chromatic dispersion ΔD. In general, however, it is not possible to fulfil these conditions given the propagation characteristics of the modes that propagate through typical FMFs (as we can see in any of the refractive index profiles simulated in chapter 3). And, even in the hypothetical case that it was possible, the differential group delay $\Delta\tau_{n,n+1}$ in the spatial diversity domain would probably be extremely high for MWP applications, (i.e., very low operating radio frequencies), limiting the fiber length to only a few meters. In addition, the contribution corresponding to the differential group delay at the reference wavelength $\Delta\tau(\lambda_0)$, (first term at the right-hand side of Eq. (4.8)), would be much greater than the contribution corresponding to the incremental dispersion $(\lambda_m-\lambda_0)\Delta D$, (second term at the right-hand side of Eq. (4.8)), so the TTDL tunability would be insignificant.

To overcome these limitations, we propose to obtain a subset of TTDL samples as a combination of different modes that propagate through the fiber instead of using a single mode per sample. With the help of in-line mode converters based on LPGs inscribed at specific positions along the FMF link [140], we can adjust the final group delay and chromatic dispersion values associated to each signal sample. This idea can be explained as follows. Suppose that the i^{th} TTDL sample is created in first place by a particular mode LP_{lm} that is injected at the fiber input and propagates over that mode for a certain distance $L_{lm}^{(i)} = l_{lm}^{(i)}L$ (with a specific group delay and chromatic dispersion), where $l_{lm}^{(i)}$ is the normalized length along which the i^{th} sample is propagated by a given LP_{lm} mode and L is the total length of the FMF link. Then, a given LPG transforms that incoming LP_{lm} mode into a different outgoing LP_{lm} mode (with a different group delay and chromatic dispersion). We can repeat this mode conversion mechanism as many times as necessary by concatenating different LPGs inscribed at the positions $\sum_{lm\in I} l_{lm}^{(i)}L$, where I is the set of indices *lm* of the LP_{lm} modes in which the i^{th} sample has been propagated before passing through the current LPG. This way, at the output of the fiber, the group delay of the i^{th} TTDL sample τ_i at a given wavelength λ_0 can be expressed as a combination of the LP_{lm} modes involved to create that sample as

$$\tau_i = \left[\left(\sum_{lm\in I}\tau_{g,lm}l_{lm}^{(i)}\right)+(\lambda-\lambda_0)\left(\sum_{lm\in I}D_{lm}l_{lm}^{(i)}\right)\right]L = \left[\tau_{eq,i}+(\lambda-\lambda_0)D_{eq,i}\right]L, \tag{4.10}$$

where $\tau_{eq,i}$ and $D_{eq,i}$ are the equivalent group delay per unit length and equivalent chromatic dispersion of the i^{th} sample at λ_0, respectively. With the appropriate series of mode combinations, we can assure a set of samples with constant incremental group delay and dispersion values between adjacent samples, where the final group delay of the i^{th} sample is given by

$$\tau_i = \tau_{eq,1} L + (i-1)\Delta\tau(\lambda_0) + (\lambda - \lambda_0)\left(D_{eq,1} + (i-1)\Delta D\right)L, \tag{4.11}$$

where $\tau_{eq,1}$ is the equivalent group delay per unit length of the first sample and $D_{eq,1}$ is the equivalent chromatic dispersion of the first sample. Figure 4.17 illustrates the basic idea beyond the mode combination mechanism in Eqs. (4.10) and (4.11) for a generic FMF link with inscribed LPGs. Figure 4.17(a) shows the evolution of the differential group delay of the samples with respect to the first one, $\tau_i - \tau_1$, at the anchor wavelength λ_0, as a function of the normalized length z/L. Each colored line corresponds to a different mode of a generic FMF, and the color of each sample corresponds to that of the final mode in which the sample propagates throw. We see that proper mode conversion in samples 2 and M allows the common basic differential delay requirement, $\Delta\tau(\lambda_0)$. In a similar way, Fig. 4.17(b) depicts the evolution of the sample differential chromatic dispersions, $D_i - D_1$, as a function of the normalized length, where we see that one can obtain as well incremental values of the chromatic dispersion with a common differential dispersion, ΔD. Finally, Fig. 4.17(c) represents the dependence of the resulting sample time delays with the optical wavelength at the output of the FMF link, where we can observe the tunability of the TTDL with the optical wavelength.

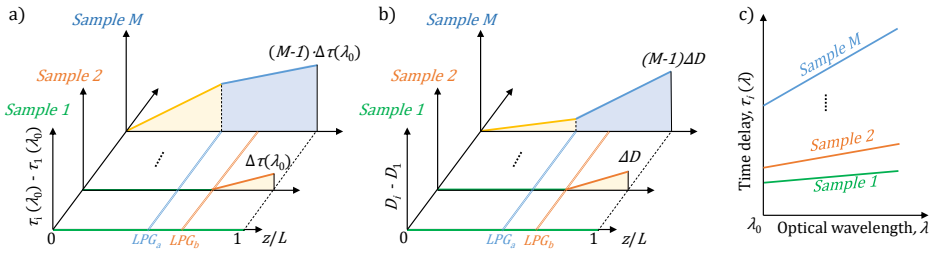

Fig. 4.17. (a) Evolution of the differential group delay of the samples, $\tau_i - \tau_1$, as a function of the normalized length; (b) Evolution of the differential chromatic dispersion, $D_i - D_1$, as a function of the normalized length; and (c) Time-delay dependence of the samples with the optical wavelength for a generic FMF link with inscribed LPGs.

4.3.2. Mode conversion using long period gratings.

A long period fiber grating is an all-fiber device that introduces a periodic perturbation on the refractive index of the optical fiber. This perturbation produces energy coupling from one of the propagating modes to another forward-propagating mode (or cladding mode) at a specific wavelength λ_B given by the Bragg condition, [141],

$$\lambda_B = \Lambda\left(n_{eff_i} - n_{eff_j}\right), \tag{4.12}$$

being Λ the perturbation period and $n_{eff,i}$ and $n_{eff,j}$ the effective indices of the involved modes. The perturbation can be generated in different ways, such as mechanically by applying pressure points or by modifying permanently the core refractive index by using ultraviolet (UV) radiation, [142].

In a FMF, a LPG can perform a mode conversion between any pair of modes that propagate along the fiber. With the help of *OptiGrating* software, from *Optiwave* company, we simulated the viability and selectivity of some mode conversions on a step-index FMF. We consider an optical fiber with a core radius of 10 μm and core and cladding refractive indices of 1.45 and 1.44, respectively, at the optical wavelength of λ = 1550 nm. The modulation index of the perturbation along the LPG was set to 10^{-3}. Fig 4.18(a) shows the transmitted power of modes LP_{01} and LP_{02} as a function of the propagation length. Orange line corresponds to the LP_{01} mode and blue line to the LP_{02}. As we can see, after 19-mm propagation length, all the LP_{01} power is coupled into the LP_{02} mode. The resulting LPG period is Λ = 404 μm. Fig. 4.18(b) depicts the spectrum of the LPG when the length is set to 19 mm, where we see a notch in the transmitted power of the LP_{01} mode at λ = 1550 nm due to the coupling into the LP_{02}.

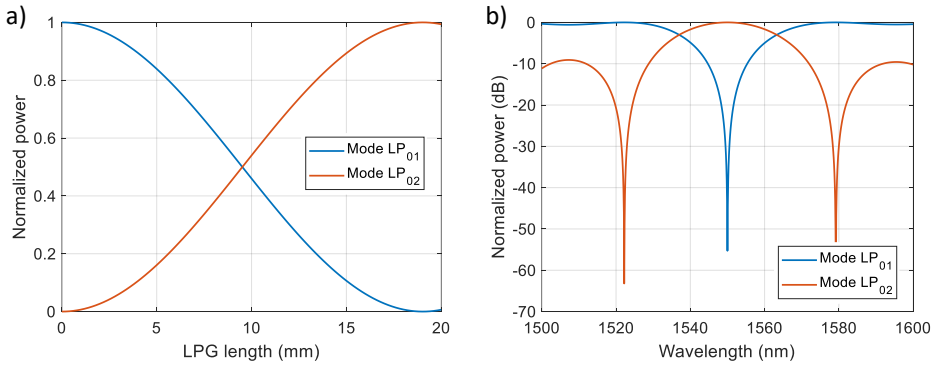

Fig. 4.18. (a) Normalized transmitted power on modes LP_{01} (orange) and LP_{02} (blue) as a function of the propagation length along the LPG; (b) LPG optical spectrum in transmission for the modes LP_{01} (orange) and LP_{02} (blue).

Since the refractive index distribution of a standard fiber is circularly symmetric, only coupling between modes of the same azimuthal symmetry is allowed for circularly symmetric refractive index changes, [141, 143]. Thus, we require an asymmetrical perturbation for the conversion between a symmetrical and an asymmetrical mode, what can be done by inscribing the LPG with a certain tilt angle, [144]. As an example, Fig. 4.19 shows the conversion between LP_{01} and LP_{11} modes. The tilt angle was set to 15º and the resulting LPG period was 1065 μm. As shown in Fig. 4.19(a), the optimum length for full mode conversion resulted in 110 mm. Figure 4.19(b) illustrates the optical spectrum, in transmission, of the LP_{01} mode and how it properly couples to the LP_{11} at λ = 1550 nm, with a coupling efficiency above 99%.

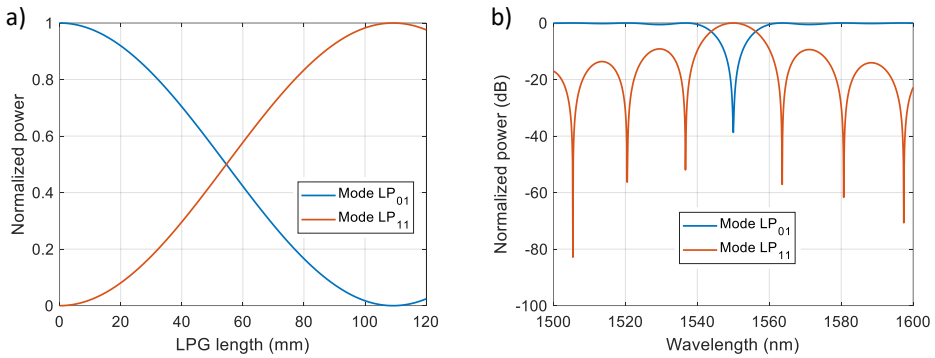

Fig. 4.19. (a) Normalized transmitted power on modes LP_{01} (orange) and LP_{11} (blue) as a function of the propagation length along the LPG; (b) LPG optical spectrum in transmission for the modes LP_{01} (orange) and LP_{11} (blue).

4.3.3. Design of a tunable true time delay line on a 7-mode fiber

We have described in section 4.3.1 the conditions that the FMF-based device must fulfil to operate as a sampled TTDL. But we need to ensure as well a low level of intermodal crosstalk between signal samples along the fiber link to avoid degradation on the target MWP signal processing functionality, what calls for modal phase propagation constants (or effective indices) as different as possible. In addition, modes with a set of chromatic dispersions as diverse as possible are desirable to allow the accomplishment of Eq. (4.10) with higher ΔD (larger delay tunability). In this regard, we have designed a particular FMF whose refractive index profile follows a ring-core step-index architecture. The use of a step-index profile reduces the mode coupling by increasing the effective index difference between modes, while the ring-core architecture provides more design versatility and allows managing the propagation characteristics of the symmetric modes with certain independence from the asymmetric modes. Figure 4.20(a) depicts the refractive index profile of the designed ring-core fiber. It consists of a SiO_2 inner layer doped with a low GeO_2 concentration (radius a_1 = 3 µm and inner-core-to-cladding relative index difference Δ_1 = 0.21%) surrounded by a SiO_2 ring-core layer doped with a higher GeO_2 concentration (radius a_2 = 10 µm and core-to-cladding relative index difference Δ_2 = 0.72%) inside a pure silica cladding. We carried out the design of the FMF refractive index profile, in this case, by using the universal characteristic equation proposed in chapter 3. Figure 4.20(b) shows the computed effective index as a function of the scale factor (i.e., the parameter that expands/compacts the whole refractive index profile in the radial axis r). When the scale factor equals 1, the refractive index profile corresponds to the designed profile. At this point, the fiber supports 7 LP modes. Table 4.4 summarizes the main characteristics of the fiber modes at a 1550-nm wavelength.

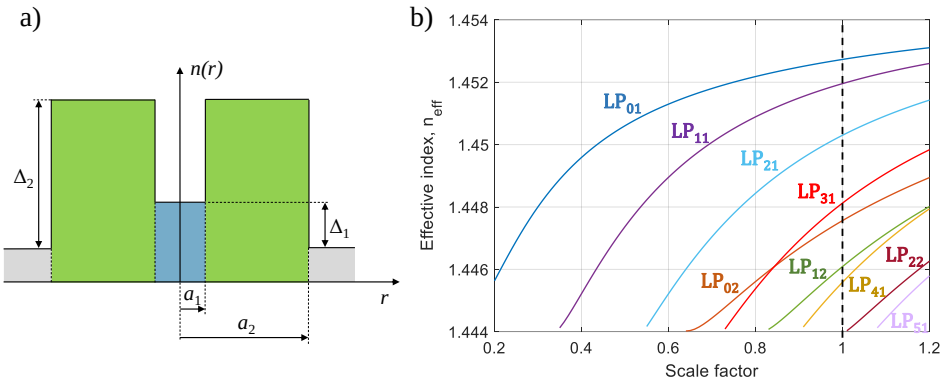

Fig. 4.20. (a) Refractive index profile of the designed ring-core fiber. (b) Computed effective index n_{eff} for every propagated mode as a function of the fiber scale factor.

Table 4.4. Mode propagation characteristics for the designed FMF at the wavelength of λ_0 = 1550 nm.

	LP_{01}	LP_{11}	LP_{21}	LP_{31}	LP_{02}	LP_{12}	LP_{41}
$\tau_{lm} - \tau_{01}$ (ps/km)	0	3489.08	8182.33	13022.34	2858.64	8912.83	17412.05
D (ps/km/nm)	18.96	23.77	27.41	29.19	17.14	11.07	25.24
n_{eff}	1.452726	1.451956	1.450294	1.448120	1.447556	1.446090	1.445584

In order to reduce the crosstalk among non-degenerate modes, we have designed the fiber to increase as much as possible the effective index difference between modes Δn_{eff}, [115, 145]. In this case, the effective index difference between neighboring modes is bigger than $0.5 \cdot 10^{-3}$ for all the modes, which is similar to the values of typical low-crosstalk commercial step-index FMFs, [87, 146]. This is the case, for instance, of the low-crosstalk 4-LP-modes FMF we have in our laboratory, which features $\Delta n_{eff} > 0.8 \cdot 10^{-3}$ and ensures mode coupling below -30 dB/km (see Annex I).

The evaluation of the modal propagation characteristics gathered in Table 4.4 suggests that a total of 5 LPGs acting as mode converters are required to perform 4-sample tunable TTDL operation, that is, mode conversions: LP_{02} to LP_{12}, LP_{12} to LP_{01}, LP_{01} to LP_{41}, LP_{12} to LP_{11} and LP_{11} to LP_{31}. Figure 4.21 illustrates the designed ring-core fiber with the inscription of the LPGs along the fiber. We see there how the modes are combined through the different LPGs to generate the output samples. Starting from the 4th sample (the one with the largest group delay), we can see that it travels into the LP_{21} mode along the whole fiber length L. The remaining samples are created through LPG mode conversion, starting from the excitation of the LP_{02} mode at the fiber input. After a given length $L_{02} = l_{02} \cdot L$, LPG_1 couples all the power coming from this mode into the LP_{12} mode. After propagating through a length $L_{12}^{(1)} = l_{12}^{(1)} \cdot L$, the LP_{12} mode creates at the output of the fiber the 1st sample (the one with the smallest group delay). The group delay of the 2nd and 3rd samples is adjusted by performing two additional mode transformations in each case. For the 2nd sample, LPG_3 couples part of the LP_{12} mode into the LP_{01} mode that propagates a distance $L_{01}^{(2)} = l_{01}^{(2)} \cdot L$ before being transformed into the LP_{41} mode in LPG_5. In the case of the 3rd sample, LPG_2 couples part of the LP_{12} mode into the LP_{11} mode that

propagates a distance $L_{11}^{(3)} = l_{11}^{(3)} \cdot L$ before being transformed into the LP_{31} mode in LPG_4.

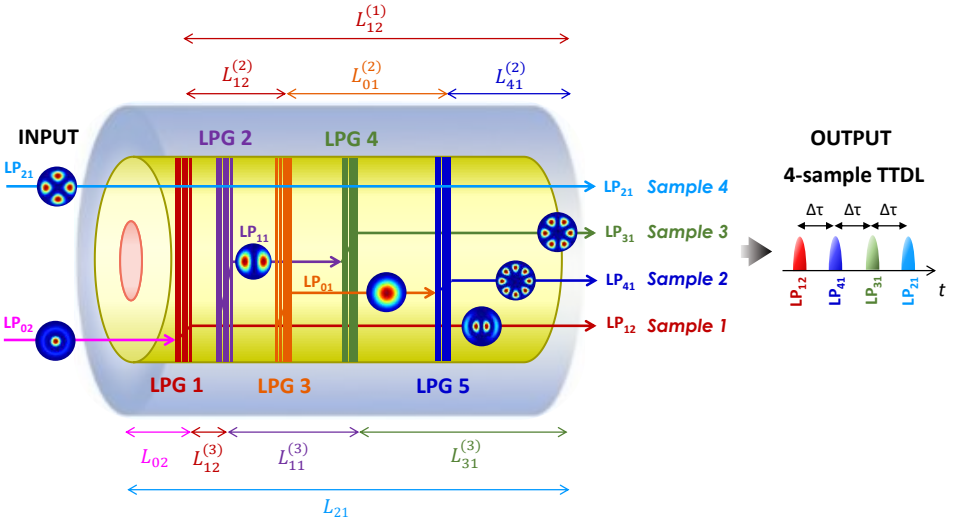

Fig. 4.21. Scheme of the designed TTDL based on a ring-core FMF link of length L with a set of 5 LPGs inscribed at specific longitudinal positions. On the right, one can see the 4 output optical TTDL samples in the time domain characterized by a constant basic differential delay $\Delta\tau$.

With the help of Eq. (4.10) and following the procedure illustrated in Fig. 4.21, we obtain the following expressions for the group delays per unit length τ_i / L of the samples at the end of the FMF link:

$$\begin{cases} \dfrac{\tau_1}{L} = \left(\tau_{02} l_{02} + \tau_{12} l_{12}^{(1)}\right) + \left(\lambda - \lambda_0\right)\left(D_{02} l_{02} + l_{12}^{(1)} D_{12}\right) \\ \dfrac{\tau_2}{L} = \left(\tau_{02} l_{02} + \tau_{12} l_{12}^{(2)} + \tau_{01} l_{01}^{(2)} + \tau_{41} l_{41}^{(2)}\right) + \left(\lambda - \lambda_0\right)\left(D_{02} l_{02} + D_{12} l_{12}^{(2)} + D_{01} l_{01}^{(2)} + D_{41} l_{41}^{(2)}\right) \\ \dfrac{\tau_3}{L} = \left(\tau_{02} l_{02} + \tau_{12} l_{12}^{(3)} + \tau_{11} l_{11}^{(3)} + \tau_{31} l_{31}^{(3)}\right) + \left(\lambda - \lambda_0\right)\left(D_{02} l_{02} + D_{12} l_{12}^{(3)} + D_{11} l_{11}^{(3)} + D_{31} l_{31}^{(3)}\right) \\ \dfrac{\tau_4}{L} = \tau_{21} l_{21}^{(4)} + \left(\lambda - \lambda_0\right) D_{21} l_{21}^{(4)} \end{cases} \quad (4.13)$$

where the superscript of the normalized length $l_{02} = l_{02}^{(1)} = l_{02}^{(2)} = l_{02}^{(3)}$ has been suppressed for simplicity. Then, by substituting the mode parameters of Table 4.4 into Eq. (4.13) and setting the basic differential delay $\Delta\tau$ to 100 ps/km while keeping an incremental dispersion parameter as big as possible, we obtained the normalized lengths $l_{lm}^{(i)}$, as Table 4.5 shows. The position in which each LPG should be inscribed is obtained as the sum of the lengths along which the sample travelled on the different modes before arriving to that specific LPG. For instance, the third sample travels along the modes LP_{02}, LP_{12}, LP_{11} and LP_{31} passing through 3 LPGs placed in l_{02}, $l_{02} + l_{12}^{(3)}$, and $l_{02} + l_{12}^{(3)} + l_{11}^{(3)}$, respectively for LP_{02} to LP_{12}, LP_{12} to LP_{11} and LP_{11} to LP_{31} mode conversions. The equivalent sample group delays $\tau_{eq,i}$ - τ_{01} (normalized to the LP_{01} group delay) per unit length are 7882.3, 7982.3, 8082.3 and 8182.3 ps/km

and the equivalent dispersions $D_{eq,i}$ are 12.1, 17.2, 22.3 and 27.4 ps/km/nm, respectively for samples 1 up to 4.

Table 4.5. Normalized lengths $l_{lm}^{(i)}$ along which the *i*-th sample travels on mode LP_{lm}.

l_{02}	$l_{12}^{(1)}$	$l_{41}^{(2)}$	$l_{01}^{(2)}$	$l_{12}^{(2)}$	$l_{31}^{(3)}$	$l_{11}^{(3)}$	$l_{12}^{(3)}$	$l_{21}^{(4)}$
0.17	0.83	0.24	0.22	0.37	0.39	0.26	0.18	1.00

The TTDL tunability is limited by the spectral bandwidth of the LPGs. To improve the wavelength operability range of the delay line, we design each LPG as to ensure broadband operation bandwidth. The Bragg wavelength (or central wavelength) of all the LPGs was set to λ_B = 1550 nm. From Eq. (4.12), we calculated the period of each LPG Λ given the effective indices of the involved modes at the Bragg wavelength. Finally, as we saw in section 4.3.2, the inscription of the LPGs with a certain chirp improves their spectral bandwidth and can provide up to a 20-nm wavelength operability range, [147]. Table 4.6 summarizes the main characteristics defining the LPGs.

Table 4.6. Calculated LPG periods and chirps for mode conversions and 20-nm tunability.

	LP_{02}-LP_{12}	**LP_{12}-LP_{01}**	**LP_{01}-LP_{41}**	**LP_{12}-LP_{11}**	**LP_{11}-LP_{31}**
Period (μm)	1057	233	217	264	404
Chirp (μm)	13	3	3	3	5
Normalized position	0.17	0.36	0.54	0.61	0.76

4.3.4. Performance

The proposed FMF link with inscribed broadband LPGs behaves as a 4-sample TTDL that can operate in an optical wavelength range between 1540 and 1560 nm. Figure 4.22 shows the computed differential group delay per unit length between the i^{th} and the first sample, $\tau_i - \tau_1$, (i = 2, 3, 4), as a function of the optical wavelength λ. As shown, the basic differential group delay can be tuned from 49 ps/km at λ = 1540 nm up to 151 ps/km at λ = 1560 nm. This allows to implement MWP applications operating at RF frequencies ranging from 6.6 up to 20 GHz·km. In comparison with the MCF-based TTDL, whose length could be up to tens of km, the length of this FMF solution is restricted to less than a kilometer due to the higher crosstalk between the spatial paths. This is the reason of not stablishing (in the spatial-diversity domain) the 0-differential delay point at the anchor wavelength [see Eq. (4.8)], as opposed to the MCF design; in other case, this would lead to very high radio frequencies of operation due to the low differential delay achieved (maximum basic delay of 100 ps/km, i.e., 10 GHz·km as the lowest radio frequency). Regarding the wavelength-diversity domain, the sample group delays grow as 10, 15, 20 and 25 ps/km/nm, respectively for samples 1 up to 4, providing similar delay tunability ranges as in the heterogeneous MCF solutions (ranging from a few ps up to ns and beyond).

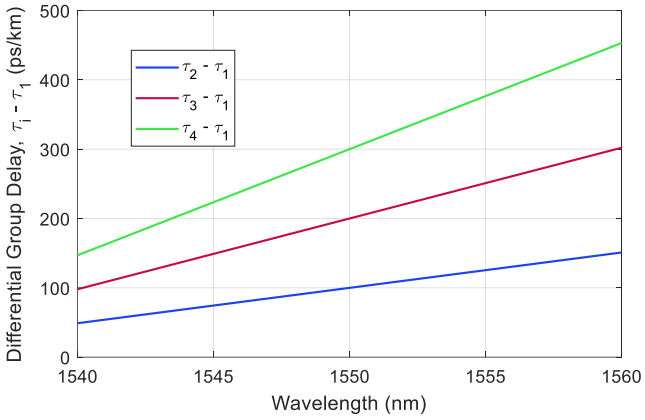

Fig. 4.22. Differential sample group delays per unit length with respect to the first sample as a function of the optical wavelength. TTDL tunability is ensured from 1540 up to 1560 nm.

To end with, we theoretically evaluate the performance of the proposed FMF-based delay line when it is applied to the same functionalities as the heterogeneous MCF-based approaches: tunable microwave signal filtering and optical beamforming for phased array antennas. We consider a fiber length of 1 km. For simplicity, we will focus only on exploiting the spatial-diversity operation regime of the TTDL. Figure 4.23(a) shows the computed RF transfer function of the resulting microwave signal filtering as a function of the radio frequency for different operation wavelengths. Blue-dashed, orange-dashed and purple-solid lines correspond, respectively, to the optical wavelengths of operation of λ = 1540.2, 1550 and 1559.8 nm. We see that we can tune the FSR of the filter from 20 GHz down to 10 GHz and 6.67 GHz by changing the operation wavelength of the optical source from 1540.2 up to 1550 and 1559.8 nm, respectively. This corresponds to increasing the basic differential delay from 50 up to 100 and 150 ps, respectively. On the other hand, Fig. 4.23(b) depicts the simulated far-field radiation pattern (or array factor) of the resulting 4-element phased array antenna as a function of the beam-pointing angle (in degrees) for a particular collection of optical wavelengths of operation. The distance between radiating elements is set to 1.5 cm and the radio frequency to 10 GHz. We see that we can tune the beam-pointing angle of the phased array antenna by changing the operation wavelength with a tuning ratio of 5 degrees per nanometer. In particular, the beam-pointing angle varies from 36 down to 11 degrees by tuning the optical wavelength from 1543.7 up to 1547.7 nm, what produces a basic differential delay variation from 70 up to 90 ps.

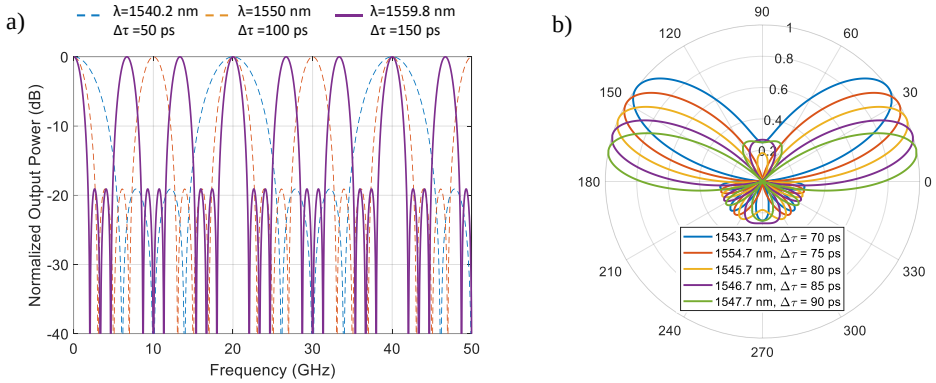

Fig. 4.23. (a) RF transfer function of the microwave photonic filter for three different operation wavelengths. (b) Array factor of the phased array antenna for five different operation wavelengths (RF frequency of 10 GHz and 1.5-cm antenna element separation).

4.4. Degradation sources

We have presented during this chapter two promising SDM technologies for the implementation of compact and reconfigurable fiber-based TTDLs. However, there could be different sources of impairment that can degrade the performance of these TTDLs, such as the intercore/intermodal crosstalk (respectively for the MCF- and FMF-based approaches), fiber bending and twisting, and possible degradations due to fabrication tolerances, temperature variations, fiber nonlinearities, etc. In this section, we will study some of these degradation sources and how can we overcome the possible detrimental effect caused to the performance of the proposed TTDLs.

4.4.1. Crosstalk

We have remarked many times the importance of adequately managing the intercore (intermodal) crosstalk in MCFs (FMFs). For this reason, we have designed the proposed TTDLs not only for proper delay line operation, but also for improving the crosstalk performance between the spatial paths.

In the case of the MCF-based approaches, the use of heterogeneous structures of trench-assisted cores that are designed to maximize the effective index difference between any pair of adjacent cores substantially reduces the intercore crosstalk. However, we have seen that bending the fiber can induce phase matching between any pair of adjacent cores. As long as the curvature radius is higher than the threshold bending radius, R_{pk}, the effect of the intercore crosstalk can be neglected, as we saw in section 4.2.3.2. In case the heterogeneous MCF is curved at a certain bending radius R_b below R_{pk}, $R_b \leq R_{pk}$, the intercore crosstalk can raise rapidly as the propagation length increases. Our MCF-based TTDL designs have a threshold bending radius of 69 mm and 103 mm, respectively for the crosstalk- and the higher-order-dispersion-optimized MCFs, what means that the first design is more robust against bend-induced intercore crosstalk. At first sight, since the bending radius in typical fiber spools is 75 mm, one may conclude that the performance of the second

design could be degraded once the fiber is coiled in the spool. However, we should note that, in a real scenario where the MCF link may span up to a few km, that situation will not take place: once the fiber is deployed, a curvature at such small bending radii for a long piece of fiber rarely occurs.

In the case of the FMF-based technology, the intermodal crosstalk becomes a more critical factor. First, the inherent nature of the spatial modes induces a higher coupling between them that is much more difficult to scale down; and, second, the LPGs used for the mode conversions can aggravate even more this effect. Regarding the fiber design, we designed the refractive index profile by following a step-index with a ring-core configuration, what allows us to increase the effective index difference between any pair of LP-modes up to 5e-4. This guarantees in theory a worst-case intermodal crosstalk level below -30 dB, as we previously discussed in section 4.3.3. However, the LPGs can enhance the mode coupling, not only for the modes involved in the LPG, but also for the remaining propagating modes. Even more, it is not easy to achieve a constant power conversion efficiency along the desired wavelength range, so that the sidebands on the LPG spectrum could produce additional intermodal crosstalk between both modes involved. Furthermore, in some cases half the power (or a certain proportion) propagating along a given mode must be coupled into another mode. This produces a decrement on the power of the transmitted power, while the coupling or interference signal remains at the same level, degrading even more the quality of the propagating signal due to the intermodal crosstalk. This effect accumulates when we use a cascade of several LPGs to generate a particular sample. In order to overcome these limitations, all the LPGs must provide a flat response in the desired wavelength range, and the number of LPGs required to generate each sample must not be excessively large.

4.4.2. Influence of fiber curvatures and twisting on the group delay

Bending and twisting the fiber can produce a variation on the propagation constants of the spatial modes of the fiber. This variation can modify the crosstalk behavior between the spatial channels, as we saw in the previous section, or even alter other propagation characteristics such as the group delay. This is particularly important for preserving the performance of the TTDLs, where a slight mismatch of a few ps on the group delay of a given spatial channel can completely degrade the delay line operability. In this section, we will study the effect of curvatures and twists on the group delay of the cores (modes) of a MCF (FMF).

4.4.2.1. Theoretical modeling

In general, in a MCF, a bent fiber core m can be described as the corresponding straight core with an equivalent refractive index distribution $n_{eq,m}$, [148]:

$$n_{eq,m} = \left[n_m^2 \left(1 + 2\frac{r_m}{R_b}\cos\theta_m \right) \right]^{1/2} \approx n_m \left(1 + \frac{r_m}{R_b}\cos\theta_m \right), \tag{4.14}$$

where R_b is the bending radius, n_m is the refractive index of core m in the corresponding straight fiber and (r_m,θ_m) are the local polar coordinates of core m, as

shown in Fig. 4.24(a). Figure 4.24(b) illustrates the refractive index profile modification due to the fiber curvature. Black solid line and black dashed line correspond, respectively, to the straight refractive index and the bent refractive index modelled by Eq. (4.14). One can observe that the curvature produces a kind of inclination to the straight refractive index profile. This slope produces a different effect on the central core than on the outer cores, in the way that the outer cores (cores 5 and 2 in Fig. 4.24) are shifted in the vertical plane while the center one remains in the same location but with a certain tilt angle. This way, we can consider separating this effect in two parts: (1) the coarse variation, which only includes the vertical displacement of the outer cores (and then it has no effect on the central core), which is depicted in red-dotted line; and (2) the slow variation, which lies for the tilt angle that affects to all of the cores. Under the assumption of weak intercore crosstalk, we can simplify even more the modal analysis and treat each core in isolation, without loss of generality. Attempting to Fig. 4.24(b), one can realize that, in the outer cores, the coarse variation is much bigger than the slow variation when the cores are located in the curvature plane (i.e., orthogonally to the tangential plane). Since we are interested on evaluating the worst-case scenario, we can simplify the model to the red one shown in Fig. 4.24(b) and thus neglect the effect of the slow variation. This way, we can directly make use of the characteristic equation model derived in chapter 3 to solve the modal propagation of each core without the need of modifying the model as to include a more complex effect, such as the tilt angle on the refractive index profile produced due to the curvature, which, at the end of the day, will induce a negligible effect (in the worst-case scenario) as compared to the coarse variation.

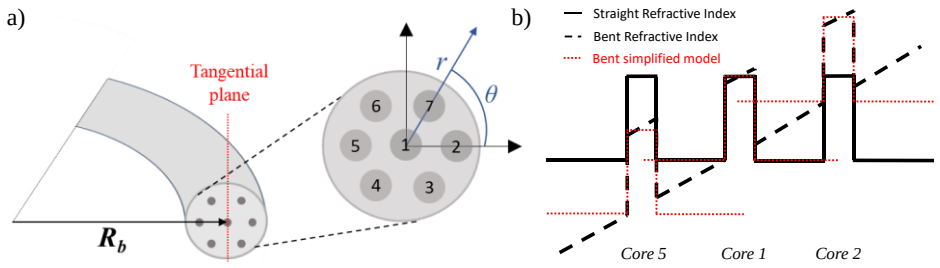

Fig. 4.24. (a) Multicore fiber curvature with a bending radius R_b and local polar coordinates (r,θ) indicated in the MCF cross section. (b) Effect of the fiber curvature on the refractive index profile of cores 1, 2 and 5 as compared to the straight condition.

Considering, then, the simplified model described above, Eq. (4.14) must be accordingly modified by assuming that the local coordinates (r_m,θ_m) are constant at each fiber mode, and they take the value of the central point of the core layer (i.e., the value of the origin of the new core local coordinates). Then, for a given core m, the propagation constant under bent condition (or equivalent propagation constant), $\beta_{eq,m}$, can be expressed as

$$\beta_{eq,m} = k_0 n_{eff_{eq,m}} = \sqrt{k_0^2 n_{eq,m}^2 - \frac{u_{eq}^2}{a_m^2}}, \tag{4.15}$$

where a_m is the core radius, k_0 is the wavenumber, $n_{eff\ eq,m}$ is the equivalent effective index and u_{eq} is the normalized transverse propagation constant of the bent core, $u_{eq} = k_0 a_m (n_{eq,m}^2 - n_{eff\ eq,m}^2)^{1/2}$. In the case the fiber core m has a classic step-index profile, we obtain the parameter u_{eq} by solving the well-known characteristic equation for step-index optical fibers, [92]. We can derive the equivalent group delay per unit length ($\tau_{eq,m}/L$) from Eq. (4.14) as

$$\frac{\tau_{eq,m}}{L} = \frac{d\beta_{eq,m}}{d\omega} = \frac{1}{c\beta_{eq,m}}\left[k_0 n_{eq,m}^2 - 2\pi n_{eq,m}\frac{dn_{eq,m}}{d\lambda} + \frac{2\pi}{a_m^2 k_0^2}u_{eq}\frac{du_{eq}}{d\lambda}\right], \tag{4.16}$$

where ω is the optical angular frequency and c the light velocity in vacuum. We must note that Eqs. (4.15) and (4.16) are valid for any circular refractive index profile distribution by using the proper characteristic equation to calculate the parameter u_{eq}, even considering multi-layer refractive profiles, as derived in chapter 3.

From Eq. (4.14), we see that the highest variation on the equivalent refractive index due to fiber curvatures occurs when the core forms an angle of $\theta = k\pi$, $k \in Z$, to the curvature plane. In addition, as Fig. 4.24(b) shows, the equivalent refractive index of cores located in the 2nd and 3rd section quadrants decreases with respect to the equivalent straight fiber, while those located in the 1st and 4th quadrants increase their refractive indices. In addition, Eqs. (4.15) and (4.16) show that this effect is also translated to the core phase propagation constant and the group delay. Actually, the phase propagation constant variation due to fiber curvatures has been widely studied in many works, [127, 110], but there is a lack of investigation on how curvatures affect to the group delay.

The effect of fiber twisting with a constant twist rate γ (rad/m) can be understood as a linear rotation of the fiber cross section along a given fiber length L; in other words, as a linear increment of the angle θ_m for a given core m. If we applied an ideal curvature with a fixed bending radius over the whole fiber length, the angle θ_m of each core m would be preserved. The differential group delay (DGD) between the outer cores and the central core would then accumulate linearly with the fiber length unless that core m is placed at an angle $\theta = \pi/2 + k\pi$, $k \in Z$ (where the core belongs to the curvature tangential plane and the DGD is cancelled out). We can denote the longitudinal evolution of the angular coordinate of core m in the cross-sectional area of the fiber as $\theta_m = \theta_{m,i} + \gamma z$, being z the longitudinal coordinate and $\theta_{m,i}$ the initial angular position (i.e., when $z = 0$). Thus, for a given core m, the DGD with respect to the corresponding straight condition τ_m is a function of z: $DGD(z) = \tau_{eq,m}(z) - \tau_m$. After a given propagation length L, the accumulated DGD is given by

$$\begin{aligned} DGD_{accumulated} &= \int_0^L DGD(z)dz \\ &= \frac{1}{c}\int_0^L \left[\begin{array}{l} \frac{1}{\beta_{eq,m}}\left(k_0 n_{eq,m}^2 - 2\pi n_{eq,m}\frac{dn_{eq,m}}{d\lambda} + \frac{2\pi}{a_m^2 k_0^2}u_{eq}\frac{du_{eq}}{d\lambda}\right) - \\ \frac{1}{\beta_m}\left(k_0 n_m^2 - 2\pi n_m\frac{dn_m}{d\lambda} + \frac{2\pi}{a_m^2 k_0^2}u\frac{du}{d\lambda}\right) \end{array}\right] dz \end{aligned}. \tag{4.17}$$

In order to find an analytical solution for the accumulated DGD, we can simplify Eq. (4.17) if we assume that the effective index follows the same equivalent distribution than the refractive index of Eq. (4.14), which is a consistent approximation under weakly guiding condition. Thus, we can approximate the equivalent effective index of core *m* as

$$n_{eff_{eq,m}} \approx n_{eff}\left(1+\frac{r_m}{R_b}\cos\theta_m\right). \tag{4.18}$$

Substituting Eq. (4.18) into Eq. (4.16), the equivalent group delay results

$$\tau_{eq,m} \approx \tau_m\left(1+\frac{r_m}{R_b}\cos\theta_m\right), \tag{4.19}$$

and, thus, the DGD with respect to the corresponding straight condition is given by

$$DGD(z) = \tau_{eq,m} - \tau_m = \frac{\tau_m r_m}{R_b}\cos\left(\theta_{m,i}+\gamma z\right), \tag{4.20}$$

leading to the following analytical expression for Eq. (4.17):

$$DGD_{accumulated} = \int_0^L DGD(z)dz = \frac{\tau_m r_m}{R_b\gamma}\sin\left(\theta_{m,i}+\gamma L\right). \tag{4.21}$$

For the worst case that gives the maximum value of DGD, i.e. $\theta_{m,i} = k\pi$, we have:

$$DGD_{Worst\ case,\ accumulated} = \frac{\tau_m r_m L}{R_b}\operatorname{sinc}\left(\gamma L\right)(-1)^k. \tag{4.22}$$

Figure 4.25 shows the computed worst-case accumulated DGD for a given core *m* (r_m = 35 μm and $\theta_{m,i}$ = 0) as a function of the total twist, γL (rad), for a fiber length L = 1 km under different bent conditions. Solid and dashed lines correspond, respectively, to the worst-case accumulated DGD simulated from Eq. (4.17) and to the simplified model of Eq. (4.22). Blue, green and orange lines correspond to a bending radius of 50, 75 and 150 mm, respectively. As shown, both models are in excellent agreement. We see that increasing the bending radius tends to decrease the DGD, as expected. We can observe that the DGD due to fiber curvatures has an important effect on the outer cores that cannot be disregarded, but it decreases rapidly as the twist is increased following a sinc shape, as Eq. (4.22) suggested. Thus, we can conclude that applying a forced twist helps to reduce the DGD between cores caused by fiber curvatures. Note that the bending radius of R_b = 75 mm is the typical radius of optical fiber spools, so that the green curve actually represents typical laboratory measurement conditions. We must also note that the same will happen to the small variations discarded in this simplified model but in a lower level effect, so that we can also conclude that inserting an intentional twist will mitigate the DGD between cores created by the small variation effect due to the fiber curvature.

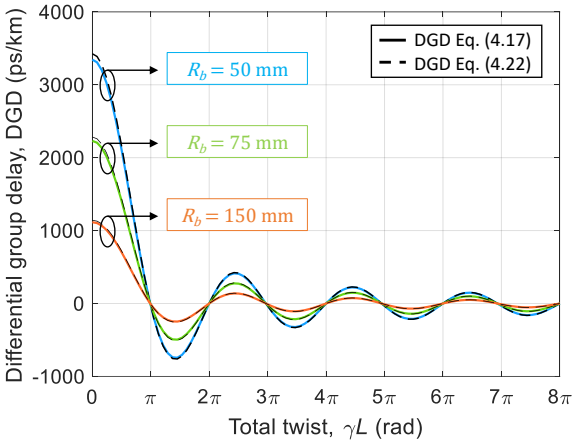

Fig. 4.25. Computed differential group delay (DGD) as a function of the total twist (rad) for a 1-km MCF link and different bending radii (R_b = 50, 75, 150 mm), comparing the results from Eqs. (4.17) and (4.22).

In the case of a FMF, the effect of the DGD is less critic than in a MCF. Since these fibers are composed of a single core, only the slow variations described in Fig. 4.24(b) will affect the fiber refractive index profile and thus the coarse variations are zero. This analysis is then analog to that of the central core of the MCF, which is negligible as compared to the coarse effect on the outer cores. We proved in the MCF case that this small variation effect is also compensated by the introduction of intentional fiber twists, so that the same will occur in the FMF case.

4.4.2.2. Experimental evaluation

We have experimentally evaluated both bending and twisting effects on the DGD of a commercial homogeneous 7-core fiber, provided by *Fibercore*. The fiber has step-index cores (core radius a = 4 µm and core-to-cladding relative index difference Δ = 0.31%) and a core pitch of 35 µm. Annex I summarizes the main characteristics of the fiber.

Figure 4.26 represents the experimental setup for the DGD measurement. We measured the DGDs between straight and bent fiber conditions over a small piece of fiber (L = 1 m). This way, we can carry out the straight fiber measurements and properly manage the applied twist while curving the fiber. Small bending radii of 25, 35 and 50 mm (below the typical fiber spool radius) are applied to force a representative variation in the core group delays when the fiber is bent. The fiber is locked with clamps at both ends: before fiber winding, a first clamp holds the fiber at one point, while the second clamp maintains the curvature and twisting conditions after winding.

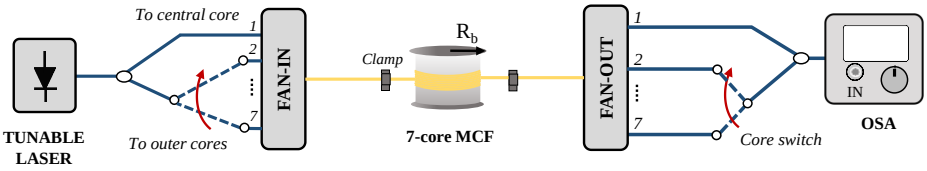

Fig. 4.26. Experimental setup to measure DGDs between the central and the outer cores.

We measured the DGD between cores by means of an optical interferometric based technique, [149]. As Fig. 4.26 shows, the optical signal coming from a tunable laser is injected into the central core (Core 1) and one of the outer cores (Cores 2-7) of the MCF. Prior to each measurement, we adjusted the optical paths for the central core to have a differential delay of around 20 ps greater than the outer cores to avoid zero-DGD situations in which the DGD measurement method is not accurate. At the fiber output, both signals are coupled together and injected into an Optical Spectrum Analyzer (OSA). Sweeping the optical wavelength of the laser reveals the interference pattern from which we measure the differential delay between both cores. Figure 4.27 illustrates a photograph of the experimental setup mounted in our laboratory, where we can observe the different cylinders we prepared to carry out the experiments. In order to keep identical conditions between the different experiments, we mounted the fan-in device in a movable solid platform to properly handle the straight and bent experiments. Every section of the interferometer was fixed with tape to avoid any undesired delay fluctuation which might not be produced by the curvature itself.

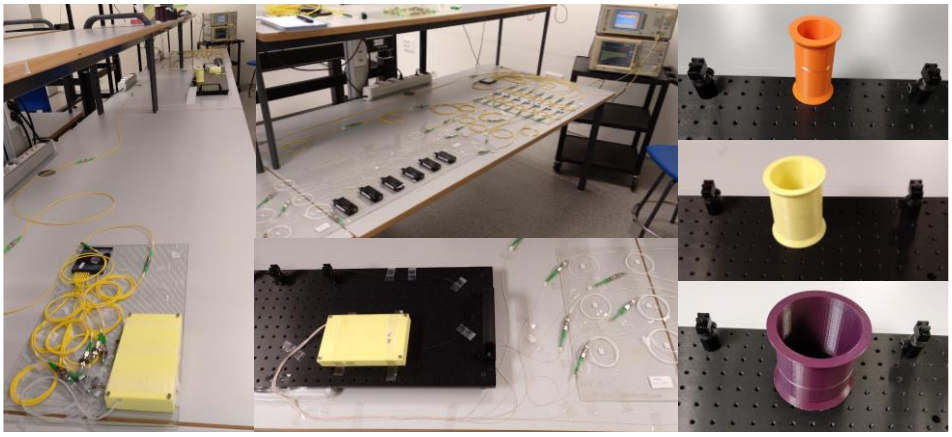

Fig. 4.27. Photograph of the experimental setup for measuring the DGDs between the central and the outer cores for different fiber curvature conditions. Left: Whole setup in straight condition. Middle: Zoomed area of the delay compensation stage and the fan-out device. Right: Fiber wound over the different cylinders with curvatures of 25-mm (orange), 35-mm (yellow) and 50-mm (purple) bending radius.

As an example, Fig. 4.28(a) represents the measured interference pattern between cores 1 and 2 when the fiber is bent at a 25-mm radius within a 10-nm optical wavelength range (from 1545 to 1555 nm). This pattern is then Fourier transformed

into the time domain to obtain the temporal representation of Fig. 4.28(b); the difference between these two peaks determines the DGD due to the curvature.

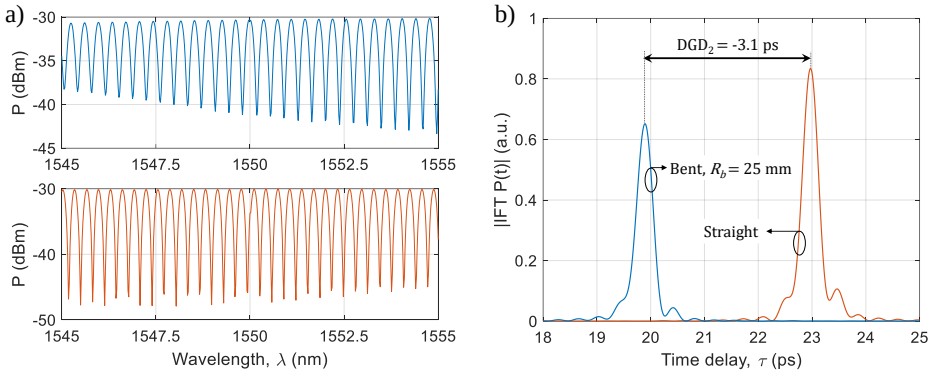

Fig. 4.28. (a) Interference pattern (optical power) measured by the OSA when the fiber is bent at a 25-mm radius (upper) and in straight condition (lower); and (b) temporal waveforms obtained from the inverse Fourier Transform of the interference patterns when the fiber is bent at a 25-mm radius (blue) and in straight condition (orange).

Table 4.7 gathers the measured DGD values between the outer and central cores for the three bending radii when two different conditions are applied: (a) the fiber is bent among the cylinder carefully trying not to induce any fiber twist; and (b) the fiber is bent while forcing an intentional twist. For the forced twist experiments, the fiber twisting was manually performed by introducing several intentional rotations distributed along the 1-m fiber while fiber winding. We can see, as expected, that the DGD is bigger as the bending radius is smaller, as well as how twisting the fiber produces an important reduction on the core DGDs. Slightly asymmetric behavior between the cores with opposite delay variation can be attributed to both fabrication mismatches on the core positions (radial, r_m, and angular, $\theta_{m,i}$) with respect to the ideal configuration and also to measurement tolerances.

Table 4.7. Normalized inter-core DGD (ps/m) values measured between different pairs of cores for different bending and twisting conditions

Cores	No twist			Intentional Twist		
	25 mm	35 mm	50 mm	25 mm	35 mm	50 mm
1-2	-3.1	-2.0	-2.7	-1.0	-0.8	-0.7
1-3	2.1	1.3	-0.4	-0.5	0.1	-0.3
1-4	4.8	3.5	2.3	0.7	0.9	0.2
1-5	2.2	1.9	2.4	1.0	0.1	0.0
1-6	-2.4	-1.6	-0.3	0.3	-0.4	0.3
1-7	-6.0	-4.1	-3.3	-1.2	-1.3	-1.1

Figure 4.29(a) depicts the core DGDs located inside the fiber cross-section for the representative case of R_b = 35 mm with and without twist. The position of the tangential plane has been estimated from the core DGD measurements gathered in Table 4.7. As shown, cores located at one side of the tangential plane have DGDs

with opposite signs than those located in the other side. Moreover, the DGD of those cores located in opposite radial positions (i.e., $\theta_{m,i}$ - $\theta_{n,i}$ = $k\pi$) have similar absolute value (ideally identical) but opposite signs. The worst-case DGD variation occurs when the core forms an angle of $\pm\pi/2$ with the tangential plane, but this case cannot actually be measured with precision since we do not have control over the curvature plane (which we assume random) during the measurement process. However, we can estimate the worst-case DGD from the measured values by doing a plane correction. For instance, in the case of the tangential planes of Fig. 4.29(a), we can apply the plane correction θ_c (in degrees) that satisfies:

$$\frac{DGD_2}{\cos(60-\theta_c)} = \frac{DGD_7}{\cos(\theta_c)}, \tag{4.23}$$

being DGD_2 and DGD_7 the differential group delays of cores 2 and 7, respectively. Once the angle of the plane correction θ_c is calculated, we can estimate the worst-case DGD as $DGD_{worst\text{-}case} = DGD_7/\cos(\theta_c)$. Following an analog procedure, we can estimate the worst-case DGD for each measured case. Figure 4.29(b) shows the estimated worst-case DGD from the measured values as compared to the theoretical curves obtained from Eqs. (4.17) and (4.22), (solid and dashed lines, respectively), when we fix the twist rate to 0 rad/m. We see that the measured worst-case DGDs in the absence of twist are well matched with the theoretical curves. On the other hand, we observe an important reduction on the worst-case DGD when an intentional twist is applied while bending the fiber, as expected.

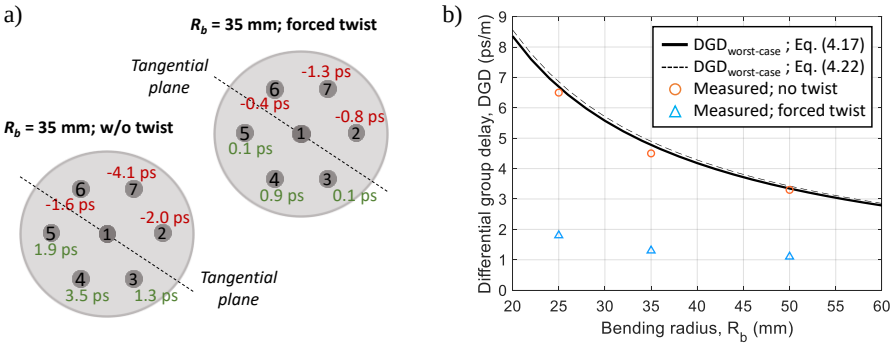

Fig. 4.29. (a) Measured core differential group delays between bent and unbent fiber for a bending radius of 35 mm with and without twist. (b) Differential group delay dependence on the bending radius: Solid and dashed lines correspond to the worst-case computed theoretical responses without twist, while circles and triangles represent the worst-case experimental values (red circles: no twist, blue triangles: forced twist).

4.4.2.3. Impact on microwave signal processing applications

Non-desired group delay variations between cores could affect applications where time-delay control and synchronization play a crucial role. This is the case, for instance, of fiber-distributed RF signal processing. We have experimentally evaluated how bending and twisting affect a delay-sensitive application such as Microwave Photonics signal filtering. We implemented a 7-tap finite impulse response filter with a Free Spectral Range of 10 GHz by adjusting the group delay

difference between adjacent filter samples (or basic differential delay) to $\Delta\tau$ = 100 ps. The filter frequency response was measured for two different fiber conditions: (1) bent without intentional twist and (2) bent with a forced twist, each one for three different bending radii: 25, 35 and 50 mm.

Figure 4.30 depicts the experimental setup implemented in our laboratory for measuring the filter electrical response. The optical carrier is generated by filtering the optical signal coming from a broadband source (BS) by a 0.2-nm bandwidth optical filter. The use of a BS makes the filter response incoherent, that is, insensitive to environmental changes such as temperature or vibrations. The optical signal is then modulated and split into all cores by means of a 1x8 coupler and the fan-in device. At the fiber output, SMF pigtails with 2-cm incremental lengths (approximately 100-ps delay) were added after the fan-out device, together with a series of variable delay lines (VDLs) to finely tune the sample incremental delays to 100 ps. To obtain a uniform amplitude distribution between the filter taps, we used Variable Optical Attenuators (VOAs). The output signals are combined and photodetected together to generate the electrical filtering response, which is measured by a Vector Network Analyzer (VNA).

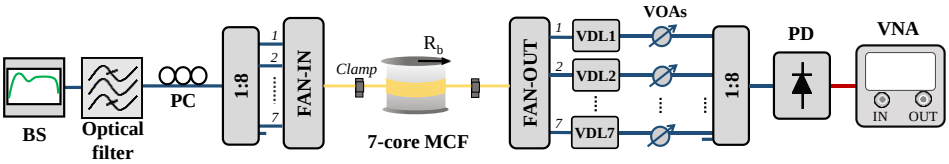

Fig. 4.30. Setup scheme for the experimental measure of MWP signal filtering response.

Figure 4.31 illustrates the measured filter transfer function as a function of the RF frequency for the different bending/twisting conditions stated before. Blue solid line corresponds to the experiment in which the fiber is wound around the cylinder with a forced regular twist, while red dashed line corresponds to the measurement when the fiber is bent trying not to produce any twist. In the absence of twist, we see that the filter response for the smallest bending radius (Fig. 4.31(a)) experiences distortions even in the first resonance. When the curvature radius is increased up to 35 mm (Fig. 4.31(b)), the distortions are less important but still present at high-frequency resonances. Finally, in the last case (Fig. 4.31(c)), distortions only appear importantly at the last resonance represented. In all cases, the filter response greatly improves when the intentional twist is applied due to the reduction in the DGDs between cores, as we have seen in section 4.4.2.2. This is particularly important for high-frequency resonances where bent-induced DGD deviations have greater effect on the RF response. These results show how applying a moderate twist to the fiber helps to reduce the DGD variations introduced by the fiber itself and, thus, improve the performance of the implemented signal processing functionality.

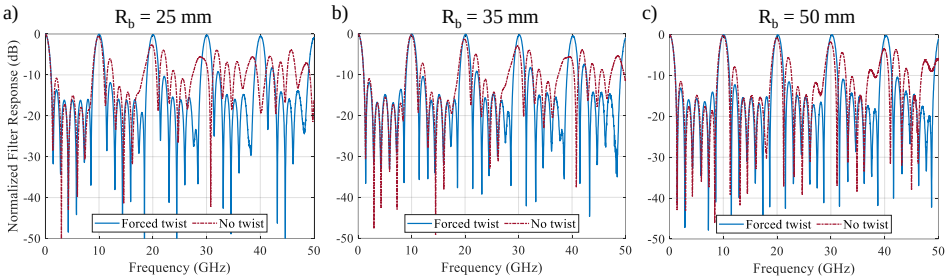

Fig. 4.31. Measured filter response for: (solid blue lines) fiber bent with high twist, (dash-dotted red lines) fiber bent with low twist; and different bending radius: a) 25 mm b) 35 mm c) 50 mm.

4.4.2.4. Final remark

In conclusion, we have proved that twist-induced perturbations will contribute to cancel the expected bend-induced variations on the group delay of the spatial modes of the fiber (either modes in a FMF or cores in a MCF). In the case of a FMF, fiber curvatures will be less critic than in a MCF and, even more, the lengths considered in the FMF cases could be 10 or 20 times shorter than in the MCF, with its associated reduction on this delay variability. We must note that our analysis has been performed by considering that the whole fiber link is coiled in the same spool, so we must take into account that in real scenarios the fiber will experience multiple random curvatures (different bending radii) and twists along its length. If we model these variations as a random variable with 0-mean value, what is coherent with the random nature of the twisting produced during the fiber deployment, we can assume that the expected value of these variations will tend to zero. Therefore, this effect will not reach the critical importance shown, for instance, in Fig. 4.25 in non-laboratory conditions (and, in any case, twist-induced perturbations will help to minimize this effect).

4.4.3. Influence of fabrication tolerances

Fabrication inaccuracies are one of the most critical aspects for our customized fiber designs in the sense that a slight mismatch on any of the refractive index profile parameters could perturb the propagation characteristics of the TTDL samples. Thus, it is necessary to determine how can we improve the robustness of our designs in terms of fabrication tolerances, and, if needed, readapt our designs to improve this robustness given the feedback from fiber providers.

First, we analysed the impact of fabrication mismatches on MCFs. The current manufacturing tolerances for the MCF technology are in the order of ±0.1 μm for the radial dimensions and around ±0.01% for the relative refractive index differences. We have numerically evaluated possible variations on the group delay and chromatic dispersion values of the MCF cores due to these fabrication imprecisions. In particular, we are interested on how rapidly those parameters vary for a slight fluctuation on the radial dimensions or refractive index of the cores; the smaller the variation, the higher the robustness against fabrication inaccuracies. As we saw in section 4.2.2, the trench width has almost negligible impact on both the group delay

and the chromatic dispersion, so we discard it for the analysis. Figure 4.32 shows the computed chromatic dispersion derivative with respect to (a) a_1, (b) Δ_1 and (c) a_2 for fixed values of the remaining design parameters. In each case, we simulated the derivative of the chromatic dispersion and the group delay per increment of each parameter fabrication tolerances. As we see, the core radius is the parameter that has more impact on the chromatic dispersion; the lower the core radius, the higher the variation. And, in the case of the group delay, the core-to-cladding relative index difference has the highest impact, followed by the core radius. In the case of the core radius, we see again that lower core radius leads to higher group delay variabilities, while the effect of the core-to-cladding relative index difference provides almost a constant variation over its entire range. The core-to-trench distance provides moderate variabilities in both parameters.

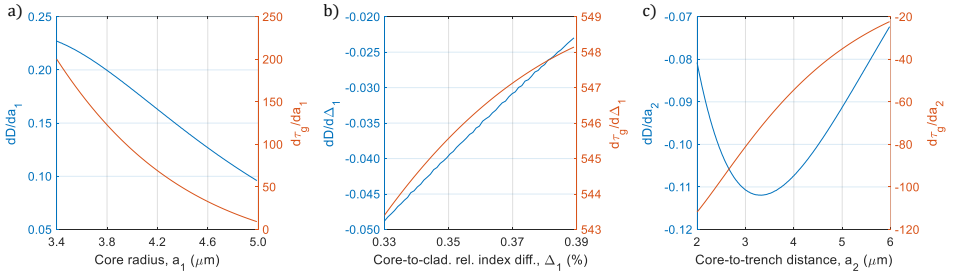

Figure 4.32. Chromatic dispersion (blue) and group delay (orange) derivatives with respect to (a) the core radius, (b) the core-to-cladding relative index difference and (c) the core-to-trench distance for fixed values of the remaining design parameters.

We then evaluated possible variations in the group delay and chromatic dispersion of the MCF cores due to expected fabrication tolerances. For simplicity, we consider only the radial variations on the different fiber core layers as to model possible fabrication errors without modifying the refractive indices; that is, we increase or decrease the radial dimensions without deforming its refractive index shape (keeping it as an ideal step-index form). This model allows us to simplify our analysis by letting the refractive indices untouched, but the effect of varying the radial dimensions without smoothing the layer interfaces (what occurs in real situations) provokes higher variations on the core propagation properties than if those radial dimensions are followed by smoother interfaces. Thus, we set a random perturbation with uniform distribution between ±0.1 μm for each core radius to diminish the mentioned overstated conditions when the refractive indices are left unvaried. Since this effect will be similar in both MCF designs, we focus our analysis, for example, on the higher-order-dispersion optimized design. Figure 4.33(a) represents the computed core group delays as a function of the optical wavelength when these fabrication tolerances are considered. We see that the performance of the delay line is degraded mostly due to the mismatches of the group delays at the anchor wavelength. We can observe, however, that the group delays slopes (i.e., the chromatic dispersions) almost maintain the same value. The group delay degradation can, then, be avoided by properly compensating the variation of the core group delays at the anchor wavelength via external delay lines. The chromatic dispersion variation is less critical to fabrication tolerances, and its robustness could be furtherly improved

if we enlarge the incremental dispersion ΔD between cores. Figure 4.33(b) shows the computed core group delays as a function of the optical wavelength when we compensate the fabrication error on the group delays. We must note as well that the required group delay compensation would also induce a minor variation on the core chromatic dispersion that we can considered negligible. For instance, the effect of adding a meter of SMF at the output of a certain core introduces around 5 ns to the group delay but below $2 \cdot 10^{-2}$ ps/nm to the $D \cdot L$ term (considering a group index of 1.5 and a chromatic dispersion below 20 ps/km/nm). Comparing this response with Fig. 4.13(a), we can see that we can mostly overcome the effect of the fabrication tolerances by externally compensating the errors on the group delay at the anchor wavelength.

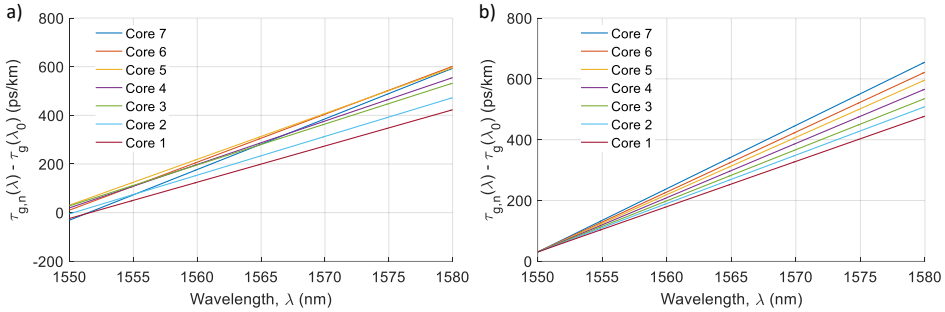

Figure 4.33. Computed core group delays versus optical wavelength when a random perturbation with uniform distribution between ±0.1 μm is applied to the radial dimensions of the cores to emulate possible mismatches due to fabrication tolerances. (a) Without delay compensation; (b) with delay compensation at the anchor wavelength.

In summary, we have seen that fabrication inaccuracies highly affect the group delay of the fiber cores. However, this variation can be externally compensated without harming the TTDL performance of the MCF. Regarding chromatic dispersion, we showed that cores with smaller radius are more susceptible to be affected by fabrication, and this effect cannot be compensated a posteriori. A robust-to-fabrication core design should then have a larger core radius if possible. Nevertheless, it is worth mentioning that the abovementioned manufacturing imprecisions can be further alleviated by executing several fabrication rounds; that is, after properly optimizing the fabrication process and readapting our initial design given the feedback received from the fabrication itself.

In contrast, in the case of the FMF-based TTDL we must note that, up to a certain degree, this approach is robust against possible fiber fabrication deviations. Once the fiber is fabricated and its propagation characteristics are known (i.e., modal differential group delays and chromatic dispersions), we can modify the LPG positions to balance out possible group delay and chromatic dispersion mismatches between experimental and theoretical values.

4.4.4. Other possible degradation sources

We must consider as well the effect of possible nonlinear interactions in both MCF and FMF based delay lines, such as the Kerr effect, [150]. Nonlinear effects in optical

fibers depend on the transmission length and the effective cross-sectional area of the fiber $A_{eff,}$ [151]. Nonlinearity grows with the optical power intensity in the fiber. For a given optical power, the intensity is inversely proportional to the effective area. Therefore, and in combination with the TTDL and crosstalk requirements already discussed, we aim for effectives areas as large as possible in both MCFs and FMFs.

In the case of the MCF, from both Table 4.2 and Table 4.3, we see, as expected, that the effective area increases with the core radius. Actually, the effective areas are gathered around two values: 60 μm^2 for groups of cores 1 and 2, and 80 μm^2 for group 3. Note here that the typical value for a SMF is 80 μm^2. Since the fiber-wireless application scenarios that we consider require link lengths usually below 20 km and low levels of optical power at the input of each core (below 0 dBm), we can discard the existence of nonlinear optical effects for those values of effective areas. In the case of FMFs, this effect is even less important: the mode effective areas are higher and the fiber lengths are smaller (below 1 km) than in the MCF case, with similar optical power levels. So, we expect the nonlinear optical effects to be also negligible in the FMF approach.

One important degradation source that we were not able to evaluate in this Thesis – and thus it is left for future research – is the effect of temperature variations on the sample group delays. In the case of the MCF, the fact that each core has a different material composition might lead to different temperature-dependent propagation properties. It is necessary to evaluate how different are the temperature behaviors of the core group delays to determine the possible detrimental effects produced in the TTDL performance. In general, we expect higher sensitivity on the group delay than in the chromatic dispersion, as we have observed in the different degradation effects evaluated along this section (manufacturing errors, curvatures and twisting). If perturbations induced on the core group delays due to temperature are excessively high, we should proceed to isolate the fiber (if possible) or find a dynamic solution to readapt the group delays at the anchor wavelength, in a similar way than in the group delay mismatching compensation due to fabrication tolerances (but, in this case, adaptive). In the case of the FMF approach, the temperature variations may play a greater role, since the LPGs act in addition as temperature sensors that may change their Bragg wavelength slightly as the temperature varies. Thus, we will certainly need to isolate each one of the LPGs as to preserve the performance of the TTDL.

4.5. Conclusions

In this chapter, we have proposed, for the first time to our knowledge, novel approaches for the design of sampled TTDLs for radiofrequency signals built upon a single SDM optical fiber link (using either a heterogeneous MCF or a FMF). They offer unique 2D and reconfigurable true time delay operation by exploiting both spatial- and wavelength-diversity domains. The fabrication and characterization of the proposed TTDLs will be described in chapter 5.

For the MCF-based TTDLs, 7-sample operation has been developed on a heterogeneous trench-assisted 7-core fiber link, where each core features an independent group delay. By suitable modifications of the material composition and

the radial dimensions of each core trench-assisted step-index profile, we obtained a particular set of cores that satisfy a common group delay with linearly incremental chromatic dispersions at an anchor wavelength λ_0. We found an important trade-off between optimizing the TTDL in terms of intercore crosstalk and optimizing it in terms of higher-order dispersion. We designed and compared a higher-order-dispersion optimized design with a crosstalk-optimized design, where we observe the importance of a proper management of the dispersion slope of the cores for broadband operation. We analyzed the influence of the trench-assisted refractive index profile on the group index, chromatic dispersion and dispersion slope of a multicore fiber. As far as we know, this analysis is the first one carried out for trench-assisted core configurations and provides a useful tool for the design of both homogeneous and heterogeneous MCFs, not only in the context of MWP signal processing, but also in other applications fields such as minimization of the optical pulse broadening in high-speed broadband fiber communications (including spatial division multiplexing transmission), fiber-distributed sensing or chromatic dispersion compensation. All these applications will benefit from the extension of the operation optical wavelength range in terms of group delay nonlinearities, especially in WDM schemes with a high number of transmission channels. In the particular scenario of microwave signal processing for fiber-wireless networks, this optimization is essential for the implementation of true time delay lines that can operate in a broad optical wavelength range, giving support to different functionalities in the same single optical fiber. As a proof of concept, we have compared both TTDL designs when they are applied to reconfigurable microwave signal filtering and radio beam-steering for phased array antennas, showing the importance of properly managing the higher-order dispersion for broadband operation.

In the case of the FMF solution, we propose to achieve the required control over both the group delay and the chromatic dispersion of the signal samples by the custom design of a ring-core step-index FMF where the inscription of a series of LPGs allows to excite higher-order modes at specific longitudinal locations along the fiber. In particular, we have designed a 4-sample TTDL approach that combines the design of a 7-LP-mode ring-core fiber and the inscription of 5 LPGs. This scheme requires to inject only the LP_{02} and LP_{21} modes into the fiber input while the 4 TTDL samples are given by the signals recovered from the LP_{21}, LP_{12}, LP_{31} and LP_{41} modes at the fiber output. We have evaluated the performance of the designed tunable TTDL when it is applied to reconfigurable microwave signal filtering and radio beam-steering in phased array antennas. While in the heterogeneous MCF-based approach we can improve the wavelength operability range of the TTDL up to a hundred of nanometers by properly tailoring the higher order dispersion parameter, in the FMF solution this range will be limited by the spectral width of the inscribed broadband LPGs, that could reach up to a 20-nm wavelength operability range. In both the FMF and the MCF solutions, a particular potential field of application can be found in fiber-wireless radio access networks where different functionalities can be implemented while transmitting the signal, for instance, between a central office and a given remote antenna.

Finally, we have studied the main degradation sources that can affect the performance of the designed TTDLs and propose possible solutions to overcome them. We found that while the MCF approach is more resistant to the crosstalk between spatial channels, the FMF solution presents an important advantage in terms of robustness against fabrication tolerances and could compensate those errors a posteriori by relocating the position of the LPGs. One of the most important sources of degradation that could compromise the performance of time-delay sensitive applications relates to possible bending and twisting effects. We have theoretically and experimentally evaluated how fiber bending and twisting induce group delay variations between cores in a MCF. We have obtained analytical expressions for the computation of the bend-induced DGD accumulated on a given fiber length for a constant twist rate, which have been experimentally verified. Although the analysis of the effect of fiber curvatures showed an important variability on the sample group delays that could deteriorate the performance of the TTDL (especially in the MCF case), we concluded that twists that will take place in a real deployment will compensate this detrimental effect. These findings are generally applicable to time-delay sensitive application areas such as radio-over-fiber distribution and MWP signal processing in fiber-wireless access networks, as well as high-capacity digital communications where digital MIMO processing may be required.

Chapter 5

True time delay lines: Design, fabrication and characterization

5.1. Introduction

The actual implementation of the TTDL proposals presented in the previous chapter requires the fabrication of customized optical fibers that behave with particular propagation characteristics. However, we must keep in mind that current fabrication tolerances can considerably impair the proper performance of these devices. In this chapter, we adapt our previous design strategy to experimentally implement preliminary TTDLs built upon both multicore and few-mode fibers. In the case of the multicore fiber approach, we focused on robust-to-fabrication-tolerances designs that renounce certain design requirements with the aim of reducing the effect of probable fabrication variabilities. In the few-mode fiber technology, we aim at demonstrating the proper mode conversion by means of LPGs to manipulate the sample delays as desired. In this regard, we use a commercial FMF instead of looking for a particular custom fiber design, which would considerably increase the costs and the difficulty of the LPG inscription.

Part of the work carried out in this chapter was the result of several collaborations. First, we fabricate an MCF in collaboration with CREOL, the College of Optics and Photonics (in the University of Central Florida, Florida, USA) during my 3-month research stay. And, second, the LPG inscription for the FMF approach was carried out in collaboration with the grating inscription research line (leaded by Prof. Salvador Sales), which is part of our research group (the PRL) at iTEAM Research Institute.

5.2. Multicore fibers

5.2.1. Introduction

Fabrication technologies of MCF fiber links and devices have been extensively researched and developed in the last decade reducing, in general, their manufacturing cost and tolerances as compared to initial MCF approaches [70]. However, customized heterogeneous MCFs still demand improved fabrication procedures. First, because current MCF fabrication tolerances are still excessively coarse as to yield sufficiently small fabrication variabilities on parameters such as the group delay or chromatic dispersion. In order to minimize the fabrication tolerances, several design-fabrication-characterization rounds may be required, where both design and fabrication can be properly readapted if required given the feedback received from the fabrication itself. And, second, because heterogeneous core structures (especially if different preforms are required) involve higher costs than homogeneous ones. As a rough estimation, the fabrication of a customized heterogeneous MCF can vary from a few thousands of euros up to tens or hundreds of thousands of euros, depending on several factors such as the number of cores, the number of different preforms or the fiber length.

We have designed and fabricated two different dispersion-engineered heterogeneous MCFs with a hexagonal 7-core configuration. The first fiber was fabricated by the Chinese company YOFC (https://en.yofc.com). We designed each core independently, following the design procedure described in chapter 4, so that each core is built from an independent preform. In the second fiber, however, we tried to reduce costs by using a single preform to draw all the cores instead of using a different preform per core. This fiber was fabricated in collaboration with the research center *CREOL, the College of Optics and Photonics* (University of Central Florida, FL, USA), (https://www.creol.ucf.edu/), during my 3-month research stay. In comparison with the first fiber, it has an important advantage in terms of cost-saving at the expense of slightly worsening the TTDL performance and crosstalk.

For the preliminary MCF designs, it is essential to ensure a certain robustness against possible fabrication inaccuracies in order to guarantee a proper performance of ensuing proof-of-concept testing applications while acquiring key information to improve future fabrication processes. In addition, our goal is to guarantee the maximum number of samples available in the MCF. That is, the cores more sensitive to fabrication errors must provide consecutive samples in a way that the most vulnerable core is located at one of the end-points of the TTDL (first or last sample), followed by the next most sensitive core, etc. This way, we can assure with a certain probability that if some cores are affected by fabrication errors, we will maximize the number of available consecutive samples.

5.2.2. YOFC Fiber

5.2.2.1. Design

The first MCF (from now, *YOFC fiber*) was designed by following the design strategy presented in the previous chapter: each core refractive index profile was tailored

independently to fulfill a set of specific rules. It comprises 7 trench-assisted cores with a core pitch Λ = 40 μm inside a 150-μm-diameter cladding. The core refractive index profiles consist of a GeO_2-doped core layer (core radius a_1 and core-to-cladding relative index difference Δ_1) surrounded by a pure silica inner cladding (core-to-trench distance a_2) and a 1%-Fluorine-doped trench (trench width w).

In chapter 4, we saw there that there are essentially four basic parameters that govern the modal propagation along a MCF that have to be properly managed for optimum TTDL operation with low intercore crosstalk: τ_g, D, n_{eff} and S. However, the addition of a new design condition –the robustness against fabrication tolerances– to the existing ones –TTDL operation and crosstalk– requires prioritizing some of these design parameters among the others. In first place, τ_g and D are essential parameters that must be fulfilled to ensure tunable delay line operation. One the other hand, the effective index optimization minimizes the intercore crosstalk, while the S optimization increases the wavelength operability range. For a proof-of-concept design, it is preferable to ensure TTDL operation on a certain wavelength range without distortion, so that we decided to make the restrictions on S more flexible to ensure the better accomplishment of the other parameters.

We designed the MCF by means of the numerical software *Fimmwave*. First, attending to crosstalk optimization, we know that a 7-core fiber requires at least 3 groups of cores –each group containing a set of cores with similar effective indices– to ensure that each core is surrounded by cores with sufficiently different effective indices. The larger the effective index difference between cores of dissimilar groups, the better the crosstalk performance. In order to maximize the effective index difference between core groups, one of the groups (let's say, group #1) must be composed of cores having high effective indices (tending to the core refractive index value), another one (group #2) of cores with low effective indices (near the cladding refractive index) and the last group (group #3) of cores having intermediate effective index values (i.e., near the midpoint between the core and cladding refractive indices). It is clear that cores inside group #2 are low confined and thus we saw that they are more probable to be affected by fabrication inaccuracies, so we choose a single core (i.e., the central core) to form this group.

In second place, we must distribute the chromatic dispersion values attending also to fabrication robustness conditions. The selection of the central core to be low-confined (one of the cores most prone to fabrication errors) implies that it should provide one of the firsts or lasts samples (lowest or highest chromatic dispersions). On the other hand, we saw in the previous chapter that low chromatic dispersion values require low core radii while, at the same time, cores with lower core radii are highly sensitive to fabrication tolerances. From both the above observations, we conclude that the central core must experience one of the lowest chromatic dispersions to adequately set the most probable affected cores as consecutive samples. To avoid affecting to much its dispersion slope (see Fig. 4.12), we finally designated it as the second sample (i.e., with the second lowest chromatic dispersion).

Taking into account the above-mentioned considerations, we designed the fiber as to minimize the effect of fabrication errors on the TTDL performance. By properly

tailoring the core design parameters a_1, a_2, w and Δ_1, we were able to set a common group delay (or group index, n_g) to all cores at an anchor wavelength λ_0 = 1530 nm and a range of chromatic dispersion D_n values from 14.3 up to 20.3 ps/km/nm with a 1-ps/km/nm incremental dispersion at λ_0, respectively for cores 1 up to 7. The core distribution inside the cross-sectional area of the MCF was set to minimize the intercore crosstalk: group #1 is formed by core 2; group #2 by cores 1, 3 and 4; and group #3 by cores 5 up to 7. The minimum effective index difference between adjacent cores is $7 \cdot 10^{-4}$, leading to a threshold bending radius of 80 mm. Table 5.1 gathers the core design parameters.

Table 5.1. Core design parameters and properties for the YOFC fiber design at λ_0 = 1530 nm

Core *n*	Core design parameters				Core Properties			
	a_1 (μm)	Δ_1 (%)	a_2 (μm)	w (μm)	n_g	D (ps/km/nm)	n_{eff}	S (ps/(km·nm^2))
1	3.3	0.335	5.8	3.2	1.4671000	14.3	1.4455	0.066
2	3.2	0.300	2.4	4.1	1.4671000	15.3	1.4448	0.047
3	3.5	0.315	4.5	4.0	1.4671000	16.3	1.4455	0.065
4	3.7	0.301	3.7	3.6	1.4671000	17.3	1.4455	0.062
5	4.8	0.293	5.8	3.0	1.4671000	18.3	1.4463	0.064
6	5.0	0.287	4.6	6.0	1.4671000	19.3	1.4463	0.065
7	5.3	0.279	3.3	6.0	1.4671000	20.3	1.4463	0.065

From Table 5.1, we observe that, while the dispersion slope variability between any pair of cores (excluding core #2) is below 0.004 ps/km/nm^2, the dispersion slope of the central core (core #2) was significantly dissimilar due to the robustness against fabrication tolerances requirement, reaching a maximum difference of 0.019 ps/km/nm^2 with the others. By using Eq. (4.3), we can estimate the wavelength operability range of the TTDL in which the spatial-diversity group delay relative error remains below a 10%. Figures 5.1(a) and (b) show the computed core group delays and differential group delay contributions due to the nonlinear dispersion effect, respectively, as a function of the optical wavelength. As we can see, cores 3-7 present a group delay relative error below 5% up to a 30-nm range, while the wavelength operability range for core 2 is limited to 10 nm. For proof-of-concept demonstrations, this range is large enough for the implementation of a wide range of MWP applications operating in the μ-wave and mm-wave bands with only a few-km-long MCF. For instance, the spatial-diversity differential delay can be tuned up to 10 ps/km without excessive degradation due to the nonlinear dispersion, allowing applications operating above 100 GHz·km. And, in addition, 5-sample operation using cores 3-7 can also be implemented for MWP applications working at lower RF frequencies (~33 GHz·km at λ = 1560 nm). All this keeping in mind that the first 2 samples, which are the ones limiting the wavelength operability range, are also the one more prone to fabrication inaccuracies.

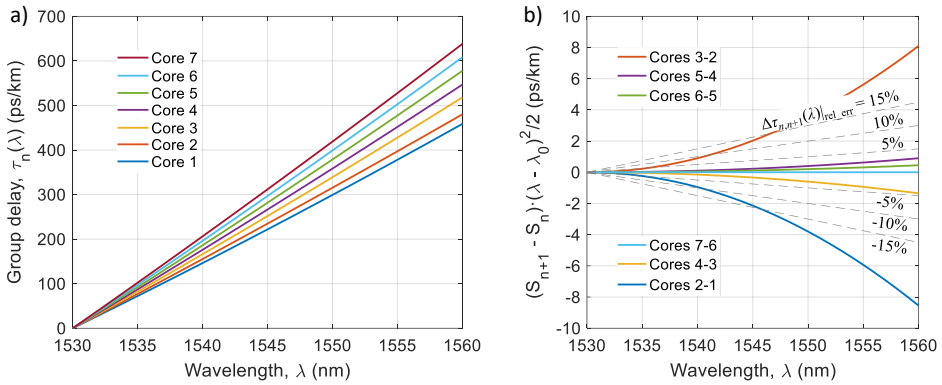

Fig. 5.1. (a) Computed core group delays as a function of the optical wavelength for the YOFC fiber; (b) Computed differential group delay contribution due to the nonlinear dispersion effect as a function of the optical wavelength for the YOFC fiber.

5.2.2.2. Fabrication

The fabrication of the MCF was carried out by the Chinese company YOFC. The fiber has a length of 5038 meters and is coiled in a 150-mm-diameter spool. The MCF cladding diameter is 147.54 µm and the average core pitch is 40.99 µm. A couple of fan-in/fan-out devices are spliced at both fiber ends to inject/extract the light to/from the cores. Figure 5.2 shows a photograph of the MCF, where each core can be distinguished by its particular radial dimensions according to Table 5.1 parameters. A couple of markers were made to ease the identification of the cores. The measured core-to-core distances or pitches are annexed at the right part of Fig. 5.2.

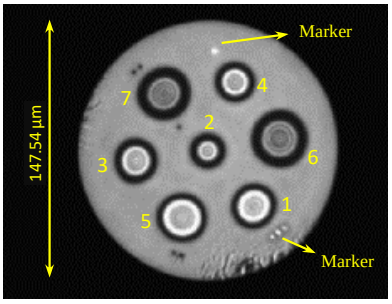

Measured core pitches

Cores	1-2	1-3	1-4	1-5	1-6	1-7
Λ (µm)	40.45	40.81	40.93	42.00	41.30	40.46
Cores	2-3	3-4	4-5	5-6	6-7	7-2
Λ (µm)	41.31	41.22	40.67	41.04	40.61	41.10

Fig. 5.2. (Left) Photograph of the fabricated MCF. (Right) Measured core pitches, provided by YOFC.

Seven different preforms were required to fabricate this MCF. Each preform constitutes an individual core and was created according to the core design parameters by properly scaling the radial dimensions and matching the refractive indices. Figure 5.3 shows the measured refractive index profile of the seven preforms, provided by the company. The insets correspond to the *scanning electron microscope* (SEM) images of the fabricated cores.

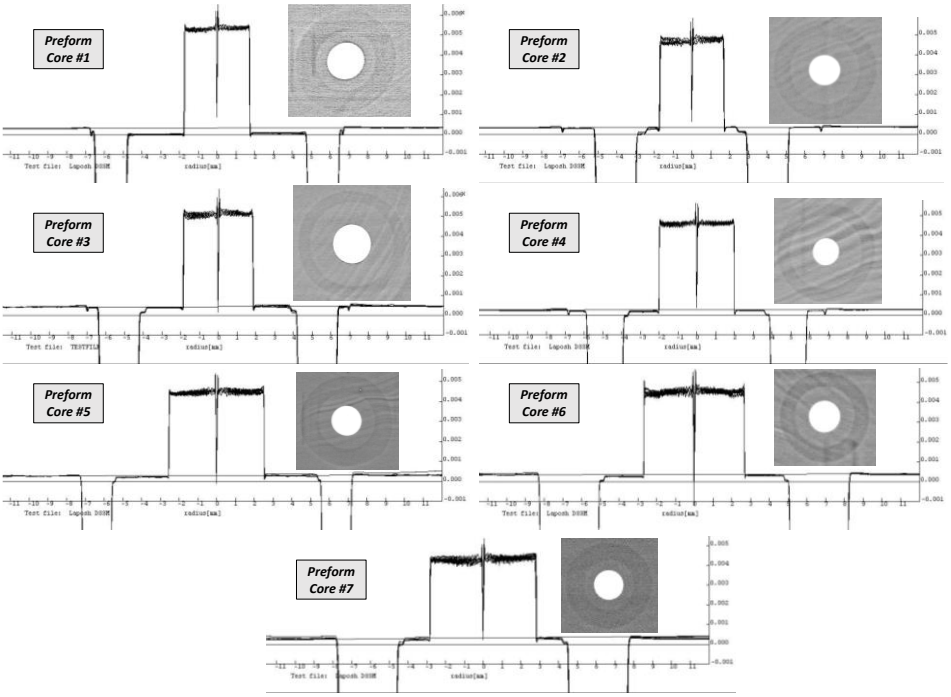

Fig. 5.3. Refractive index profile measurements of the preforms of the seven cores for the YOFC fiber. Insets: SEM images of the fabricated cores.

With the help of the preform refractive index profile measurements, we can obtain a first estimation of the radial proportionalities and the refractive indices. Table 5.2 compares the relations of the core-to-cladding distance and trench width with respect to the core radius, together with the core refractive indices, between the designed cores and the measured preforms. As shown, all the preforms seem to be a priori in accordance to our design, with slight mismatches that can be attributed either to fabrication mismatches or measurement inaccuracies.

Table 5.2. Comparison between designed and measured parameters for the YOFC fiber at λ = 633 nm.

Core n	Designed			Measured		
	a_2/a_1	w/a_1	n_1	a_2/a_1	w/a_1	n_1
1	1.758	0.970	1.46194	1.762	0.972	1.46234
2	0.750	1.281	1.46142	0.742	1.265	1.46173
3	1.286	1.143	1.46165	1.282	1.141	1.46213
4	1.000	0.973	1.46144	0.975	0.976	1.46162
5	1.208	0.625	1.46132	1.211	0.623	1.46152
6	0.920	1.200	1.46123	0.903	1.175	1.46158
7	0.623	1.132	1.46111	0.617	1.121	1.46133

5.2.2.3. Characterization

Once the fiber was fabricated, we measured the power losses and power coupling between cores after the 5-km propagation. Table 5.3 contains the measured intercore crosstalk and insertion losses at the anchor wavelength λ_0 = 1530 nm. Positive values represent the insertion losses and negative values the intercore crosstalk. Symbol "/" indicates that the measured crosstalk was below the sensitivity of the power meter. These values include the 5-km propagation link, the fan-in/fan-out devices and the splices between the MCF and the fan-in/fan-out devices. The average insertion losses are 5.8 dB and the worst-case intercore crosstalk is below -33 dB.

Table 5.3. Measured insertion losses and intercore crosstalk (in dB) for the YOFC fiber at λ_0 = 1530 nm.

Core *n* In\out	1	2	3	4	5	6	7
1	5.8	-34	-47	-47	-44	-37	/
2	-33	6.7	-34	-39	-43	-40	-48
3	-48	-33	5.5	-40	-37	-47	-34
4	-43	-34	-34	6.0	-45	-37	-33
5	-40	-38	-39	-46	5.8	-44	-46
6	-40	-40	-45	-39	-43	5.5	-47
7	/	-43	-31	-36	-41	-49	5.5

We then characterized the performance of the fabricated MCF in terms of TTDL operability. First, we need to compensate the group delay mismatches at the anchor wavelength λ_0 = 1530 nm. We measured the differential group delay between cores by means of an optical interferometric based technique (analogously as in section 4.4.2.2). Figure 5.4 depicts the experimental setup used for the time-delay measurements. The optical signal generated by a tunable laser is coupled into two of the MCF cores (core #1 was used as the reference arm and the others were used to interfere, one by one, with it). After the 5-km propagation, the signals pass throw VDLs prior to be coupled together and injected into the OSA. The interference pattern is obtained by slightly sweeping the operation wavelength of the tunable laser.

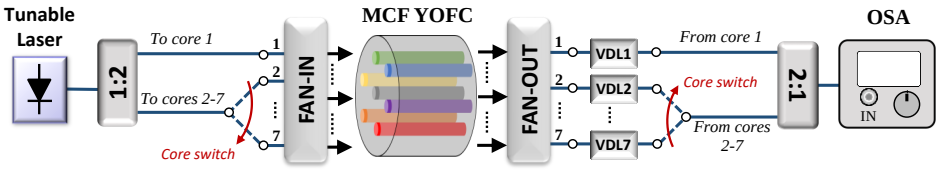

Fig. 5.4. Experimental setup for the differential group delay measurement.

As a first step, we compensated the differential delays between the two paths formed by the optical couplers and VDLs in order to isolate the effect due to the MCF itself. The purpose of the VDLs is to finely equalize the time delays of the two paths when the MCF is not inserted in-between the two couplers. After the equalization, we inserted the MCF and measured the core differential group delays. To avoid cutting and splicing the fan-in/fan-out devices, the core differential group delays

measurements include both fabrication fluctuations of the MCF and possible length mismatches between the paths of the fan-in/fan-out devices. The measured differential delays between cores ranged from hundreds of ps up to a couple of ns. Since our VDLs can only compensate delays up to 250 ps, we used an additional coarse delay compensation stage formed by SMF pigtails with different lengths (below 1 meter). Note that, as a rough estimation, the group delay of a SMF can be approximated as 50 ps/cm.

In second place, we measured the chromatic dispersion of the cores at λ_0 by evaluating the carrier suppression effect (CSE) that affects the RF response of the 5-km link, [152]. It is worth noting here that the additional lengths added by the pigtails, couplers or the VDLs induce a negligible effect on the overall chromatic dispersion. Figure 5.5(a) shows the scheme of the CSE measurement setup. Here, a laser is modulated in double side band and injected into one core. At the fiber output, the signal is photodetected and injected into the VNA. Figure 5.5(b) depicts the received RF power as a function of the modulation frequency for each core at the anchor wavelength. The estimated chromatic dispersion values are 14.4, 15.2, 16.6, 17.6, 18.6, 19.6 and 20.6 ps/km/nm, respectively for cores 1 up to 7. We see that cores 3-7 preserve the 1-ps/km/nm incremental dispersion values, while cores 1 and 2 diverge from the rest. These two cores have been more affected by fabrication inaccuracies.

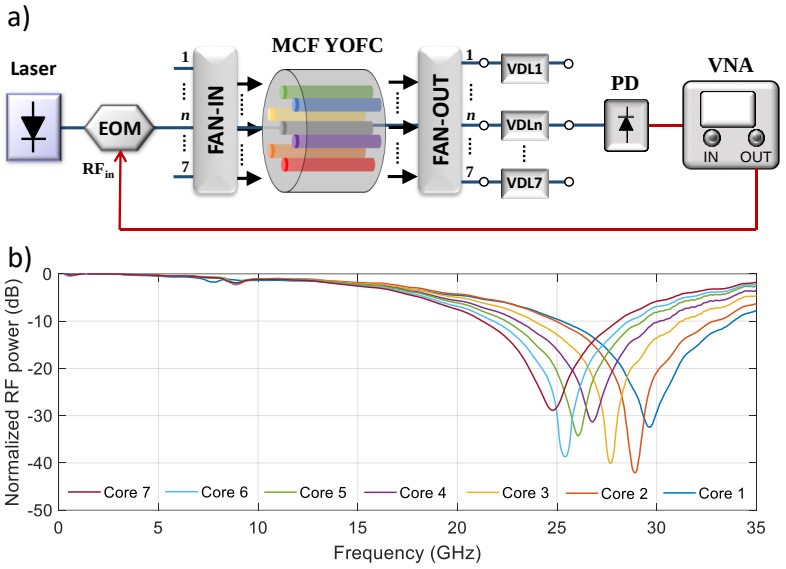

Fig. 5.5. (a) Experimental setup for the chromatic dispersion measurement via the carrier suppression effect. (b) Measured carrier suppression effect in the RF response for each core at λ = 1530 nm.

Finally, we measured the differential group delays between cores for different optical wavelengths ranging from 1535 up to 1560 nm. Figure 5.6 shows the measured differential delays between core 7 and the remaining cores. Circle markers represent the experimental values, while solid lines correspond to the computed differential delays for the designed MCF. We see that the measured differential delays of core 3

to 7 are well-matched with the designed values up to a 30-nm wavelength range, while cores 1 and 2 do not agree with the design. Although these two cores cannot operate as the first 2 TTDL samples when we exploit the spatial diversity of the MCF, they can however be devoted to distribute 2 additional signal channels or to implement other applications that do not require space-diversity signal processing. All in all, TTDL operation by using wavelength diversity can be implemented anyway with all seven cores.

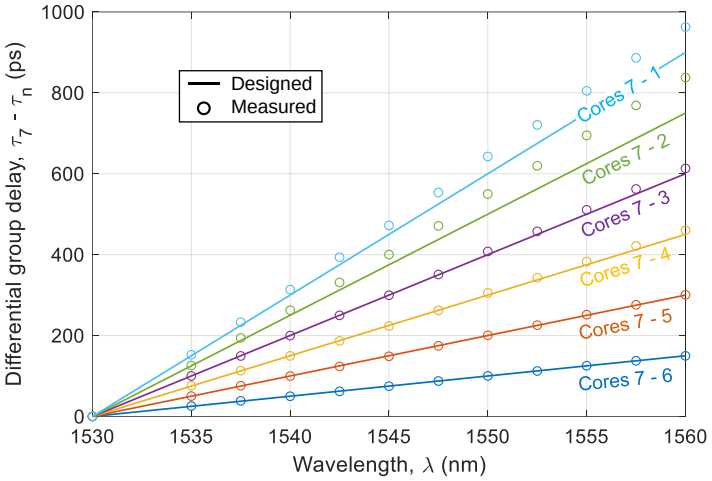

Fig. 5.6. Measured differential group delays for all the cores with respect to core #7 for the YOFC fiber.

The fabricated MCF-based TTDL can operate in both the spatial and optical wavelength diversity domains, what translates into different delay line possibilities within the same fiber link. For the spatial diversity regime, we can implement a 5-sample TTDL by using cores 3-7, since they preserve similar differential group delays. The linear evolution of these 5 core differential delays between 1530 and 1560 nm allows continuous basic differential delay tuning between 0 and 150 ps. On the other hand, all 7 cores are applicable to work in the wavelength diversity regime.

The main reason cores 1 and 2 were most affected by fabrication errors can be understood if we analyze how the chromatic dispersion of the designed cores varies with respect to the radial dimensions of each core. In order to take into account all 3 radial dimensions (i.e., a_1, a_2 and w) at the same time, we can define an additional parameter that covers all of them: the scale factor. The scale factor represents how the whole radial dimensions of the core are affected by fabrication as a single structure; that is, if a certain layer is increased by a factor 1%, every layer is increased a 1%. A scale factor of 1 corresponds to the current dimensions of each core. We then look for the effect of the fabrication tolerances (i.e., ±0.1 μm) on the whole structure ($a_1 + a_2 + w$). We computed the variation on the chromatic dispersion of each core caused by an increment of 0.1 μm on the overall structure. This parameter can be calculated by using the derivative of the chromatic dispersion with respect to the scale factor multiplied by a term that includes the 0.1-μm variation on the whole structure:

$$DF_n(1)=\left.\frac{dD_n}{dFactor}\right|_{Factor=1}\cdot\frac{0.1}{a_{1,n}+a_{2,n}+w_n}=\lim_{h\to 0}\frac{D_n(1+h)-D_n(1)}{h}\cdot\frac{0.1}{a_{1,n}+a_{2,n}+w_n}, \quad (5.1)$$

where $DF_n(Factor)$ and $D_n(Factor)$ are functions of the scale factor, and $D_n(1)$, $a_{1.n}$, $a_{2,n}$ and w_n are the designed parameters for the core n (i.e., for a scale factor of 1, $Factor = 1$). Evaluating Eq. (5.1) for each core, we obtain that core 2 presents a DF parameter above 0.3 ps/km/nm, what means that a variation of 0.1 μm in the overall core radial dimension induces a variation above 0.3 ps/km/nm on the chromatic dispersion. The rest of the cores present a DF value below 0.1 ps/km/nm.

In order to find out the main source that causes core 1 to be more affected by fabrication than cores 3-7, we also evaluate the effect of the fabrication tolerances on the core-to-cladding relative index difference. Since each core has a different dopant concentration, this error will affect the cores differently. In this case, we can simulate how a 0.01% variation in the core-to-cladding relative index difference (i.e., the current best-case fabrication tolerance) affects the chromatic dispersion. For cores 1 and 2, we obtain an absolute variation for the chromatic dispersion of 0.13 and 0.20 ps/km/nm, respectively, while cores 3-7 present a variation below 0.1 ps/km/nm. Furthermore, if we look at Table 5.2, we see that the difference between the measured and designed core refractive index values is higher in core 1 than in the others. Then, by combining the analysis of both effects, we can determine that core 2 was the core most prone to fabrication errors, followed by core 1.

5.2.3. CREOL Fiber

In the second MCF fabricated (from now, CREOL fiber), the idea was to reduce the fabrication costs by using a single preform to create all the cores. This work was carried out during my 3-month stay in the research center CREOL, the College of Optics and Photonics, University of Central Florida (UCF), Florida, USA.

However, the use of a single preform to design all the 7 cores limits the number of design parameters to one: the scale factor that determines the expansion or contraction of the radial dimensions. With a single parameter, it is not possible to fulfill, at the same time, all the propagation requirements to act as a TTDL. In general, we can assume that we can tailor one propagation characteristic per design parameter. Therefore, we must find the propagation parameter that is essential to provide TTDL operation by itself. We saw in the previous section that the restrictions on S can be made more flexible for proof-of-concept demonstrations. Finally, we have seen in the YOFC fiber that, even in case the design core group delays match at the anchor wavelength, the fabrication process can induce variations up to a few nanoseconds. Actually, we compensated these variations easily by means of a delay compensation stage without significant impact on the TTDL performance. In view of the above, the chromatic dispersion is the unique essential parameter to ensure TTDL operability. Thus, we focused on ensuring the linearly incremental chromatic dispersion requirement, while keeping the differential group delay at the anchor wavelength below a few nanoseconds (< 10 ns, which we can compensate with a couple of meters of SMF).

We chose one of the preforms available in the laboratories of CREOL to design the MCF. It consists of a trench-assisted structure with a pure silica outer cladding, a GeO_2-doped core layer of radius a_1, slightly Fluorine-doped inner cladding of width a_2 and a Fluorine-doped trench of width w. Figure 5.7 depicts the normalized refractive index profile of the preform. At the optical wavelength of 1550 nm, the core-to-cladding relative index difference Δ_1, inner-cladding-to-cladding relative index difference Δ_2 and trench-to-cladding relative index difference Δ_3, are, respectively, $4.8\cdot10^{-3}$, $-0.22\cdot10^{-3}$ and $-7.46\cdot10^{-3}$. The radial proportionalities $\phi_1 = a_1/(a_1 + a_2 + w) = 0.292$, $\phi_2 = (a_1 + a_2)/(a_1 + a_2 + w) = 0.702$ and $\phi_3 = (a_1 + a_2 + w)/(a_1 + a_2 + w) = 1$ are preserved in each core, scaling them accordingly by the scale factor f (in μm).

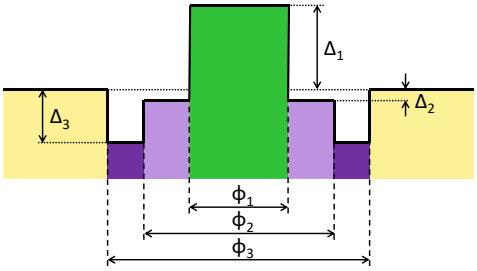

Fig. 5.7. Normalized refractive index preform for the CREOL fiber.

The fabrication of the MCF was performed in a 3-stage process to minimize the fabrication tolerances. Making several fabrication rounds with a given preform can further improve the fabrication tolerances, allowing the manufacturer to adapt the parameters of the fabrication process (such as the stretching speed) according to the information acquired in the previous rounds. In the first two stages, we fabricated 2 different single-core fibers with the preform. Each fiber had different radial dimensions, but the relation between the radii keeps constant, as well as the refractive indices. From the measurement of the refractive index profile and chromatic dispersion of both fibers, we found a more accurate generic model that better fits the measured results. The last stage corresponds to the final MCF design and fabrication based on the knowledge acquired in the first stages.

5.2.3.1. Stage 1

We fabricated a first draw of a single-core fiber from the preform shown in Fig. 5.7 (draw-1 fiber). In first place, we measured its refractive index profile to obtain a new estimation of the design parameters. Figure 5.8(a) shows the measured refractive index profile of the draw-1 fiber (blue-solid line) at the optical wavelength of 633 nm. The estimated radial dimensions are 4.12, 5.23 and 3.91 μm, respectively for the core radius, core-to-trench distance and trench width. The normalized radial dimensions result, then, $\phi_1 = 0.311$, $\phi_2 = 0.705$ and $\phi_3 = 1$. Slight differences from the initial values can be observed. In order to obtain the wavelength dependence of the layer refractive indices, we must determine their material composition. From the measured refractive indices, we calculate the mol.-% dopant concentration by using the Sellmeier equations for the GeO_2-SiO_2 and F-SiO_2 compositions (see Annex II).

The estimated dopant concentrations are 3.41 mol.% GeO_2, 0.026 mol.% F, and 1.83 mol.% F, respectively for the core, inner-cladding and trench layers. We plot in red-dashed line the simplified model according to the estimated values. Figure 5.8(b) illustrates the SEM image of the fabricated fiber.

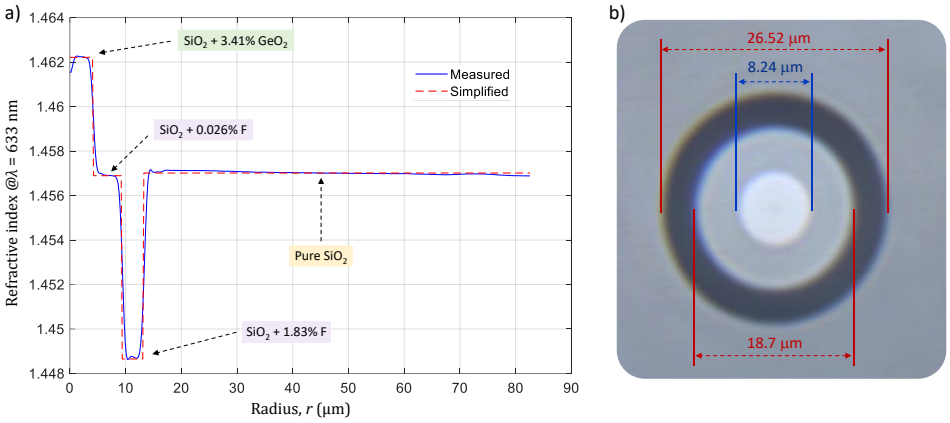

Fig. 5.8. (a) Measured refractive index profile and (b) SEM image of the draw-1 fiber.

Then, we measured the chromatic dispersion of the draw-1 fiber by means of a white-light spectral interferometry method, [153, 154]. Figure 5.9(a) depicts the experimental setup for the chromatic dispersion measurement. The broadband spectrum signal generated by the white light source (WLS) is split into the two paths of the interferometer. The fiber under test (FUT) is placed in one of the arms, while the other one is a free-space path. Then, a beam-splitter combines both paths and the OSA receives the interference pattern. The interference patterns (or spectral fringes) are then post-processed to obtain the resulting chromatic dispersion values. Figure 5.9(b) shows a photograph of the experimental setup mounted in the laboratory.

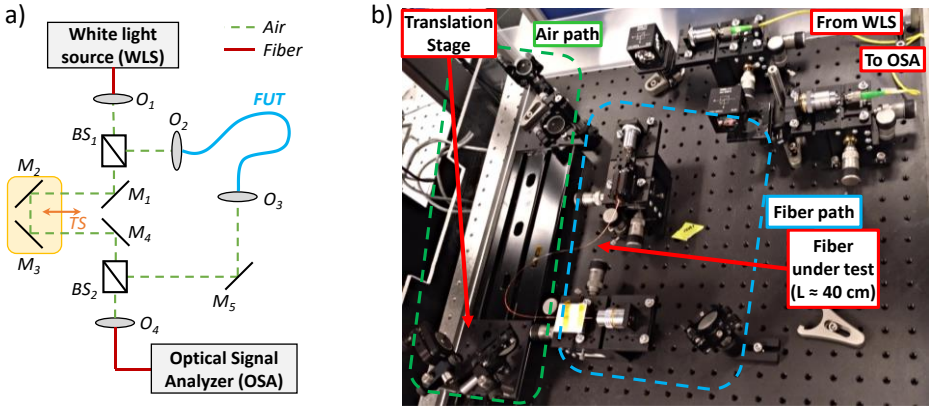

Fig. 5.9. (a) Schematic and (b) photograph of the experimental setup for the chromatic dispersion measurement. FUT: fiber under test; WLS: white light source; O: Objective; BS: Beam splitter; M: Mirror; TS: Translation stage.

Figure 5.10 illustrates the recovery procedure of the chromatic dispersion from the measured spectral fringes. From the interference pattern (Fig. 5.10(a)), we extract the evolution of the phase difference between the two interfering beams with respect to the optical wavelength by means of the interference order method (Fig. 5.10(b)), [154]. Then, we use a modified Cauchy dispersion formula, [154, 155], to determine the chromatic dispersion from the calculated phase difference (Fig. 5.10(c)).

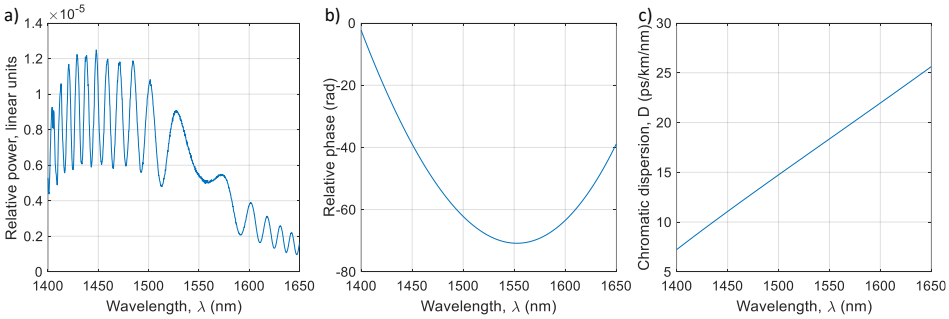

Fig. 5.10. Calculation of the chromatic dispersion from the measured interference pattern. (a) Measured interference pattern; (b) Estimated phase difference between the two arms of the interferometer; (c) Calculated chromatic dispersion.

We measured the interference pattern in different conditions (i.e., by slightly varying the air path length by means of the translation stage) to improve the measurement accuracy. Figure 5.11(a) shows the measured chromatic dispersions as a function of the optical wavelength. We see that all measures converge at the central part of the spectrum, with a slight deviation at the extremes of the measurement range. At the anchor wavelength λ_0 = 1550 nm, the maximum fluctuation is below 0.5 ps/km/nm. We then simulated the chromatic dispersion of the estimated refractive index profile of the draw-1 fiber by using *Fimmwave*. Figure 5.11(b) compares the computed chromatic dispersion with the average measured dispersions of Fig. 5.11(a). We see that both curves follow the same tendency, but the computed curve is above the averaged one with an offset of around 0.5 ps/km/nm at 1550 nm. This mismatch is attributed to the effect of having 2 more objectives (dispersive elements) in the fiber path than in the air path and could be corrected by simply correcting that in the experimental setup (in our case, we had no more objectives available so we could not compensate it). In any case, both curves are in a good agreement and the refractive index model used seems to be in a good accordance to that of the fabricated fiber.

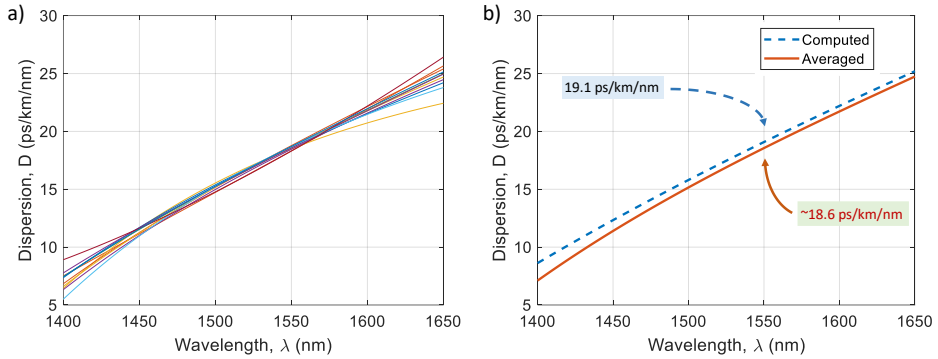

Fig. 5.11. (a) Measured and (b) computed (blue-dashed) versus average measured (red-solid) chromatic dispersions for the draw-1 fiber as a function of the optical wavelength.

5.2.3.2. Stage 2

In the second stage, we fabricate a second single-core fiber from the same preform (draw-2 fiber). Figure 5.12(a) shows the measured refractive index profile (blue-solid line) and the estimated simplified model (red-dashed line) for the draw-2 fiber. The measured radial dimensions are 3.72, 4.63 and 3.49 μm, respectively for the core, inner-cladding and trench layers. The normalized radial dimensions result in ϕ_1 = 0.314, ϕ_2 = 0.705 and ϕ_3 = 1. The measured layer refractive indices coincide with those of the draw-1 fiber. Figure 5.12(b) illustrates the SEM image of the fabricated fiber. As we can see, both the draw-1 and draw-2 refractive index profile models are almost identical, what means that the optimization process in terms of the refractive index profile modeling has been successfully performed. The draw-2 normalized profile was then chosen as the model for the MCF core design.

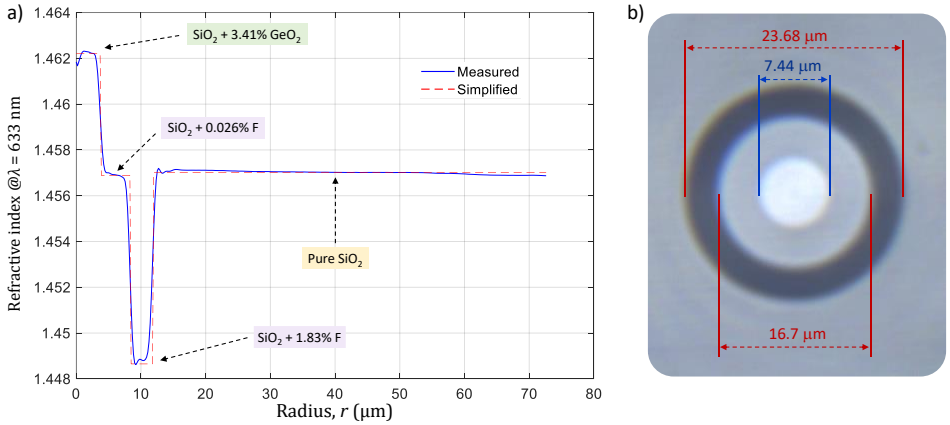

Fig. 5.12. (a) Measured refractive index profile and (b) SEM image of the draw-2 fiber.

We measured the chromatic dispersion of the draw-2 fiber by means of the white light interferometric setup. Figure 5.13(a) shows the measured chromatic dispersions as a function of the optical wavelength. We see, again, the proper convergence of all measurements. We then simulated the chromatic dispersion of the estimated refractive index profile of the draw-2 fiber by means of the numerical software

Fimmwave. Figure 5.13(b) compares the computed chromatic dispersion with the average measured dispersions of Fig. 5.13(a). We see, again, that both curves follow the same tendency, but the computed curve is above the averaged one with an offset of around 0.5 ps/km/nm at 1550 nm due to the effect of having 2 more objectives in the fiber path than in the air path.

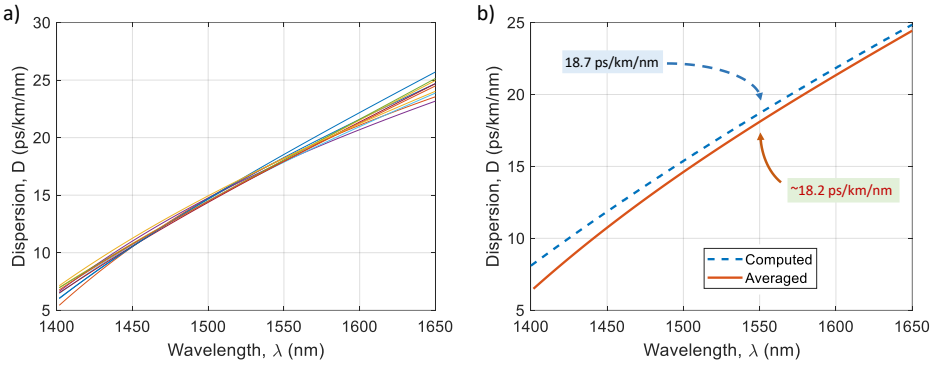

Fig. 5.13. (a) Measured and (b) computed (blue-dashed) versus average measured (red-solid) chromatic dispersions for the draw-2 fiber as a function of the optical wavelength.

5.2.3.3. Final stage

Once we determined an accurate model for the core refractive index profiles, we proceed with the final design of the MCF by using Fimmwave. We set the anchor wavelength to 1550 nm and calculated the scale factor that determines the refractive index profile of each core. Table 5.3 summarizes the design parameters and the main propagation characteristics of the cores. The scale factors are between 18.22 up to 38.09 μm, leading to core-layer radial dimensions from 2.86 up to 5.98 μm.

Table 5.3. Core design parameters and properties for the CREOL fiber design at λ_0 = 1550 nm

Core n	Core design parameters				Core Properties			
	Scale factor, f (μm)	a_1 (μm)	a_2 (μm)	w (μm)	n_g	D (ps/km/nm)	n_{eff}	S (ps/(km·nm^2))
1	18.22	2.86	3.56	2.68	1.467653	16.3	1.44466	0.053
2	18.98	2.98	3.71	2.80	1.467741	17.1	1.44484	0.059
3	20.45	3.21	4.00	3.01	1.467868	17.9	1.44517	0.063
4	23.69	3.72	4.63	3.49	1.468060	18.7	1.44577	0.065
5	28.03	4.40	5.48	4.13	1.468212	19.5	1.44638	0.063
6	32.45	5.09	6.34	4.78	1.468282	20.3	1.44685	0.063
7	38.09	5.98	7.44	5.61	1.468291	21.1	1.44730	0.063

Figure 5.14 shows the dependence of the chromatic dispersion D and the relative group delay τ_g (relative to τ_g at f = 18 μm) with respect the scale factor f. Colored circles represent the designed cores. The incremental dispersion parameter resulted in 0.8 ps/km/nm, and the chromatic dispersion ranged from 16.3 up to 21.1 ps/km/nm, respectively for cores 1 up to 7. The maximum group delay variability between cores is 2.1 ns/km.

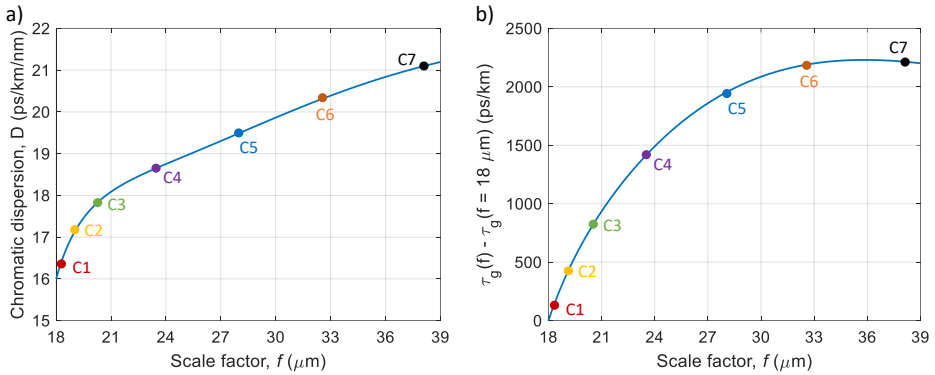

Fig. 5.14. Computed (a) chromatic dispersion and (b) group delay for the CREOL fiber as a function of the scale factor.

The lower limit for the scale factor was fixed to 18 μm in order to avoid excessively low-confined cores, what might lead to non-robust-to-fabrication cores. Figure 5.15(a) represents the derivative of the chromatic dispersion with respect to the scale factor per increment of 0.1 μm on the scale factor. The vertical axis displays, then, the variation on the chromatic dispersion (in ps/km/nm) occurred by a mismatch of 0.1 μm on the scale factor due to fabrication (i.e., a variation in the order of the current fabrication tolerances). We see there how the derivative increases rapidly as the scale factor diminishes below 21 μm, what means that slight variations on the scale factor will induce larger deviations on the chromatic dispersions. In particular, we see that the chromatic dispersion of all the cores varies below 5% of ΔD (i.e., below 0.04 ps/km/nm) per increment of 0.1 μm on the scale factor, except cores 1 and 2 whose variation is around the 10% and the 15% of ΔD, respectively. Furthermore, we see that this variability decreases as the core number increases, showing that not only each individual core is quite robust against fabrication inaccuracies, but also our TTDL is robust against fabrication in the sense that the most probably affected cores are consecutive samples located in the first part of the TTDL.

On the other hand, we chose the upper limit on the scale factor to avoid exciting the higher order modes significantly. Figure 5.15(b) shows the computed normalized propagation constant as a function of the scale factor. As we can see, all the cores are single-mode except core #7, in which however the higher-order mode is very low-confined and will not propagate through the link.

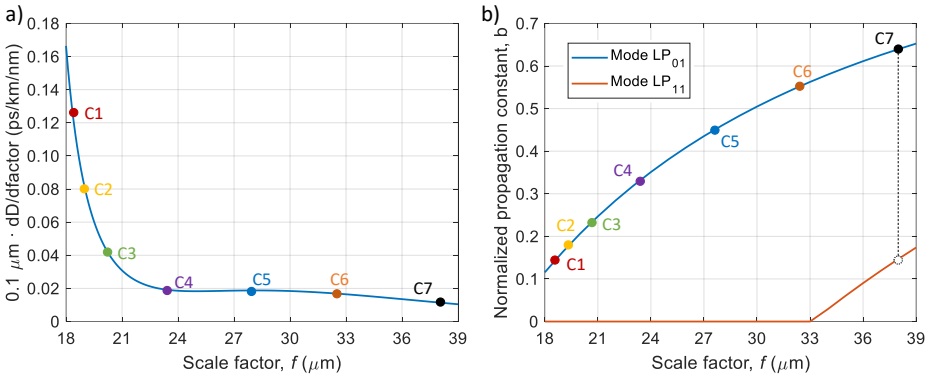

Fig. 5.15. (a) Computed chromatic dispersion derivative with respect the scale factor *f* per increment of 0.1 μm on *f* for the CREOL fiber. (b) Simulated normalized propagation constant as a function of the scale factor for the CREOL fiber.

We theoretically evaluated the performance of the fabricated fiber in terms of intercore crosstalk. Figure 5.16(a) shows the computed crosstalk dependence on the bending radius for the worst-case scenario, that is, for those adjacent cores that have the closest effective indices. As we can see, the threshold bending radius resulted in 112 mm and is given by the phase-matching condition between cores #3 and #4. As depicted in Fig. 5.16(b), we distributed the cores inside the cross-sectional area as to maximize the effective index difference between adjacent cores.

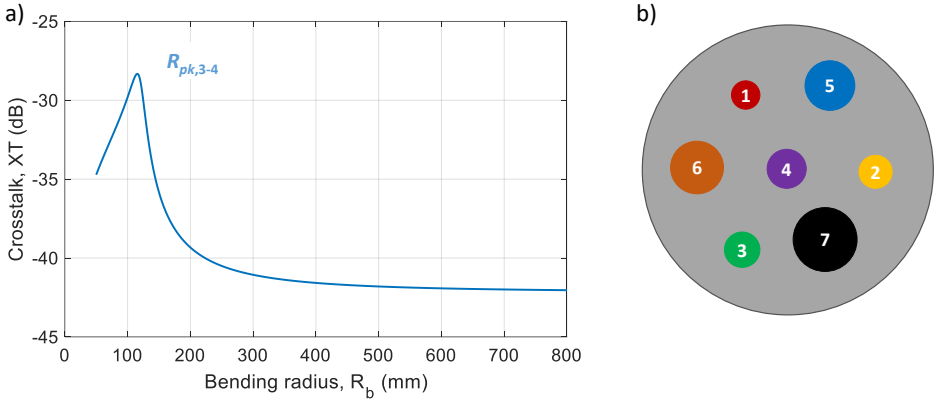

Fig. 5.16. (a) Computed intercore crosstalk between cores #3 and #4 for the CREOL fiber as a function of the bending radius. (b) Core location for the CREOL fiber.

We then evaluated the performance of the MCF in terms of TTDL operation. First, we corrected the differential group delay mismatch at the anchor wavelength λ_0 = 1550 nm. Figure 5.17(a) represents the computed group delay of the cores as a function of the optical wavelength. In order to further improve the wavelength operability range of the TTDL, we set an offset of 30 ps/km at the anchor wavelength. This allows us to diminish the detrimental effect caused by the dispersion slope at optical wavelengths relatively far from the anchor wavelength. Figure 5.17(b) shows the dependence of the core group delays with the optical wavelength after the compensation up to a 30-ps/km at the anchor wavelength. As we can observe, the

sample group delays increase almost linearly with the optical wavelength, with linearly incremental group delay slopes. From Table 5.3, we see that the dispersion slope variability between adjacent cores reaches a maximum difference of 0.006 ps/km/nm^2. Figure 5.17(c) shows the relative error caused by the dispersion slope variability as a function of the optical wavelength. We see that we can have up to a 35-nm operability range with a relative error below 5%. This error has been further reduced by the insertion of the offset group delay at the anchor wavelength. Then, we can tune the basic differential delay from 14 up to 46 ps/km by changing the operation wavelength from 1530 up to 1570 nm. For a 3-km long MCF, this allows us to implement MWP applications operating at RF frequencies ranging from 7.2 up to 23.8 GHz by tuning the operation wavelength from 1570 down to 1530 nm.

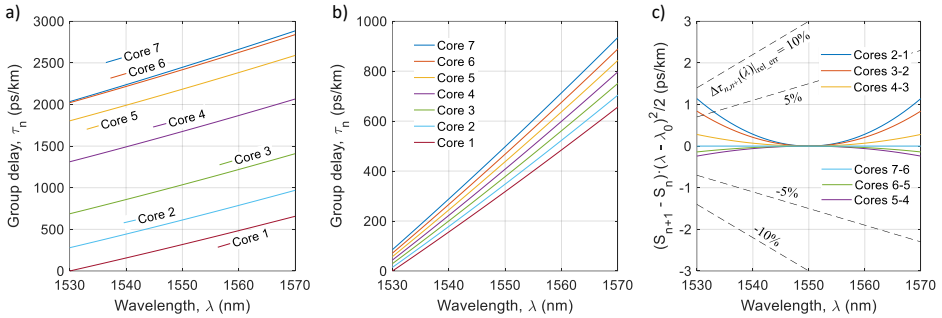

Fig. 5.17. Computed group delay as a function of the optical wavelength for the cores of the CREOL fiber: (a) without delay compensation at the anchor wavelength and (b) with delay compensation with an offset of 30 ps/km at the anchor wavelength λ_0 = 1550. (c) Simulation of the group delay relative error induced by the nonlinear term of the group delay Taylor series expansion.

Finally, 3 km of the optimized MCF were fabricated in CREOL drawing facilities. Figure 5.18 shows a photograph of the MCF, where we see the different dimensions of the cores named with the corresponding core numbering. The estimated dimensions for the core layers are 2.8, 2.9, 3.2, 3.7, 4.4, 5.1 and 5.9 μm, respectively for cores 1 up to 7. Comparing with Table 5.3 values, we see that there is a good agreement between both the designed and the fabricated cores. The cladding diameter is 165 μm and the core pitch 50 μm. The characterization of the fabricated MCF is left to a future line due to the current non-availability of the fan-in/fan-out devices.

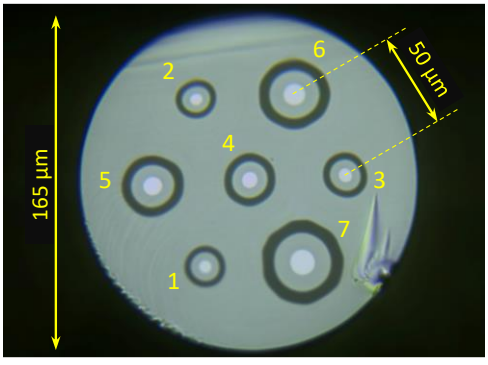

Fig. 5.18. Photograph of the cross section of the fabricated CREOL fiber.

5.2.4. Comparison between both multicore fibers

We show in Table 5.4 a comparison between both MCFs in terms of fabrication characteristics and performance. Here, the symbol ~ is used to indicate "in the order of". In terms of cost, the CREOL fiber is one order of magnitude cheaper than the YOFC fiber. First (and mainly), because we only used one preform and, second, because the CREOL fiber length is 3/5 times that of the YOFC fiber. Regarding the performance, we first analyze the intercore crosstalk. Although we could not measure the intercore crosstalk for the CREOL fiber yet, we see that the YOFC fiber is more robust against intercore crosstalk induced by fiber curvatures than the CREOL fiber, having a threshold bending radius almost half of that for the CREOL fiber. It is worth mentioning here that the amount of crosstalk measured for the YOFC fiber is highly affected by the fact that the current fiber spool has a 75-mm radius, which is in the order of the threshold bending radius for this fiber. This could be the reason of the relatively high crosstalk measured. Nevertheless, we have also left for a future line the recoiling of the MCF in a 150-mm-radius spool that we recently achieved in order to determine the intercore crosstalk above the threshold bending radius. Something similar will occur in the case of the CREOL fiber. However, it is important to remark that, even for spool radii below the threshold bending radius, the intercore crosstalk is below -30 dB, which is enough by far for our proposal applications.

Table 5.4. Comparison between the YOFC and the CREOL fibers in terms of fabrication characteristics and performance.

		YOFC fiber	CREOL fiber
COST	Length	5 km	3 km
	Number of cores	7	7
	Number of preforms	7	1
	Cost	~10 k€	~ k€
PERFORMANCE	$XT_{worst\text{-}case}$ (measured)	-31 dB	-
	R_{pk} (theoretical)	80 mm	121 mm
	$\Delta\tau(\lambda_0)$ (design)	0 ps	90 ps
	ΔD	1 ps/km/nm	0.8 ps/km/nm
	ΔS_{max}	0.019 ps/km/nm^2	0.006 ps/km/nm^2
	$\Delta S_{mean\_cores\ 3\text{-}7}$	0.0015 ps/km/nm^2	0.0022 ps/km/nm^2
	$\Delta\tau$ (1530 – 1560 nm)	0 – 150 ps	42 – 114 ps
	Δf_{RF} (1530 – 1560 nm)	Down to 6.67 GHz	23.81 – 8.77 GHz

In the case of the TTDL performance, the differential group delay of the YOFC fiber is less linear than that of CREOL fiber for 7-sample operation; for cores 3-7, however, both fibers are similar and behave properly. Regarding time-delay tunability, the YOFC fiber provides delay tunability from 0 up to 150 ps, leading to MWP application operating at RF frequencies above 6.67 GHz. In the case of the CREOL fiber, a 90-ps differential delay offset was required at the anchor wavelength in order to improve the delay tunability; in other case, a poor tunability from 0 up to 72 ps could only be achieved in a 30-nm range, leading to excessively high operating RF frequencies. With the offset delay, the time delay tunability of the CREOL fiber

ranges from 42 up to 114 ps, leading to MWP applications operating at RF frequencies from 23.81 down to 8.77 GHz. In summary, we have seen that there is a trade-off between the performance of the TTDL and the fabrication cost. The YOFC fiber has a better performance, but its fabrication cost can be one order of magnitude higher than that for the CREOL fiber.

5.3. Few-mode fibers

5.3.1. Introduction

In the case of the FMF technology, we implemented a sampled TTDL built upon a commercial FMF provided by the French quarters of the company *Prysmian Group* (https://www.prysmiangroup.com). We carried out the grating inscription in the laboratory facilities of our group in collaboration with the research line leaded by Professor Salvador Sales. Although the use of a non-customized FMF limits the performance of the TTDL (it will not allow time-delay tunability, as we will see later), our goal was to demonstrate the feasibility of the selective mode conversion by means of the inscription of LPGs in a FMF before looking for a specific FMF design that would require more complex LPG inscription.

5.3.2. True time delay line design

The Prysmian FMF has a classic step-index refractive index profile with a 15-μm-diameter core surrounded by a 125-μm diameter cladding and a relative index contrast of 1.1%. It supports 4-LP modes (LP_{01}, LP_{11}, LP_{21} and LP_{02}) with a minimum effective index difference between them above $0.8 \cdot 10^{-3}$. The typical mode DGDs per unit length relative to LP_{01} mode at a wavelength of 1550 nm are 4.4, 8.9 and 7.9 ps/m, respectively for LP_{11}, LP_{21} and LP_{02} modes. The chromatic dispersions are 21, 26, 19 and 8 ps/nm/km respectively for LP_{01}, LP_{11}, LP_{21} and LP_{02} modes at 1550 nm. The light is injected/extracted into/from each mode by using mode multiplexers based on multi-plane light conversion that are provided by the French company *Cailabs* (www.cailabs.com). The average insertion losses and maximum modal crosstalk at 1550 nm for the pair comprising the mode multiplexer and demultiplexer when they are spliced together are 7.4 dB and below -20 dB, respectively. Annex I supplies the main aspects of the fiber and multiplexer/demultiplexer datasheets.

Sampled TTDL operation for discrete-time signal processing requires a constant basic differential delay $\Delta\tau$ between adjacent samples. In our approach, the signals carried by the 4 LP modes at the FMF output correspond to 4 TTDL samples. To obtain 4 equally-spaced time samples, we propose to excite only the fundamental mode LP_{01} at the FMF input. Then, 3 mode converters based on LPGs are inscribed at certain positions along the fiber to couple the signal to the remaining modes while adjusting the amplitude and delay of the corresponding samples. The 3 LPGs convert: 1) LP_{01} to LP_{11} mode; 2) LP_{11} to LP_{21} mode; and 3) LP_{01} to LP_{02} mode. Each LPG must couple 50% of the power from the incoming to the generated mode to maintain the output samples with similar power level. Figure 5.19(a) depicts this concept.

Figure 5.19(b) shows the temporal evolution of the four samples referred to the first sample, t-t_{01}, as a function of the propagation length z. At a given distance l_{11} from

the fiber output, half the power of LP_{01} mode (blue) couples to LP_{11} mode (green) in the corresponding LPG mode converter. At the fiber output, the time delay of these samples is given by $t_{01}=l_{11}\tau_{01}$ and $t_{11} = l_{11}\tau_{11}$, respectively for sample 1 (output LP_{01} mode) and sample 3 (output LP_{11} mode), being τ_n the group delay per unit length of the n-th LP mode, $n = \{01, 11, 21, 02\}$, as given by Eq. (4.7). At a given distance l_{21} measured from the fiber output, a second LPG is inscribed to couple half the power of LP_{11} into LP_{21} mode (yellow), $0 < l_{21} < l_{11}$, so that the delay of sample 4 (output LP_{21} mode) is given by $t_{21} = (l_{11} - l_{21})\tau_{11} + l_{21}\tau_{21}$. In a similar way, at a distance l_{02} from the fiber output, $0 < l_{02} < l_{11}$, the last LPG is inserted to couple half the remaining LP_{01} power into LP_{02} mode (red), so that the delay of sample 2 (output LP_{02} mode) satisfies $t_{02} = (l_{11} - l_{02})\tau_{01} + l_{02}\tau_{02}$. For TTDL operation, the time delay difference coming from modes LP_{11}, LP_{21}, LP_{02} related to LP_{01} mode must satisfy:

$$\begin{pmatrix} t_{02}-t_{01} \\ t_{11}-t_{01} \\ t_{21}-t_{01} \end{pmatrix} = \begin{pmatrix} \tau_{02}-\tau_{01} & 0 & 0 \\ 0 & \tau_{11}-\tau_{01} & 0 \\ 0 & \tau_{11}-\tau_{01} & \tau_{21}-\tau_{11} \end{pmatrix} \begin{pmatrix} l_{02} \\ l_{11} \\ l_{21} \end{pmatrix} = \begin{pmatrix} \Delta\tau \\ 2\Delta\tau \\ 3\Delta\tau \end{pmatrix}. \tag{5.2}$$

Once we fix $\Delta\tau$ and the operation wavelength, we obtain the lengths l_{11}, l_{21} and l_{02} from Eq. (5.2). As it is clear from all the above, since the chromatic dispersion condition for TTDL operation is not fulfilled, this configuration allows only time-delay performance for a single operation wavelength. This implies that the TTDL is not tunable, so that the basic differential delay cannot be changed.

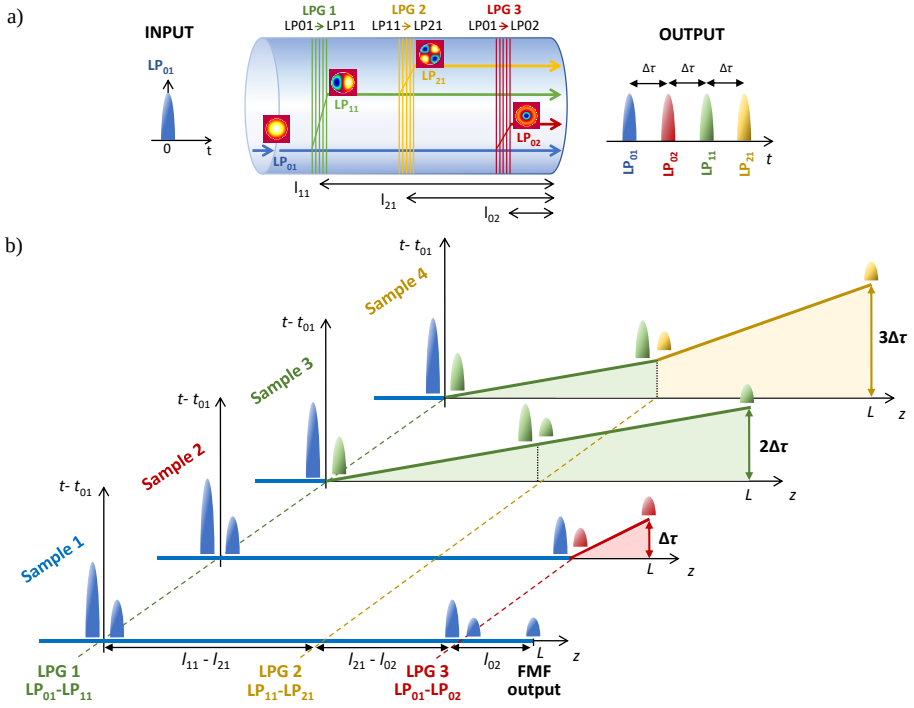

Fig. 5.19. FMF-based TTDL principle of operation: a) Scheme of the TTDL built upon the inscription of 3 LPGs; b) Evolution of the group delay normalized to the first sample group delay (t-t_{01}) of the 4 TTDL samples with the propagation length z.

5.3.3. Long period grating inscription

The fabrication of the LPGs was carried out in our group laboratory facilities, where we have a specific room dedicated to fiber grating inscription. We use UV radiation provided by a frequency-doubled argon-ion laser emitting an output power up to 60 mW at an optical wavelength of 244 nm. Prior to the grating inscription, the fiber must be hydrogen loaded at ambient temperature for 2 weeks at a constant pressure of 50 bar to increase the fiber UV photosensitivity. To inscribe the LPGs, we set the width of the light spot at the inscription point at 100 µm and swept along the fiber at a rate of 7 µm/s until the required period is completed. The length of every LPG was set in real time during the inscription process once the energy began to couple back to the input mode.

First, we must determine the period of the LPGs to ensure proper mode conversion. From Eq. (4.12), we see the effective indices of the LP-modes have to be known at the Bragg wavelength λ_B. We obtained the effective indices by inscribing a FBG into a piece of FMF. We use a phase mask with a period of Λ = 1070.4 nm. Figure 5.20 shows the measured optical spectrum in reflection for each LP mode. For every mode, the maximum power reflected occurs at the Bragg wavelength, while the smaller peaks are caused by intermodal crosstalk. By using the measured Bragg wavelengths and the FBG periods, we calculated the effective indices of every mode as $n_{eff} = \lambda_B/(2\Lambda)$. The estimated effective indices are 1.45238, 1.45013, 1.44727 and 1.44643, respectively for modes LP_{01}, LP_{11}, LP_{21} and LP_{02}. With the help of these values, we finally calculated the periods of the LPGs, which resulted in 685, 545.2 and 262.5 µm, respectively for LPGs 1 up to 3.

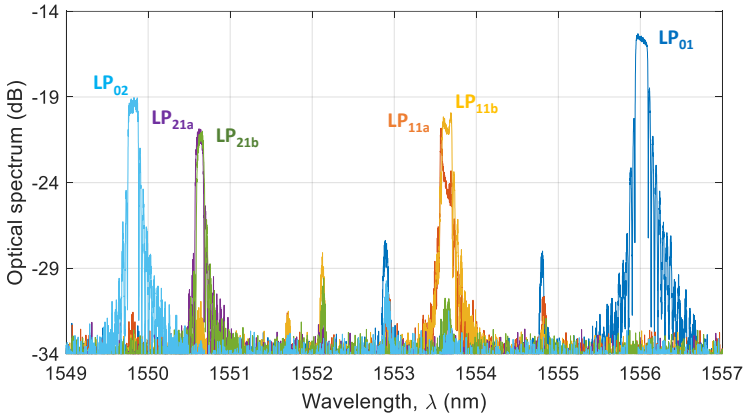

Fig. 5.20. Measured optical power reflected in the FBG inscribed in the FMF. Dark blue: LP_{01} mode; Orange (Yellow): LP_{11a} (LP_{11b}) mode; Purple (Green): LP_{21a} (LP_{21b}) mode; and light blue: LP_{02} mode.

Then, we inscribed the three LPGs using direct point-by-point UV radiation provided by the argon-ion laser emitting an output power of 60 mW. To optimize the LPG length for the asymmetrical mode conversions (i.e., LP_{01} to LP_{11} and LP_{11} to LP_{21} transformations), the LPGs were inscribed with a specific tilt of 15º, measured perpendicularly to the fiber longitudinal axis. This tilt angle was determined experimentally and is given by a tradeoff between a bigger angle, which would

produce a reduction on the visibility of the fringe pattern, and a lower angle, which would reduce the coupling efficiency and thus increase the coupling length. We must note that the power conversion efficiency of these asymmetrical modes strongly depends on the polarization state of the incoming optical field, so we must ensure operation at the optimal polarization state. Table 5.5 summarizes the main parameters describing the inscribed LPGs.

Table 5.5. Characteristics of the inscribed LPGs

	LP_{01} to LP_{11}	LP_{11} to LP_{21}	LP_{01} to LP_{02}
Period (μm)	685.0	545.2	262.5
Length (mm)	59.64	40.21	34.91
Tilt (deg)	15	15	0

After the inscription, heat annealing was done to ensure LPG stabilization by heating up the fiber to 200 ºC for 2 hours, accelerating the degradation effects derived from hydrogen diffusion and refractive index thermal decay, [156]. Figure 5.21 shows the optical spectrum in transmission of the three LPGs for all the LP modes once the LPGs reached a stable state after heat annealing. In the case of the asymmetrical LP modes, we represent the sum of both degenerate spatial modes, that is, LP_{11a} + LP_{11b} and LP_{21a} + LP_{21b}. The worst-case extinction ratio on the input mode is -10 dB (i.e., LP_{11} to LP_{21}) at the optical wavelength λ_B, where almost all power is coupled to the mode excited, which is by far sufficient to allow the required 50% coupling efficiency for our TTDL scheme at a given wavelength near λ_B. The desired mode optical output powers can be adjusted by slightly tuning the operating wavelength to modify the mode conversion efficiency. At the wavelength of λ_0 = 1558 nm, the mode conversion efficiencies are 0.58, 0.54 and 0.46 for each LPG (LP_{01} to LP_{02}, LP_{01} to LP_{11} and LP_{11} to LP_{21}, respectively), which allows to keep a similar amplitude level in all samples at the fiber output. Regarding crosstalk raised by the LPGs, we can see intermodal coupling values below -18 dB in all cases for the operating wavelength of 1558 nm, which are mainly due to the refractive index perturbation introduced by the LPG itself.

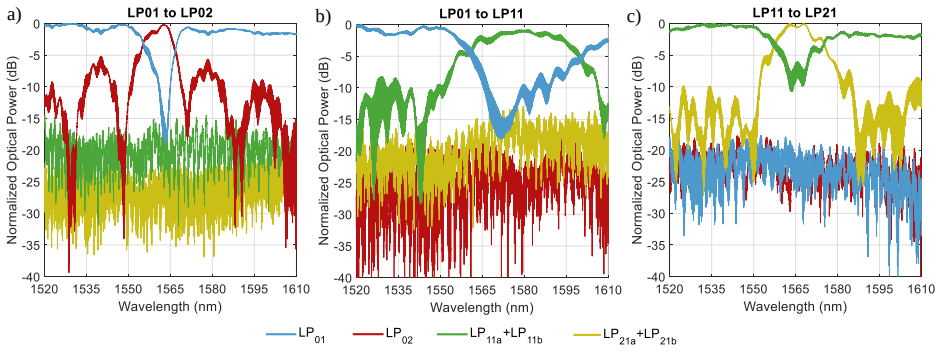

Fig. 5.21. Measured optical spectral response of each LPG in transmission for all the LP modes propagated through the FMF: a) LP_{01} to LP_{02} conversion; b) LP_{01} to LP_{11} conversion; c) LP_{11} to LP_{21} conversion.

5.3.4. Implementation and characterization

The implementation of the TTDL required first to obtain the longitudinal position where each LPG must be inscribed. We set the operation wavelength to λ_0 = 1558 nm and looked for a sample differential delay of $\Delta\tau$ = 100 ps. Prior to the LPG inscription, we characterized the mode DGDs by using an optical interferometric-based technique (analogously as it was done in the YOFC fiber) over a small piece of FMF, getting τ_{11}- τ_{01} = 4.5 ps/m, τ_{21}- τ_{01} = 9.0 ps/m and τ_{02}- τ_{01} = 8.6 ps/m. Inserting these values into Eq. (5.2) for $\Delta\tau$ = 100 ps, we obtained the longitudinal positions where the LPGs should be inscribed as l_{11} = 44.4, l_{21} = 22.1 and l_{02} = 11.6 m. Since only the fundamental mode is launched into the fiber, the total length of the TTDL corresponds to the distance between the first LPG and the mode demultiplexer, l_{11}.

Figure 5.22 shows a photograph of the experimental implementation of the FMF-based TTDL. The setup was mounted in optical breadboards to provide vibrations isolation. The LPGs were held with clamps to keep them in straight condition and the FMF sections spliced after the LPGs were coiled in spools.

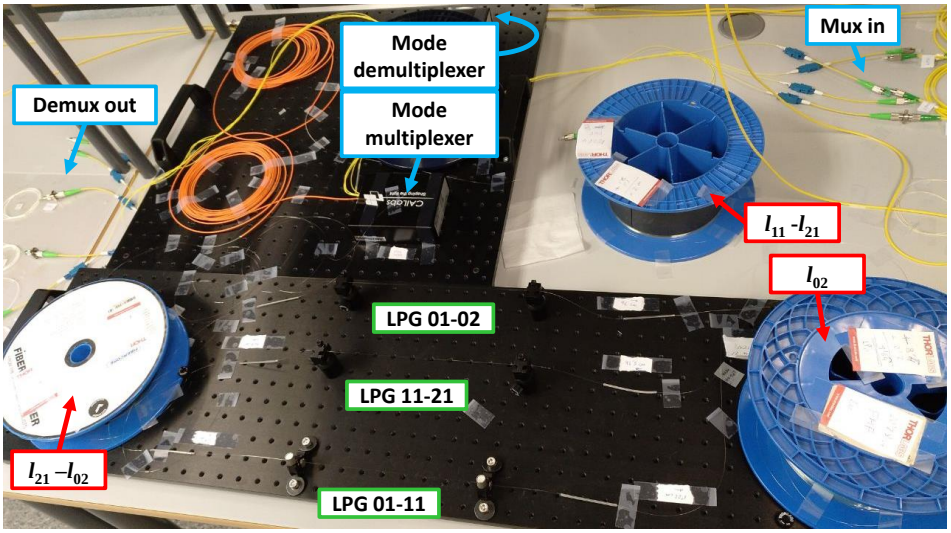

Fig. 5.22. Photograph of the FMF-based TTDL implemented in our laboratories.

We finally characterized the TTDL performance by measuring the sample differential delays. We first compensate with VDLs any small inference to the desired DGDs that is not produced by the TTDL itself but by external mismatches (as, for instance, those produced by inevitable differences in the fiber lengths of the mode multiplexers). To do so, we include the VDLs at the FMF output and normalize the differential delays between modes when both the mode multiplexer and demultiplexer are spliced together. After the normalization, we spliced again the TTDL in between the mode multiplexers. The measured sample differential delays relative to the first sample are 99.1, 200.3 and 299.5 ps, respectively for samples 2 up to 4. We see that all samples were highly matched with the designed values.

5.4. Conclusions

We have presented, for the first to our knowledge, the first fabrication of dispersion-engineered heterogeneous MCFs that operate as sampled TTDLs. We designed and fabricated two different 7-core trench-assisted MCFs. The first MCF was designed by following the approach presented in chapter 4 and was fabricated by YOFC company. Seven different preforms were required to fabricate the fiber (one preform per core), what considerably increased the fabrication costs. The second fiber was fabricated with the aim of reducing the fiber fabrication costs, so a single preform was shared between all the cores. We carried out this work in collaboration with CREOL at the University of Central Florida, during my 3-month stay. The different propagation characteristics were achieved, in this case, by scaling the radial dimensions of the preform. The fabrication costs were one order of magnitude lower than in the YOFC fiber, but in compromise with the TTDL performance. We characterized the performance of the YOFC fiber and we observe that although the first two cores were more affected by fabrication, cores 3-7 behaved as designed, guarantying 5-sample TTDL operation up to a 30-nm range. We left the characterization of the CREOL fiber to a future line due to the absence of adequate fan-in fan-out devices in time.

We also proposed and experimentally demonstrated a new approach for 4-sample TTDL operation. The TTDL was fabricated by using a commercial FMF, provided by *Prysmian* company. The fiber has a step-index refractive index profile and supports 4-LP modes. Although the use of a non-customized FMF limited the performance of the TTDL to single-wavelength operation, in this preliminary approach our goal was to demonstrate the ability of the LPGs to excite higher-order modes selectively and properly manage the time delay of the samples. While only the fundamental mode is injected at the fiber input, a set of 3 LPGs excite the remaining LP modes at convenient longitudinal positions so that the sample delays are adjusted to provide a constant differential delay. The length of this fiber-based device is 44.4-m. The inscription of the LPGs was carried out in our laboratories, in collaboration with our colleagues from the fiber grating research line. We successfully demonstrated TTDL operation at the optical wavelength of 1558 nm.

Chapter 6
Application to distributed radiofrequency signal processing

6.1. Introduction

In the previous chapter, we designed and fabricated TTDLs built upon both FMFs and MCFs that can operate as distributed radiofrequency signal processing links. In this chapter, we experimentally demonstrate different MWP functionalities implemented on these systems.

In the case of MCF approaches, we experimentally demonstrated both tunable microwave signal filtering and optical beamforming for phased array antennas implemented with the YOFC fiber. The absence of fan-in/fan-out devices for the CREOL fiber at the time of Thesis writing did not permit us to carry out any experimental demonstration of signal processing functionalities on this fiber, so they are left to a future research line. Lastly, we proposed the implementation of multi-cavity optoelectronic oscillators based on MCFs. Different architectures have been considered, based either on homogeneous MCFs or heterogeneous MCFs. We experimentally demonstrated the performance of the homogeneous MCF approaches built upon a commercial homogeneous 7-core fiber.

In the case of the FMF technology, we experimentally demonstrated the performance of the Prysmian FMF-based TTDL when it is applied to RF signal filtering. In this case, the lack of delay tunability of the TTDL implies that the filter operates for a fixed RF frequency.

6.2. Multicore fiber approaches

6.2.1. MWP signal filtering on a heterogeneous multicore fiber link

First, we experimentally demonstrated the performance of the YOFC fiber when it is applied to microwave signal filtering. The basic operation principle of a MWP signal filter was introduced in chapter 2. The filtering response or filter transfer function (see Eq. (2.1)) depends on the sample differential delay, $\Delta\tau$, and the sample amplitude distribution given by the coefficients a_n. Two different experiments have been carried out depending on the diversity regime exploited. For the spatial dimension, we saw in section 5.2.2 that cores 1 and 2 do not fully satisfy the TTDL condition, so we can implement up to 5-sample operation by using cores 3-7. Here, a single optical carrier is modulated and injected into these cores, so that the RF filtering response results from the optical combination of the cores at the MCF output. For the wavelength dimension, an array of lasers operating at different but equally spaced optical wavelengths is modulated and injected into a certain core (note that, now, we can use all of them) to create, after the 5-km MCF propagation, the RF filtering response.

Figure 6.1 depicts the experimental setup for the RF filtering response measurement. The optical signal is generated by either: (a) a broadband source (required to avoid optical coherent interference) followed by a 0.1-nm-bandwidth optical filter (needed to avoid high-frequency fading effects due to the broadband source, [157]) for the spatial diversity domain; or (b) a tunable 4-laser array for the wavelength diversity domain. An electro-optical modulator modulates the optical signal with the RF signal generated by the Vector Network Analyzer. We used single sideband modulation to avoid the carrier suppression effect, [152]. The signal is then split and injected into all MCF cores. After 5-km propagation, the signals are treated differently depending on the operation regime. In the spatial diversity domain, all cores are combined at the fiber output and a set of VOAs finely equalize the output power of the samples for uniform amplitude distribution. In the wavelength diversity domain, a single core is chosen to create the RF filtering functionality. In both schemes, VDLs were used to compensate the core group delay fabrication mismatches at the anchor wavelength.

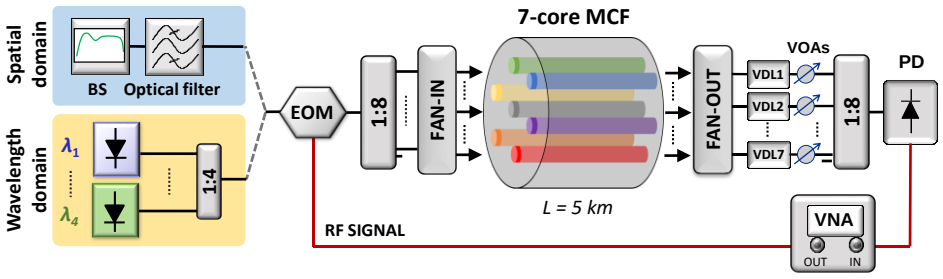

Fig. 6.1. Experimental setup for measuring the RF filter transfer function for the spatial and wavelength diversity domains.

Figure 6.2 illustrates a photograph of the experimental setup mounted in the laboratory to measure the filter transfer function. In the upper part, we have: (1) the VOAs; (2) the delay compensation stage (pigtails with different lengths and VDLs); and (3) the YOFC fiber. In the lower part, we have the generation of the optical signal:

(left) the broadband source and the optical filter; (right): the 4-laser array and an OSA showing the optical signals generated from the lasers.

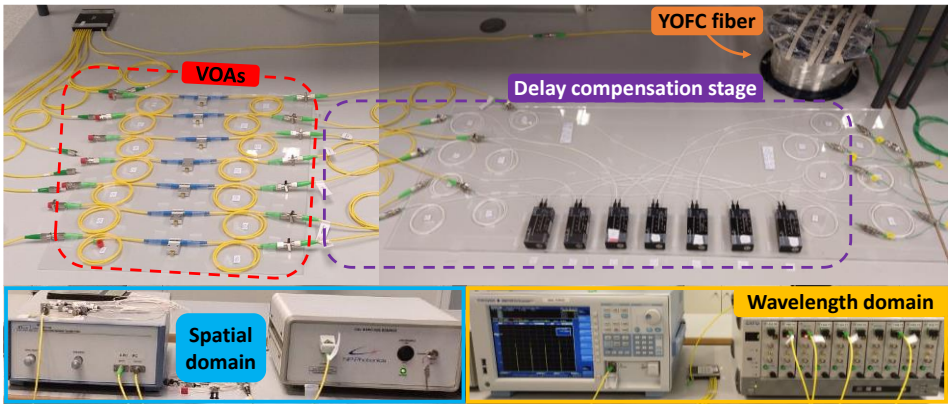

Fig. 6.2. Photograph of the experimental setup mounted in the laboratory for the filter transfer function measurement in both spatial and wavelength diversity domains.

In the space-diversity experiment, we evaluate the 5-tap filter built by cores 3-7 in the spatial diversity domain. Figure 6.3 shows the measured RF filter transfer function up to an RF frequency of 30 GHz for different operation wavelengths. Blue dotted, orange dashed, yellow solid, purple dash-dotted and green solid lines correspond to the measured filtering responses at the operation wavelengths of 1540, 1545, 1550, 1555 and 1560 nm, respectively. We see that varying the operation wavelength changes the filter FSR from 20 GHz at 1540 nm down to 13.3, 10, 8 and 6.7 GHz at 1545, 1550, 1555 and 1560 nm, respectively, with no significant degradation on the filter responses. We must keep in mind that the FSR is given by the inverse of the differential delay between samples (in this case, between cores). The main-to-secondary lobe level is below -12 dB in all cases for the first filter resonances, while in the case of large operation wavelengths it increases up to –8 dB for the highest resonances. For operation wavelengths below 1540 nm, the filter FSR increases rapidly up to tens or hundreds of GHz, allowing us to continuously reconfigure the filter FSR from 6.7 GHz up to the mm-band by properly tuning the operation wavelength from 1560 down to 1530 nm.

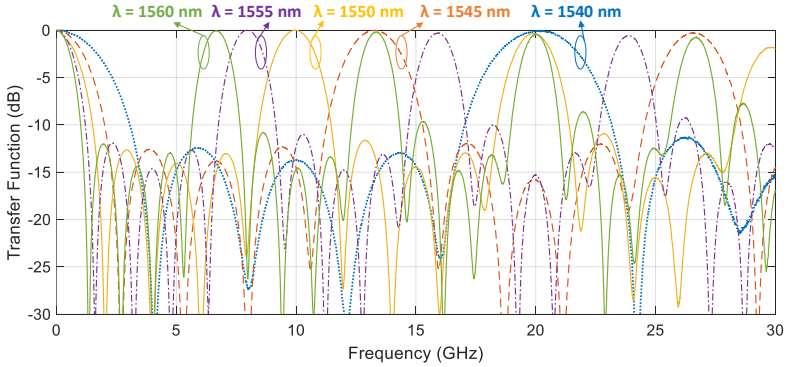

Fig. 6.3. Measured RF transfer function for the 5-tap filter built upon the YOFC fiber when we operate in the spatial-diversity domain.

In the wavelength-diversity experiment, we use an array of 4 lasers operating at optical wavelengths ranging from 1540 up to 1543 nm with 1-nm separation. Figure 6.4(a) shows the measured transfer functions of the 4-tap filters created in cores 1 (black solid line), 2 (green dashed line) and 4 (red dash-dotted line). In this case, the filter FSR depends inversely on the chromatic dispersion of the core, so that the resulting FSRs decrease from 14 GHz for core 1 down to 13.2 and 11.3 GHz, respectively for cores 2 and 4. For each core, the filter FSR reconfigurability is given by the wavelength separation between the optical sources. Figure 6.4(b) shows the measured RF transfer functions of the same filters when the separation between lasers is increased up to 2 nm, with the lasers operating at optical wavelengths ranging from 1540 up to 1546 nm. We see how the increment on the wavelength separation between lasers induces a reduction on the filter FSR down to 7, 6.6 and 5.65 GHz, respectively for cores 1, 2 and 4. In all cases, the secondary lobes are kept below -10 dB even for the highest filters resonances.

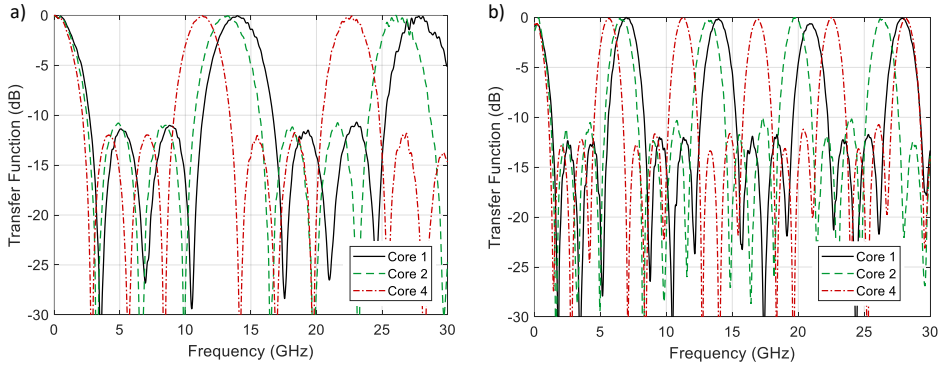

Fig. 6.4. Measured RF transfer function for the 4-tap filter built upon the YOFC fiber when we operate in the wavelength-diversity domain using a 4-laser array with: (a) 1-nm and (b) 2-nm wavelength separation between lasers.

6.2.2. Optical beamforming on a heterogeneous multicore fiber link

In a second scenario, we applied the YOFC fiber to implement optical beamforming for phased array antennas. As we saw in chapter 2, optical beamforming networks follow discrete-time signal processing schemes, similarly to MWP signal filtering, with the particularity that the N delayed samples are converted to the electrical domain by means of N independent photodiodes. Each one of the N RF output signals feeds then one of the N radiating elements that comprise the phased array antenna.

We used the TTDL in the spatial-diversity domain, so that the far-field pattern is created by the phase difference between the MCF cores at the fiber output. This phase can directly be inserted in Eq. (2.2) instead of the phase term $2\pi f_{RF}\Delta\tau_{7,n}$ to obtain the array factor, being $\Delta\tau_{7,n}$ the differential delay between cores 7 and n. Figure 6.5 depicts the experimental setup used to measure the phase difference between the photodetected RF signals. Here, the optical signal coming from a tunable laser is modulated by an electro-optical modulator with the RF signal generated by the Vector Signal Generator (VSG). The signal is then amplified by an EDFA, split and injected into all cores. After the 5-km MCF propagation, the signals are photodetected

independently using seven different photodetectors (PD). Analogously as in the filter architectures, we use VOAs to finely equalize the output optical power of the samples for uniform amplitude distribution and VDLs to compensate the core group delay fabrication mismatches at the anchor wavelength (and any other differential delay that is not caused by the TTDL itself). After photodetection, the digital phosphor oscilloscope (DPO) measures the phase difference between core 7 (taken as the reference signal) and the rest.

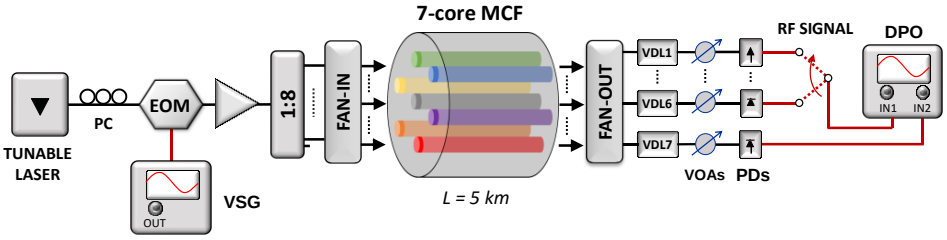

Fig. 6.5. Experimental setup for the implementation of the optical beamforming network with the YOFC fiber.

Figure 6.6 shows the measured temporal waveforms photodetected at the output of each core for an RF frequency of 10 GHz at the optical wavelength of 1540 nm. The RF phase difference (or time delay difference $\Delta\tau$) can be obtained as the difference between the phase of each core with respect to that of core 7. Table 6.1 gathers the measured average RF phase difference between adjacent cores for an RF frequency of 10 GHz and four different optical wavelengths of operation: 1540, 1545, 1550 and 1555 nm. For proper TTDL operation, the electrical phase difference between adjacent cores must be as similar as possible (analogous to the differential delay condition). We see from Table 6.1 that, as concluded in chapter 5, cores 3 up to 7 almost satisfy the differential phase (or differential group delay) condition up to the wavelength of 1555 nm. Small discrepancies between these values and the expected ones from the differential delays measured in the TTDL characterization of the previous chapter are attributed to phase measurement errors, which are actually caused by the DPO's measurement limitations.

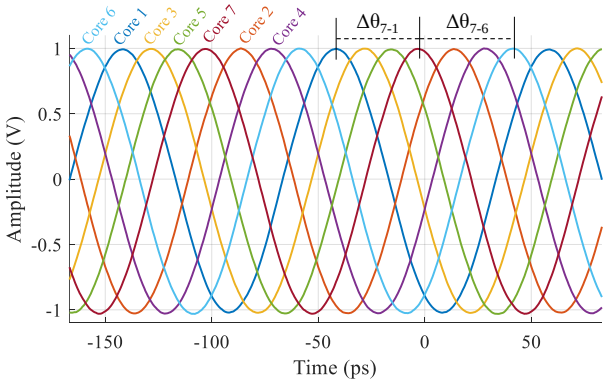

Fig. 6.6. Measured RF temporal waveforms at the output of each core for an RF frequency of 10 GHz and an optical wavelength of 1540 nm.

Table 6.1. Measured RF phase differences between cores

Wavelength	Cores 1-2	Cores 2-3	Cores 3-4	Cores 4-5	Cores 5-6	Cores 6-7
1540 nm	196.1º	205.7º	199.4º	199.8º	198.9º	194.9º
1545 nm	255.8º	328.8º	286.1º	281.3º	267.8º	270.2º
1550 nm	321.6º	111.8º	19.2º	20.6º	15.0º	3.4º
1555 nm	29.9º	259.6º	96.7º	90.8º	92.4º	78.6º

By inserting the measured values from Table 6.1 into Eq. (2.2), we computed the array factor created by cores 3 up to 7. Figure 6.7(a) represents the array factor of the 5-element phased array antenna for an RF frequency of 10 GHz and different optical operation wavelengths. The separation between radiating elements was set to d = 1.5 cm. Blue, red, yellow and purple lines represent the array factors for operation wavelengths of 1540, 1545, 1550 and 1555 nm, respectively. As we see, the beam-pointing angle can be easily tuned by simply changing the operation wavelength of the optical source. Here, the beam-pointing angle is swept from -60.5º at the wavelength of 1540 nm up to -28.1º at 1545 nm, 5.8º at 1550 nm and 33.8º at 1555 nm. From the TTDL characterization of the previous chapter, one can observe that, in this situation, the maximum angle of radiation can be continuously tuned along the whole angular plane by properly changing the operation wavelength in a 20-nm range, which corresponds to a differential group delay variation range of 100 ps.

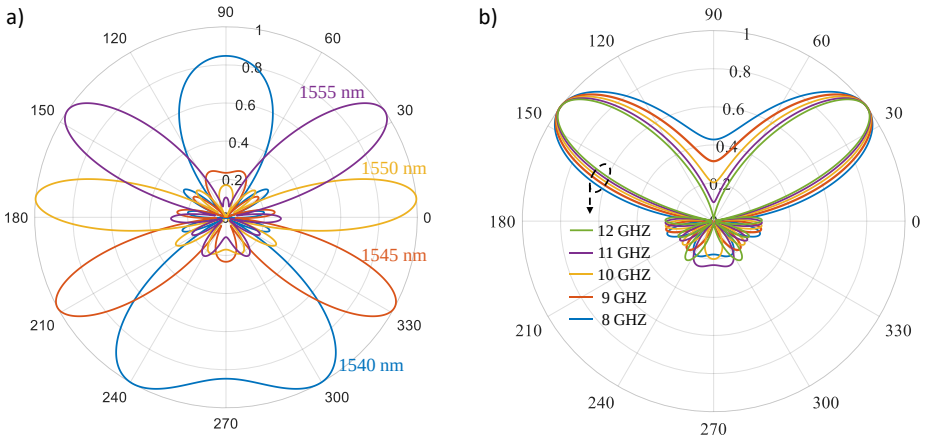

Fig. 6.7. Computed array factor from the measured true time delay values for: (a) an RF frequency of 10 GHz and different operation wavelengths; and (b) different RF frequencies and an operation wavelength of 1535 nm.

In addition, we demonstrated wideband operation avoiding squint-beam effects (i.e., the beam-pointing angle does not depend on the RF frequency), as expected since our optical beamforming network is built upon a TTDL. Figure 6.7(b) represents the computed array factor for a 5-element phased array antenna characterized by an element separation d = 1.25 cm for different RF frequencies. Blue, red, yellow, purple and green lines represent the array factor for the RF frequencies of 8, 9, 10, 11 and 12 GHz, respectively. The optical wavelength was set to 1535 nm, which provides 25-ps delay difference between adjacent samples. We observe no beam-squint degradation as the beam-pointing angle is fixed at 36.5º for all RF frequencies.

6.2.3. Optoelectronic oscillation over multicore fibers

6.2.3.1. Multi-cavity OEO model

Figure 6.8 shows the general layout of the proposed multi-cavity OEO. Its principle of operation is similar to the single-cavity OEO described in chapter 2, with the particularity that each cavity has its own photodetector while the optical source, modulator, RF amplifier and RF filter are shared by all the cavities (here labeled as k = 1, 2, ...N). Each cavity is implemented in the optical domain using different cores of a single MCF and features a different round-trip complex-valued gain g_k, given by

$$\begin{aligned} |g_k| &= G_k |H_k(\omega)| \\ \phi_k &= \arg\left[H_k(\omega)\right] \end{aligned}, \tag{6.1}$$

where G_k represents the voltage gain coefficient and $\tilde{H}_k(\omega)=|H_k(\omega)|\exp(i\phi_k)$ the unitless complex filter function that accounts for the combined effect of all frequency dependent components in the cavity.

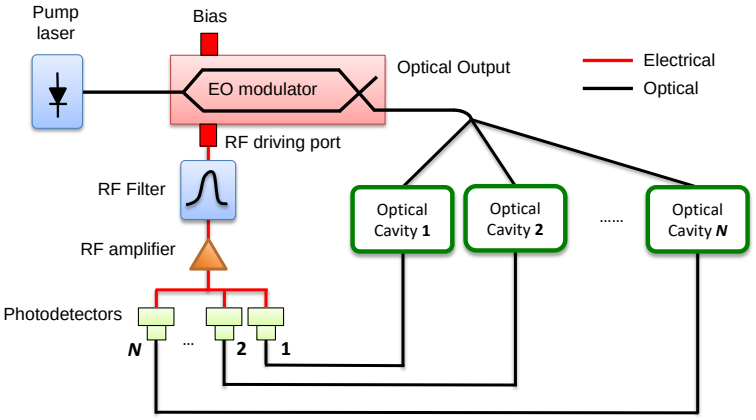

Fig. 6.8. General layout of a multi-cavity optoelectronic oscillator.

Following a similar procedure as Yao and Maleki, [50], the recursive relationship for the complex amplitude of the circulating field after the r^{th} round trip can be expressed as

$$\tilde{V}_r(\omega) = \tilde{V}_{r-1}(\omega)\left[\sum_{k=1}^{N}|g_k|e^{i(\omega\tau_k+\phi_k)}\right]. \tag{6.2}$$

Hence, if the oscillation starting voltage is given by $G_a\tilde{V}_{in}(\omega)$ where G_a is the RF amplifier voltage gain, then the application of Eq. (6.2) yields

$$\tilde{V}_{out}(\omega) = \sum_{r=0}^{\infty}\tilde{V}_r(\omega) = \frac{G_a\tilde{V}_{in}(\omega)}{1-\sum_{k=1}^{N}|g_k|e^{i(\omega\tau_k+\phi_k)}}, \tag{6.3}$$

and the corresponding RF power

$$P(\omega)=\frac{\left|\tilde{V}_{out}(\omega)\right|^2}{2R}= \frac{G_a^2\left|\tilde{V}_{in}(\omega)\right|^2\big/2R}{1+\sum_{k=1}^{N}|g_k|^2+2\sum_{\substack{k=1\\l>k}}^{N}|g_k||g_l|\cos\left[\Phi_k(\omega)-\Phi_l(\omega)\right]-2\sum_{k=1}^{N}|g_k|\cos\left[\Phi_k(\omega)\right]}, \tag{6.4}$$

where R represents the load impedance of the RF amplifier and

$$\Phi_k(\omega)=\omega\tau_k+\phi_k. \tag{6.5}$$

For oscillations to start collectively in all the cavities at an angular frequency ω_o, we need

$$\begin{aligned}&\Phi_k(\omega_o)=2m_k\pi;\\&\Phi_k(\omega_o)-\Phi_l(\omega_o)=2(m_k-m_l)\pi;\qquad m_k,m_l\in Z\end{aligned} \tag{6.6}$$

Under these conditions,

$$P(\omega_o)=\frac{G_a^2\left|\tilde{V}_{in}(\omega_o)\right|^2\big/2R}{1+\sum_{k=1}^{N}|g_k|^2+2\sum_{\substack{k=1\\l>k}}^{N}|g_k||g_l|-\sum_{k=1}^{N}|g_k|}. \tag{6.7}$$

For oscillations to start from noise, the denominator in Eq. (6.7) must vanish

$$1+\sum_{k=1}^{N}|g_k|^2+2\sum_{\substack{k=1\\l>k}}^{N}|g_k||g_l|-\sum_{k=1}^{N}|g_k|=0. \tag{6.8}$$

A simple case is when the gain coefficients have equal moduli in all cavities, $|g_k| = g$ $\forall k$, and Eq. (6.8) leads to

$$|g|=1/N. \tag{6.9}$$

The noise model for the multi-cavity OEO follows from the double-cavity case developed by Yao and Maleki, [46], where the starting oscillations build up from the RF noise power at the photodetector output. Hence,

$$\rho_N(\omega)\Delta f=\frac{\left|\tilde{V}_{in}(\omega)\right|^2}{2R}, \tag{6.10}$$

where $\rho_N(\omega)$ is the power spectral density of the input noise and Δf its bandwidth. Note that $\rho_N(\omega)$, which is given by Eq. (30) in [47], takes into account all the technical noise sources in the OEO, including thermal, shot, relative intensity noise (RIN) and, when applicable, amplified spontaneous emission (ASE) noise. It is

usually represented by a value in the range of -180 to -160 dB/Hz [47, 158]. Substituting Eq. (6.10) into Eq. (6.4) and taking Eq. (6.5) and Eq. (6.6) into consideration, we find the following expression for the power spectral density of the mode oscillating at ω_o:

$$S_{RF}(f') \equiv \frac{P(f')}{\Delta f P_{osc}} = \frac{G_a^2 \rho_N / P_{osc}}{1 + \sum_{k=1}^{N} |g_k|^2 + 2\sum_{\substack{k=1 \\ l>k}}^{N} |g_k||g_l| \cos\left[2\pi f'(\tau_k - \tau_l)\right] - 2\sum_{k=1}^{N} |g_k| \cos\left[2\pi f' \tau_k\right]}, \quad (6.11)$$

being $f' = (\omega - \omega_0)/(2\pi)$ the offset frequency from the RF carrier, where P_{osc} represents the RF oscillation power.

6.2.3.2. Multi-cavity OEO architectures

We propose the implementation of different multi-loop OEO architectures based on multicore fibers. MCFs provide an ideal medium for the implementation of multiple parallel cavities, where all cavities are subject to practically identical mechanical and environmental conditions. We can consider our proposal an improvement of earlier reported systems for three reasons. In first place, it allows for the implementation not only of multi-cavity OEOs where cavity lengths are a multiple of a given reference value, as proposed in [50, 158], but also of multi-cavity OEOs where cavity lengths are slightly different exploiting the Vernier effect, [54]. In second place, the use of a single MCF structure to host all the cavities provides an integrated hosting medium for enhancing their relative stability against environmental fluctuations. In third place, the use of MCF-based TTDLs potentially enables the implementation of tunable multi-loop OEOs.

6.2.3.2.1. Based on homogeneous multicore fibers

The identical multiple cores of a homogeneous MCF can be used to implement both double- and multi-cavity OEOs.

a) Double unbalanced cavity

Figure 6.9(a) shows the layout of a double-cavity OEO based on an N-core homogeneous MCF. Here k_1 ($k_1 < N/2$) cores are linked to form the first (short) cavity while the remaining N-k_1 cores form the second (long) cavity. If the core lengths are all equal to L and the group delay per unit of length is given by τ_{go}, then each core provides a group delay given by $\tau = \tau_{go} L$.

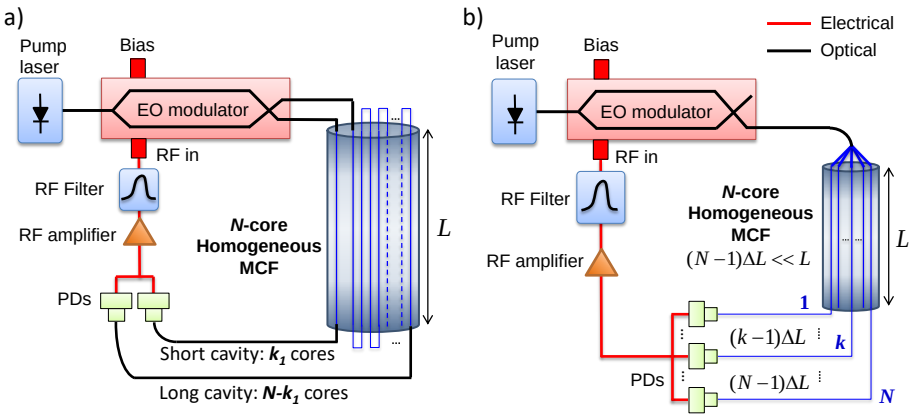

Fig. 6.9. Schematics of (a) double unbalanced cavity OEO and (b) Vernier OEO using an *N*-core homogeneous MCF. PD: Photodetector; EO: electro-optical.

The oscillation frequency must verify:

$$f_o = \frac{m}{k_1 \tau_{go} L}, \qquad m = 1, 2, \ldots . ; \tag{6.12}$$

$$f_o = \frac{n}{(N - k_1)\tau_{go} L}, \qquad n = 1, 2, \ldots . .$$

The first expression in Eq. (6.12) determines the required value of L, taking as a starting point the knowledge of f_o, N, k_1, τ_{go} and a set value for m. Then, the value of n is calculated from the second expression for the resulting L. For example, for an oscillation frequency of f_o = 10 GHz, and a typical seven core MCF (N = 7), if k_1 = 1 and τ_{go} = 5 ns/m, setting m = 1000 yields L = 2 m and n = 6000, leading to a short cavity of 2 m and a long cavity of 12 m. If k_1 = 2 and L is kept fixed to 2 m, then m = 2000 and n = 5000 leading to a short cavity of 4 m and a long cavity of 10 m. If k_1 = 3 then m = 3000 and n = 4000 leading to a short cavity of 6 m and a long cavity of 8 m. In all cases, the spectrum periodicities are above 100 MHz, so that an RF filter centered at 10 GHz with a maximum bandwidth of 100 MHz is enough for single-mode oscillation

Figure 6.10 shows the computed phase noise spectra for the above examples. We use standard noise of ρ_n = -180 dBm/Hz, an RF gain of G_a = 10 and an oscillation power of P_{osc} = 16 dBm. Almost identical phase noise behavior is obtained in all three cases, as the change in the longer cavity length (up to 4 m) has almost negligible impact in the resonance quality factor. The high level of phase noise close to the carrier can be explained by the fact that the longest cavity length ranges from 8 to 12 m, so that since the phase noise is dominated by the spectral width of the longest cavity resonance, [50], a high level is expected.

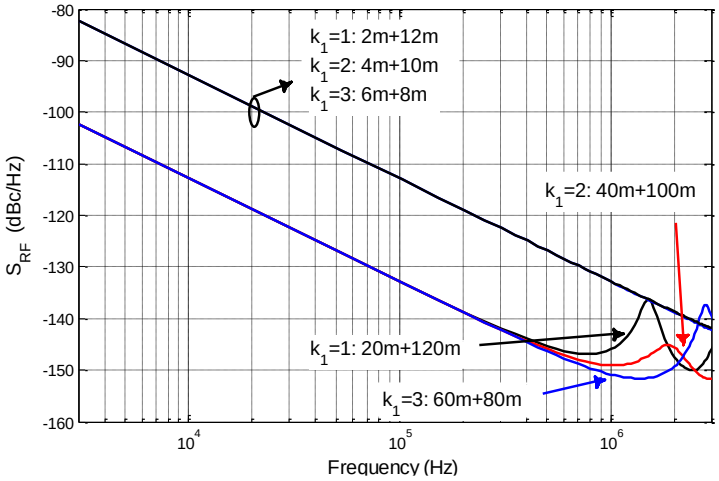

Fig. 6.10. (Upper traces) Phase noise spectra computed for the three cases of Fig. 3. (Lower traces) Phase noise spectra computed for the same three cases when L = 20 m. Standard noise (ρ_n = -180 dBm/Hz), RF gain (G_a = 10) and oscillation power (P_{osc} = 16 dBm) values have been employed.

It is possible to improve the phase noise characteristic by extending the basic cavity length. In the former example setting m = 10000 yields L = 20 m and n = 60000, leading to a short cavity of 20 m and a long cavity of 120 m. If k_1 = 2 and L is kept fixed to 20 m, then m = 20000 and n = 50000 leading to a short cavity of 40 m and a long cavity of 100 m. If k_1 = 3 then m = 30000 and n = 40000 leading to a short cavity of 60 m and a long cavity of 80 m. Oscillation at 10 GHz requires, however, a higher selectivity RF filter, with up to a 10-MHz bandwidth. As Fig. 6.10 shows, a 20-dB reduction on the phase noise is observed for the longer cavity design.

b) Vernier

Figure 6.9(b) depicts the layout for a multi-cavity OEO where the different cores are used to build cavities with slightly different physical lengths. Since all MCF cores have, obviously, the same length L, the fan-out device can be properly fabricated with different (but evenly spaced by ΔL) physical lengths in its output ports. This fan-out device features in consequence incremental delays between adjacent ports given by $\Delta\tau = \tau_{go}\,\Delta L$. In this case, Eq. (6.5) results

$$\Phi_k(\omega) = \omega\tau_{go}L + (k-1)\omega\tau_{go}\Delta L + \phi_k \quad \text{for } k = 1, 2, \ldots N\,. \tag{6.13}$$

Assuming $\phi_k = 0\ \forall k$, the oscillation frequency must verify

$$f_o = \frac{m}{\tau_{go}L}\,, \tag{6.14}$$

and thus the required value of L can be determined by taking as a starting point the knowledge of f_o, τ_{go} and a set value for m. For the remaining cavities, in order to have Vernier effect operation and constructive interference at f_o, we require

$$2\pi f_o \Delta\tau = 2\pi \;\Rightarrow\; f_o = \frac{1}{\tau_{go}\Delta L}. \tag{6.15}$$

From Eq. (6.14) and Eq. (6.15) we have $L/\Delta L = m$. Hence, although the free spectral range of each cavity is approximately $1/\tau$, the free spectral range value of the coupled-cavity configuration is $1/\Delta\tau = m/\tau$ due to the Vernier effect. For example, for an oscillation frequency f_o = 10 GHz and a MCF featuring τ_{go} = 5 ns/m setting m = 1000 yields L = 20 m and ΔL = 2 cm, which is an incremental value that can be easily achieved in a compact fan-in/fan-out device closing the MCF. Figure 6.11 shows the oscillation spectra for this example computed from Eq. (6.4) when a 7-core fiber is considered and the number of parallel cavities ranges from 2 up to 7.

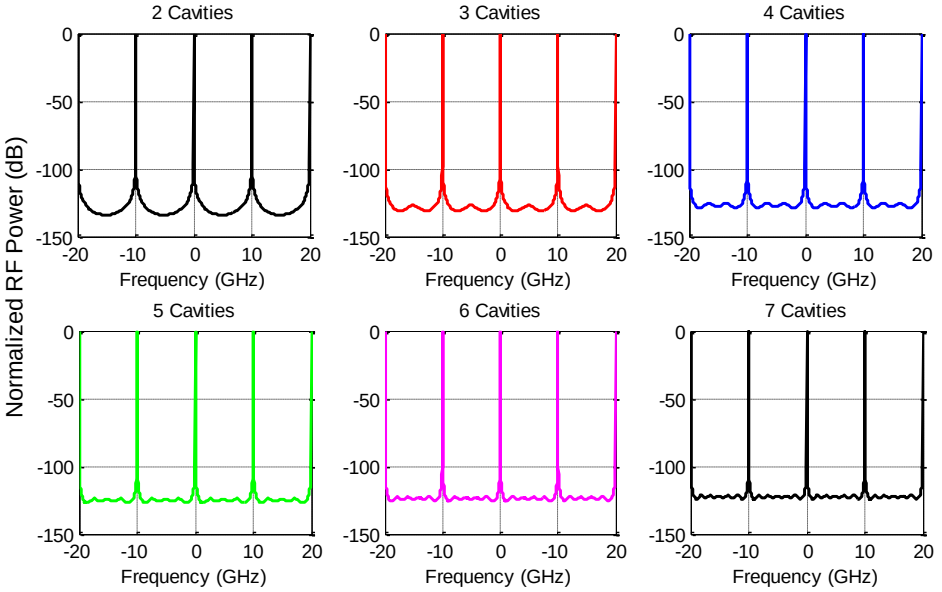

Fig. 6.11. Oscillation spectra for a multi-cavity Vernier OEO using a 20-meter 7-core homogeneous fiber.

It is remarkable that in all cases the overall coupled cavity free spectral range is 10 GHz, despite the fact that the free spectral range values for the individual cavities are around 10 MHz. In consequence, mode selection does not require a selective RF filter since a bandwidth of 1 GHz is more than enough to select the 10-GHz oscillation line. Adding more cavities apparently results in a reduction in the oscillation linewidth. An interesting feature of this configuration is that the spurious modes generated in this OEO configuration are further rejected by increasing the number of the involved cavities. As in the former case, we also computed the phase noise spectra for standard noise (ρ_n = -180 dBm/Hz), RF gain (G_a = 10) and oscillation power (P_{osc} = 16 dBm) values. The results are almost independent from the number of cavities as these are very similar in length. For instance, when two cavities are considered, the longest one is 20.02 m, while for the case of seven cavities, the longest one is 20.12 m. Under these conditions and bearing in mind that it is the longest cavity that dictates the noise linewidth, the differences can be considered negligible. Figure 6.12 shows,

as a representative example, the phase noise spectra for the case of 7 cavities. The phase noise decreases from -102 dBc/Hz at 10 kHz to -141 dBc/Hz at 1 MHz, which is almost a 20-dB/decade reduction. The phase noise curves for the different cavity configurations are all overlapped and no difference is appreciable, as the FSR ranges from 10.334 down to 10.280 MHz for the 2- up to the 7-cavity cases, respectively.

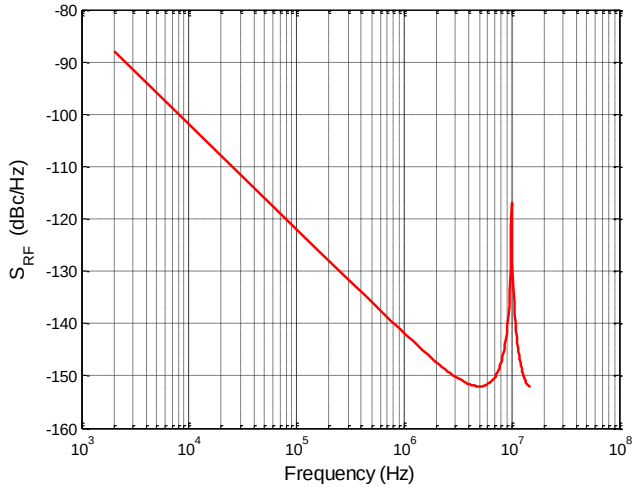

Fig. 6.12. Phase noise spectra computed for a multi-cavity Vernier OEO using a homogeneous MCF for standard noise (ρ_n = -180 dBm/Hz), RF gain (G_a = 10) and oscillation power (P_{osc} = 16 dBm) values.

6.2.3.2.2. Based on heterogeneous multicore fibers

Tunable multi-cavity OEOs can be implemented by using TTDLs built upon heterogeneous MCFs. In this configuration, the Vernier effect is achieved by the different group delays that characterize each one of the cores. Figure 6.13 shows the basic concept beyond the proposed configuration.

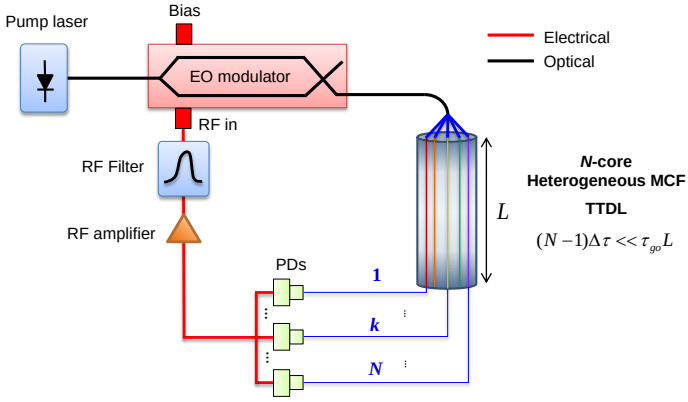

Fig. 6.13. Multi-cavity Vernier OEO configuration using a heterogeneous MCF.

Following a procedure analogous to the homogeneous MCF Vernier OEO, the oscillation frequency must satisfy, for each core *n*,

$$f_o = \frac{m_n}{\tau_{go,n} L}, \tag{6.16}$$

where $\tau_{go,n}$ is the group delay per unit length of core n. In order to have Vernier operation at this frequency, the incremental phase shift introduced by each cavity must provide constructive interference. Hence,

$$f_o = \frac{1}{\Delta\tau \cdot L}, \tag{6.17}$$

being $\Delta\tau$ the differential group delay between adjacent samples. For instance, using a first-order Taylor series expansion for the core group delays and assuming that the common group delay condition is satisfied at an anchor wavelength λ_0, the differential group delay at an operation wavelength λ is given by $\Delta\tau = \Delta D(\lambda - \lambda_0)$, being ΔD the incremental dispersion parameter between adjacent samples.

Since $\Delta\tau$ could be in the order of up to tens of ps/km, the fulfillment of Eq. (6.17) for GHz-frequency resonances will lead to multi-km cavity lengths, leading to lower phase-noise characteristics as compared to homogeneous MCF OEO designs. For example, for an oscillation frequency f_o = 10 GHz and a MCF featuring τ_{go} = 5 ns/m and ΔD = 1 ps/km/nm, Eq. (6.17) gives $L(\lambda - \lambda_0) = 10^2$ km·nm. Therefore, one possible solution is given by L = 5 km and $(\lambda - \lambda_0)$ = 20 nm. Figure 6.14 shows the oscillation spectra for this example computed from Eq. (6.4) when a heterogeneous 7-core fiber is considered and the number of parallel cavities ranges from 2 to 7.

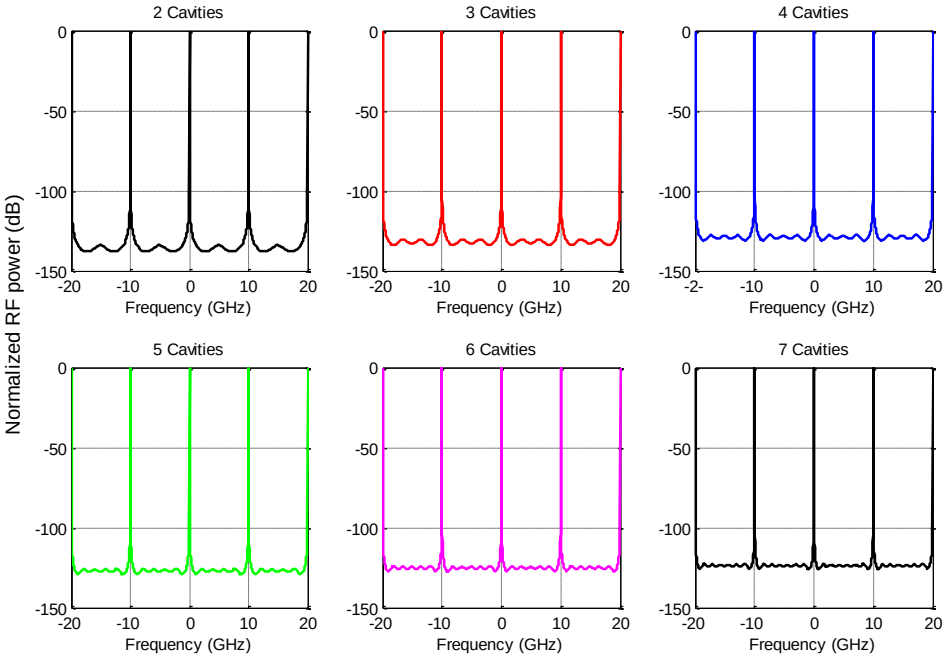

Fig. 6.14. Oscillation spectra for a multi-cavity Vernier OEO using a 5-km 7-core heterogeneous fiber.

In all cases, again, the overall coupled cavity FSR is 10 GHz despite the fact that the free spectral range values for the individual cavities are in the order of a few kHz. In consequence, mode selection does not require a selective RF filter since a bandwidth of 1 GHz is more than enough to select the 10-GHz oscillation line. As in the homogeneous MCF case, adding more cavities results in a reduction of the oscillation linewidth. Again, as in the former case, we also computed the phase noise spectra for standard noise (ρ_n = -180 dBm/Hz), RF gain (G_a = 10) and oscillation power (P_{osc} = 16 dBm) values. The results are almost independent of the number of cavities as these provide almost the same delay. Figure 6.15 shows, as a representative example, the phase noise spectra for the case of 7 cavities, where phase noise changes from -110 dBc/Hz at 100 Hz to -150 dBc/Hz at 10 kHz.

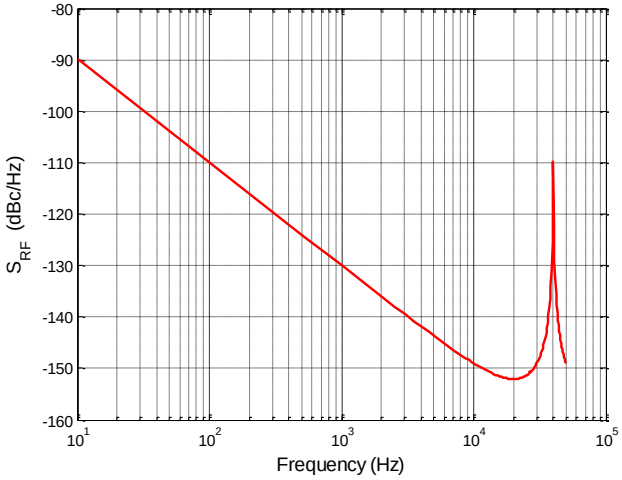

Fig. 6.15. Phase noise spectra computed for a multi-cavity Vernier OEO implemented with a heterogeneous MCF using standard noise (ρ_n = -180 dBm/Hz), RF gain (G_a = 10) and oscillation power (P_{osc} = 16 dBm) values.

A distinctive feature of this OEO is the possibility of tuning the oscillation frequency by changing the operation wavelength of a tunable laser. For the example considered above, the specific relationship is f_o = 200 GHz/(λ - λ_0), where (λ - λ_0) is expressed in nm. Figure 6.16 shows this relationship (left) and the oscillation frequencies (right) in between 10 and 20 GHz, computed from Eq. (6.4) for a set of values of (λ - λ_0).

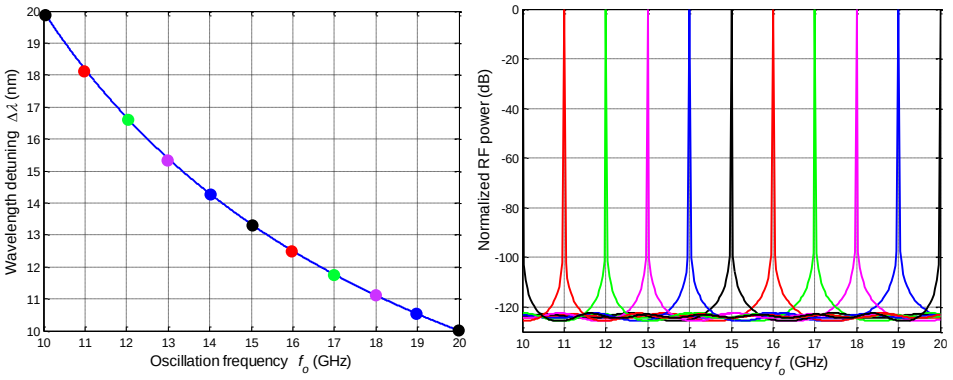

Fig. 6.16. (Left) Oscillation frequency versus wavelength detuning and (Right) set of possible oscillation frequencies for a Vernier multi-cavity OEO based on a 7-core heterogeneous fiber for τ_{go} = 5 ns/m, ΔD = 1 ps/km.nm and L = 5 km.

6.2.3.3. Experimental demonstration

We have experimentally demonstrated both unbalanced dual-cavity and multi-cavity Vernier OEO configurations implemented over a commercial homogeneous 7-core fiber. We use a 20-m-long section of the Fibercore MCF spliced to a couple of fan-in/fan-out devices (see Annex II for further information about the fiber). The fan-in/fan-out devices are provided by Optoscribe and have a maximum level of insertion loss of 2.5 dB in each way, including additional 1-dB losses due to the MCF splices. The measured intercore crosstalk, considering both the fan-in/fan-out devices and the MCF, is lower than -50 dB, low enough to assure independent cavity transmission.

Figure 6.17 shows the experimental setup for dual-cavity unbalanced operation, where 3 different configurations were implemented: 1- and 6-core cavities (k_1 = 1) corresponding to 20- and 120-m cavities; 2- and 5-core cavities (k_1 = 2) corresponding to 40- and 100-m cavities; and 3- and 4-core cavities (k_1 = 3) corresponding to 60- and 80-m cavities. To compensate for the optical losses, mainly due to the fan-in/fan-out devices, optical amplification stages of 20 and 40 dB were included, respectively, in the short and long loops. A 1-nm-bandwidth optical filter is placed at each loop before photodetection to suppress the residual phase noise of the EDFAs. After detection and RF amplification, a tunable RF filter centered at 4.5 GHz with a bandwidth of 5 MHz allows for single-mode oscillation. A power splitter is set at the output of the RF filter to allow the continuous monitoring of the RF spectrum. The cavity gain control is carried out by placing variable optical attenuators before photodetection.

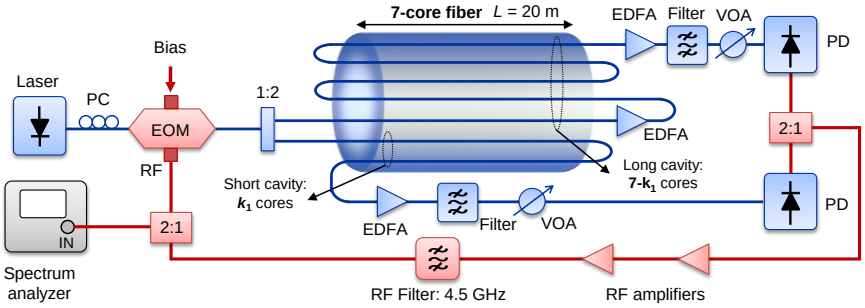

Fig. 6.17. Experimental setup for the dual-cavity unbalanced OEO over a 20-meter 7-core fiber. We demonstrated three different configurations: 1- and 6-core cavities (k_1 = 1), 2- and 5-core cavities (k_1 = 2), 3- and 4-core cavities (k_1 = 3). PC: polarization controller, RF: radiofrequency, EOM: electro-optic modulator, EDFA: Erbium-doped fiber amplifier, VOA: variable optical attenuator, PD: photodetector.

Figure 6.18 shows the experimental setup used to build a 3-cavity Vernier OEO with the 7-core fiber. Since we use a homogeneous MCF, the slightly different delays of the cavities can be obtained by adding an incremental length ΔL to each cavity, which can be done compactly by properly designing the physical length of each fan-in/fan-out arm. For simplicity, we have used a 3-m standard singlemode fiber to produce the required incremental delay between cavities, and variable delay lines to finely adjust the delay difference between cavities. Again, 20-dB optical amplification is included in each loop to compensate the insertion losses of the system. Once the signals have been photodetected, coupled together and amplified, a 4.4 to 5.0 GHz tunable RF filter with a 30-MHz bandwidth selects the desired oscillation frequency.

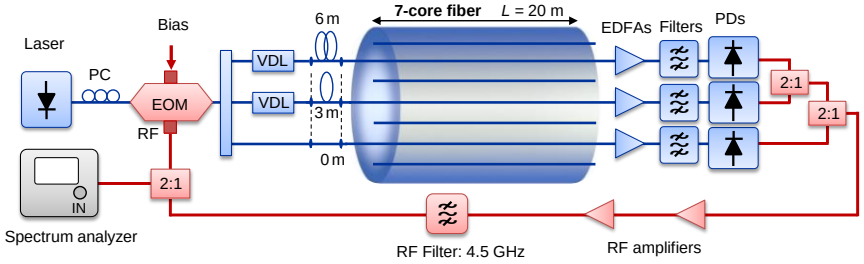

Fig. 6.18. Experimental setup for the multi-cavity Vernier OEO over a 7-core fiber. We compared both 2- and 3-cavity OEOs. PC: polarization controller, RF: radiofrequency, EOM: electro-optic modulator, VDL: variable delay line, EDFA: Erbium-doped fiber amplifier, VOA: variable optical attenuator, PD: photodetector.

Figure 6.19 illustrates the measured RF oscillation spectra for the 3 dual-cavity unbalanced configurations around a central frequency of 4.5 GHz: (a, d) 1- and 6-core cavities (k_1 = 1); (b, e) 2- and 5-core cavities (k_1 = 2) and (c, f) 3- and 4-core cavities (k_1 = 3). The upper figures (a-c) show the spectrum of each individual cavity in isolation and the lower figures (d-f) the spectra for the dual-loop OEOs, each one for 3 consecutive oscillating frequencies given by 3 different frequency tuning positions of the RF filter (blue, yellow and orange curves). We see how the oscillating frequencies correspond to those modes that are, at the same time, fulfilling the

oscillation conditions in the short and long loops, leading to a dual-loop spectrum periodicity of 6.7, 11.4, and 11.3 MHz, respectively for k_1 = 1, 2 and 3.

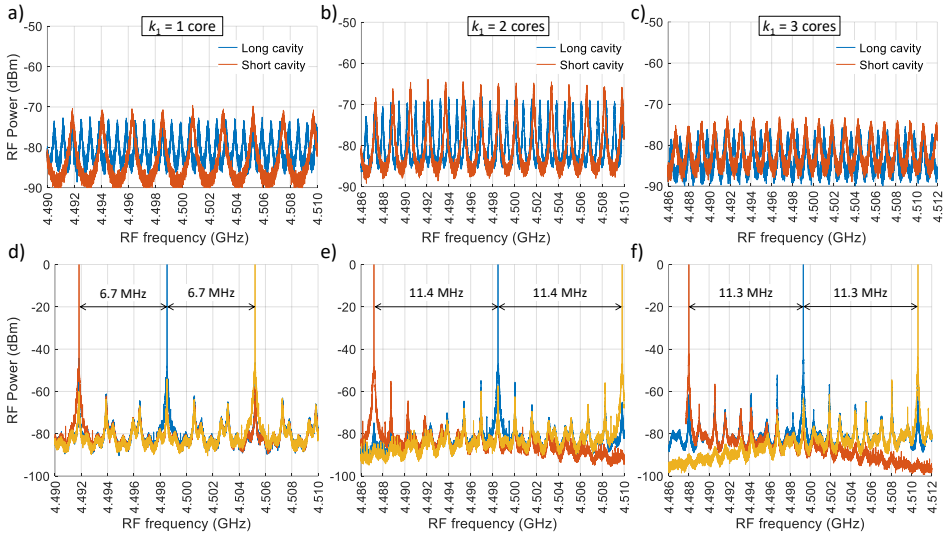

Fig. 6.19. Experimental oscillation spectra of a dual-cavity unbalanced OEO using a 20-meter 7-core fiber for three different configurations: (a, d) 1- and 6-core cavities (k_1 = 1); (b, e) 2- and 5-core cavities (k_1 = 2); (c, f) 3- and 4-core cavities (k_1 = 3). Upper figures correspond to the cavities in isolation and lower figures to the resulting dual-loop OEO.

We have also measured the oscillation frequencies of the 2- and 3-cavity Vernier OEOs. Figure 6.20(a) illustrates the measured spectrum for each isolated cavity, where we see, as expected, that the oscillation condition is not fulfilled as the open loop gain of each cavity is less than unity. With the help of the VDLs placed at the first and second cavities, we matched the oscillating modes of all cavities at the frequency located near 4.494 GHz. The resulting spectrum of the oscillating mode at 4.494 GHz for both the 2- and 3-loop OEOs are compared in Fig. 6.20(b). An important reduction of 10 dB is observed at the spurious peaks corresponding to the minor oscillating modes of the single cavities when increasing the number of cavities to 3. After finely adjusting the delay of each cavity, the single-loop delays are 499.2, 482.9, and 466.6 ns, respectively, for isolated cavities 1, 2 and 3. Figures 6.20(c) and 6.20(d) show 3 consecutive oscillating modes for the 2- and 3-loop Vernier configuration, respectively. As expected from Eq. (6.15), both the 2- and 3-cavity FSRs are identical with a value of 61 MHz. The 30-MHz RF filter bandwidth is then, by far, sufficiently narrow to allow single-mode oscillation for the Vernier OEO. We observe that increasing the number of cavities reduces the level of the minor oscillating modes of the single cavities.

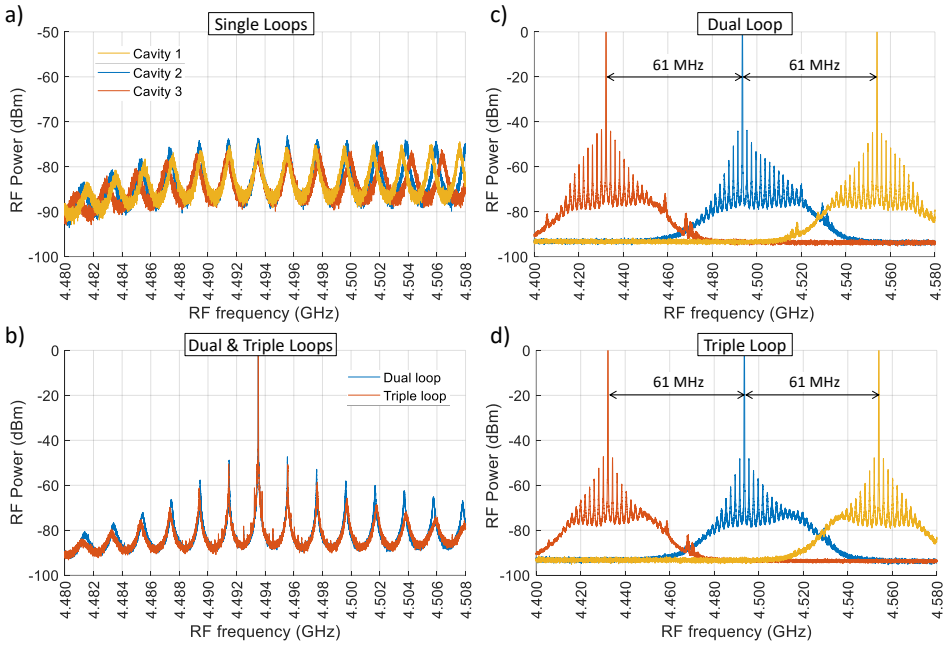

Fig. 6.20. Experimental oscillation spectra of a multi-cavity Vernier OEO using a 20-meter 7-core fiber for (a) each of the 3 cavities in isolation, (b) dual- versus triple-loop configurations, and 3 consecutive oscillation frequencies for (c) dual- and (d) triple-loop OEOs.

The measured phase noise spectrum for a representative case (k_1 = 2) of the unbalanced OEO is shown in the left part Fig. 6.21. As expected, the measured phase noise of all 3 unbalanced configurations behave similarly. A phase noise around -90 dBc/Hz is achieved at a 10-kHz offset from the carrier, while it is downshifted below -125 dBc/Hz above 1 MHz. The high level of phase noise for frequency offsets below 10 kHz can be explained by different causes. First, possible fluctuations of the pump current applied to the EDFAs may contribute to the phase noise in the low-frequency region, [159]. This is particularly important in the long cavity since it requires a double-stage EDFA. Moreover, the phase noise performance is degraded by fluctuations that may occur in both fiber loops and the RF delay, as well as by the lack of proper setup environmental isolation. The spurs observed for frequency offsets above 1 MHz, corresponding to the minor oscillation modes, are below -95 dBc/Hz.

The right part of Fig. 6.21 shows the measured phase noise spectrum of both 2- and 3-cavity Vernier OEO configurations, which exhibit very similar responses. In both cases, we observe a -85-dBc/Hz phase noise level at a 10-kHz offset from the carrier, while it decreases down to -130 dBc/Hz for a 1-MHz offset. The main difference is the 10-dB reduction in the spurious peak level above 1 MHz (i.e., the minor oscillating modes of the single cavities) when the number of cavities increases from 2 to 3, as reported in [160, 161]. This fact relates to the spectral purity of the oscillating mode, as we have theoretically evaluated in section 6.2.3.2.1.b).

Although the phase noise values of both unbalanced and Vernier schemes are, in principle, not comparable to those reported for ultra-low phase noise OEOs, [162], they can be reduced by using low-residual phase noise components (RF amplifiers and photodetectors) and by reducing the optical losses and thus suppressing the need for optical amplifiers. In addition, the phase noise performance can be improved if we use a laser with lower RIN and higher optical power, a Mach-Zehnder modulator with a lower V_π value or a photodiode with better responsivity, [162]. Although the use of 1-nm-bandwidth optical filtering reduces the ASE noise induced by the EDFAs, we still observe a considerable noise level. We observe this more clearly in the unbalanced configuration since a double-stage EDFA amplification is placed in the long loop. In the multi-cavity Vernier OEO, we can improve the spectral purity of the oscillation by increasing the number of cavities, while we can further diminish the phase noise level by increasing the MCF length. As opposed to single-cavity OEOs, this will not alter the FSR of the OEO that will actually be preserved by the Vernier effect, as Eq. (6.15) shows. In contrast, the unbalanced OEO could not benefit from a fiber length increase since it is configured using a relatively small number of cores and, therefore, it is inherently linked to shorter cavity lengths to avoid the use of RF filters with extremely high selectivity. In that case, by increasing the number of cores, the length of the long cavity could be considerably increased as compared to the short one, improving as a consequence the phase noise performance.

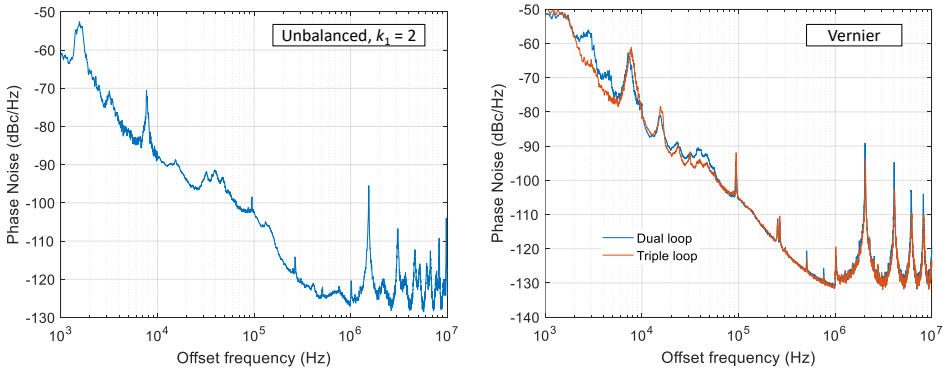

Fig. 6.21. Experimental phase noise of the multi-cavity OEO for (Left) dual-cavity unbalanced OEO with 2- and 5-core cavities (k_1 = 2), and (Right) 2- and 3-cavity Vernier configurations.

6.3. Few-mode fiber approaches

In the case of the FMF technology, we have experimentally evaluated the performance of the fabricated FMF-based TTDL in the context of MWP signal filtering. As we saw in chapter 5, this TTDL consists of a 44.4-m link of a commercial step-index FMF with a set of 3 LPGs inscribed at specific locations along the fiber. At the fiber output, it provides 4 signal samples (each one corresponding to a different LP mode) with a constant differential delay between them. Due to the lack of wavelength tunability –and, thus, delay tunability– of this TTDL, we performed a single experiment as a proof-of-concept demonstration. The optimum operation

wavelength of this TTDL corresponds to that in which the three LPGs provide almost a -3-dB mode conversion efficiency, what occurs at λ_0 = 1558 nm. At this wavelength, the sample differential delay is $\Delta\tau$ = 100 ps, what translates into a RF filtering FSR of 10 GHz. Note that the lack of wavelength tunability implies that the wavelength-diversity operation regime cannot be exploited, so we restrict our experiments to the space-diversity operation regime.

Figure 6.22 depicts the experimental setup for measuring the RF filter response, where we consider two different scenarios. In the first scenario, we evaluate the filter transfer function of the TTDL in isolation, where the 44.4-m processing FMF segment was directly spliced to both mode multiplexers (upper arm at the FMF input in Fig. 6.22). Here, the optical signal coming from a broadband source followed by a 0.1-nm-bandwith optical filter is amplified by an EDFA and then modulated in single-sideband by an electro-optical intensity modulator with the RF signal generated by a vector network analyzer. An additional polarization controller at the TTDL input sets the optimum polarization required for the subsequent LPG mode conversions. The signal is then injected to the fundamental mode of the FMF, which properly distributes the signal to the rest of modes through the LPGs. After the TTDL, all 4 output modes are demultiplexed and coupled together before detection. We include VDLs at the TTDL output to compensate any small inference to the desired DGDs that is not produced by the TTDL itself but by external mismatches (as, for instance, those produced by inevitable differences in the fiber lengths of the coupler arms), while VOAs finely equalize the sample output powers for uniform windowing. We must note that, since we are using direct detection without MIMO signal processing, there is a strong coupling between the degenerate modes that cannot be avoided and, therefore, it is preferable to select the degenerate mode that carries most of the optical power associated to that sample. In our work, the majority of the power was received in LP_{11a} and LP_{21a} modes with a low level of losses. In a real application scenario, optical or electrical diversity combining techniques could be introduced to combine the degenerate modes properly, [163].

In the second scenario, we included a 1-km FMF link before the TTDL (lower arm at the FMF input in Fig. 6.22) to emulate a distribution link that may be required in a real MWP scenario, such as radio access networks for wireless communications. At the TTDL operation wavelength, this additional link propagates only the fundamental mode LP_{01} to preserve the TTDL performance. We must note that at any other wavelength outside the operation spectrum of the set of inscribed LPGs, all LP modes can behave as mere distribution channel media (i.e., avoiding any signal processing) without any significant degradation caused by the LPGs. This suggests the potential use of different optical wavelengths for the simultaneous implementation of both parallel distribution and processing functionalities.

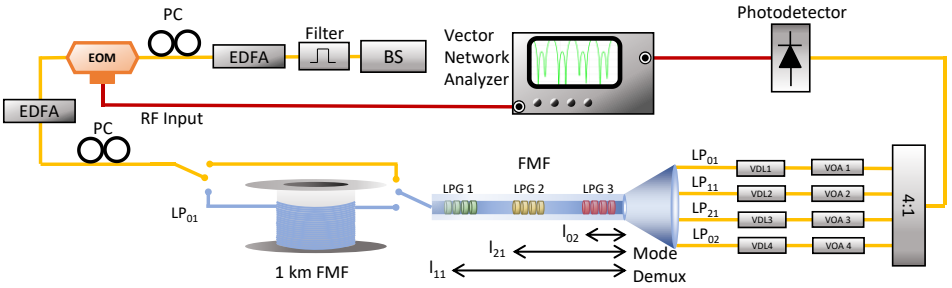

Fig. 6.22. Experimental setup for MWP signal filtering based on the 4-sample FMF TTDL. BS: broadband source; EDFA: Erbium-doped fiber amplifier; EOM: electro-optic modulator; PC: polarization controller; VDL: variable delay line; VOA: variable optical attenuator.

Figure 6.23 shows the measured RF 4-tap filter transfer function for both scenarios as compared to the theoretical transfer function up to an RF frequency of 40 GHz. Black-dotted, green-dashed and red-solid lines correspond to the computed ideal response with uniform sample distribution, the first scenario and the second scenario, respectively. We see that the experimental results in both scenarios are in a good agreement with the theoretical ones. Slight discrepancies in the main-to-sidelobe levels come as a consequence of random variations in the TTDL sample amplitudes that may be produced mainly by: (1) small temperature variations or vibrations that affect the mode conversion efficiency of the LPGs since these are not protected by any fiber coating; and (2) low intermodal crosstalk between the LP groups of modes, which is more significant (as expected) when we introduce the 1-km FMF link.

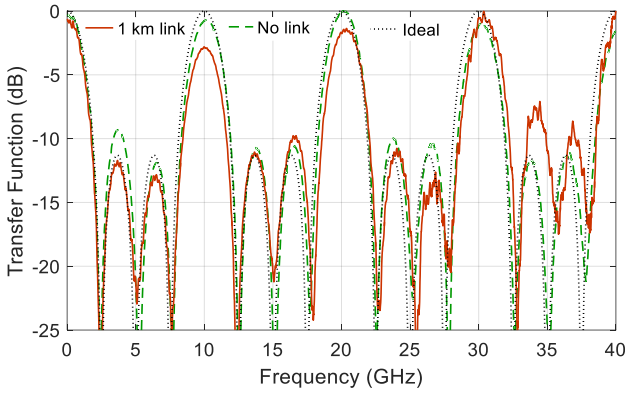

Fig. 6.23. Measured MWP filter transfer function for both scenarios. Black-dotted line: theoretical response; green-dashed line: measured response for the TDDL segment (first scenario); red-solid line: measured response for 1-km FMF link + TTDL segment (second scenario).

6.4. Conclusions

In this chapter, we have presented the application of different TTDL solutions, based on either MCF or FMF links, to a set of representative scenarios of distributed radiofrequency signal processing.

Starting with the MCF-based approaches, we have experimentally demonstrated reconfigurable RF signal filtering in both spatial and wavelength diversity domains, as well as optical beamforming networks for phase array antennas, by applying the TTDL implemented with the customized heterogeneous MCF manufactured by YOFC. For the filtering experiment, we successfully demonstrated 5-sample operation in the spatial-diversity regime by using cores 3-7, where the filter FSR was tuned from 6.7 GHz up to the mm-band by changing the operation wavelength from 1560 nm down to 1530 nm. In the wavelength diversity experiment, the filter FSR was tuned either by changing the wavelength separation between elements of the 4-laser array or by choosing a different core. In the beamforming experiment, we saw that the beam-pointing angle of the 5-element antenna created by cores 3-7 in the spatial-diversity domain can be continuously tuned along the whole angular plane by properly changing the operation wavelength in a 20-nm range. We have also proposed the use of both homogeneous and heterogeneous MCFs for the implementation of multi-cavity optoelectronic oscillators. Since all the cavities are hosted within the same cladding, this approach provides a fiber integrated medium for enhancing the OEO relative stability against environmental and mechanical fluctuations. Design equations and examples have been presented that show the potential of unique performance in terms of spectral selectivity, tunability and high-frequency operation. Homogeneous MCFs allow both for highly unbalanced two-cavity OEOs as well as for multi-cavity Vernier OEO operation where moderate and long cavity lengths (> 2 m) are compatible with a high-spectral purity and multi-GHz oscillation mode spectral separation. OEOs based on heterogeneous MCFs allow for ultralong cavity length (> 1 km) compatibility with high-spectral purity and multi-GHz oscillation mode spectral separation, while provide much lower phase noise operation. In addition, they bring the potential of featuring the tunability of the oscillation frequency by feeding the OEO system with a wavelength-tunable laser. We have experimentally demonstrated, for the first time to our knowledge, the implementation of multi-cavity OEOs built upon a 20-m long commercial homogeneous 7-core fiber. We have been successfully demonstrated both unbalanced 2-cavity and multi-cavity Vernier OEO configurations.

For the FMF approach, we have experimentally demonstrated RF signal filtering on a FMF-based sampled TTDL. We implemented a 4-tap RF filter with an FSR of 10 GHz upon the 44.4-m FMF processing device described in the previous chapter. In addition, we successfully demonstrated that this TTDL can coexist in short-reach radio-over-fiber scenarios, such as a radio access networks, where an additional distribution link may be required, showing no significant degradation over the TTDL performance. Since the use of a non-customized FMF restricted the TTDL operation regime to a single operating wavelength, (where the three LPGs provide a -3-dB mode conversion efficiency), delay line tunability has not been addressed. This experiment must be seen as a consequence as a proof-of-concept validation. The experimental demonstration of a tunable FMF-based TTDL requires the fabrication of a custom FMF and the inscription of broadband LPGs as mode converters, as we saw in chapter 4, and is left to future research work.

Chapter 7
Summary, conclusions and future lines

7.1. Summary and conclusions

We have proposed, for the first time to our knowledge, a new approach for the implementation of sampled true time delay lines for radiofrequency signals built upon SDM fibers. The TTDL is implemented by using a single optical fiber, either a FMF or a heterogeneous MCF, where the different spatial paths are provided either by the cores of the MCF or by the modes of the few-mode fibers. They offer unique 2D and reconfigurable true time delay operation by exploiting both spatial- and wavelength-diversity domains in a broad optical wavelength range of operation. We fabricated two different MCF-based TTDLs and a FMF-based TTDL device that have been successfully applied to experimentally demonstrate different MWP signal processing functionalities built upon a single SDM fiber.

In chapter 2, we reviewed the fundamentals of MWP signal processing systems and described the key element that take place in almost every MWP signal processor: the optical TTDL. Optical beamforming networks for phased array antennas, MWP signal filters or multi-cavity optoelectronic oscillators are some examples that benefit from TTDL operability. We also revised the state-of-the-art of SDM fibers, focusing on both multicore and few-mode fiber technologies.

The electromagnetic wave propagation in SDM fibers play an important role in the design of the proposed TTDLs and has been studied on chapter 3. First, we characterized the wave propagation in the uncoupled mode regime as the modal solutions of the unperturbed wave equation. We proposed, for the first time to our knowledge, a theoretical model deriving the universal characteristic equation for multi-layer optical fibers whose refractive index profile comprises any number of concentric circular layers with arbitrary radial dimensions and refractive index

values. The developed universal characteristic equation provides outstanding insights for the modal propagation in optical fibers. It will benefit a variety of optical communications and signal processing scenarios where multi-layer fibers are particularly needed, such as space- and mode-division multiplexing, fiber sensing, optical interconnects, loss and dispersion management, as well as high-power amplifiers and lasers. In second place, we introduced the modal coupling effect and its impact on spatially multiplexed systems. We reviewed the basic concepts behind crosstalk between the spatial paths in both multicore and few-mode fibers by means of the CMT and the CPT.

In Chapter 4, we presented the concept for TTDL operation in each fiber. For the MCF approach, 7-sample operation was developed on a heterogeneous trench-assisted 7-core fiber link, where each core featured an independent group delay. By suitable modifications of the material composition and the radial dimensions of each core trench-assisted step-index profile, we obtained a particular set of cores that satisfied a common group delay with linearly incremental chromatic dispersions at an anchor wavelength. The optimization of the higher-order dispersion parameter ensured a large operability wavelength range. In the case of the FMF solution, we proposed to achieve the required control over both the group delay and the chromatic dispersion of the signal samples by the custom design of a ring-core step-index FMF where the inscription of a series of LPGs allows to excite higher-order modes at specific longitudinal locations along the fiber. In particular, we designed a 4-sample TTDL approach that combines the design of a 7-LP-mode ring-core fiber and the inscription of 5 LPGs. In this solution, the wavelength operability range will be limited by the spectral width of the inscribed broadband LPGs, which could reach up to a 20-nm range.

In addition, we studied the main sources of impairment that can affect the performance of the proposed TTDLs. One of the most important adverse effects relates to fiber curvatures and twists. We theoretically and experimentally evaluated how fiber bending and twisting induce group delay variations between cores in a MCF. We obtained analytical expressions for the computation of the bend-induced DGD accumulated on a given fiber length for a constant twist rate, which have been experimentally verified. Although the analysis of the effect of fiber curvatures showed an important variability on the sample group delays that could deteriorate the performance of the TTDL (especially in the MCF case), we concluded that twists that will take place in a real deployment will compensate this detrimental effect.

The particular design, fabrication and characterization of different TTDLs was carried out in chapter 5. Regarding MCFs, we designed and fabricated two different heterogeneous 7-core trench-assisted fibers that operate as sampled TTDLs. The first one was fabricated by the Chinese company YOFC with a length of 5 km. Each core featured an independent refractive index profile by suitable modifications of the core material composition and the radial dimensions of core and trench, so that it required 7 different preforms (1 preform per core), what considerably increased the fabrication costs. The second MCF was fabricated in collaboration with CREOL at the University of Central Florida, during my 3-month stay. Here, with a 3-km length, a single preform was shared between all the cores to reduce the fabrication costs. The

TTDL characteristics for the cores were achieved by properly scaling the radial dimensions of the preform. The fabrication costs were one order of magnitude lower in the CREOL fiber than in the YOFC fiber, but in compromise with the TTDL performance. We characterized the performance of the YOFC fiber and we observe that although the first two cores were more affected by fabrication, cores 3-7 behaved as designed, guarantying 5-sample TTDL operation up to a 30-nm range. We left the characterization of the CREOL fiber to a future line due to the absence of adequate fan-in fan-out devices at that time.

In the case of FMFs, we proposed and experimentally demonstrated a new approach for 4-sample TTDL operation. The TTDL was fabricated by using a 4-LP-mode commercial FMF, provided by *Prysmian* company. Although the use of a non-customized FMF limited the performance of the TTDL to single-wavelength operation, in this preliminary approach our goal was to demonstrate the ability of the LPGs to excite higher-order modes selectively and properly manage the time delay of the samples. While only the fundamental mode is injected at the fiber input, a set of 3 LPGs excite the remaining LP modes at convenient longitudinal positions so that the sample delays are adjusted to provide a constant differential delay. The inscription of the LPGs was carried out in our laboratories, in collaboration with our colleagues from the fiber grating research line. We successfully demonstrated TTDL operation at the optical wavelength of 1558 nm.

Finally, in chapter 6, we experimentally demonstrated the implementation of specific MWP signal processing functionalities over SDM fibers. We successfully demonstrated reconfigurable RF signal filtering in both space- and wavelength-diversity domains, as well as optical beamforming networks for phase array antennas by using the YOFC multicore fiber. For the space-diversity experiments, we show that by varying the operation wavelength in a 20-nm range, we were able to tune the filter FSR and the beampointing angle for the phased array antennas in a continuous way, while in the wavelength-diversity experiments the tunability was achieved either by varying the wavelength spacing between the optical sources or by choosing a different core. We also proposed the use of both homogeneous and heterogeneous multicore fibers for the implementation of multi-cavity optoelectronic oscillators. Since all the cavities are hosted within the same cladding, this approach provides a fiber integrated medium for enhancing the OEO relative stability against environmental and mechanical fluctuations. We experimentally demonstrated, for the first time to our knowledge, the implementation of multi-cavity OEOs built upon a 20-m long commercial homogeneous 7-core fiber. Both unbalanced 2-cavity and multi-cavity Vernier OEO configurations have been successfully demonstrated. Finally, we have experimentally demonstrated RF signal filtering on a FMF-based sampled TTDL. We implemented a 4-tap RF filter upon the FMF processing device fabricated on a 4-LP-modes fiber.

In summary, we have proposed a new approach for tunable sampled TTDL operation, basis of many MWP signal processing functionalities, built upon a single SDM fiber. The proposed TTDLs are a compact and versatile solution to provide, in a single optical fiber, both signal distribution and signal processing functionalities. A wide range of RF signal processing applications, such as tunable microwave signal

filtering, optical beamforming for phased array antennas, multi cavity optoelectronic oscillation or arbitrary waveform generation, can be implemented by this approach. It can be applied, in addition, to a wide range of optical or RF signal processing systems that require to modify/compensate the chromatic dispersion or group delay in both analogue and digital communications.

7.2. Future lines

Despite the considerable amount of work carried out during this PhD Thesis in the field of fiber-distributed signal processing, there are still some issues that have to be addressed and several future lines of research that can be performed during the next few years:

- Development of a specific tool for the dynamic control over the sample group delays at the anchor wavelength. Up to date, our experiments have been done in laboratory conditions, where we have full control over the transmission link. However, in real scenarios, we must deal with several issues related to time-delay performance stability in distributed signal processing applications. We saw in chapter 4 that TTDLs for RF signals are very sensitive to slight variations on the sample differential time delays due to fiber curvatures and twists or changes on the environmental conditions (specially for the FMF approach). A dynamic control and optimization mechanism over the sample group delays at the anchor wavelength could further overcome these limitations. In that sense, the development of a specific tool to automatically control and reconfigure the external variable delay lines to maintain a group delay stability at the anchor wavelength could be a promising solution.

- The characterization of the fabricated CREOL multicore fiber and the proof-of-concept demonstration of MWP signal processing functionalities among it. The CREOL fiber was designed and fabricated as a cost-saving solution to facilitate the adoption of these novel TTDLs. However, up to date, we have not been able to test the fiber and compare its performance with the YOFC fiber due to the absence of proper fan-in/fan-out devices to inject/extract the light into/from the MCF.

- The experimental validation of multi-cavity OEOs implemented with heterogeneous MCFs. Both the CREOL and the YOFC fibers could be used to demonstrate multi-cavity OEOs implemented by heterogeneous MCF-based TTDLs.

- The experimental demonstration of other MWP signal processing applications. In this Thesis, we demonstrated RF signal filtering, optical beamforming for phased array antennas and multi-cavity optoelectronic oscillation implemented over MCFs, as well as RF signal filtering on a FMF processing device. One of the experiments that is still pending is the demonstration of wireless transmission in optical beamforming networks in a MWP scenario (i.e., including a set of antenna elements to implement the

beamforming network). Other MWP signal processing functionalities, such as arbitrary waveform generation for microwave and millimeter-wave signals, [138], or time-stretched analog-to-digital converters, [22], could also be demonstrated among the proposed TTDLs.

- Evaluation of the sample group delay and chromatic dispersion dependence with temperature variations. Slight temperature variations along the fiber link could induce non-desired time-delay fluctuations on the TTDL samples. In that sense, it would be desirable to evaluate experimentally the sample group delay and chromatic dispersion dependence with temperature variations.

- Fabrication of chirped LPGs to increase the spectral bandwidth of the LPG mode converters. Chirped LPGs will be required for the implementation of tunable FMF-based TTDLs. Further research has to be carried out to improve the grating fabrication process and allow the inscription of broadband LPGs that behave as selective mode converters in customized FMFs.

- The fabrication of a custom FMF along with the inscription of LPGs for tunable sampled TTDL operation over FMFs. Customized FMF approaches are required to ensure time-delay tunability on the TTDL. The fabrication of the ring-core FMF designed in chapter 4, together with the broadband LPG inscription, could provide the desired TTDL tunability.

- Look for MCF designs with higher number of cores. Increasing the number of cores has been the tendency in the past years to increase the fiber capacity transmission. Similarly, we can increase the number of samples available in the TTDL by designing dispersion-engineered MCFs with a higher number of cores. For instance, we could look for a design of up to 19 cores whose chromatic dispersions vary from 12 up to 21 ps/km/nm with an incremental dispersion parameter of 0.5 ps/km/nm. The number of different preforms in this case must be optimized as to avoid a substantial increase in manufacturing costs and complexity.

Annex I:
Commercial fibers and multiplexing devices data

A.I.1. Prysmian few-mode fiber and Cailabs mode multiplexers

The Prysmian few-mode fiber has a step-index refractive index profile composed of a 15-μm-diameter core surrounded by a 150-μm-diameter cladding, with a core-to-cladding relative index difference of 0.73% at an optical wavelength λ = 1550 nm. It supports 4 LP modes in the C band. Large effective index differences ($> 0.8 \cdot 10^{-3}$) between the non-degenerated modes ensures low mode coupling (< -30 dB/km). Below we can see the typical optical characteristics of the fiber modes (Table A.I.1) and the measured insertion losses (Table A.I.2) and intermodal crosstalk (Table A.I.3) for a 20-m Prysmian FMF spliced to the Cailabs mode multiplexers. Note that the Cailabs multiplexers cannot distinguish between the degenerated modes of an LP mode.

Table A.I.1. Typical values for the optical characteristics of the Prysmian FMF at λ = 1550 nm.

Attribute	LP_{01}	LP_{11}	LP_{21}	LP_{02}
Differential group delay with respect to LP_{01} (ps/m)	-	4.4	8.9	7.9
Chromatic dispersion (ps/km/nm)	21	26	19	8
Attenuation (dB/km)	≤ 0.25	≤ 0.25	≤ 0.25	≤ 0.25

Table A.I.2. Measured insertion losses (in dB) for a 20-m Prysmian FMF spliced with the Cailabs multiplexers at λ = 1550 nm.

Mode In	LP_{01}	LP_{11a}	LP_{11b}	LP_{21a}	LP_{21b}	LP_{02}
Insertion Losses (dB)	7.2	8.2	7.8	7.2	7.5	6.7

Table A.I.3. Measured intermodal crosstalk (in dB) for a 20-m Prysmian FMF spliced with the Cailabs multiplexers at λ = 1550 nm.

Mode In\out	LP_{01}	LP_{11a}	LP_{11b}	LP_{21a}	LP_{21b}	LP_{02}
LP_{01}	N/A	-26.7	-26.7	-25.4	-25.4	-22.3
LP_{11a}	-25.5	N/A	N/A	-23.3	-23.3	-23.5
LP_{11b}	-26.3	N/A	N/A	-26.1	-26.1	-26.9
LP_{21a}	-25.9	-28.2	-28.2	N/A	N/A	-29.6
LP_{21b}	-25.1	-24.5	-24.5	N/A	N/A	-30.8
LP_{02}	-21.5	-28.7	-28.7	-30.8	-30.8	N/A

A.I.2. Fibercore multicore fiber

The Fibercore multicore fiber consists of 7 homogeneous cores placed in hexagonal disposition inside a 125-μm-diameter cladding, with a core pitch of Λ = 35 μm. The cores have a step-index refractive index profile, with a core radius a = 4 μm and a core-to-cladding relative index difference Δ = 0.31%. Tables A.I.4 and A.I.5 show, respectively, the measured intercore crosstalk and insertion losses for a 5-km MCF link coiled in a 150-mm-diameter spool (including the fan-in/fan-out devices). The core numbering is depicted in Fig. A.I.1.

Table A.I.4. Measured intercore crosstalk (in dB) for a 5-km link (including the fan-in/fan-out devices) for the Fibercore MCF at λ = 1550 nm.

Core *n* In\out	1	2	3	4	5	6	7
1	N/A	-56	-60	-56	-60	-62	-63
2	-55	N/A	-66	-56	-55	-56	-56
3	-55	-65	N/A	-57	-57	-53	-62
4	-51	-55	-53	N/A	-58	-53	-49
5	-58	-58	-65	-57	N/A	-58	-58
6	-58	-61	-56	-58	-61	N/A	-59
7	-58	-57	-66	-57	-58	-66	N/A

Table A.I.5. Measured insertion losses (in dB) for a 5-km link (including the fan-in/fan-out devices) for the Fibercore MCF at λ = 1550 nm.

Core *n*	1	2	3	4	5	6	7
Insertion Losses (dB)	5.7	6.5	5.9	6.2	6.0	5.9	5.6

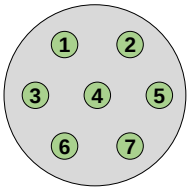

Fig. A.I.1. Core numbering for the Fibercore MCF.

Annex II:
Material databases

The refractive index dependence on the optical wavelength, $n(\lambda)$, can be modelled by means of the well-known three-term Sellmeier equation, [164]:

$$n^2(\lambda)=1+\sum_{i=1}^{3}A_i\frac{\lambda^2}{\lambda^2-B_i^2}\,, \qquad (\mathbf{A}.\text{II}.1)$$

were A_i and B_i are the Sellmeier coefficients. These coefficients have been obtained for several material compositions. Table A.II.1 summarizes the Sellmeier coefficients for the SiO_2, GeO_2, and SiO_2 doped with 1% F and 2% F concentrations, [165, 166]. The refractive index dependence on the optical wavelength for SiO_2 doped with GeO_2 can be obtained by using a linear combination of the SiO_2 and GeO_2 Sellmeier coefficients, [165]:

$$n^2(\lambda)=1+\sum_{i=1}^{3}\frac{\left[SA_i+X\left(GA_i-SA_i\right)\right]\lambda^2}{\lambda^2-\left[SB_i+X\left(GB_i-SB_i\right)\right]^2}\,, \qquad (\mathbf{A}.\text{II}.2)$$

where *SA*, *SB*, *GA* and *GB* are the Sellmeier coefficients for the SiO_2 and GeO_2 glasses, respectively, and *X* is the mole fraction of GeO_2.

Table A.II.1. Sellmeier coefficients for the SiO_2, GeO_2, SiO_2 + 1% F and SiO_2 + 2% F materials, [165, 166].

Glass	A_1	B_1	A_2	B_2	A_3	B_3
SiO_2	0.69616630	0.068404300	0.40794260	0.11624140	0.89747940	9.8961610
GeO_2	0.80686642	0.068972606	0.71815848	0.15396605	0.85416831	11.841931
SiO_2 + 1% F	0.69325	0.06724	0.39720	0.11714	0.86008	9.7761
SiO_2 + 2% F	0.67744	0.06135	0.40101	0.12030	0.87193	9.8563

For the Fluorine-doped silica, there are not enough values tabulated in the literature as to obtain a fitted equation valid for any Fluorine dopant concentration. With the help of both the tabulated material compositions, we studied the validity of linearly fitting the SiO_2 coefficients with the 1%-F versus with the 2%-F dopant concentration coefficients. Analogously to Eq. (A.II.2), the refractive index will follow the linear fitting expression:

$$n^2(\lambda)=1+\sum_{i=1}^{3}\frac{\left[SA_i+X\left(FA_i-SA_i\right)\right]\lambda^2}{\lambda^2-\left[SB_i+X\left(FB_i-SB_i\right)\right]^2}, \qquad (\mathbf{A}.\text{II}.3)$$

where now the coefficients *FA* and *FB* are those of the 1% or 2% Fluorine doped silica. Figure A.II.1(a) shows the computed refractive index for the 1%-F dopant concentration fitting at the optical wavelength of λ = 1550 nm. Red asterisks correspond to the calculated values from the tabulated Sellmeier coefficients, while blue circles represent the estimated values from Eq. (A.II.3) for the 1%-Fluorine doped Sellmeier coefficients. Figure A.II.1(b) depicts the computed refractive indices for a 2%-F dopant concentration estimated from Eq. (A.II.3) by using the 1%-F dopant concentration Sellmeier coefficients in comparison with the tabulated data for the 2%-Fluorine doped silica from [166]. We observe a significant mismatch between the tabulated and the estimated values.

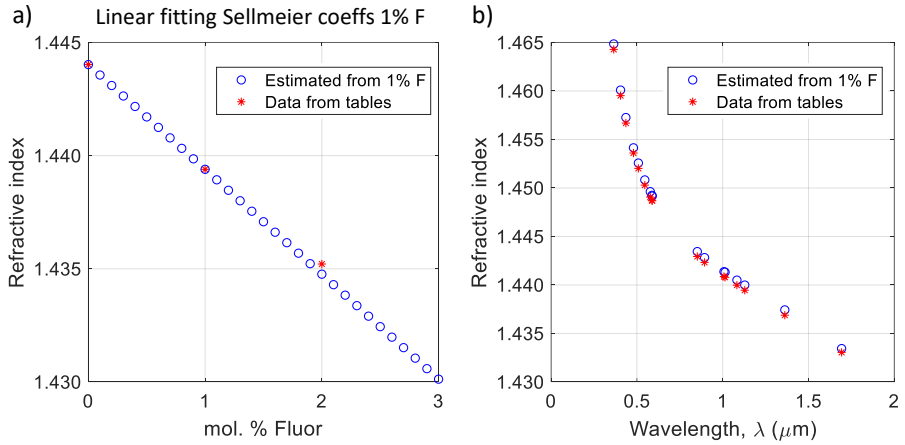

Fig. A.II.1. (a) Computed refractive index for the 1%-F dopant concentration fitting at the optical wavelength of λ = 1550 nm. (b) Computed refractive index for the 2%-F dopant concentration estimated from Eq. (A.II.3) by using the 1%-F dopant concentration Sellmeier coefficients in comparison with the tabulated data for the 2%-Fluorine doped silica from [166].

Figure A.II.2(a) shows the computed refractive index for the 2%-F dopant concentration fitting at the optical wavelength of λ = 1550 nm. Red asterisks correspond to the calculated values from the tabulated Sellmeier coefficients, while blue circles represent the estimated values from Eq. (A.II.3) for the 2%-Fluorine doped Sellmeier coefficients. Figure A.II.2(b) depicts the computed refractive indices for a 1%-F dopant concentration estimated from Eq. (A.II.3) by using the 2%-F dopant concentration Sellmeier coefficients in comparison with the tabulated data for

the 1%-Fluorine doped silica from [166]. In this case, we observe a better correspondence between both the tabulated and the estimated values, what indicates that the linear fitting between the SiO_2 and the SiO_2 + 2%-F Sellmeier coefficients is a better candidate to estimate the refractive indices for non-tabulated Fluorine dopant concentrations.

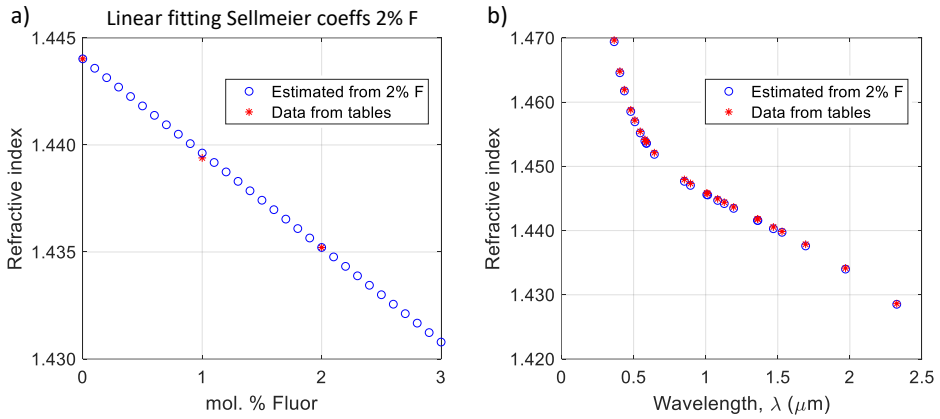

Fig. A.II.2. (a) Computed refractive index for the 2%-F dopant concentration fitting at the optical wavelength of λ = 1550 nm. (b) Computed refractive index for the 1%-F dopant concentration estimated from Eq. (A.II.3) by using the 2%-F dopant concentration Sellmeier coefficients in comparison with the tabulated data for the 1%-Fluorine doped silica from [166].

Author's Publication List

Peer-reviewed international Journal Publications

[J1]. **S. García** and I. Gasulla, "Design of heterogeneous multicore fibers as sampled true-time delay lines," Opt. Letters, vol. 40, no. 4, pp. 621-624, (2015).

[J2]. **S. García** and I. Gasulla, "Multi-cavity optoelectronic oscillators using multicore fibers," Opt. Express, vol. 23, no. 3, pp. 2403-2415, (2015).

[J3]. **S. García** and I. Gasulla, "Dispersion-engineered multicore fibers for distributed radiofrequency signal processing," Opt. Express, vol. 24, no. 18, pp. 20641-20654, (2016).

[J4]. **S. García** and I. Gasulla, "Experimental demonstration of multi-cavity optoelectronic oscillation over a multicore fiber," Opt. Express, vol. 25, no. 20, pp. 23663-23668, (2017).

[J5]. **S. García**, D. Barrera, J. Hervás, S. Sales, and I. Gasulla, "Microwave Signal Processing over Multicore Fiber," Photonics 4, no. 4, 49, (2017).

[J6]. R. Guillem, **S. García**, J. Madrigal, D. Barrera and I. Gasulla, "Few-mode fiber true time delay lines for distributed radiofrequency signal processing," Opt. Express, vol. 26, no. 20, pp. 25761-25768, (2018).

[J7]. **S. García**, R. Guillem, J. Madrigal, D. Barrera, S. Sales and I. Gasulla, "Sampled true time delay line operation by inscription of long period gratings in few-mode fibers," Opt. Express, vol. 27, no. 16, pp. 22787-22793, (2019).

[J8]. **S. García**, R. Guillem and I. Gasulla, "Ring-core few-mode fiber for tunable true time delay line operation," Opt. Express, vol. 27, no. 22, pp. 31773-31782, (2019).

[J9]. **S. García**, M. Ureña and I. Gasulla, "Bending and twisting effects on multicore fiber differential group delay," Opt. Express, vol. 27, no. 22, pp. 31290-31298, (2019).

[J10]. **S. García** and I. Gasulla, "Universal characteristic equation for multi-layer optical fibers," Special issue on Emerging Applications of Multimode, Multicore and Specialty Fibers of the IEEE Journal of Selected Topics in Quantum Electronics, (2020).

International Conference Publications

[C1]. **S. García** and I. Gasulla, "Crosstalk-optimized multicore fiber true time delay lines," in proceedings of 2015 International Topical Meeting on Microwave Photonics (MWP), Paphos, Cyprus, (2015).

[C2]. **S. García** and I. Gasulla, "Application of Multicore fibers to Microwave Photonics," in proceedings of 36th Progress in Electromagnetics Research Symposium, Prague, Czech Republic, (2015).

[C3]. I. Gasulla, D. Barrera, J. Hervás, **S. García**, and S. Sales, "Multi-cavity microwave photonics devices built upon multicore fibres," in proceedings of 2016 18th International Conference on Transparent Optical Networks (ICTON), Trento, Italy, (2016). (Invited).

[C4]. **S. García** and I. Gasulla, "Distributed radiofrequency signal processing using multicore fibers", SPIE/COS Photonics Asia 2016, Beijing, China, (2016). (Invited).

[C5]. I. Gasulla and **S. García**, "Multicore fibers for distributed signal processing," International Conference on Optoelectornics and Microelectronics Technology and Application (MPTA 2016), Shanghai, China, (2016). (Invited).

[C6]. **S. García** and I. Gasulla, "Dispersion-engineered heterogeneous multicore fibers for true time delay operation," in proceedings of 2016 International Topical Meeting on Microwave Photonics (MWP), Long Beach, US, (2016).

[C7]. **S. García** and I. Gasulla, "Dispersion-optimized multicore fiber true time delay for icrowave signal processing," in proceedings of 2016 IEEE Photonics Conference (IPC), Hawaii, US, (2016).

[C8]. I. Gasulla, **S. García**, D. Barrera, J. Hervás, and S. Sales, "Fiber-distributed signal processing: Where the space dimension comes into play," in Advanced Photonics 2017, New Orleans, US, (2017). (Invited).

[C9]. I. Gasulla, **S. García**, D. Barrera, J. Hervás, and S. Sales, "Space-division Multiplexing for fiber-wireless communications," in proceedings of 2017 19th International Conference on Transparent Optical Networks (ICTON), Girona, Spain, (2017). (Invited).

[C10]. I. Gasulla, **S. García**, D. Barrera, J. Hervás, and S. Sales, "Selective grating inscription in multicore fibers for radiofrequency signal processing," in Proceedings of 2017 Optical Fiber Communications Conference (OFC), Los Angeles, US, W4B.6, (2017).

[C11]. **S. García**, J. Hervás, and I. Gasulla, "Demonstration of multi-cavity optoelectronic oscillators based on multicore fibers," in proceedings of 2017 International Topical Meeting on Microwave Photonics (MWP), Beijing, China, (2017).

[C12]. **S. García** and I. Gasulla, "RF photonic delay lines using space-division multiplexing," Steep Dispersion Engineering and Opto-Atomic Precision Metrology XI, San Francisco, California (United States), (2018).

[C13]. **S. García**, M. Ureña, R. Guillem and I. Gasulla, "Multicore fiber delay line performance against bending and twisting effects," in proceedings of 2018 European Conference on Optical Communication (ECOC), Rome, Italy, (2018).

[C14]. **S. García**, R. Guillem, J. Madrigal, D. Barrera, S. Sales and I. Gasulla, "Few-mode fibre delay lines with inscribed long period gratings for radiofrequency signal processing," in proceedings of 2019 European Conference on Optical Communication (ECOC), Dublin, Ireland, (2019).

[C15]. **S. García**, R. Guillem and I. Gasulla, "Few-mode fiber true time delay lines," in proceedings of 2019 International Conference on Transparent Optical Networks (ICTON), Angers, France, (2019). (Invited).

[C16]. **S. García**, M. Ureña and I. Gasulla, "Demonstration of distributed radiofrequency signal processing on heterogeneous multicore fibres," in proceedings of 2019 European Conference on Optical Communication (ECOC), Dublin, Ireland, (2019).

[C17]. **S. García**, M. Ureña and I. Gasulla, "Heterogeneous multicore fiber for optical beamforming," in proceedings of 2019 International Topical Meeting on Microwave Photonics (MWP), Ottawa, Canada, (2019).

[C18]. **S. García**, R. Guillem, M. Ureña and I. Gasulla, "Space division multiplexing for microwave photonics," in proceedings of 2019 OptoElectronics and Communications Conference (OECC) and 2019 International Conference on Photonics in Switching and Computing (PSC), Fukuoka, Japan, (2019).

[C19]. M. Ureña, **S. García** and I. Gasulla, "Space-division multiplexing fibers for microwave signal processing," to be presented at 2020 Conference on Lasers and Electro-Optics (CLEO), San José, US, (2020). (Invited).

[C20]. **S. García**, R. Guillem, M. Ureña and I. Gasulla, "Space-division multiplexing fibers for radiofrequency signal processing," to be presented at 2020 IEEE Summer Topical Meeting, Cabo San Lucas, Mexico, (2020). (Invited).

[C21]. **S. García**, M. Ureña and I. Gasulla, "Microwave signal processing along a heterogeneous multicore fiber," to be presented at 2020 International Conference on Transparent Optical Networks (ICTON), Bari, Italy. (Invited).

References

[1] M. Agiwal, A. Roy and N. Saxena, "Next generation 5G wireless networks: a comprehensive survey," *IEEE Communications Surveys & Tutorials,* vol. 18, no. 3, pp. 1617-1655, 2016.

[2] S. Rommel, T. R. Raddo and I. Tafur, "The fronthaul infrastructure of 5G mobile networks," *in proceedings of 2018 IEEE 23rd International Workshop on Computer Aided Modeling and Design of Communication Links and Networks (CAMAD),* pp. 1-6, 2018.

[3] S. Rommel, D. Perez-Galacho, J. M. Fabrega, R. Muñoz, S. Sales and I. T. Monroy, "High-capacity 5G fronthaul networks based on optical space division multiplexing," *IEEE Transactions on Broadcasting,* vol. 65, no. 2, pp. 434-443, 2019.

[4] K. Zeb, X. Zhang and Z. Lu, "High capacity mode division multiplexing based MIMO enabled all-optical analog millimeter-wave over fiber fronthaul architecture for 5G and Beyond," *IEEE Access,* vol. 7, pp. 89522-89533, 2019.

[5] A. Checko, H. L. Christiansen, Y. Yan, L. Scolari, G. Kardaras, M. S. Berger and L. Dittmann, "Cloud RAN for mobile networks - a technology overview," *IEEE Commun. Surveys Tuts.,* vol. 17, no. 1, pp. 405-426, 2015.

[6] I. A. Alimi, A. L. Teixeira and P. P. Monteiro, "Toward an efficient C-RAN optical fronthaul for future networks: A tutorial on technologies, requirements, challenges, and solutions," *IEEE Commun. Surveys Tuts.,* vol. 20, no. 1, pp. 708-769, 2018.

[7] K. Nakajima, T. Matsui, K. Saito, T. Sakamoto and N. Araki, "Space division multiplexing technology: Next generation optical communication strategy," *in proceedings of 2016 ITU Kaleidoscope: ICTs for a Sustainable World (ITU WT),* pp. 1-7, 2016.

[8] C. Kuhlins, B. Rathonyi, A. Zaidi and M. Hogan, "Cellular networks for massive IoT," *Ericsson white paper,* 2020.

[9] M. S. Moreolo, J. M. Fabrega, L. Nadal, R. Martínez and R. Casellas, "Synergy of photonic technologies and software-defined networking in the

hyperconnectivity era," *Journal of Lightwave Technology,* vol. 37, no. 16, pp. 3902-3910, 2019.

[10] J. Yao, "Microwave photonics," *Journal of Lightwave Technology,* vol. 27, no. 3, pp. 314-335, 2009.

[11] D. Novak and J. Capmany, "Microwave photonics combines two worlds," *Nature Photonics,* pp. 319-330, 2007.

[12] J. Capmany, J. Mora, I. Gasulla, J. Sancho, J. Lloret and S.Sales, "Microwave photonics signal processing," *Journal of Lightwave Technology,* vol. 31, no. 4, pp. 571-586, 2013.

[13] D. Novak, "The evolution of Microwave Photonics," *IEEE Microwave Magazine,* pp. 8-12, 2009.

[14] D. Marpaung, J. Yao and J. Capmany, "Integrated microwave photonics," *Nature Photonics,* pp. 80-90, 2019.

[15] S. Iezekiel, M. Burla, J. Klamkin, D. Marpaung and J. Capmany, "RF engineering meets optoelectronics," *IEEE Microwave Magazine,* pp. 28-45, 2015.

[16] J. Capmany, G. Li, C. Lim and J. Yao, "Microwave photonics: current challenges towards widespread application," *Optics Express,* vol. 21, no. 19, pp. 22862-22867, 2013.

[17] A. Seeds, "Microwave photonics," *IEEE Transactions on Microwave Theory and Techniques,* vol. 50, no. 3, pp. 877-887, 2002.

[18] J. Capmany, B. Ortega and D. Pastor, "A tutorial on microwave photonic filters," *Journal of Lightwave Technology,* vol. 24, no. 1, pp. 201-229, 2006.

[19] H. Rousell and R. Helkey, "Optical frequency conversion using a linearized LiNbO3 modulator," *IEEE Microwave Guided Wave Letters,* vol. 8, no. 11, pp. 408-410, 1998.

[20] J. Chou, Y. Han and B. Jalali, "Adaptative RF-photonic arbitrary waveform generator," *IEEE Photonics Technology Letters,* vol. 15, no. 4, pp. 581-583, 2003.

[21] H. Zmuda, R. A. Soref, P. Payson, S. Johns and E. N. Toughilian, "Photonic beamformer for phased array antennas using a fiber grating prism," *IEEE Photonics Technology Letters,* vol. 9, no. 2, pp. 241-243, 1997.

[22] Y. Han and B. Jalali, "Photonic time-stretched analog-to-digital converter: fundamental concepts and practical considerations," *Journal of Lightwave Technology,* vol. 21, no. 12, pp. 3085-3103, 2003.

[23] D. Marpaung, C. Roeloffzen, R. Heideman, A. Leinse, S. Sales and J. Capmany, "Integrated microwave photonics," *Lasers Photon. Rev.*, vol. 7, no. 4, pp. 506-538, 2013.

[24] T. R. Raddo, S. Rommel, B. Cimoli and I. T. Monroy, "The optical fiber and mmWave wireless convergence for 5G fronthaul networks," *in proceedings of 2019 IEEE 2nd 5G World Forum (5GWF)*, pp. 607-612, 2019.

[25] D. Novak, R. B. Waterhouse, A. Nirmalathas, C. Lim, P. A. Gamage, T. R. Clark, M. L. Dennis and J. A. Nanzer, "Radio-over-fiber technologies for emerging wireless systems," *IEEE Journal of Quantum Electronics*, vol. 52, no. 1, pp. 1-12, 2016.

[26] A. J. Seeds and K. J. Williams, "Microwave photonics," *Journal of Lightwave Technology*, vol. 24, no. 12, pp. 4628 - 4641, 2006.

[27] R. A. Minasian, "Photonic signal processing of microwave signals," *IEEE Transactions on Microwave Theory and Techniques*, vol. 54, no. 2, pp. 832-846, 2006.

[28] X. Yi and R. Minasian, "Microwave photonics for analog signal processing," in *in proceedings of International Conference on Optical Communications and Networks (ICOCN)*, Nanjing, 2015.

[29] R. Waterhouse and D. Novak, "Realizing 5G: Microwave Photonics for 5G mobile wireless systems," *IEEE Microwave Magazine*, vol. 16, no. 8, pp. 84-92, 2015.

[30] R. A. Minasian, "Advances in microwave photonic signal processing for 5G and IoT Keynote Paper," *in proceedings of 2018 28th International Telecommunication Networks and Applications Conference (ITNAC)*, pp. 1-4, 2018.

[31] J. Capmany, B. Ortega, D. Pastornd and S. Sales, "Discrete-time optical processing of microwave signals," *Journal of Lightwave Technology*, vol. 23, no. 2, pp. 702-723, 2005.

[32] I. Frigyes and A. J. Seeds, "Optically generated true-time delay in phased-array antennas," *IEEE Transactions on Microwave Theory and Techniques*, vol. 43, no. 9, pp. 2378-2386, 1995.

[33] W. Ng, A. A. Walston, G. L. Tangonan, J. J. Lee, I. L. Newberg and N. Bernstein, "The first demonstration of an optically steered microwave phased array antenna using true-time-delay," *Journal of Lightwave Technology*, vol. 9, no. 9, pp. 1124-1131, 1991.

[34] K. E. Alameh, R. A. Minasian and N. Fourikis, "High capacity optical interconnects for phased array beamformers," *Journal of Lightwave Technology,* vol. 13, no. 6, pp. 1116-1120, 1995.

[35] R. Esman, M. Y. Frankel, J. L. Dexter, L. Goldberg, M. G. Parent, D. Stilwell and D. G. Cooper, "Fiber-optic prism true time-delay antenna feed," *IEEE Photonics Technology Letters,* vol. 5, no. 11, pp. 1347-1349, 1993.

[36] A. Molony, C. Edge and I. Bennion, "Fibre grating time delay element for phased array antennas," *Electronics Letters,* vol. 31, no. 17, pp. 1485-1486, 1995.

[37] C. Wang and J. Yao, "Fiber Bragg gratings for microwave photonics subsystems," *Optics Express,* vol. 21, no. 19, pp. 22868-22884, 2013.

[38] P. A. Morton and J. B. Khurgin, "Microwave photonic delay line with separate tuning of the optical carrier," *Photonics Technology Letters,* vol. 21, no. 22, pp. 1686-1688, 2009.

[39] J. Sanho, J. Bourderionnet, J. Lloret, S. Combrié, I. Gasulla, S. Xavier, S. Sales, P. Colman, G. Lehoucq, D. Dolfi, J. Capmany and A. D. Rossi, "Integrable microwave filter based on a photonic crystal delay line," *Nature Communications,* vol. 3, p. 1075, 2012.

[40] F. Ohman, K. Yvind and J. Mork, "Slow light in a semiconductor waveguide for true-time delay applications in microwave photonics," *Photonics Technology Letters,* vol. 19, no. 15, pp. 1145-1147, 2007.

[41] B. Skubic, M. Fiorani, S. Tombaz, A. Furuskär, J. Mårtensson and P. Monti, "Optical transport solutions for 5G fixed wireless access," *IEEE/OSA Journal of Optical Communications and Networking,* vol. 9, no. 9, pp. D10-D18, 2017.

[42] G. Kalfas, C. Vagionas, A. Antonopoulos, E. Kartsakli, A. Mesodiakaki, S. Papaioannou, P. Maniotis, J. Vardakas, C. Verikoukis and N. Pleros, "Next generation fiber-wireless fronthaul for 5G mmWave networks," *IEEE Communications Magazine,* vol. 57, no. 3, pp. 138-144, 2019.

[43] Z. G. Tegegne, C. Decroze, P. D. Bin, T. Fromenteze and C. Aupetit-Berthelemot, "Single channel microwave photonics digital beamforming radar imaging system," *Journal of Lightwave Technology,* vol. 36, no. 3, pp. 675-681, 2018.

[44] J. Yao, "A tutorial on Microwave Photonics," *IEEE Photonics Society Newsletter,* pp. 5-12, 2012.

[45] R. J. Mailloux, Phased array antenna handbook, 2nd edition, Artech House Publishing Co., 2000.

[46] X. S. Yao and L. Maleki, "Converting light into spectrally pure microwave oscillation," *Optics Letters*, vol. 21, no. 7, pp. 483-485, 1996.

[47] X. S. Yao and L. Maleki, "Optoelectronic microwave oscillator," *J. Opt. Soc. Am. B*, vol. 13, no. 8, pp. 1725-1735, 1996.

[48] X. S. Yao and L. Maleki, "Optoelectronic oscillator for photonic systems," *IEEE Journal of Quantum Electronics*, vol. 32, no. 7, pp. 1141-1149, 1996.

[49] X. S. Yao, L. Maleki, Y. Ji, G. Lutes and M. Tu, "Dual-loop opto-electronic oscillator," *IEEE International Frequency Control Symposium*, pp. 545-549, 1998.

[50] X. S. Yao and L. Maleki, "Multiloop optoelectronic oscillator," *IEEE Journal of Quantum Electronics*, vol. 36, no. 1, pp. 79-84, 2000.

[51] L. Maleki, "Sources: The optoelectronic oscillator," *Nature Photonics*, vol. 5, no. 12, pp. 728-730, 2011.

[52] L. Li, G. Wang, J. Zhang and J. Yao, "A parity-time-symmetric optoelectronic oscillator based on dual-wavelength carriers in a single spatial optoelectronic loop," *in proceedings of 2019 International Topical Meeting on Microwave Photonics (MWP)*, pp. 1-4, 2019.

[53] A. B. Matsko, L. Maleki, A. A. Savchenkov and V. S. Ilchenko, "Whispering gallery mode based optoelectronic microwave oscillator," *Journal of Modern Optics*, vol. 50, no. 15-17, pp. 2523-2542, 2003.

[54] K. Volyanskiy, P. Salzenstein, H. Tavernier, M. Pogurmirskiy, Y. K. Chembo and L. Larger, "Compact optoelectronic microwave oscillators using ultra-high Q whispering gallery mode disk-resonators and phase modulation," *Optics Express*, vol. 18, no. 21, pp. 22358-22363, 2010.

[55] D. Eliyahu, W. Liang, E. Dale, A. A. Savchenkov, V. S. Ilchenko, A. B. Matsko, D. Seidel and L. Maleki, "Resonant widely tunable opto-electronic oscillator," *IEEE Photonics Technology Letters*, vol. 25, no. 15, pp. 1535-1538, 2013.

[56] K. Saleh, R. Henriet, S. Diallo, G. Lin, R. Martinenghi, I. V. Balakireva, P. Salzenstein, A. Coillet and Y. K. Chembo, "Phase noise performance comparison between optoelectronic oscillators based on optical delay lines and whispering gallery mode resonators," *Optics Express*, vol. 22, no. 26, pp. 32158-32173, 2014.

[57] M. Aspelmeyer, T. J. Kippenberg and F. Marquardt, "Cavity optomechanics," *Reviews of Modern Physics*, vol. 86, no. 4, pp. 1391-1452, 2014.

[58] X. S. Yao and L. Maleki, "Dual microwave and optical oscillator," *Optics Letters*, vol. 22, no. 24, pp. 1867-1869, 1997.

[59] X. S. Yao, L. Davis and L. Maleki, "Coupled optoelectronic oscillators for generating both RF signals and optical pulses," *Journal of Lightwave Technology,* vol. 18, no. 1, pp. 73-78, 2000.

[60] J. Tang, T. Hao, W. Li, D. Domenech, R. Baños, P. Muñoz, N. Zhu, J. Capmany and M. Li, "Integrated optoelectronic oscillator," *Optics Express,* vol. 26, no. 9, pp. 12257-12265, 2018.

[61] I. Kaminow, T. Li and A. Willner, Optical fiber telecommunications VI, 6 ed., vol. A and B, 2013.

[62] D. J. Richardson, J. M. Fini and L. E. Nelson, "Space-division multiplexing in optical fibers," *Nature Photonics,* vol. 7, pp. 354-362, 2013.

[63] R. J. Essiambre, R. Ryf, N. K. Fontaine and S. Randel, "Breakthroughs in Photonics 2012: Space-division multiplexing in multimode and multicore fibvers for high-capacity optical communications," *IEEE Photonics Journal,* vol. 5, no. 2, 2013.

[64] D. J. Richardson, "New optical fibres for high-capacity optical communications," *Philosophical Transaction of the Royal Society A: Mathematical, Physical and Engineering Sciences,* vol. 374, 2016.

[65] P. J. Winzer, "Making spatial multiplexing a reality," *Nature Photonics,* vol. 8, pp. 345-348, 2014.

[66] J. M. Kahn and D. A. B. Miller, "Communications expands its space," *Nature Photonics,* vol. 11, pp. 5-8, 2017.

[67] R. Kawamura and Y. Miyamoto, "NTT technical review," [Online]. Available: https://www.ntt-review.jp/archive/ntttechnical.php?contents=ntr201706fa1.html.

[68] G. Li, N. Zhao and C. Xia, "Space-division multiplexing: the next frontier in optical communication," *Advances in Optics and Photonics,* vol. 6, pp. 413-487, 2014.

[69] R. Ryf, N. K. Fontaine, S. Wittek, K. Choutagunta, M. Mazur, H. Chen and J. C. Alvarado-Zacarias, "Recent advances in mode-multiplexed transmission over multimode fibers," *in proceedings of 2019 Conference on Lasers and Electro-Optics (CLEO),* pp. 1-2, 2019.

[70] K. Saitoh and S. Matsuo, "Multicore fiber technology," *Journal of Lightwave Technology,* vol. 34, no. 1, pp. 55-66, 2016.

[71] T. Sakamoto, K. Saitoh, S. Saitoh, K. Shibahara, M. Wada, Y. Abe, A. Urushibara, K. Takenaga, T. Mizuno, T. Matsui, K. Aikawa, Y. Miyamoto and K. Nakajima, "Few-mode multi-core fiber technologies for repeated dense

SDM transmission," *in proceedings of 2018 IEEE Photonics Society Summer Topical Meeting Series (SUM)*, pp. 145-146, 2018.

[72] G. Labroille, B. Denolle, P. Jian, P. Genevaux, N. Treps and J. Morizur, "Efficient and mode selective spatial mode multiplexer based on multi-plane light conversion," *Optics Express*, vol. 22, no. 13, pp. 15599-15607, 2014.

[73] T. A. Birks, I. Gris-Sánchez, S. Yerolatsitis, S. G. Leon-Saval and R. R. Thomson, "The photonic lantern," *Advances in Optics and Photonics*, vol. 7, no. 2, pp. 107-167, 2015.

[74] Z. S. Eznaveh, J. E. Antonio-Lopez, J. C. A. Zacarias, A. Schülzgen, C. M. Okonkwo and R. A. Correa, "All-fiber few-mode multicore photonic lantern mode multiplexer," *Optocs Express*, vol. 25, no. 14, pp. 16701-16707, 2017.

[75] N. K. Fontaine, C. R. Doerr, M. A. Mestre, R. R. Ryf, P. J. Winzer, L. L. Buhl, Y. Sun, X. Jiang and R. L. Jr, "Space-division multiplexing and all-optical MIMO demultiplexing using a photonics integrated circuit," *OFC/NFOEC 2012*, p. PDBPB5B1, 2012.

[76] M. Koshiba, "Design aspects of multicore optical fibers for high-capacity long-haul transmission," *in proceedings of 2014 International Topical Meeting on Microwave Photonics (MWP)*, pp. 318-323, 2014.

[77] B. Zhu, T. Taunay, M. Fishteyn, X. Liu, S. Chandrasekhar, M. F. Yan, J. M. Fini, E. M. Monberg and F. V. Dimarcello, "112-Tb/s Space-division multiplexed DWDM transmission with 14-b/s/Hz aggregate spectral efficiency over a 76.8-km seven-core fiber," *Optics Express*, vol. 19, no. 17, pp. 16665-16671, 2011.

[78] J. Sakaguchi, B. J. Puttnam, W. Klaus, Y. Awaji, N. Wada, A. Kanno, T. Kawanishi, K. Imamura, H. Inaba, K. Mukasa, R. Sugizaki, T. Kobayashi and M. Watanabe, "19-core fiber transmission of 19×100×172-Gb/s SDM-WDM-PDM-QPSK signals at 305Tb/s," *OFC/NFOEC*, pp. 1-3, 2012.

[79] B. J. Puttnam, R. S. Luis, W. Klaus, J. Sakaguchi, J.-M. D. Mendinueta, Y. Awaji, N. Wada, Y. Tamura, T. Hayashi, M. Hirano and J. Marciante, "2.15 Pb/s transmission using a 22 core homogeneous single-mode multi-core fiber and wideband optical comb," *in proceedings of 2015 European Conference on Optical Communication (ECOC)*, pp. 1-3, 2015.

[80] M. Koshiba, K. Saitoh and Y. Kokubun, "Heterogeneous multi-core fibers: proposal and design principle," *IEICE Electronics Express*, vol. 6, no. 2, pp. 98-103, 2009.

[81] T. Mizuno, K. Shibahara, F. Ye, Y. Sasaki, Y. Amma, K. Takenaga, Y. Jung, K. Pulverer, H. Ono, Y. Abe, M. Yamada, K. Saitoh, S. Matsuo, K. Aikawa, M. Bohn, D. J. Richardson, Y. Miyamoto and T. Marioka, "Long-haul dense space-division multiplexed transmission over low-crosstalk heterogeneous

32-core transmission line using a partial recirculating loop system," *Journal of Lightwave Technology,* vol. 35, no. 3, pp. 488-498, 2017.

[82] Y. Sasaki, K. Takenaga, K. Aikawa, Y. Miyamoto and T. Morioka, "Single-mode 37-core fiber with a cladding diameter of 248 μm," *in proceedings of Optical Fiber Communication Conference (OFC), OSA Technical Digest,* no. paper Th1H.2, 2017.

[83] T. Sakamoto, K. Saitoh, S. Saitoh, K. Shibahara, M. Wada, Y. Abe, A. Urushibara, K. Takenaga, T. Mizuno, T. Matsui, K. Aikawa, Y. Miyamoto and K. Nakajima, "Six-mode seven-core fiber for repeated dense space-division multiplexing transmission," *Journal of Lightwave Technology,* vol. 36, no. 5, pp. 1226-1232, 2018.

[84] D. Soma, Y. Wakayama, S. Beppu, S. Sumita, T. Tsuritani, T. Hayashi, T. Nagashima, M. Suzuki, M. Yoshida, K. Kasai, M. Nakazawa, H. Takahashi, K. Igarashi, I. Morita and M. Suzuki, "10.16-Peta-B/s Dense SDM/WDM Transmission Over 6-Mode 19-Core Fiber Across the C+L Band," *Journal of Lightwave Technology,* vol. 36, no. 6, pp. 1362-1368, 2018.

[85] J. v. Weerdenburg, R. Ryf, J. C. Alvarado-Zacarias, R. A. Alvarez-Aguirre, N. K. Fontaine, H. Chen, R. Amezcua-Correa, T. Koonen and C. Okonkwo, "138 Tbit/s Transmission over 650 km Graded-Index 6-Mode Fiber," *in proceedings of 2017 European Conference on Optical Communication (ECOC),* pp. 1-3, 2017.

[86] G. Rademacher, R. S. Luís, B. J. Puttnam, T. A. Eriksson, R. Ryf, E. Agrell, R. Maruyama, K. Aikawa, Y. Awaji, H. Furukawa and N. Wada, "High capacity transmission with few-mode fibers," *Journal of Lightwave Technology,* vol. 37, no. 2, pp. 425-432, 2019.

[87] D. Soma, S. Beppu, Y. Wakayama, K. Igarashi, T. Tsuritani, I. Morita and M. Suzuki, "257-Tbit/s Weakly Coupled 10-Mode C + L-Band WDM Transmission," *Journal of Lightwave Technology,* vol. 36, no. 6, pp. 1375-1381, 2018.

[88] J. Liu, G. Zhu, J. Zhang, Y. Wen, X. Wu, Y. Zhang, Y. Chen, X. Cai, Z. Li, Z. Hu, J. Zhu and S. Yu, "Mode division multiplexing based on ring core optical fibers," *IEEE Journal of Quantum Electronics,* vol. 54, no. 5, pp. 1-18, 2018.

[89] X. Q. Jin, A. Gomez, K. Shi, B. C. Thomsen, F. Feng, G. S. D. Gordon, T. D. Wilkinson, Y. Jung, Q. Kang, P. Barua, J. K. Sahu, S. Alam, D. J. Richardsion, D. C. O'Brien and F. P. Payne, "Mode coupling effects in ring-core fibres for space-division multiplexing systems," *Journal of Lightwave Technology,* vol. 34, no. 14, pp. 3365-3372, 2016.

[90] M. Hirano, Y. Yamamoto, Y. Tamura, T.Haruna and T. Sasaki, "Aeff-enlarged pure-silica-core fiber having ring-core profile," *in proceedings of Optical Fiber Conference (OFC)*, no. Paper OTh4I.2, 2012.

[91] G. P. Agrawal, Fiber-optic communications systems, 4th ed., John Wiley & Sons, 2010.

[92] D. Gloge, "Weakly guiding fibers," *Applied Optics*, vol. 10, no. 10, pp. 2252-2258, 1971.

[93] S. Kawakami and S. Nishida, "Perturbation theory of a doubly clad optical fiber with a low-index inner cladding," *IEEE Journal of Quantum Electronics*, vol. 11, no. 4, pp. 130-138, 1975.

[94] K. C. Kao and G. Hockham, "Dielectric-fibre surface waveguides for optical frequencies," *in proceedings of the Institution of Electrical Engineers*, vol. 113, no. 7, pp. 1151-1158, 1966.

[95] M. Monerie, "Propagation in doubly clad single-mode fibers," *IEEE Journal of Quantum Electronics*, vol. 18, no. 4, pp. 535-542, 1982.

[96] K. Mikoshiba and H. Kajioka, "Transmission characteristics of multimode W-type optical fiber: experimental study of the effect of the intermediate layer," *Applied Optics*, vol. 10, no. 12, pp. 2836-2841, 1978.

[97] S. Kawakami and S. Nishida, "Characteristics of a doubly clad optical fiber with a low-index inner cladding," *Journal of Quantum Electronics*, vol. 10, no. 12, pp. 879-887, 1974.

[98] S. Kawakami, S. Nishida and M. Sumi, "Special issue paper. Transmission characteristics of W-type optical fibres," *in proceedings of the Institution of Electrical Engineers*, vol. 123, no. 6, pp. 586-590, 1976.

[99] E. Snitzer, H. Po, F. Hakimi, R. Tumminelli and B. C. McCollum, "Double clad, offset core Nd fiber laser," *in Proceedings of Optical Fiber Sensors, Vol. 2 of OSA Technical Digest Series*, p. paper PD5, 1988.

[100] R. Romaniuk, "Basic properties of ring-index optical fibers," *in proceedings of SPIE 5028 Optical Fibers and Their Applications VIII*, no. 19-25, 2003.

[101] V. Pelodya and S. K. Raghuwanshi, "Design and parametric study of depressed core optical fiber," *in proceedings of Int. Conf. on Inform. and Comm. Technol. (ICICT 2014)*, pp. 1385-1392, 2014.

[102] M. Hautakorpi and M. Kaivola, "Modal analysis of M-type-dielectric-profile optical fibers in the weakly guiding approximation," *J. Opt. Soc. Am. A*, vol. 22, no. 6, pp. 1163-1169, 2005.

[103] P. Sillard, M. Bigot-Astruc and D. Molin, "Few-mode fibers for mode-division-multiplexed systems," *Journal of Lightwave Technology*, vol. 32, no. 16, pp. 2824-2829, 2014.

[104] B. Ainslie and C. Day, "A review of single-mode fibers with modified dispersion characteristics," *Journal of Lightwave Technology*, vol. 4, no. 8, pp. 967-979, 1986.

[105] P. L. Francois, "Propagation mechanisms in quadruple-clad fibres: mode coupling, dispersion and pure bend losses," *Electron. Lett.*, vol. 19, no. 21, pp. 885-886, 1983.

[106] L. d. Montmorillon, P. Sillard, M. Astruc-Bigot, B. Dany, P. Nouchi, B. Lavigne, E. Balmefrezol, J. Antona and O. Leclerc, "Transmission fiber optimized for metro optical network," *in proceedings of Optical Fiber Communication Conference and Exposition and The National Fiber Optic Engineers Conference, Technical Digest (CD) (Optical Society of America)*, p. paper OFH1, 2005.

[107] P. R. Watekar, L. H. S. Ju and W. T. Han, "A simple and reliable method to determine LP11 cutoff wavelength of bend insensitive fiber," *Optics Express*, vol. 18, no. 13, pp. 13761-13771, 2010.

[108] K. Saitoh, T. Matsui, T. Sakamoto, M. Koshiba and S. Tomita, "Multi-core hole-assisted fibers for high core density space division multiplexing," *in proceedings of OECC 2010 Technical Digest*, pp. 164-165, 2010.

[109] B. Yao, "Reduction of crosstalk by hole-walled multi-core fibers," *in proceedings of Optical Fiber Communication Conference, OSA Technical Digest*, p. paper OM2D.5, 2012.

[110] M. Koshiba, K. Saitoh, K. Takenaga and S. Matsuo, "Analytical expression of average power-coupling coefficients for estimating intercore crosstalk in multicore fibers," *IEEE Photonics Journal*, vol. 4, no. 5, pp. 1987-1995, 2012.

[111] D. Marcuse, "Coupled mode theory of round optical fibers," *The Bell System Technical Journal*, vol. 52, no. 6, pp. 817 - 842, 1973.

[112] A. W. Snyder and J. Love, Optical Waveguide Theory, Springer US, 1983.

[113] D. Marcuse, Theory of dielectric optical waveguides, Second ed., Academic Press, INC, 1991.

[114] A. W. Snyder, "Coupled-mode theory for optical fibers," *Journal of the Optical Society of America*, vol. 62, no. 11, pp. 1267-1277, 1972.

[115] D. Marcuse, "Derivation of coupled power equations," *The Bell System Technical Journal*, vol. 51, no. 1, pp. 229 - 237, 1972.

[116] P. D. McIntyre and A. W. Snyder, "Power transfer between optical fibers," *Journal of the Optical Society of America,* vol. 63, no. 12, pp. 1518-1527, 1973.

[117] B. E. A. Saleh and a. R. M. Abdula, "Optical interference and pulse propagation is multimode fibers," *Fiber and Integrated Optics,* vol. 5, no. 2, pp. 161-201, 1985.

[118] R. Olshansky, "Mode coupling effects in graded-index optical fibers," *Applied Optics,* vol. 14, no. 4, pp. 935-945, 1975.

[119] C. Antonelli, A. Mecozzi, M. Shtaif and a. P. J. Winzer, "Random coupling between groups of degenerate fiber modes in mode multiplexed transmission," *Optics Express,* vol. 21, no. 8, pp. 9484-9490, 2013.

[120] K.-P. Ho and a. J. M. Kahn, "Linear propagation effects in mode-division multiplexing systems," *Journal of Lightwave Technology,* vol. 32, no. 4, pp. 614-628, 2014.

[121] D. Marcuse, "Fluctuations of the power of coupled modes," *The Bell System Technical Journal,* vol. 51, no. 8, pp. 1793 - 1800, 1972.

[122] A. Yariv, "Coupled-mode theory for guided-wave optics," *IEEE Journal of Quantum Electronics,* Vols. QE-9, no. 9, pp. 919-933, 1973.

[123] K. Okamoto, Fundamentals of Optical Waveguides, Elsevier Academic Press, 2006.

[124] D. Gloge, "Optical power flow in multimode fibers," *The Bell System Technical Journal,* vol. 51, no. 8, pp. 1767 - 1783, 1972.

[125] J. A. Arnaud, "Transverse coupling in fiber optics. Part IV: crosstalk," *The Bell System Technical Journal,* vol. 54, no. 8, pp. 1431 - 1450, 1975.

[126] L. Palmieri and A. Galtarossa, "Coupling effects among degenerate modes in multimode optical fibers," *IEEE Photonics Journal,* vol. 6, no. 6, pp. 1-8, 2014.

[127] M. Koshiba, K. Saitoh, K. Takenaga and S. Matsuo, "Multi-core fiber design and analysis: coupled-mode theory and coupled-power theory," *Optics Express,* vol. 19, no. 26, pp. B102 - B111, 2011.

[128] R. O. J. Soeiro, T. M. F. Alves and a. A. V. T. Cartaxo, "Inter-core crosstalk in weakly coupled MCFs with arbitrary core layout and the effect of bending and twisting on the coupling coefficient," *Optics Express,* vol. 27, no. 1, pp. 74-91, 2019.

[129] T. Hayashi, T. Sasaki, E. Sasaoka, K. Saitoh and M. Koshiba, "Physical interpretation of intercore crosstalk in multicore fiber: effects of macrobend,

structure fluctuation, and microbend," *Optics Express,* vol. 21, no. 5, pp. 5401 - 5412, 2013.

[130] J. Tu, K. Saitoh, M. Koshiba, K. Takenaga and S. Matsuo, "Design and analysis of large-effective-area heterogeneous trench-assisted multi-core fiber," *Optics Express,* vol. 20, no. 14, pp. 15157 - 15170, 2012.

[131] A. Macho, M. Morant and R. and Llorente, "Unified model of linear and nonlinear crosstalk in multi-core fiber," *Journal of Lightwave Technology,* vol. 34, no. 13, pp. 3035-3046, 2016.

[132] A. Macho, C. García-Meca, F. J. Fraile-Peláez, M. Morant and R. and Llorente, "Birefringence effects in multi-core fiber: coupled local-mode theory," *Optics Express,* vol. 24, no. 19, pp. 21415-21434, 2016.

[133] C. Antonelli, G. Riccardi, T. Hayashi and A. Mecozzi, "Role of polarization-mode coupling in the crosstalk between cores of weakly-coupled multi-core fibers," *Optics Express,* vol. 28, no. 9, pp. 12847-12861, 2020.

[134] J. Wang, R. Ashrafi, R. Adams, I. Glesk, I. Gasulla, J. Capmany and L. R. Chen, "Subwavelength grating enabled on-chip ultra-compact optical true time delay line," *Scientific Reports,* vol. 6, no. 30235, pp. 1-10, 2016.

[135] J. Tu, K. Saitoh, M. Koshiba, K. Takenaga and S. Matsuo, "Optimized design method for bend-insensitive heterogeneous trench-assisted multi-core fiber with ultra-low crosstalk and high core density," *Journal of Lightwave Technology,* vol. 31, no. 15, pp. 2590-2598, 2013.

[136] J. Tu, K. Long and K. Saitoh, "An efficient core selection method for heterogeneous trench-assisted multi-core fiber," *IEEE Photonics Technology Letters,* vol. 28, no. 7, pp. 810-813, 2016.

[137] J. Mu, L. Han, Z. Yu, L. Liu, X. Wu, H. Yin and X. Song, "Study of trench-assisted single mode optical fiber," *in proceedings of 2013 3rd International Conference on Consumer Electronics, Communications and Networks,* pp. 627-629, 2013.

[138] I. Gasulla and J. Capmany, "Microwave photonics applications of multicore fibers," *IEEE Photonics Journal,* vol. 4, no. 3, pp. 877-888, 2012.

[139] T. Hayashi, T. Taru, O. Shimakawa, T. Sasaki and E. Sasaoka, "Ultra-low-crosstalk multi-core fiber feasible to ultra-long-haul transmission," *in proceedings of 2011 Optical Fiber Communication Conference and Exposition and the National Fiber Optic Engineers Conference,* pp. 1-3, 2011.

[140] X. Zhao, Y. Liu, Z. Liu, Y. Zhao, T. Wang, L. Shen and S. Chen, "Mode converter based on the long-period fiber gratings written in the two-mode fiber," *Optics Express,* vol. 24, no. 6, pp. 6186-6195, 2016.

[141] T. Erdogan, "Cladding-mode resonances in short- and long-period fiber grating filters," *J. Opt. Soc. Am. A*, vol. 14, no. 8, pp. 1760-1773, 1997.

[142] W. J. Bock, I. Gannot and S. Tanev, Optical waveguide sensing and imaging, Springer Science & Business Media, 2007.

[143] R. Slavik, "Coupling to circularly asymmetric modes via long-period gratings made in a standard straight fiber," *Optics Communications*, vol. 275, no. 1, pp. 90-93, 2007.

[144] K. S. Lee and T. Erdogan, "Transmissive tilted gratings for LP01-to-LP11 mode coupling," *Photonics Technology Letters*, vol. 11, no. 10, pp. 1286-1288, 1999.

[145] K. Ogawa, "Simplified theory of the multimode fiber coupler," *Bell System Tech. J.*, vol. 56, no. 5, pp. 729-745, 1977.

[146] P. Sillard, M. Bigot-Astruc, D. Boivin, H. Maerten and L. Provost, "Few-mode fiber for uncoupled mode-division multiplexing transmissions," *in proceedings of 2011 European Conference on Optical Communication (ECOC)*, no. Paper Tu.5.LeCervin.7, 2011.

[147] S. Ramachandran, J. Wagener, R. Espindola and T. Strasser, "Effects of chirp in long period gratings," *in proceedings of Bragg Gratings, Photosensitivity, and Poling in Glass Waveguides 33, Trends in Optics and Photonics Series*, no. paper BE1, 1999.

[148] D. Marcuse, "Influence of curvature on the losses of doubly clad fibers," *Applied Optics*, vol. 21, no. 23, pp. 4208-4213, 1982.

[149] C. Dorrer, N. Belabas, J. Likforman and M. Joffre, "Spectral resolution and sampling issues in Fourier-transform spectral interferometry," *J. Opt. Soc. Am. B*, vol. 17, no. 10, pp. 1795-1802, 2000.

[150] A. Yariv and P. Yeh, Photonics. Optical electronics in modern communications, Chapter 14, Oxford University, 2007.

[151] G. Agrawal, Nonlinear fiber optics, 5th ed., Academic Press, 2013.

[152] G. H. Smith, D. Novak and Z. Ahmed, "Novel technique for generation of optical SSB with carrier using a single MZM to overcome fiber chromatic dispersion," *in proceedings of the 1996 International Topical Meeting on Microwave Photonics (MWP '96), Technical Digest. Satellite Workshop (Cat. No.96TH8153)*, pp. 5-8 suppl, 1996.

[153] P. Merritt, R. P. Tatam and D. A. Jackson, "Interferometric chromatic dispersion measurements on short lengths of monomode optical fiber," *Journal of Lightwave Technology*, vol. 7, no. 4, 1989.

[154] P. Hlubina, M. Kadulová and D. Ciprian, "Spectral interferometry-based chromatic dispersion measurement of fibre including the zero-dispersion wavelength," *J. Europ. Opt. Soc. Rap. Public.*, 2012.

[155] M. Tsubokawa, N. Shibata, T. Higashi and S. Seikai, "Loss of longitudinal coherence as a result of the birefringence effect," *Journal of the Optical Society of America A*, vol. 4, no. 10, pp. 1895-1901, 1987.

[156] G. Bai, T. Hwa, H. Siu, L. Shun and D. Xiao, "Growth of long-period gratings in H2-loaded fiber after 193-nm UV inscription," *IEEE Photonics Technology Letters*, vol. 12, no. 6, pp. 642-644, 2000.

[157] F. Grassi, J. Mora, B. Ortega and J. Capmany, "Subcarrier multiplexing tolerant dispersion transmission system employing optical broadband sources," *Optics Express*, vol. 17, no. 6, pp. 4740-4751, 2009.

[158] T. Bánky, B. Horváth and T. Berceli, "Optimum configuration of multiloop optoelectronic oscillators," *J. Opt. Soc. Am. B*, vol. 23, no. 7, pp. 1371-1380, 2006.

[159] W. Li and J. Yao, "An optically tunable optoelectronic oscillator," *Optics Express*, vol. 28, no. 18, pp. 2640-2645, 2010.

[160] D. Eliyahu and L. Maleki, "Low phase noise and spurious level in multi-loop opto-electronic oscillators," *in proceedings of IEEE International Frequency Control Symposium and PDA Exhibition Jointly with the 17th European Frequency and Time Forum*, pp. 405-410, 2003.

[161] K. Mikitchuk, A. Chizh and S. Malyshev, "Modeling and design of delay-line optoelectronic oscillators," *IEEE Journal of Quantum Electronics*, vol. 52, no. 10, pp. 1-8, 2016.

[162] O. Lelièvre, V. Crozatier, G. Baili, P. Berger, G. Pillet, D. Dolfi, L. Morvan, F. Goldfarb, F. Bretenaker and O. Llopis, "Ultra-low phase noise 10 GHz dual loop optoelectronic oscillator," *in proceedings of 2016 IEEE International Topical Meeting on Microwave Photonics (MWP)*, pp. 106-109, 2016.

[163] I. Gasulla and J. M. Kahn, "Performance of direct-detection mode-group-division multiplexing using fused fiber couplers," *Journal of Lightwave Technology*, vol. 33, no. 9, pp. 1748 - 1760, 2015.

[164] W. Sellmeier, "Zur Erklärung der abnormen Farbenfolge im Spektrum einiger Substanzen," *Annalen der Physik*, vol. 219, no. 6, pp. 272-282, 1871.

[165] J. W. Fleming, "Dispersion in GeO2-SiO2 glasses," *Applied Optics*, vol. 23, no. 24, pp. 4486-4493, 1984.

[166] J. W. Fleming and D. L. Wood, "Refractive index dispersion and related properties in fluorine doped silica," *Applied Optics*, vol. 22, no. 19, pp. 3102-3104, 1983.